Spring 2012

# The dynamics of spanwise vorticity on a rotating flat plate in a starting motion

Craig James Wojcik
*University of Iowa*

# THE DYNAMICS OF SPANWISE VORTICITY ON A ROTATING FLAT PLATE IN A STARTING MOTION

by

Craig James Wojcik

A thesis submitted in partial fulfillment of the
requirements for the Master of Science
degree in Mechanical Engineering
in the Graduate College of
The University of Iowa

May 2012

Thesis Supervisor: Assistant Professor James H. J. Buchholz

Graduate College
The University of Iowa
Iowa City, Iowa

CERTIFICATE OF APPROVAL

---

MASTER'S THESIS

---

This is to certify that the Master's thesis of

Craig James Wojcik

has been approved by the Examining Committee for the thesis requirement for the Master of Science degree in Mechanical Engineering at the May 2012 graduation.

Thesis Committee: _____
James H. J. Buchholz, Thesis Supervisor

_____
Pablo M. Carrica

_____
Albert Ratner

To My Family and Friends

## ACKNOWLEDGEMENTS

First and foremost, I would like to thank Professor James Buchholz for giving me the opportunity to work with him on this project. His guidance, encouragement, and passion for the subject have made this a rich and rewarding experience. I will also like to thank him for extending me the privilege of presenting at several conferences which immersed me in a fruitful environment and enhanced my overall experience. Thanks must also be extended to Professors Pablo Carrica and Albert Ratner for agreeing to serve on my committee and providing valuable insight into this thesis.

I want to also thank my colleagues; James Akkala, Juan Correa, Azar Eslam Panah, and Seyed Mohammad "Haji" Hajimirzaie; for making this a memorable experience.

This journey would not have gone by as smoothly without my friends providing an escape from school work and research when things became too stressful. In that respect, special thanks goes to Jenna Aleo, Jaci Amundsen, Mike Carbone, Nate Chase, Allie Dale, Joe Dvorak, Matt Flannigan, Justin Harrill, Alicia Kouri, Steph Lindeman, Matias Perret, José Ponce, Blake Rasing, Therese Samp, Andy Shaw, Steph Swanson, and Max Van Inwegen.

I want to especially thank my parents for providing an enormous amount of support during this process. I am especially grateful for the many trips they have made to take me to dinner and give me groceries when funds got low.

This work was supported in part through NSF EPSCoR grant EPS1101284 and IIHR - Hydroscience & Engineering.

## ABSTRACT

The starting rotational motion of flat, rectangular plates in quiescent flow was studied experimentally using two-dimensional and stereoscopic particle image velocimetry. The study examined the vortex dynamics of spanwise vorticity created on the suction surface of plates of aspect ratio 2 and 4, which consists primarily of a leading-edge vortex and a region of counter-rotating vorticity on the surface, directly below the leading-edge vortex. Reynolds numbers of 4,000, 8,000, and 16,000 based on the tip velocity and angles of attack of 25°, 35°, and 45° were investigated at five different azimuthal locations ($\psi$ = 90°, 180°, 235°, 270°, and 320°). The 25% and 50% spanwise positions for the aspect ratio 4 plate and 50% spanwise position for the aspect ratio 2 plate were studied. For the 25% and 50% spanwise location for the aspect ratio 4 and 2 plate, respectively, the leading-edge vortex structure's shape and coherence evolve in time as the plate begins its initial motion. The circulation of the leading-edge vortex was found to vary only weakly with azimuthal position in most cases and in many cases, exhibited variations that were commensurate with the circulation of the counter-rotating region beneath it. The leading-edge vortex circulation was shown to be proportional to the theoretical bound circulation of thin airfoil theory with the aspect ratio 2 plate at the 50% spanwise position being approximately 1.25 times greater than the theoretical values while the aspect ratio 4 plate generated circulation values approximately double the theoretical values. It was apparent from these calculations that for both aspect ratios, the ratio of measured to theoretical

circulation values remained relatively constant for azimuthal positions greater than 180°. This also suggests that the leading-edge vortex is, indeed, a significant source of lift on a rotating plate.

Instantaneous distributions of spanwise vorticity show entrainment of the counter-rotating region into the leading-edge vortex. It was therefore hypothesized that the interactions between the leading-edge vortex and counter-rotating vorticity are an important factor in governing the dynamics and strength of the leading-edge vortex which may ultimately determine whether the leading-edge vortex remains attached. To test the hypothesis, a transport analysis of the vorticity in the leading-edge vortex was developed to determine the contributions of spanwise flux, tilting of in-plane vorticity components, the shear layer, and annihilation has on the rate of change of circulation of the leading-edge vortex in the spanwise direction. Results of this analysis indicate that a) contrary to assumptions made in the previous studies, after the initial transient ($\psi \gtrapprox 120°$), although spanwise flow on the order of the tip velocity exists at the measurement locations, it is not necessary to regulate the strength of the leading-edge vortex, and b) annihilation of the leading-edge vortex from entrainment of the counter-rotating vorticity is an important factor in governing the dynamics of the leading-edge vortex.

## TABLE OF CONTENTS

## LIST OF TABLES

Table

## LIST OF FIGURES

Figure

# CHAPTER 1
# INTRODUCTION

Rotating blades and wings can be found in a broad range of natural and engineered systems. For example, the wings of flying animals, such as birds and insects[6, 26, 61, 62, 70, 80, 94] and recent micro-air vehicles (MAVs)[11, 49, 82], experience rotation about a fulcrum at the shoulder or thorax during their flapping motions. Also, wind turbine rotors, helicopter rotors, and propellers experience continuous rotation during operation. Rotating blades and wings have been shown to achieve lift coefficients that are higher than their translating counterparts since stall is delayed until higher angles of attack[3, 57, 98, 105, 106]. In particular, for a National Renewable Energy Laboratory (NREL) S809 airfoil, Tangler [98] showed, as in Figure 1.1, that the lift coefficient increased by as much as $\approx 2.5$ times at some radial positions during rotation compared to the translation case at the same effective angle of attack. However, the fundamental mechanisms by which rotation maintains an attached flow are not fully understood[10, 30, 56, 57]. One dominant and unique feature frequently observed on rotating blades at high angles of attack is the formation of a quasi-steady leading-edge vortex (LEV), fed by a shear layer separating from the leading edge, as shown in Figure 1.2. Such a vortex can enhance lift through the suction created on the upper surface of the wing[85], and may be considered an augmentation to the bound circulation described by aerodynamic theory. In this thesis, the dynamics of the LEV on a rotating blade will be examined in detail while varying the kinematics and geometry of the blade. In particular, through measurements

and analysis of the transport of vorticity within the LEV, it is proposed that the frequently cited role of spanwise advection of vorticity does not necessarily play an important role in stabilizing the LEV. Rather, this work suggests that annihilation of the LEV due to its interaction with vorticity of opposite sign generated beneath the LEV can account for its behavior.

## 1.1 Motivation

The ultimate goal of this research is to provide fundamental insights into the physical mechanisms by which rotation influences flow attachment and aerodynamic loads on rotating blades and wings in unsteady flows. Purely rotating wings have a wide range of applications which include flapping flight, helicopters, and wind turbines. Flapping flight contains the fundamental motion of rotation with the wing rotating about the shoulder of the bird or insect. During this phase of the motion, high angles of attack have been achieved yielding high lift coefficients. Rotational effects have its unmistakable influence on helicopter and wind turbine aerodynamics, where the wing rotates about a central rotation axis.

A particular example in which these rotational effects are important is that of a wind turbine operating under conditions in which the rotor axis is yawed with respect to the local wind direction. Such misalignment results in the airfoil experiencing a time-varying effective angle of attack as it completes a rotation, which can lead to a phenomenon called dynamic stall[52, 53] in which the blade locally exceeds its static stall angle, and a leading-edge vortex is shed and convects over the blade and into the

wake. This phenomenon results in highly unsteady loads which can lead to premature failure of wind turbine structural and drive components[15, 53], and the aerodynamic loads are difficult to predict robustly when the blade is rotating[13, 33, 98]. After preliminary experiments were conducted on a continuously-rotating blade, it was decided that a simpler case to be investigated for the first part of this work is a starting rotation of a blade in a quiescent flow. Recent work by Lentink and Dickinson [57] has demonstrated that the phenomenon of the attached LEV is robust for conditions of starting rotations, periodic flapping, as well as continuous rotation, suggesting that investigation of the phenomenon under any of these conditions will likely yield insight into all of them. The following paragraphs discuss observations of the LEV and the influence of rotation in the contexts of flapping flight and helicopter and wind turbine aerodynamics, demonstrating widespread application for this type of fundamental study.

### 1.1.1 Flapping Flight

Rotation of a blade or wing can be found on flying organisms like birds and insects with the wing rotating about a fulcrum. Over the past 100 years, bird and insect flight has inspired biologists and scientists to investigate the fundamental aerodynamic principles that allow these organisms to maneuver elegantly and efficiently. From millennia of evolution, over a million different insect species and 10,000 birds and bats have developed wings that enable them to fly[25]. Amongst most of these species, flapping flight is the main mechanism that is used to generate lift and thrust.

Yet, flapping flight is one of the most complicated modes of locomotion[40], and a steady aerodynamic analysis shows that there is not enough lift generated to sustain the organism aloft[74, 86, 117, 126]. Instead, some unsteady mechanisms have been proposed to account for the extra lift; such mechanisms include: 1) wing pitching, 2) wake capturing, 3) Weis-Fogh's 'clap and fling' mechanism, and 4) delayed stall affiliated with the attachment of a LEV[2, 31, 40, 72, 87, 96, 123, 124, 125].

The first unsteady mechanism occurs when the wing begins to pitch at the beginning of the upstroke and ending of the downstroke. Dickinson el al [27] and Sun and Tang [94] showed experimentally and computationally that there was a peak in the lift coefficient during the beginning of both downstroke and upstroke. The peaks were said to be accounted for by the quick wing pitching where the wing generates a new layer of strong vorticity over a short period time during supination[94]. Supination describes the wing in the early stages of the upstroke and ending of the downstroke when the wing begins to experience a pitching-up motion.

Wake capturing was first presented as an unsteady mechanism by Dickinson in 1994. His investigations of a single stroke of a two-dimensional flat plate undergoing a flapping motion indicated there was wing-wake interaction during the upstroke. The overlap between the vortex shedding frequency and the stroke kinematics during one stroke was shown to increase the lift production in the following stoke[25]. Further investigations done by Mao and Hamdani [65] demonstrated for a flat plate that the stall vortex did not shed during the rotational stage of the motion, but during the "second" translational stage, the stall vortex and near-wake vortices would create a

small vortex street on the upper surface of the plate. The orientation of the vortices indicated an induced velocity in the direction of the translation, essentially increasing the relative speed of the plate. Since the plate is now moving at a larger speed, the lift coefficient increased providing an unsteady mechanism for lift augmentation.

One of the more prominent unsteady mechanisms explaining enhanced lift generation is the Weis Fogh's 'clap and fling' mechanism. The Weis Fogh's 'clap and fling' mechanism is well documented in the literature[59, 67, 92, 117] and was first proposed by Weis-Fogh [117] which explains the wing to wing interactions. Examining a frontal view of an insect in hovering flight, when the wings are at their apex, the two wings can be approximated theoretically as touching one another; this position is known as the 'clap' stage. In a theoretical two-dimensional approach, when the wings begin to separate from each other during the 'fling' stage, there is a vacuum created in between the wings. The low pressure region in between the wings causes air to rush into the gap creating a significant bound circulation about the wings. This is in contrast to a single "starting" wing which gradually builds bound circulation due to the Wagner effect[112].

The fourth unsteady mechanism is associated with delayed stall of the wing as the LEV remains attached during the upstroke and part of the downstroke. The LEV is created when the wing starts the upstroke as described in the first unsteady mechanism. As the wing continues into the translational motion of the upstroke, the LEV is seen to remain attached[25, 26, 30], but midway through the downstroke, the LEV is lifted from the surface of the wing and is eventually shed due to the negative

spanwise flow created from the tip vortex[34, 35, 81]. It is hypothesized that the LEV is able to remain attached from the von Kármán street created in the wake inducing a velocity in the direction of the translation as demonstrated in Figure 1.5[25]. The results that will be presented will be focusing on the fourth unsteady mechanism where delayed stall occurs.

### 1.1.2 Helicopters

Flow phenomena on a rotating blade are also relevant to helicopter aerodynamics. It is well established that helicopters experience dynamic stall during maneuvers such as turns and pull-ups, forward flight, and in some cases, strong wind gusts[53, 44]. Figure 1.6b shows a helicopter blade moving in a forward flight, and during a single revolution, the blade experiences an asymmetric velocity profile with the blade advancing and retreating in the flow. When the blade is advancing into the flow, the blade experiences lower effective angles of attack due to the higher speeds, while the retreating blade operates at higher effective angles of attack at lower speeds[53]. It is during the retreating part of the motion when the blade starts to go through dynamic stall by the creation of a large LEV that propagates down the chord, increasing the lift of the airfoil. Once the LEV enters the wake, the blade's angle of attack is too large to sustain attach flow, causing the blade to stall. Dynamic stall can lead to hysteresis in the force and moment diagrams, and during deep dynamic stall the blade could experience negative torsional damping which could cause catastrophic failure in the blade[53]. Therefore, several models have been developed to predict the onset

of dynamic stall [9, 16, 18, 32, 54, 55, 73]; however, there are several underlying issues with these models. Theoretical and computational fluid dynamics (CFD) models such as zonal methods[29, 97] are limited in development due to simplifications and assumptions, but the main hindrance is these methods require a significant amount of computational power and time to complete the analysis[84]. Semiempirical models provide a faster method for the prediction of dynamic stall, but most of the data used in the creation of these models are based off incompressible flow approximations for attached conditions and unsteady wind tunnel tests for the dynamic stall conditions[55]. These idealized conditions in the data cause losses in physical realism which limits their applications[55].

### 1.1.3 Wind Turbines

Another application for this type of research is in horizontal-axis wind turbine aerodynamics. The National Renewable Energy Laboratory has performed some studies in order to provide information on the three-dimensional, aerodynamic characteristics of full-scale horizontal-axis wind turbines[38, 89]. Tangler [98, 99] analyzed experimentally-measured pressure distributions on a wind turbine blade and demonstrated higher normal force coefficients at the inboard spanwise locations, presumably due to blade rotation. At approximately the 47% spanwise location, the normal force coefficient drops drastically, and there is an increase in the tangential force coefficient which is an identifiable characteristic of a stalled flow. Tangler claims the trailing-edge vortex, which is thought to be a standing vortex over the downstream portion

of the suction side of the blade, creates a downwash flow causing the flow to remain attached at the inboard spanwise locations by essentially lowers the angle of attack; however, he attributes the stall characteristics at the outboard spanwise locations to a separation of the trailing-edge vortex signifying a more diffuse vorticity in the downstream portion of the blade which reduces the downwash effect and increases the angle of attack which induces stall. With the increased variations in angle of attack along the spanwise direction, the outboard spanwise positions can enter deep stall, characterized by two-dimensional separated flow, while the inboard positions have an attached, three-dimensional flow. Tangler used bound circulation plots, as shown in Figure 1.3, to explain this anomaly by using horseshoe vortex pairs for simplicity at the inboard and outboard locations to indicate the onset of stall. The lift coefficients are therefore affected as seen in Figure 1.4. It is anticipated that the work presented here will help to explain the phenomena presented in Figure 1.3 and 1.4 and will establish the experimental procedures necessary to further investigate that problem.

## 1.2 Thesis Objectives and Overview

In this thesis, the dynamics of spanwise vorticity on a rotating blade are investigated. The blade geometry is simplified to a flat plate to isolate certain effects and to eliminate contributions from blade twist, camber, tapering, and leading-edge features. Experiments were conducted to examine the effects of azimuthal position, angle of attack, Reynolds number, aspect ratio, and spanwise location. Conventional two-dimensional and stereoscopic particle image velocimetry were implemented to

obtain phase-locked velocity field measurements.

Chapter 2 examines the research introduced in the literature and discusses some of the controversies related to conditions under which the LEV should remain attached. In Chapter 3, the experimental methods and examined parameters are discussed. Results are discussed Chapter 4, including qualitative characterization of the behavior of the LEV, measurements of LEV strength, and a vorticity transport analysis in the LEV. Based on this analysis, a new mechanism of LEV stabilization is proposed. Finally, Chapter 5 presents the conclusions and suggests future work in this area.

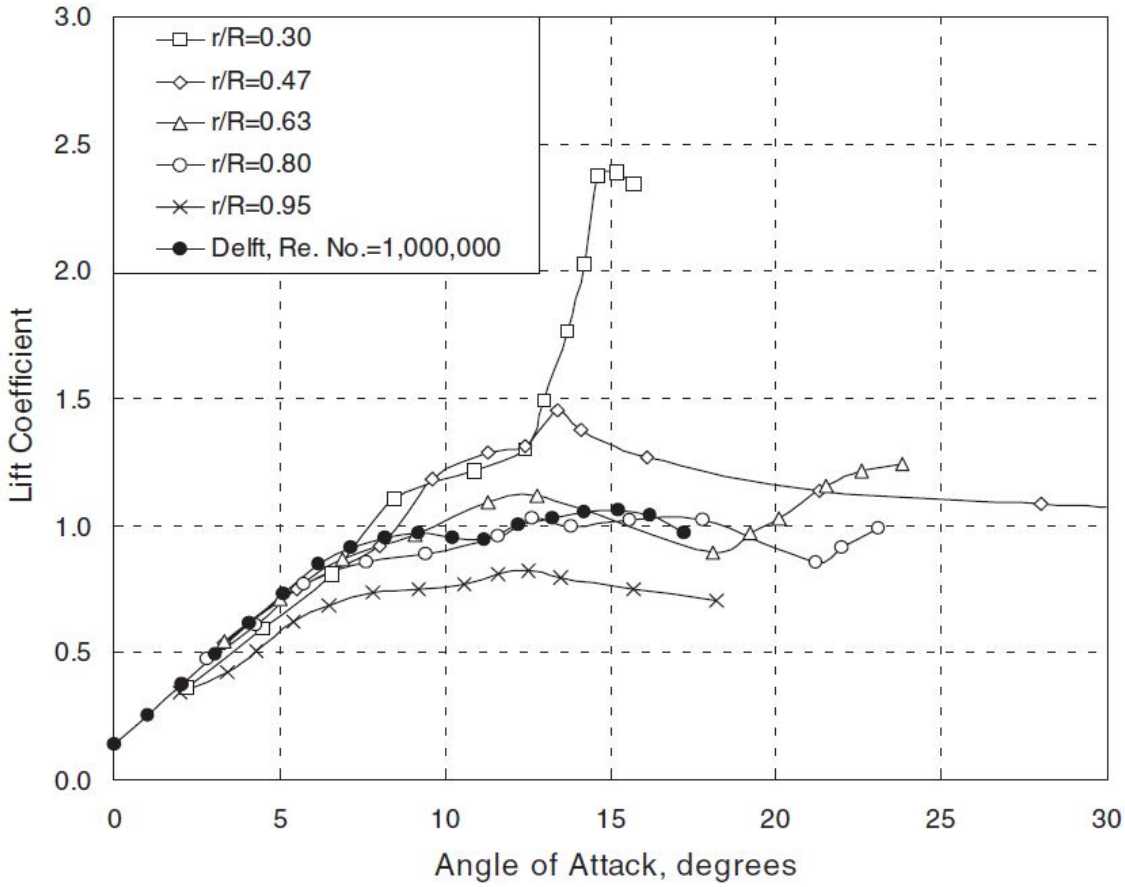


Figure 1.1: Lift coefficients at various spanwise locations for a NREL S809 airfoil in pure rotation. The filled in circles depict the lift coefficients for the two-dimensional wind tunnel tests which represent the translational lift coefficients.

---

Source: Tangler. *WIND ENERGY* **7**, 247-260 (2004).

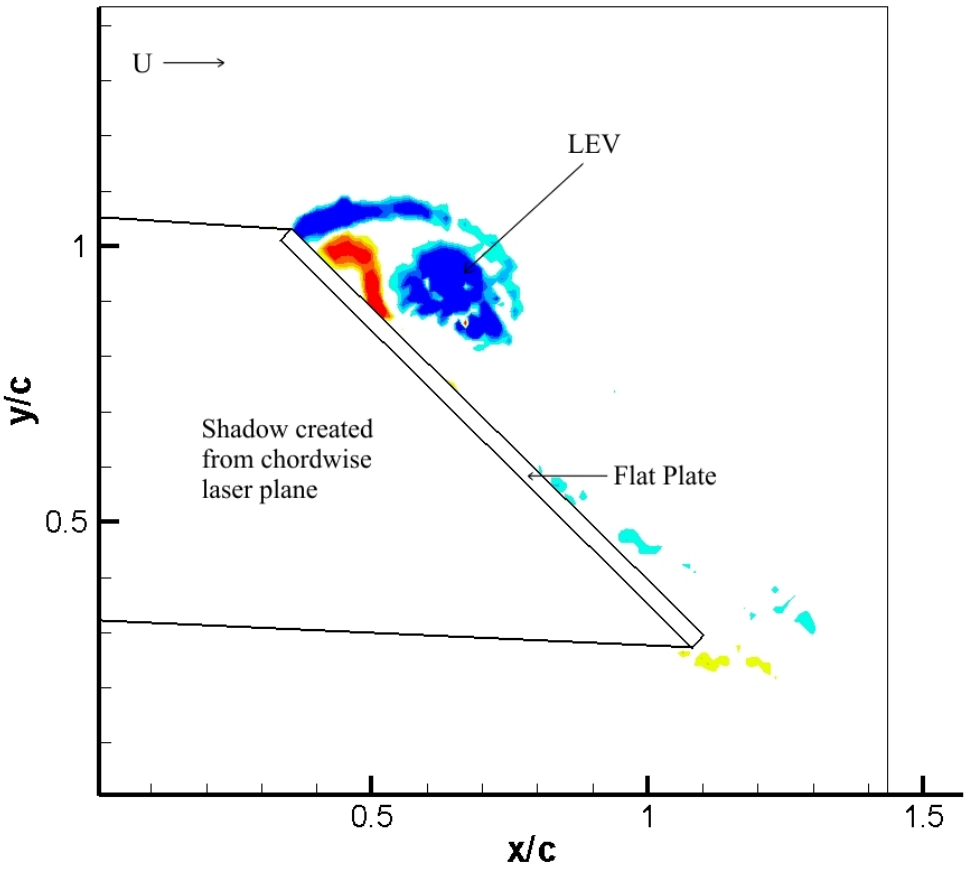


Figure 1.2: Nondimensionalized vorticity plot for an aspect ratio 4 flat plate at an angle of attack of 45°. This vorticity plot shows an instantaneous phase-locked image at an azimuthal position of 235° using conventional two-dimensional digital particle image velocimetry. The relative flow velocity in this plane, U, is from left to right as indicated in the figure. These results are discussed in detail in Chapter 4.

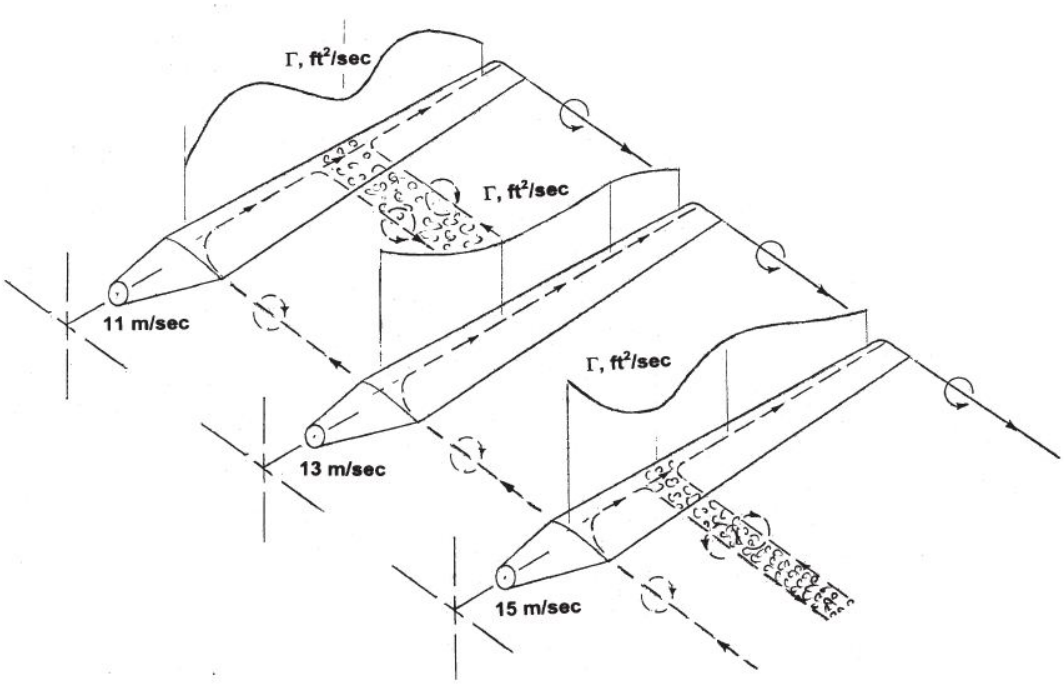


Figure 1.3: Bound circulation plots on a NREL S809 aerofoil obtained from pressure measurement data from the NASA Ames Unsteady Aerodynamic Experiments[38, 89].

---

Source: Tangler. *WIND ENERGY* **7**, 247-260 (2004).

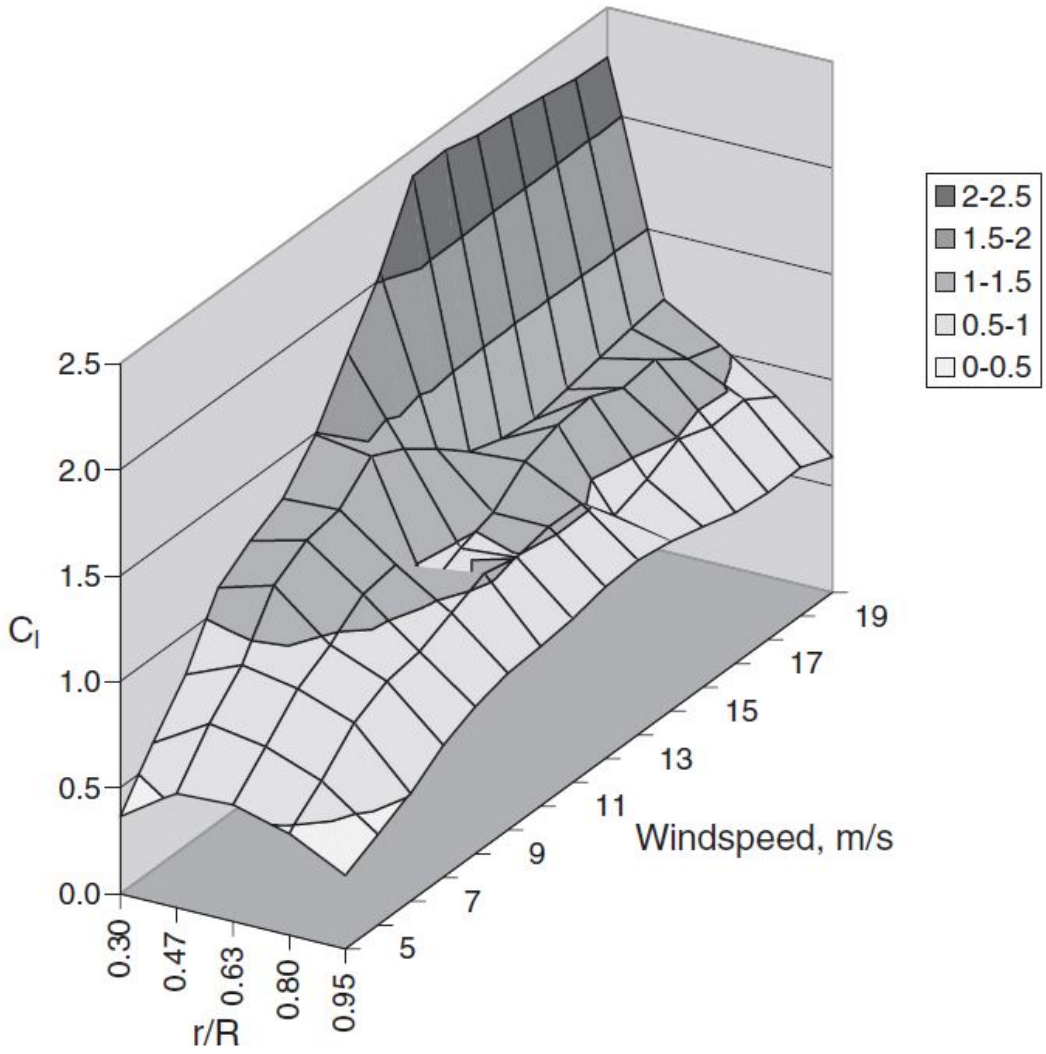


Figure 1.4: Lift coefficients for a NREL S809 aerofoil derived from pressure measurements at various spanwise locations along the surface of the blade.

---

Source: Tangler. *WIND ENERGY* **7**, 247-260 (2004).

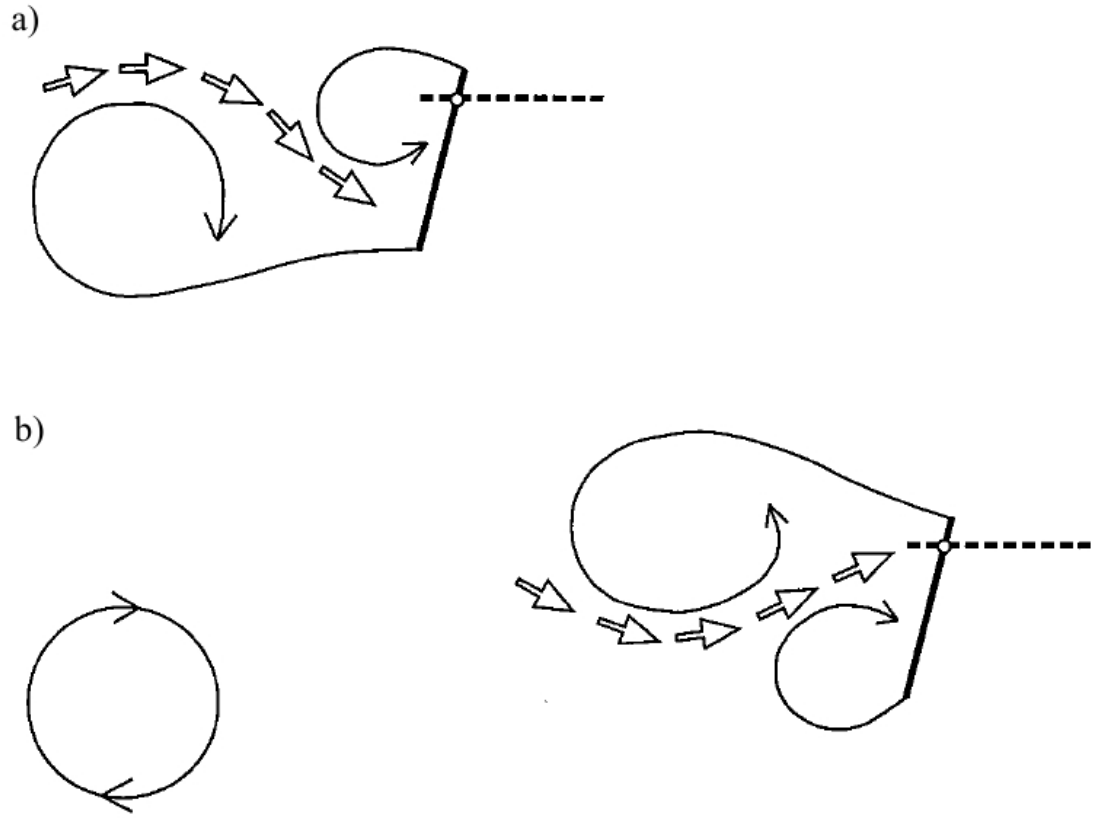


Figure 1.5: A von Kármán street is created in the wake from shedding of alternating trailing- and leading-edge vortices. a) is the start of the upstroke where the trailing-edge vortex is about to be shed into the wake. b) shows in the downstroke of the wing, the shed trailing-edge vortex induces a velocity in the direction of translation. Dickinson (1994) stated that this effect could potentially account for the higher lift values.

---

Source: Dickinson. *J. Exp. Biol.* **192**, 179-206 (1994).

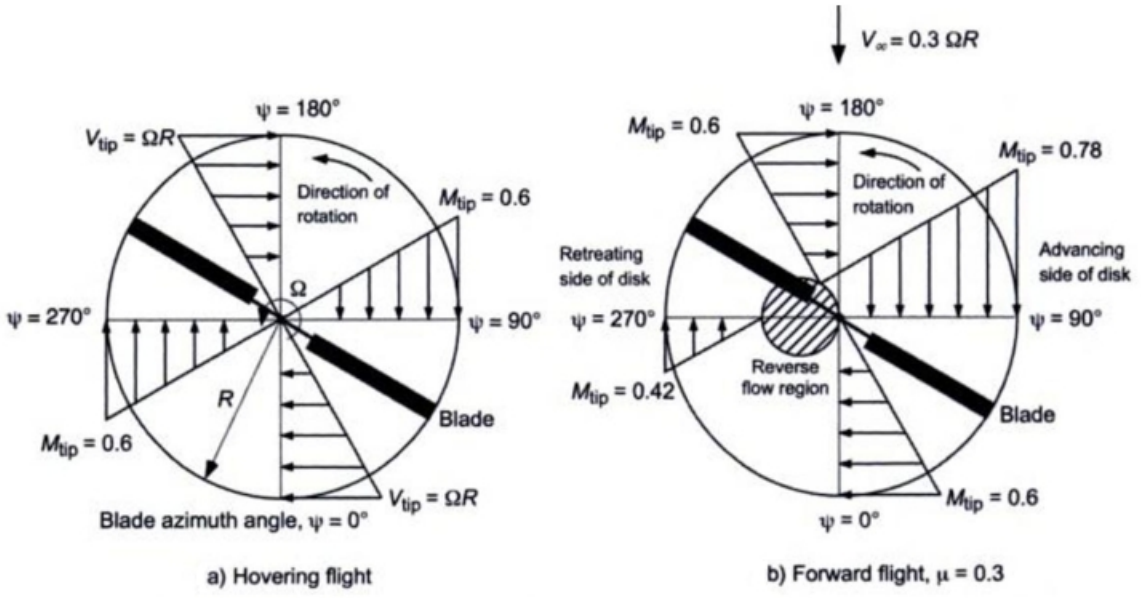


Figure 1.6: A helicopter blade's velocity profiles at varying azimuthal positions during a) hovering flight and b) forward flight. Where $\mu$ in this case is the rotor advance ratio ($U_\infty \cos\alpha / \Omega R$).

---

Source: Leishman. *Principles of Helicopter Aerodynamics* pg. 56 (2006).

# CHAPTER 2
# LITERATURE REVIEW

Chapter 1 showed that rotating blades are found in a broad range of applications. This chapter contains a detailed discussion of the observations of flow structure and aerodynamic performance of rotating blades with a particular emphasis on the basic physical mechanisms governing these observations. The studies will cover idealized representations of bird and insect wings as well as basic fluid mechanics studies isolating starting motions on simplified geometries. Flapping flight studies were considered for their emphasis on the fundamental fluids which is the same approach examined in this thesis. Hypotheses on leading-edge vortex (LEV) attachment will be discussed as well as the flow dynamics of the LEV.

Prior to beginning the discussion, some terminology needs to be explained to provide an understanding of the material. The LEV has been seen taking two major distinct flow patterns in a chordwise plane, "attached" and "shedding". In this particular work, when an LEV is said to be "attached," it is in reference to seeing a single quasi-stationary LEV on the suction surface that is concentrated towards the leading-edge of the wing. The word "stable" is used interchangeably with "attached" and is not meant to regard a stability analysis with bursting of the LEV or vortex breakdown. Lastly, a "shedding" LEV refers to a LEV that is going through a shedding process where multiple vortices are seen progressing in the streamwise direction down the chord of the blade.

## 2.1 Biological Studies

The first accounts of a LEV being observed on a rotating wing were described by Weis-Fogh [117] during his development of the 'clap and fling' model discussed in Section 1.1.1. From there on, several different LEV structures have been observed by various groups[12]. Maxworthy [67, 68, 69] continued studying the Weis-Fogh mechanism where he used particle and dye visualizations to obtain a qualitative flow structure of the LEV along the span of the plate in the initial moments of the 'fling' stage, depicted in Figure 2.1. A single vortex is seen along the surface of the wing which ultimately favorably changes the wing's effective camber and thickness. He claimed that the spanwise pressure gradient establishes a strong spanwise flow from root-to-tip which removes vorticity in the LEV from the inboard spanwise location to the outboard positions and eventually, deposits it into the tip vortex. Maxworthy [67] stated that the vortex at the root of the wings is elevated from the surface, preventing it from producing any useful lift at the inboard spanwise locations[12].

Unlike Maxworthy and Weis-Fogh, Luttges' group observed a different LEV structure on tethered dragonflies, hawkmoths, and mechanical wings[50, 63, 83, 90], where the spiraling, conical LEV structure shown in Figure 2.1 was absent. Instead, they claimed the LEV structure appeared to be uniform in size along the span of the wing. Luttges claimed that there was little to no spanwise flow inside the core of the LEV, and the flow structures were mainly two-dimensional along the length of the wing. Srygley and Thomas [93] performed flow visualizations on *Vanessa atalanta* (butterfly) where they observed a similar type of flow as Luttges' group, and they

claimed the flow is fundamentally different from the conical, spiraling vortices seen in delta wings[14, 19, 122] since the size of the LEV along the span is roughly the same, suggesting a vortex sheet rolling up uniformly and weak spanwise flow. Triantafyllou et al [101] showed experimentally for an oscillating airfoil that the optimal Strouhal number ($\mathrm{St} = f\mathrm{A}/\mathrm{U}$; where $f$ is the frequency of oscillation, $A$ is the width of the wake, and $U$ is average forward velocity) to yield the maximum thrust per unit energy is between $0.25<\mathrm{St}<0.35$ which is similar to natural fish tendencies as shown in Table 2.1. Srygley and Thomas [93] and Taylor et al [100] advocated that since the kinematics of wings are optimized by their Strouhal number, the spanwise flow is not needed unlike in pure revolving cases, and the LEV grows throughout most of the stroke without shedding because the stroke period is shorter than the time it takes for the LEV to become unstable, which is in corroboration with other work presented[48, 58, 103].

Ellington's group (Ellington et al [30], Van den Berg and Ellington [21, 22], and Willmott et al [121]) studied hawkmoth (*Manduca sexta*) wings where they observed a different structure than both Luttges' group and Maxworthy. Ellington's group claimed that the LEV was a three-dimensional structure that was increasing in size from root-to-tip, and Ellington et al [30] said that the spanwise flow was a necessity to maintain an attached LEV over the surface of the wing. They claimed the attachment of the LEV is similar to flow seen over delta wings[20, 64, 71, 76, 118], as shown in Figure 2.2, with the spanwise flow convecting vorticity down the span of the wing, stabilizing the vortex pair on the surface of the delta wing by providing

a sink of vorticity in the out-of-plane direction for a given spanwise position. This allows the vorticity to be transported downstream without the vortices becoming too large. Contrary to Maxworthy's findings, Ellington's group did not observe the LEV at spanwise locations less than 25% which led them to hypothesize that the LEV developed on each of the wings and are not one coherent vortex that stretched over the thorax of the insect. Additionally, Ellington et al [30] observed a strong root-to-tip velocity inside the vortex core which was comparable to the tip velocity of the wing. Ellington claims that the spanwise flow is likely generated by centrifugal acceleration or the induced velocity field created by the spiraling vortex.

Lentink and Dickinson [56, 57] performed a nondimensionalization of the Navier-Stokes equation in a non-inertial reference frame for a purely rotating wing at a constant angular velocity to determine the effects of rotation which is shown in Equation 2.1.

$$\frac{D\mathbf{u}}{D\mathbf{t}} + \frac{1}{Ro} \cdot \mathbf{\Omega} \times (\mathbf{\Omega} \times \mathbf{r}) + \frac{1}{Ro} \cdot 2\mathbf{\Omega} \times \mathbf{u} = -Eu \cdot \mathbf{\nabla p} + \frac{1}{Re} \cdot \mathbf{\nabla}^2 \mathbf{u} \tag{2.1}$$

Where $Eu$ is the Euler number, and the bold symbols represent a nondimensional value; for example $\mathbf{p}$ is the nondimensional pressure. From the nondimensionalization, they showed that the centripetal and Coriolis accelerations (Equations 2.2 and 2.3, respectively) are governed by the inverse of the Rossby number ($Ro = R/c$; where $R$ is the wingtip radius and $c$ is the chord length).

$$a_{cent} = \frac{1}{Ro} \cdot \mathbf{\Omega} \times (\mathbf{\Omega} \times \mathbf{r}) \tag{2.2}$$

$$a_{Cor} = \frac{1}{Ro} \cdot 2\mathbf{\Omega} \times \mathbf{u} \tag{2.3}$$

For the case of translating wings, the Rossby number tends to infinity which makes the contribution from the centripetal and Coriolis acceleration zero. However, the analysis shows that the centripetal and Coriolis accelerations could not be neglected in a rotation case since the Rossby number will be relatively low. Their conclusions supported the idea that spanwise flow caused the LEV to remain attached to the wing, but it is the centripetal and Coriolis accelerations that keep the spanwise flow on the surface of the wing by reorienting the forces in the direction of translation as a result of the spanwise velocity created by the favorable pressure gradient from root-to-tip along the span of wing. Others have also supported that the centripetal and Coriolis accelerations are the reason why the spanwise flow is maintained along the surface of the wing[6, 30, 66]. In addition to the theoretical analysis, Lentink and Dickinson [57] performed bubble visualizations and aerodynamic force measurements on a scaled *Drosophila melanogaster* (fruit fly) wing, and the results showed that the translating wing quickly shed the LEV while at the same time producing less lift when compared to rotating wing. The rotating wing was able to sustain an attached LEV which is extended to a rotating wing undergoing a reciprocating motion. Figure 2.3 shows that by simply rotating the wings, the lift is significantly augmented, resulting in lift coefficients that are approximately twice the translating wing values.

In all of these cases for a purely revolving wing, spanwise flow has been claimed to be the dominate mechanism keeping the LEV attached along the span of the wing.

However, Birch and Dickinson [10] performed a study on a *Drosophila melanogaster* robotic wing that was rotated about a central axis. In their study, they installed fences and baffles along the span of the wing to hinder spanwise flow, and using digital particle image velocimetry, they observed that the LEV still remained attached without spanwise flow. They did note though that the circulation of the LEV did drop in most cases when fences and baffles were introduced, but in one particular case, when a cylindrical wall was placed just on the fringe of the wingtip radius to prevent spanwise flow from the tip vortex, the LEV's circulation increased by 14%. Although spanwise flow was not found inside the vortex core, a large root-to-tip velocity was observed just behind the LEV on the downstream portion of the wing. Therefore, since spanwise flow was hindered and an attached LEV was observed, they hypothesized that the attached flow was maintained by the tip vortex inducing a downwash on the LEV, ultimately pushing it against the surface of the wing. This effect has also been noted by Shyy et al [88] on a flapping flat plate (aspect ratio 4) when the tip vortex was found to create a low pressure region near the tip of the wing, in turn, anchoring the LEV. A physical depiction of the previously mentioned studies can be viewed in Figure 2.4 where the described LEV pattern can be seen from a top view perspective for Maxworthy, Luttges' group, Ellington's group, and Birch and Dickinson's observations in order from top to bottom, respectively.

Another study by Lim et al [60], using a two-dimensional elliptical wing, showed that spanwise flow was observed in most cases, but did not promote the attachment of the LEV. Instead, they demonstrated, using the same cross-sectional

profile wing with a bowed out section in the direction of the oncoming flow, that it was the variability of spanwise flow along the wing which induced vortex stretching thus reduced the pressure in the vortex core and promoted LEV attachment. The vortex stretching enhanced the vorticity magnitude which reduced the vortex core pressure and maintained attachment of the LEV to the wing.

In many of these biological and biomimetic studies, spanwise flow has been observed in flapping and purely rotating cases due to the pressure gradient created along the span of a wing. While this suggests a plausible mechanism for maintaining a stable LEV, other studies have shown that spanwise flow is not essential for the maintenance of an attached LEV. In Section 4.5, a vorticity transport analysis will be presented which shows that spanwise flow is not necessary to maintain a quasi-steady state in the LEV and hence, also not promote its stability.

### 2.1.1 Geometric Variations

Several studies have been conducted on revolving modeled and real wings to isolate the effects that geometry has on the flow physics and to try and control the LEV strength. Altshuler et al [3] did a comparison of aerodynamic force coefficients for various model hummingbird wings with an actual hummingbird wing. Their investigation included examining models of varying camber, sharpness of leading-edge, and thickness at Reynolds numbers of 5,000 and 10,000. Results showed that a symmetrical sharp leading-edge feature was able to produce the highest lift values, which was enhanced even more by wing cambering. Ventral beveling of the leading-

edge produced an asymmetry in the leading-edge which at higher angles of attack produced a bluff surface to the oncoming flow, decreasing the performance of the wing.

Usherwood and Ellington [105, 106] studied a wide range of biological organisms from hawkmoths and mayflies to quails and bumblebees. Contrary to Altshuler et al [3], Usherwood and Ellington varied the leading-edge shape, twist, and camber for hawkmoth wings and saw little variation in the force coefficients. Additionally, the aspect ratio of the hawkmoth wings was varied from 4.53-15.84 and only relatively minor variation in the force coefficients were measured for angles of attack less than 50°. Furthermore, Usherwood [104] compared racing pigeon wings to flat card replicas and saw that the pigeon wing outperformed the flat card replica, achieving lift coefficients of 1.64 while the flat card replica only obtained 1.44. Nevertheless, the two models were able to generate higher lift values than what would be measured in a translating wing study in a wind tunnel.

## 2.2 Basic Fluid Mechanics Research

As previously mentioned, Lentink and Dickinson [56, 57] demonstrated that the mechanism of the LEV attachment is indeed related to rotation and showed that a starting rotation is sufficient to study the phenomenon. Studies have been conducted typically on rectangular flat plates in a starting motion where the plate is placed in a quiescent tank and accelerated through a specified azimuthal angle. Unlike the biological studies which consistently report attached LEVs, these studies

can be broken down into two different categories based on the dynamics of LEV. The first category will be called the "attached" LEV where a single quasi-stationary LEV is observed on the suction surface within a specified distance from the axis of rotation. The other category is classified as the "shedding" LEV where multiple LEVs can be seen along the chord line as they are convected downstream.

### 2.2.1 Attached LEV

Devoria et al [23] studied the starting rotation of two rectangular flat plates of aspect ratio 2 and 4 for Reynolds numbers between 4,000 and 5,600. Their dye visualizations indicated an attached LEV in both cases with a strong spanwise flow inside the LEV from root-to-tip. They noted that the smaller aspect ratio was able to prevent vortex breakdown (bursting) of the LEV longer than the aspect ratio 4 plate. A later study done by Carr et al [17] on the same mechanism using stereoscopic digital particle image velocimetry confirmed the presence of a single LEV near the leading-edge of the plate. Ensemble-averaged measurements at several parallel chordwise planes validated that the LEV was connected to the TEV through the tip vortex, creating a 'horseshoe-like' vortex over the upper surface of the plate, shown in Figure 2.5, which is also observed in their dye visualizations of a trapezoidal wing rotating at an angle of attack of 90°, simulating an idealized caudal fin[24]. For the aspect ratio 4 plate, they observed the LEV lifting from the surface of the plate at approximately the 50% spanwise location and starting to tilt into the streamwise direction. Similar to the dye visualizations done by Devoria et al [23], Carr et al [17] saw that the LEV

was able to remain attached to the surface of the airfoil due to what they claimed to be the tip vortex anchoring the LEV by inducing a downwash, supporting the observations of Shyy et al [88]. More importantly, they observed regions of both a root-to-tip and tip-to-root flow inside the LEV.

Ansari et al [5] also noted an attached, spiraling vortex on an aspect ratio 4 rectangular flat plate between Reynolds numbers of 500 and 15,000. The plate was articulated in a pure rotation motion in a stationary water tank. Their particle image velocimetry measurements show the presence of root-to-tip spanwise flow which is on the order of 80% of the wingtip speed. They also reported that the spanwise flow was more pronounced at lower Reynolds numbers which confirms computational work done by Wilkins and Knowles [119]. Wilkins and Knowles [120] showed for a thin rectangular plate low Reynolds numbers ($5<Re<25$) for a two-dimensional simulation, the LEV attachment is a function of both Reynolds number and angle of attack. Below a Reynolds number of 5 the LEV was not seen developing on the suction surface of the plate. They showed, for a two-dimensional plate at an angle of attack of 45°, the critical Reynolds number before the LEV became unstable was 25. However, when applied to a three-dimensional case, the LEV was stable through the range of Reynolds numbers investigated ($120<Re<30{,}000$). The LEV attachment appeared to be insensitive to Reynolds number and was solely governed by the angle of attack. They also showed that high aspect ratio plates ($>10$), a LEV is not able to remain stable over the whole span.

Ozen and Rockwell [75] looked at an aspect ratio 1 rectangular plate in a qui-

escent flow during a starting motion. Angles of attack from 30°-75° were investigated using two-dimensional particle image velocimetry, and in all cases, a single coherent LEV was seen attached near the leading-edge of the plate. For the extremities of angles of attack, the spanwise flow was measured to be 1.1 to 1.75 times the velocity of the plate at the radius of gyration. The LEV is shown increasing steadily in size and becoming more elevated off the surface with spanwise distance.

Spanwise flow is not always seen in engineering studies. For instance, De Vries [111] studied horizontal-axis wind turbines and claimed that spanwise flow along the blade is only minor and no large scale velocities have been seen. However, in the case of helicopters and wind turbines, spanwise flow has been seen to influence the stall characteristics of the blade[39].

### 2.2.2 Shedding LEV

Several studies have indicated that the LEV is going through a shedding phase where multiple LEVs may be seen convecting down the chord line. Jones and Babinsky [45, 46] studied a flat plate with rounded edges at Re = 10,000 and 60,000. The plate was impulsively started from rest inside a quiescent water channel. They observed a shedding pattern of LEVs, shown in Figure 2.6, where more LEVs can be seen with a higher distance traveled by the plate (x/c). They also indicated that the three-dimensional effects are likely small since the vortex shedding patterns did not vary much along the span. Venkata and Jones [107] showed using dye-visualizations a series of LEVs that are created and convected along the chord line for an aspect

ratio 2 flat plate at a Re = 5,000. They stated that the size of the LEVs was inversely related to the acceleration rates of the plate.

Lastly, Grandlund et al [36] used a nominally two-dimensional plate of aspect ratio 3.4 that was able to freely pivot about its leading-edge from angles of attack of $-45°$ to $45°$ in a rotating motion. Their dye-visualizations showed a pattern of alternating LEVs and TEVs in the wake suggesting the LEV was also going through a shedding phase. They observed little change to the pattern or flow characteristics over the range of Reynolds numbers investigated (5,000 - 30,000)

The summary of the literature presented in this chapter demonstrates significant controversy concerning the physics of the LEV. A clear pattern has not emerged that would enable one to predict under what conditions the LEV will remain attached. If the LEV does remain attached, it is not certain what role, if any, is played by spanwise flow, since attached LEVs have been observed with and without spanwise flow. The observations made in the present work indicate an attached, quasi-stationary LEV at inboard locations with increasing unsteadiness further outboard. One of the major contributions of this work is a vorticity transport analysis of the LEV which supports the hypothesis that spanwise flow is not a primary factor governing attachment of the LEV and suggests a new mechanism based on annihilation of vorticity in the LEV.

Table 2.1: Range of Strouhal numbers and Reynolds numbers used in nature for a variety of biological creatures.

| Genera | Source | Strouhal Number | Reynolds Number |
|---|---|---|---|
| Dace, Trout Goldfish | Bainbridge (1958) | 0.28-0.31 | $8\times10^4$ |
| Dolphin | Lang & Daybell (1963) | 0.30 | $8\times10^5$ |
| Bream | Bainbridge (1963) | 0.32 | $1\times10^4$ |
| Bonito, Bluefish Striped mullet | Pyatetsky (1970) | 0.28-0.33 | $6\times10^4$ |
| Trout | Webb (1971) | 0.30-0.33 | $2\times10^4$ |
| Jack mackerel | Hunter & Zweifel (1971) | 0.30-0.31 | $5\times10^5$ |
| Sockeye salmon | Webb (1973) | 0.19-0.32 | $2\times10^4$ |
| Bluefish | Dubois & Ogilvyl (1978) | 0.345 | $5\times10^4$ |
| Cod | Videler (1981) | 0.25-0.35 | $4\times10^4$ |
| Blacktip shark | Webb & Keyes (1982) | 0.254 | $3\times10^5$ |
| Saithe | Videler & Hess (1984) | 0.12-0.24 | $6\times10^5$ |
| Mackerel | Videler & Hess (1984) | 0.27-0.33 | $1\times10^6$ |
| Rainbow trout | Webb & Kostecki (1984) | 0.25-0.38 | $2.5\times10^4$ |

Source: Triantafyllou et al. *J. Fluid Struct.* **7**, 205-224 (1993).

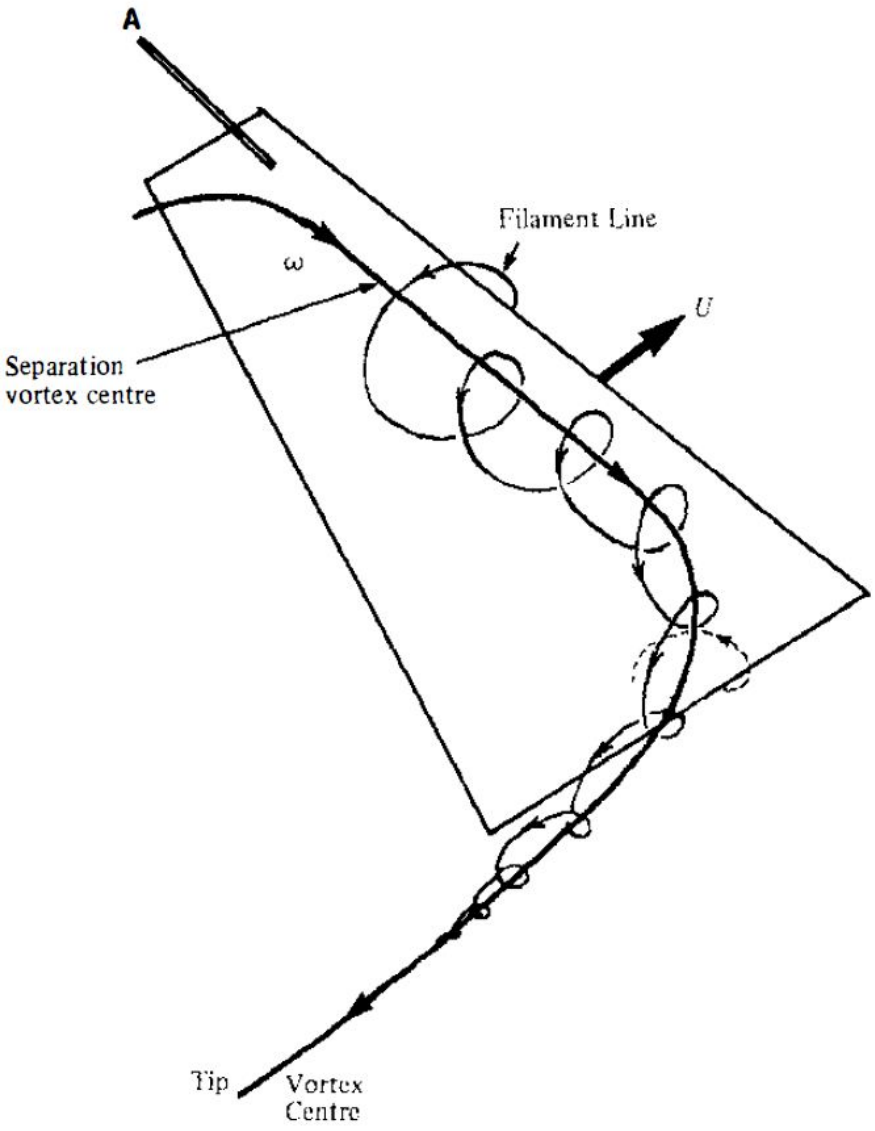


Figure 2.1: Maxworthy's depiction of the LEV development in the spanwise direction.

---

Source: Maxworthy. *Ann. Rev. Fluid Mech.* **13**, 329-350 (1981).

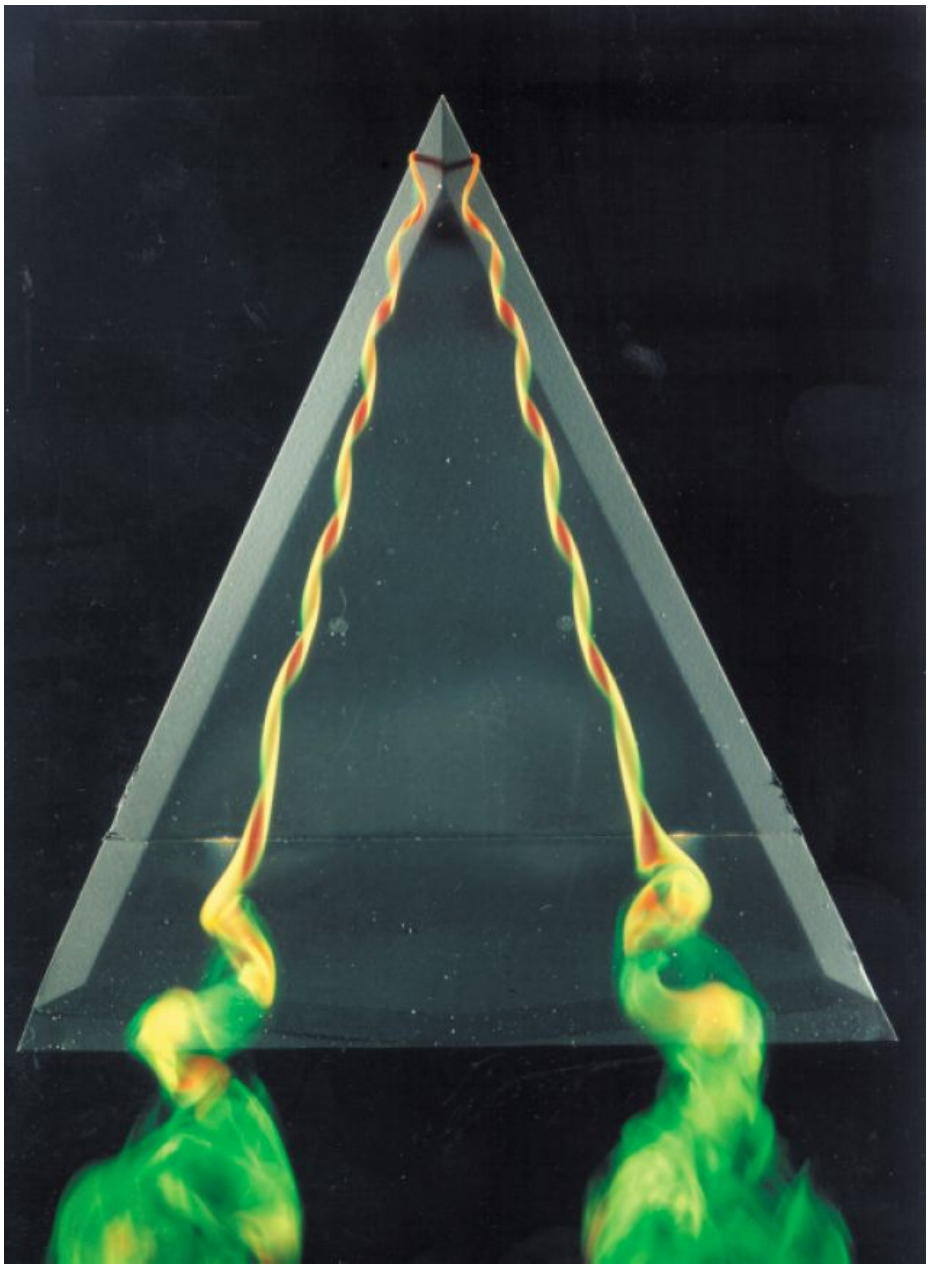

Figure 2.2: Dye Visualizations done on a delta wing showing the spiral shaped vortices being convected along the wing by spanwise velocity.

---

Source: Délery. *Ann. Rev. Fluid Mech.* **33**, 129-154 (2001).

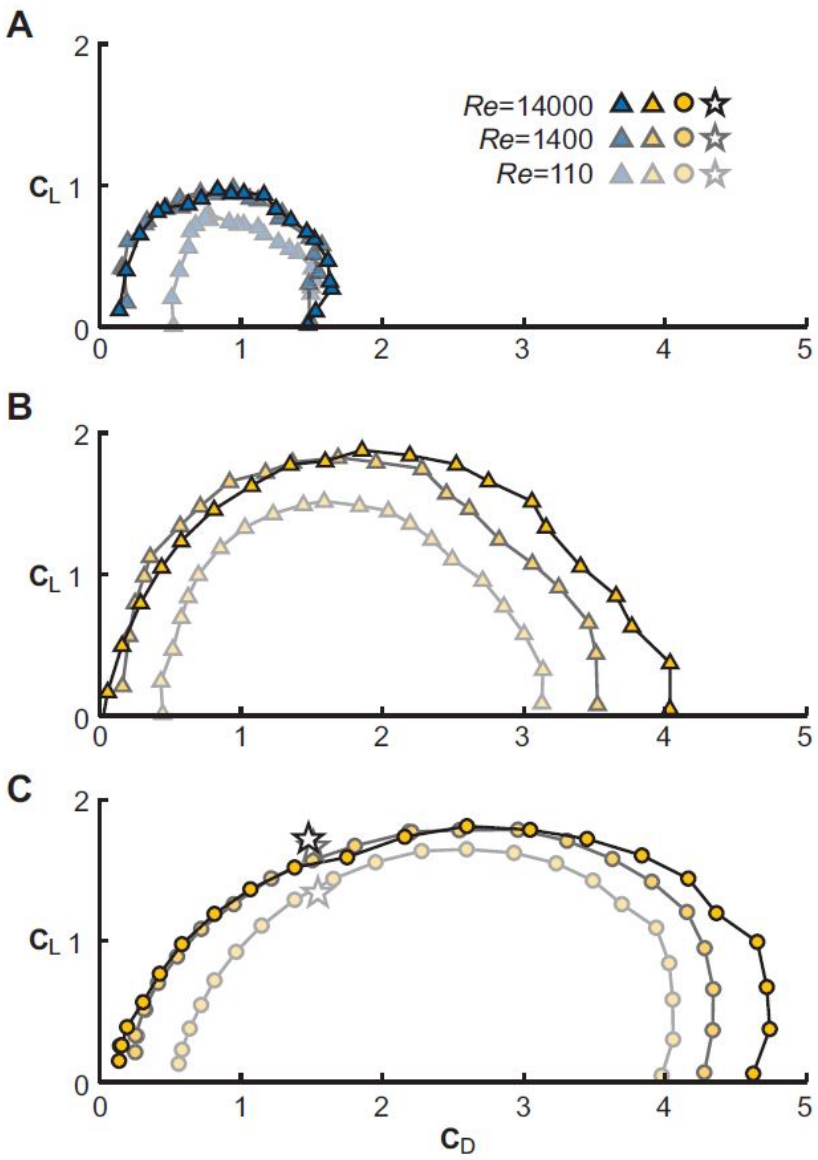


Figure 2.3: Lift and drag coefficients for a) unidirectionally translating b) unidirectional rotating and c) reciprocally rotating wings.

---

Source: Lentink & Dickinson. *J. Exp. Biol.* **212**, 2705-2719 (2009b).

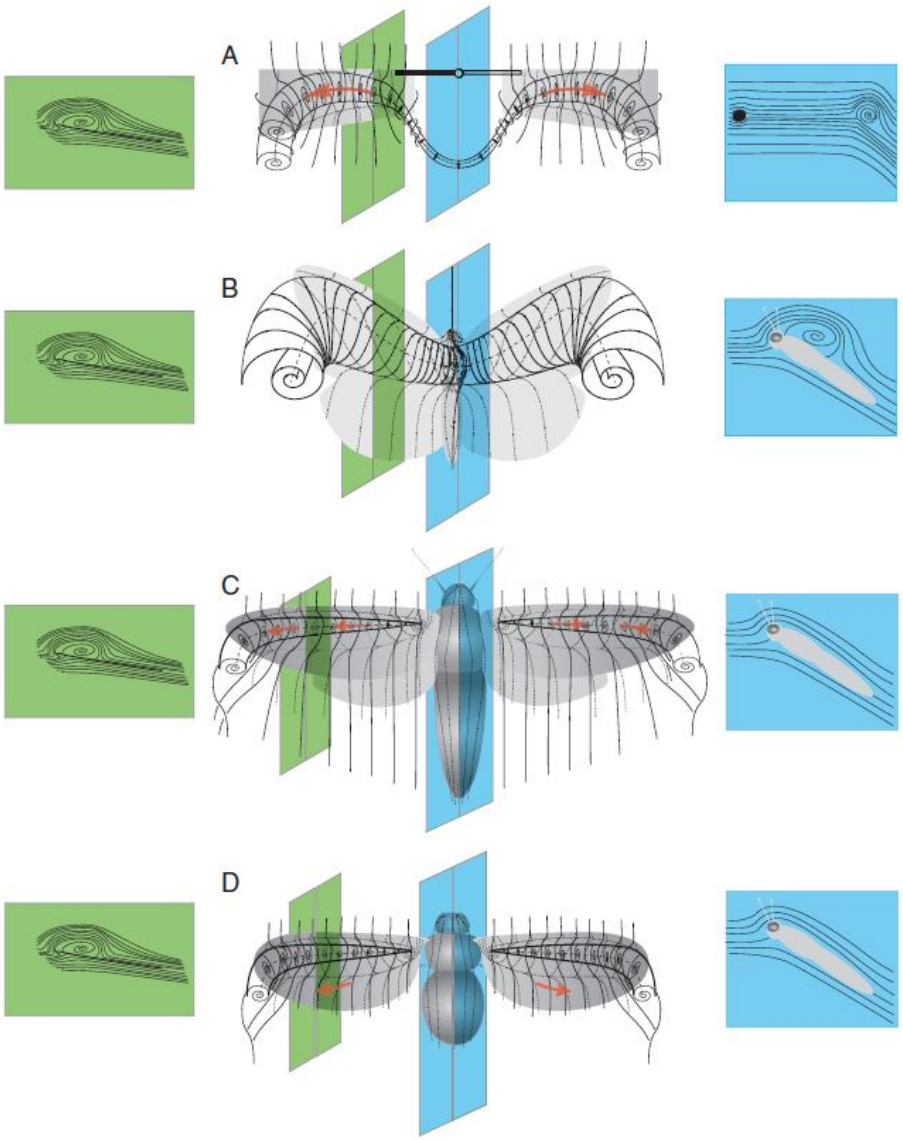


Figure 2.4: Pictorial representation of the LEV characteristics seen in biological studies. a) Maxworthy b) Luttges' group and Srygley and Thomas c) Ellington's group d) Birch and Dickinson.

---

Source: Bomphrey et al. *J. Exp. Biol.* **208**, 1079-1094 (2005).

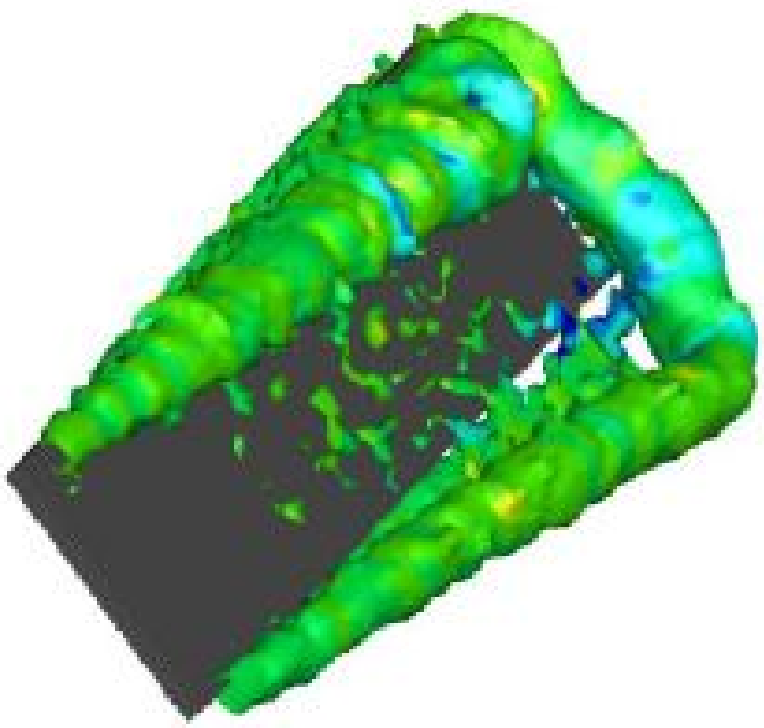

Figure 2.5: Upper surface of the plate showing the 'horseshoe-like' vortex created between the LEV, tip vortex, and trailing-edge vortex.

Source: Carr et al. *50th AIAA Aerospace Meeting* (2012).

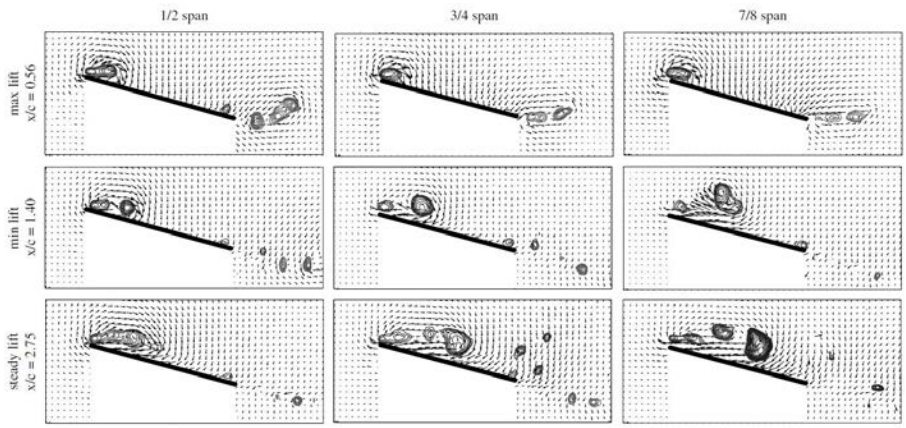


Figure 2.6: LEV shedding seen at various spanwise locations at various travel distances of the plate.

---

Source: Jones & Babinsky *J. Aircraft.*. **47**, 1013-1021 (2010).

# CHAPTER 3
# EXPERIMENTAL METHODOLOGY

Velocity and Vorticity fields were acquired on two rectangular plates rotating about a main shaft in a tank of quiescent water. Two-Dimensional Digital Particle Image Velocimetry (2D PIV) and Stereoscopic Digital Particle Image Velocimetry (SPIV) were implemented to quantify the velocity field and derive vorticity fields which were used to compute the circulation of vortical structures on the upper surface of the plates and to track the transport of vorticity along the span of the plate.

## 3.1 Mechanism Apparatus, Plate Geometry, and Kinematics

Experiments were conducted on two rectangular flat plates of aspect ratio ($\mathcal{R}$) 2 and 4. The chord, c, for each plate measured 25.4 millimeters with a thickness of 1.02 millimeters, corresponding to approximately 4% of the chord. The edges of each of the plates were square. Each one of the plates was coated with a gloss black spray paint to reduce image saturation due to reflected laser light.

The plates were rotated from rest in the center of a tank with dimensions of $0.61 \times 0.61 \times 0.61$ meters with a water depth of 0.53 meters. Figure 3.1 shows the mechanism that was designed and constructed by the author in order to articulate the blade in a rotational motion. Figure 3.2 shows how the plate was connected to the main shaft by a small connector shaft with a diameter, d, of 6 millimeters. The connector shaft had a slot cut through the center, allowing the plate to be clamped in between. There was a small gap between the root of the plate and the main shaft of

3.175 millimeters. The main shaft had a diameter D = 9.525 millimeters which was driven by a 24 VDC servo motor rated at 128 oz-in continuous torque at 380 rpm. The servo motor was driven by an ADVANCED Motion Controls model BE12A6J amplifier. In order to track the position of the main shaft throughout its rotation, an U.S. Digital model E2 quadrature optical rotary encoder with an index channel was installed on the main shaft. The transistor-transistor logic (TTL) signal from the index channel (amplified by a simple NPN transistor current amplifier) was used to trigger DPIV and SPIV data acquisition at specific locations in the rotary motion. All the circuitry was connected to a National Instruments model NI USB-6216 DAQ Card which was connected to a desktop computer equipped with LabVIEW software as shown in Figure 3.3.

LabVIEW Software was used to input a linear ramp function to the amplifier, as shown in Figure 3.4, to accelerate the plate. This was followed by a constant voltage corresponding to the desired rotational speed, also shown in Figure 3.4. The actual motion of the plate can be seen in Figure 3.5, where the plate would be in the acceleration state for approximately 45°, and beyond ≈ 45°, the blade will rotate at a constant angular velocity. The angular velocity of the plate does not exactly mimic the inputted ramp function. The noise in the velocity profile is related to the uncertainties in the azimuthal position measured by the encoder and the measurement timing. Figure 3.6 shows the position as a function of time measured by the encoder. The noise in the measurement is less than the total uncertainty for the velocity measurements during the constant velocity stage which was calculated to be ± 2°/s.

## 3.2 Digital Particle Image Velocimetry

### 3.2.1 Methodology

Digital Particle Image Velocimetry (DPIV) is a statistical Lagrangian method that estimates particle displacements between two consecutive images in a fluid flow to provide a representative velocity field in a plane[1, 79, 102]. Potters Industries Inc.'s SPHERICEL® Hollow Glass Spheres were used to seed the flow. The particles had a mean particle diameter of 10-11 µm with a density of 1.1 g/cc. These particle properties corresponded to a Stokes number (Stk = $(\tau U_{tip})/c$; where $\tau$ is the relaxation time of the particles and $U_{tip}$ and $c$ are the plate tip speed and chord length, respectively.) of $8.5 \times 10^{-4}$ which suggests the particles follow the streamlines very well and since Stk <0.1, the deviation of the particle trajectories from the actual flow displacements is <<1%[102].

A laser is usually used to illuminate a plane because of its ability to produce a high intensity, monochromatic light sheet which reduces 'chromatic aberrations'[79]. During data acquisition, the laser is set to pulse twice with a specified known time interval between each pulse which describes a double frame/single exposure recording. When the laser is fired, high speed charge coupled device (CCD) camera (or cameras), which is in synchronization with the laser pulses, is triggered to acquire an image of the particle illumination in the laser plane. The intensities of the each image are stored in a 2D distribution of gray levels with the first image representing the initial "input." Since a plane is only sampled, the best measurements that can be acquired are in-plane displacements between the particles in the first and second images. This is done

by creating an array of interrogation windows over each of the images and evaluating the movement of particle groups. A discrete cross-correlation method described by Equation 3.1 is used to determine the displacements within sub-windows of the image by matching the intensities between the image pairs, statistically.

$$R(x,y) = \sum_{i=-K}^{K} \sum_{j=-L}^{L} I(i,j)I'(i+x, j+y) \tag{3.1}$$

Where $I$ and $I'$ are the intensity values from the two images. Once the cross-correlation field has been calculated, a Gaussian function is fit to the peak, and the peak of the Gaussian gives the shift, allowing us to obtain the particle displacement and sub-pixel accuracy. Lastly, since the time between the image pairs is specified, a velocity field can be obtained from the displacements. This method can be summarized graphically as shown in Figure 3.7.

From the velocity field, the out-of-plane vorticity can be calculated discretely by taking the curl of the velocity field as shown by Equation 3.2.

$$\omega_z = \frac{\partial U_y}{\partial x} - \frac{\partial U_x}{\partial y} \approx \frac{U_{y_{i+1}} - U_{y_{i-1}}}{2X_g} - \frac{U_{x_{j+1}} - U_{x_{j-1}}}{2Y_g} \tag{3.2}$$

Where $i$ is in the x-direction while $j$ is in the y-direction. $U_x$ and $U_y$ are the velocities in the x- and y-direction, respectively, and $X_g$ and $Y_g$ are the grid spacing between the velocity vectors in the x- and y-direction, respectively. The out-of-plane vorticity component will be used heavily in Chapter 4.

### 3.2.2 Data Acquisition and Post-Processing

For both PIV configurations, A LaVision Inc. Flowmaster system was used consisting of one or two Imager Pro 4.0 CCD cameras with 2048 × 2048 pixel resolution and a 14-bit dynamic range. For planar illumination, a dual-cavity, 200 mJ/pulse Nd:YAG laser with light sheet optics was used. The image pairs were processed using LaVision DaVis 8.6 software with the standard cross-correlation analysis discussed in Section 3.2.1. Multiple pass window sizes of 64 × 64 and 32 × 32 with a 50% overlap were using during the cross-correlation analysis. The outliers in the images were removed using a median filter. Lastly, from the velocity fields, the vorticity fields were derived using Equation 3.2 as discussed in Section 3.2.1.

### 3.2.3 Two-Dimensional Digital Particle Image Velocimetry Setup

Depicted in Figure 3.8 is the 2D PIV setup used to measure spanwise vorticity on the upper surface of the plate. Reynolds numbers of 4,000, 8,000, and 16,000 based on tip velocity were tested because those Reynolds numbers are in the range of larger insects and small birds[3, 30]. The study looked at three different angles of attack ($\alpha$) for each aspect ratio; 25°, 35°, and 45°. As shown in Figure 3.2, the plate's angle of attack was adjusted about the 0.5c point. The plate is rotated in a clockwise direction as shown in Figure 3.9, where the current position of the plate is when the camera is perpendicular to the chord line which represents an azimuthal position of 0°. This is the location where data acquisition occurs. The azimuthal position ($\psi$) was measured from the data acquisition position in the direction opposite of rotation

(counterclockwise) to the initial starting position as indicated in Figure 3.9. A total of five different azimuthal positions ($\psi$) were examined; 90°, 180°, 235°, 270°, and 320°; which are represented by the dash lines in Figure 3.8. A vertical (chordwise) laser sheet was created at b = 25.4 millimeters from the root of the plate which corresponded to relative spanwise positions (b/s) of 50% and 25% for the $\mathcal{R}$= 2 and 4 plates, respectively. The 50% spanwise location was also investigated for the $\mathcal{R}$= 4 plate as indicated in Figure 3.10 by dashed green lines symbolizing chordwise laser planes. Due to reflections generated by the small attachment rod connecting the plate to the main shaft causing significant saturation of particle intensities in the PIV images, the 25% spanwise position was not investigated for the $\mathcal{R}$= 2 plate. Unless otherwise indicated, a total of three PIV measurements were taken for each configuration of angle of attack, aspect ratio, azimuthal position, Reynolds number, and spanwise position. Since the experiment is conducted in quiescent water, it was necessary to wait between experiments for the motion of the water to dissipate. The fluid motion was characterized by the normalized root-mean-square (RMS) velocity magnitude defined below and can be seen dissipating over time in Figure 3.11.

$$V^*_{RMS} = \frac{1}{N}\sum_{i=1}^{N}\frac{\sqrt{\overline{u'}^2 + \overline{v'}^2}}{U_{tip}} \times 100\% \tag{3.3}$$

Where $\overline{u'}$ and $\overline{v'}$ are the RMS velocities averaged over 50 realizations in the x- and y-direction, respectively. $N$ is the total number of vectors in the PIV field of view. During these experiments, the $\Delta t$ was optimized for the initial readings and was left constant throughout the range of times investigated, which could explain the

relative flatness of $V^*_{RMS}$ in the later measurements. After $\approx$ 250 seconds, a steady-state is reached (limited by the random error in the PIV measurements). For that reason, the tank was left undisturbed for 5 minutes to allow for the flow to subside which is in agreement with the tests done by Ansari et al [5]. The five minute wait time corresponded to average $V^*_{RMS}$ of $\approx$ 2.5%, 1.3%, and 0.63% for the image for Re = 4,000, 8,000, and 16,000, respectively.

### 3.2.4 Stereoscopic Digital Particle Image Velocimetry Setup

Two-dimensional, three-component (2D 3C) Stereoscopic Digital Particle Image Velocimetry (SPIV) experiments were also conducted, and the setup is shown in Figure 3.12. The setup is similar to the 2D PIV measurements discussed in Section 3.2.3 except two cameras were used instead of one. The cameras were oriented such that their axes were coplanar with the chord line of the plate. Scheimpflug mounts were implemented on the CCD cameras and prisms were installed on the side of the tank to bring the viewing plane into focus and to minimize particle distortion in the image. In this particular setup, only one specific case was investigated; the aspect ratio 4 plate at the 25% spanwise location for a Reynolds number of 8,000 at an angle of attack of 35°. Again, represented by dash lines in Figure 3.12, five azimuthal positions were examined; 75°, 90°, 120°, 180°, and 270°.

A vorticity transport analysis is discussed in Section 4.5 which requires the use of a second-order central difference scheme to evaluate a few of the terms in Equation 4.5. To complete the second-order central difference scheme, three chordwise laser

planes, shown in Figure 3.13, are created at the 25% spanwise location for the $AR$= 4 plate. The rails supporting the mechanism in Figure 3.12 contain small pin holes that were manufactured using a Haas CNC machine that were separated by 1 millimeter. These pins allowed for precise translation of the mechanism of 1 millimeter intervals to obtain the *k-1*, *k*, and *k+1 planes* shown in Figure 3.13.

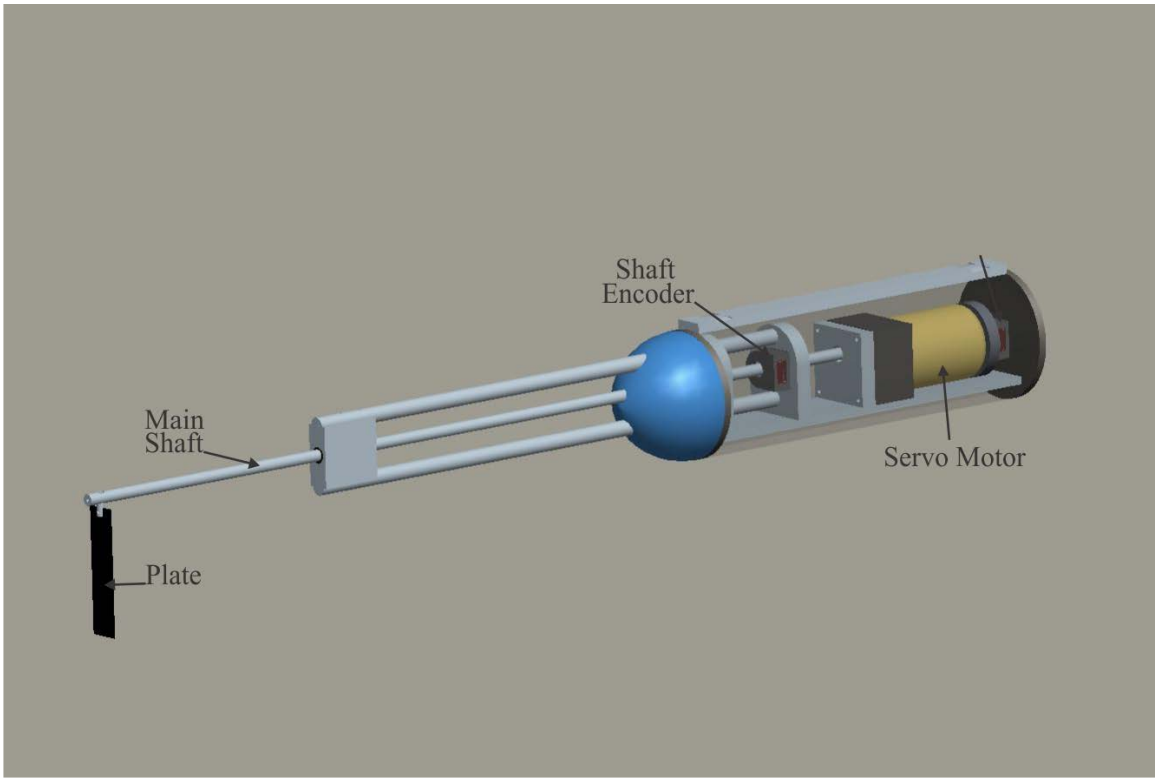


Figure 3.1: Mechanism used to rotate the plate.

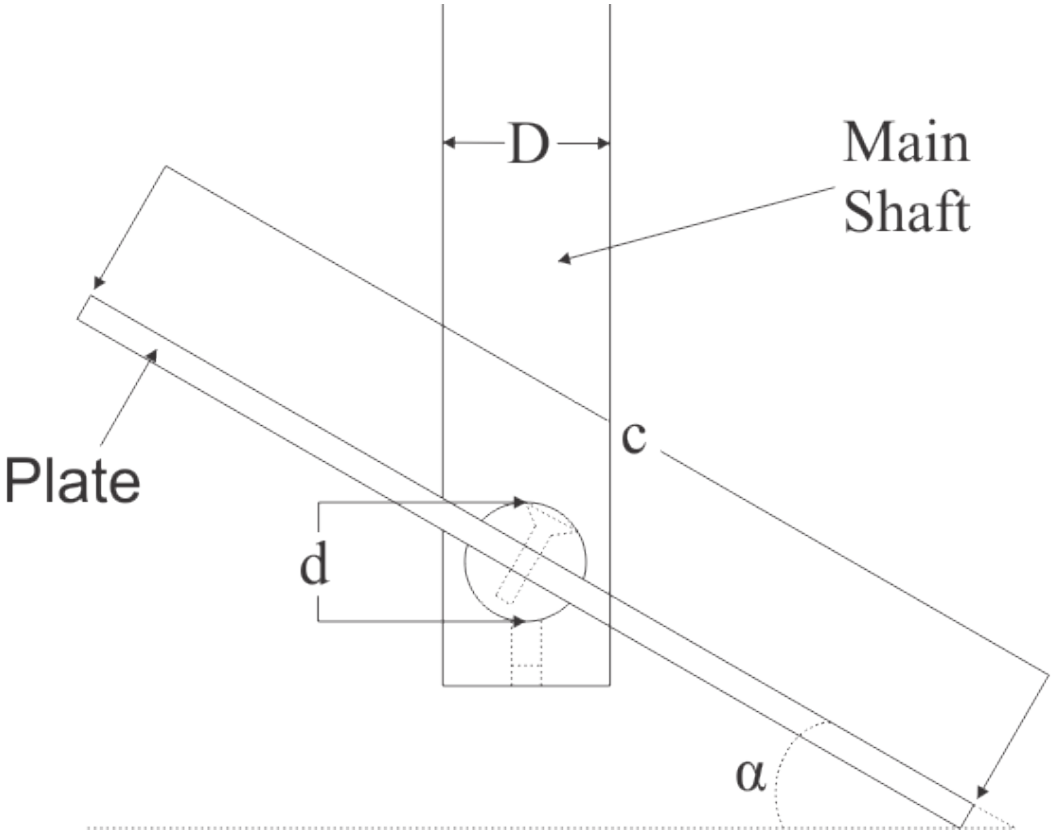


Figure 3.2: A spanwise view of the plate and main shaft.

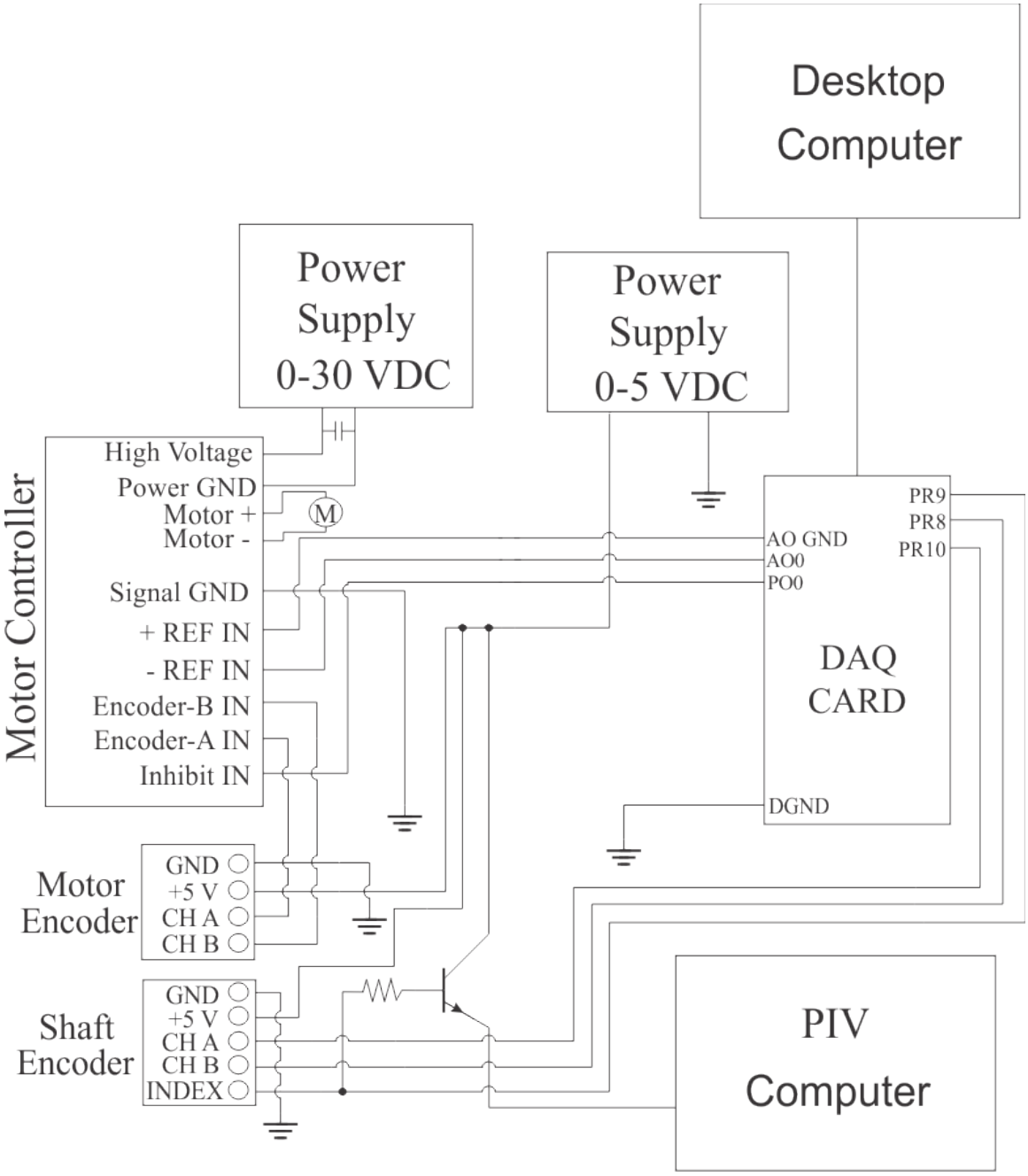


Figure 3.3: Circuitry layout used to control the plate's motion and to synchronize data aquistion with the plate's position.

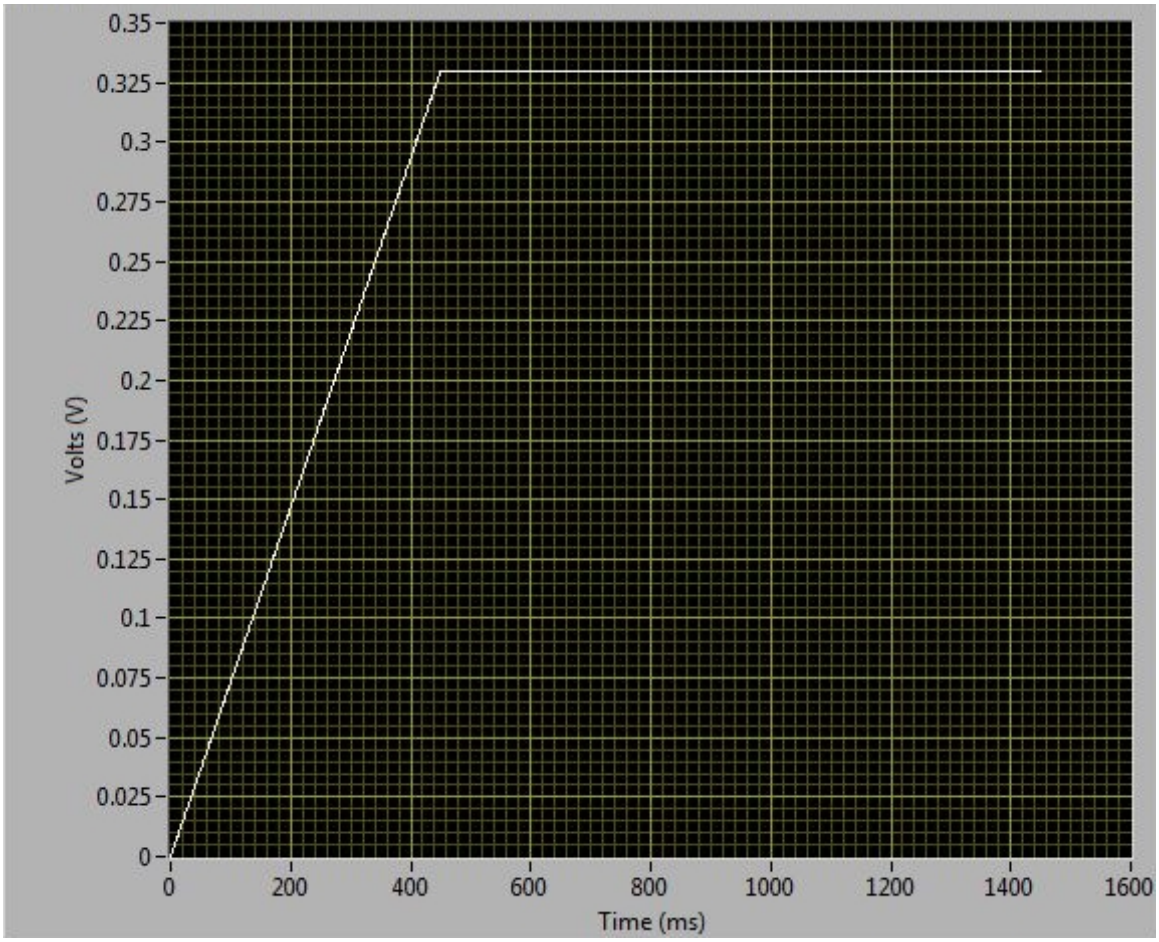


Figure 3.4: Linear ramping-up function generated using LabVIEW.

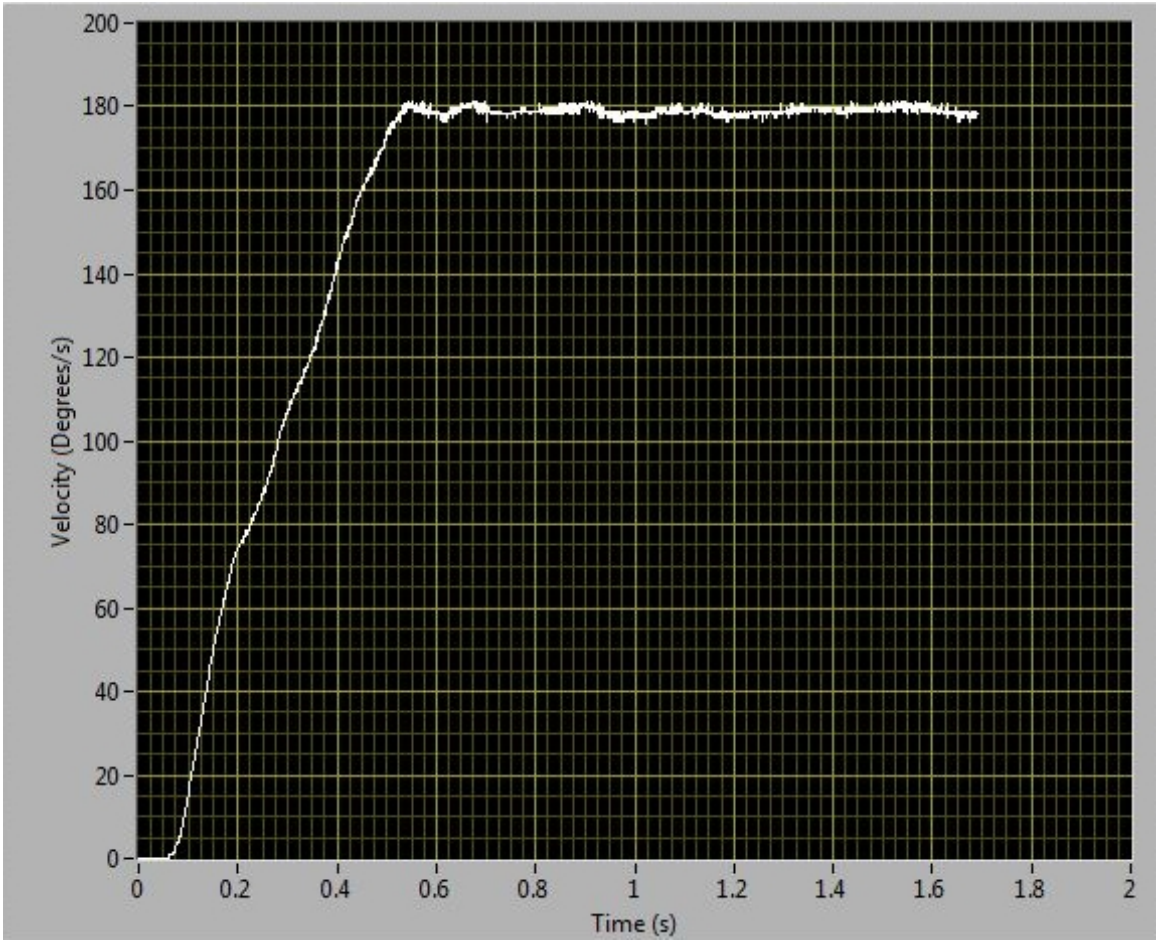


Figure 3.5: Actual plate's motion with the inputted linear function shown in Figure 3.4.

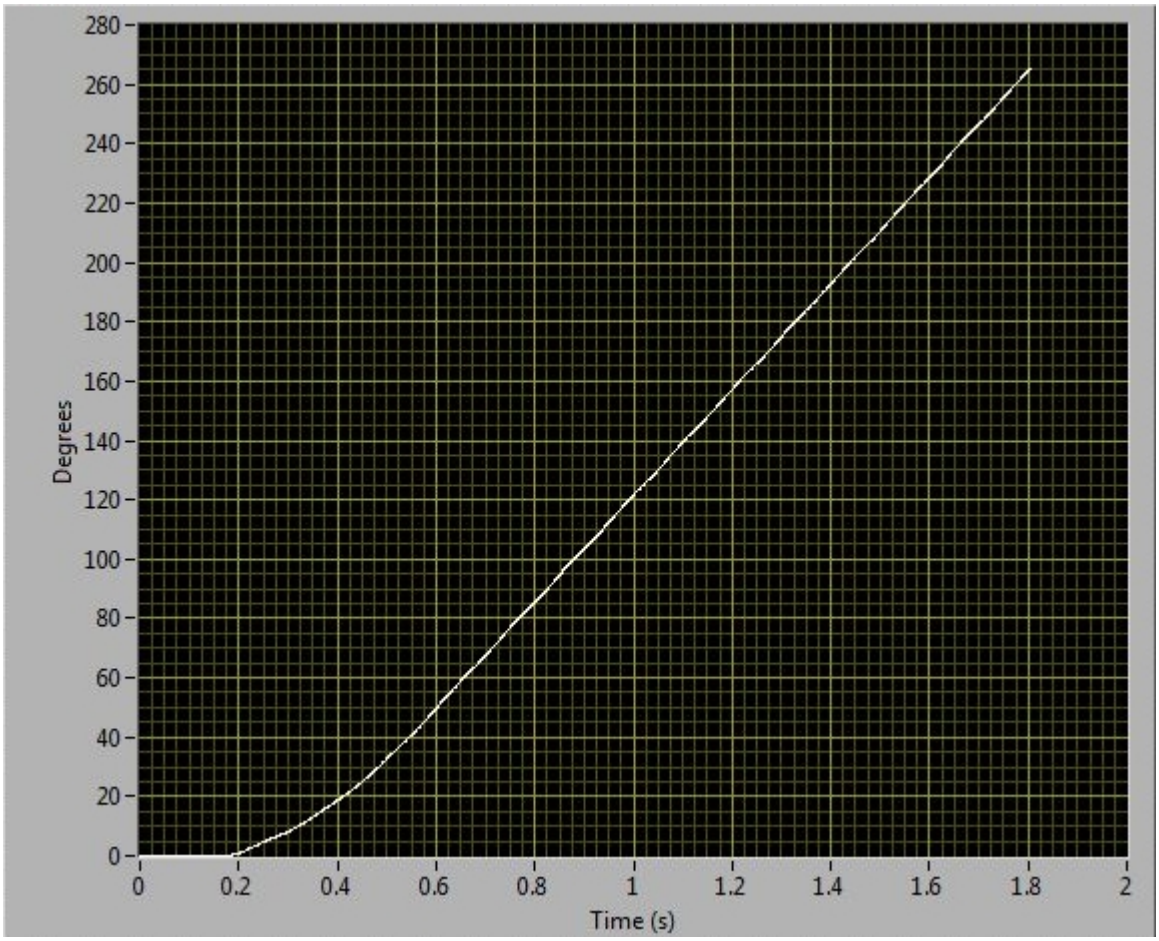


Figure 3.6: Plate's position as a function of time measured by the rotary encoder.

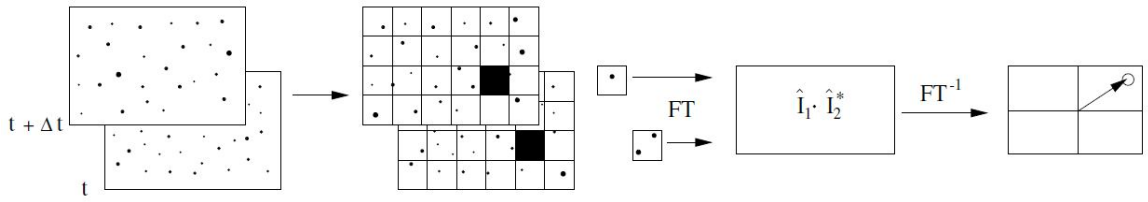


Figure 3.7: [Physical representation of the cross-correlation method used to calculate velocity fields in PIV for a double frame/single exposure recording.

---

Source: Raffel et al. *Particle Image Velocimetry: A Practical Guide* pg. 128 (2007).

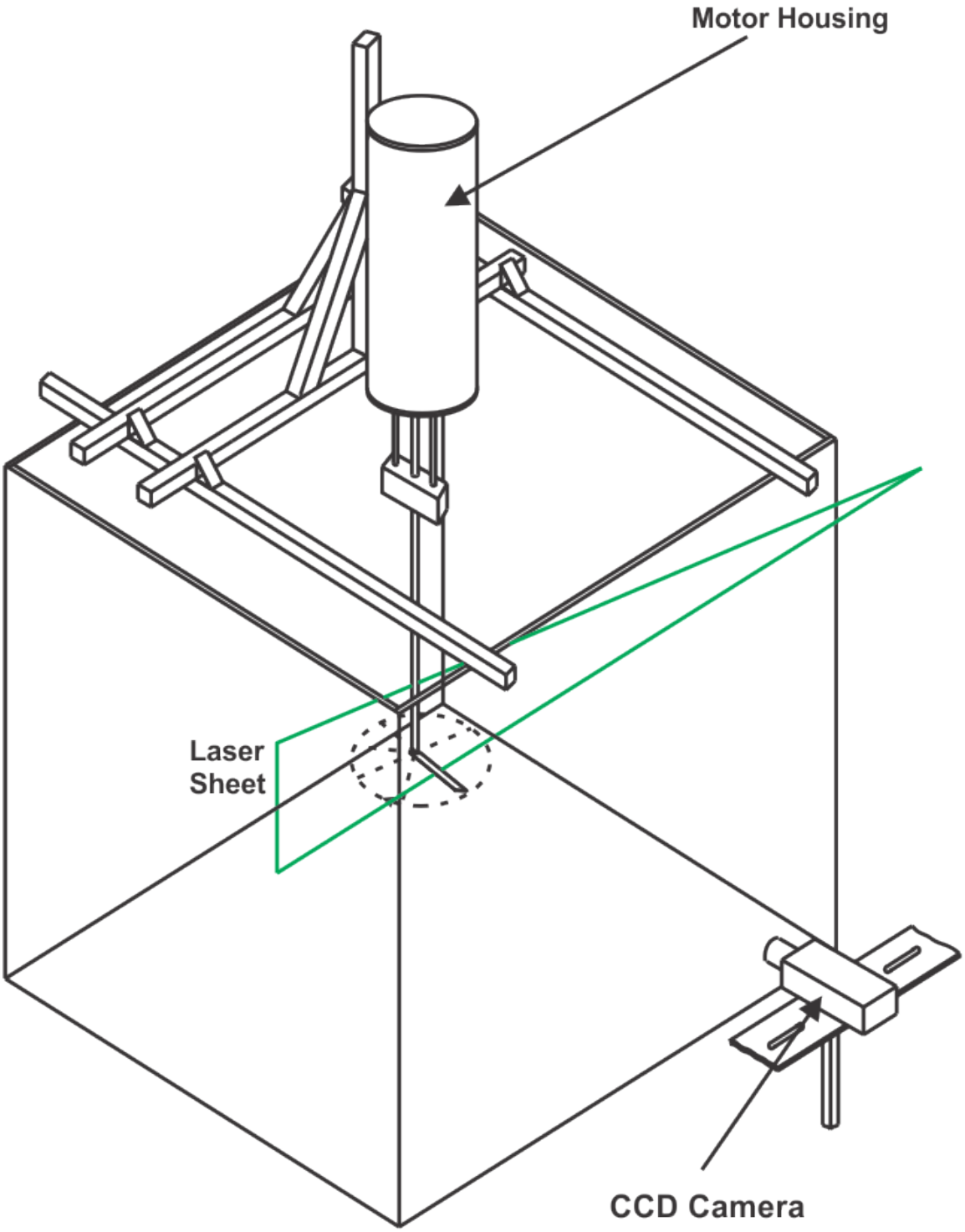


Figure 3.8: 2D PIV experimental setup used to view spanwise vorticity.

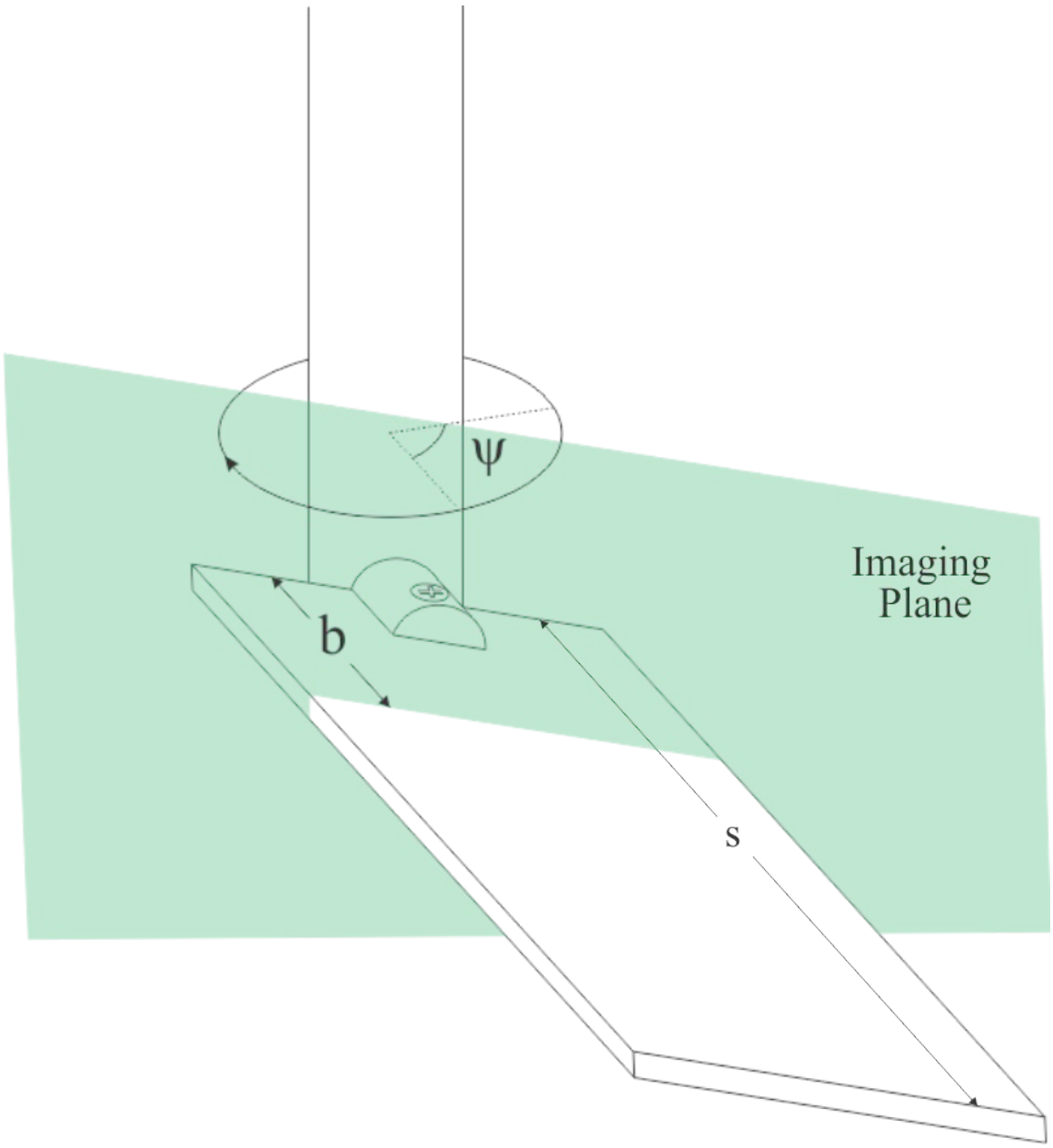


Figure 3.9: Visualizations of the laser position and azimuthal angle definition.

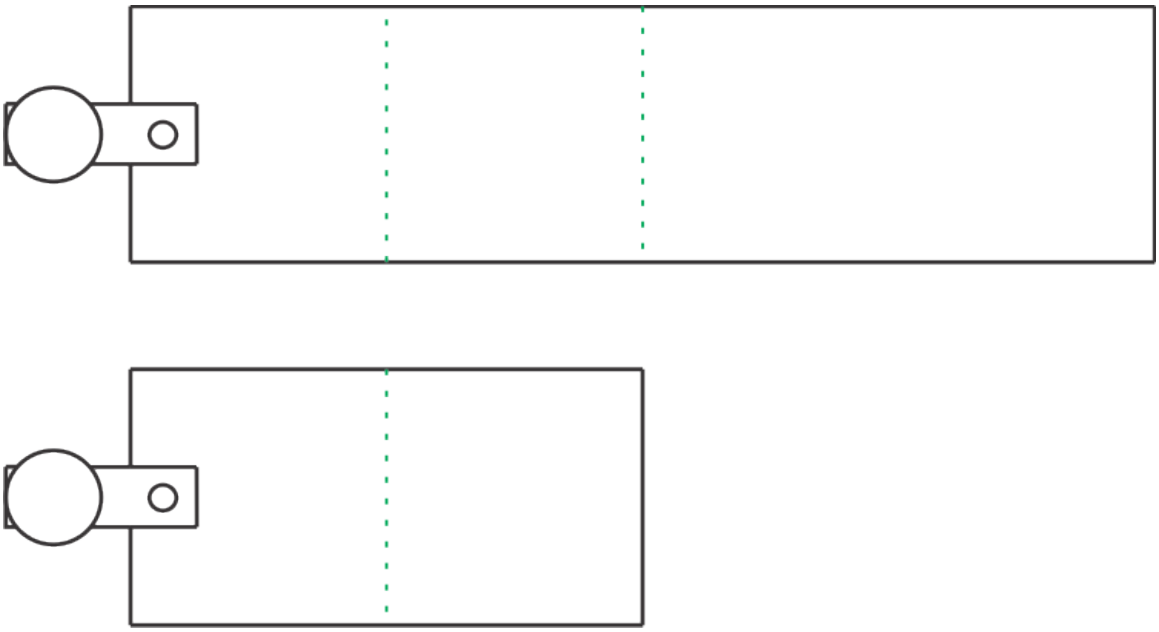

Figure 3.10: Top view of both aspect ratio plates showing the locations of chordwise laser planes by green dashed lines. The top part of the figure shows the two relative spanwise positions obtained for the $\mathcal{R}4$ plate while the bottom portion shows the single spanwise position acquired for the $\mathcal{R}2$ plate.

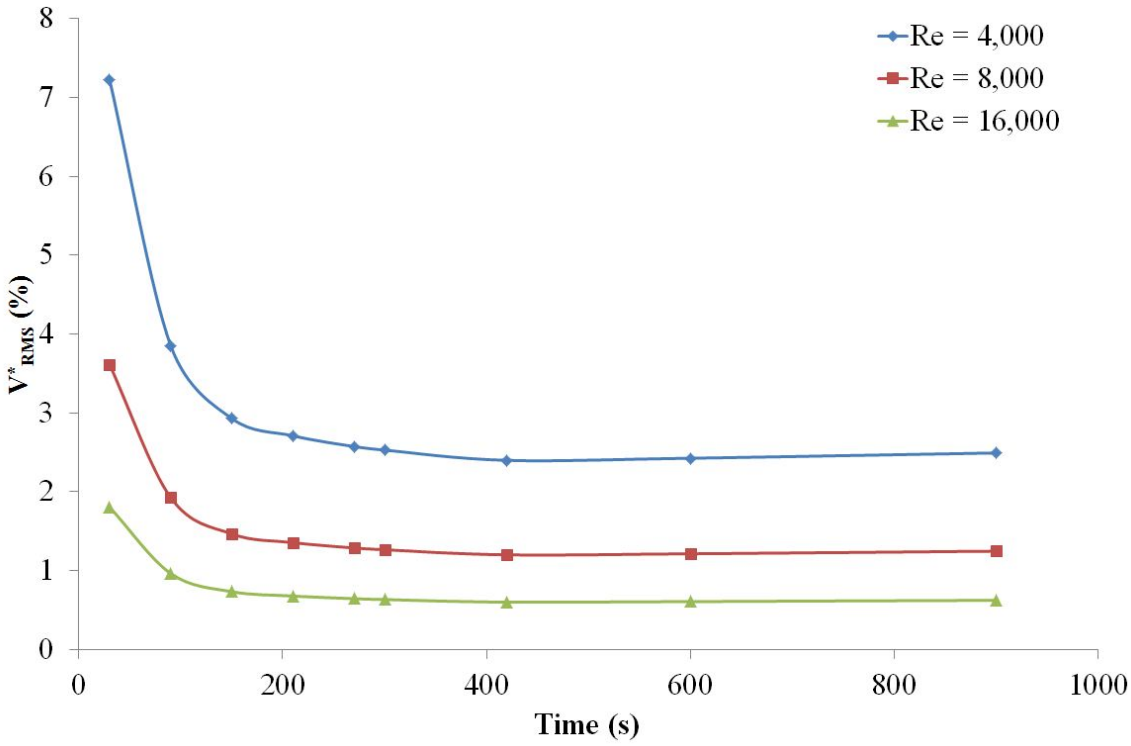


Figure 3.11: Average turbulence intensity for each Reynolds number.

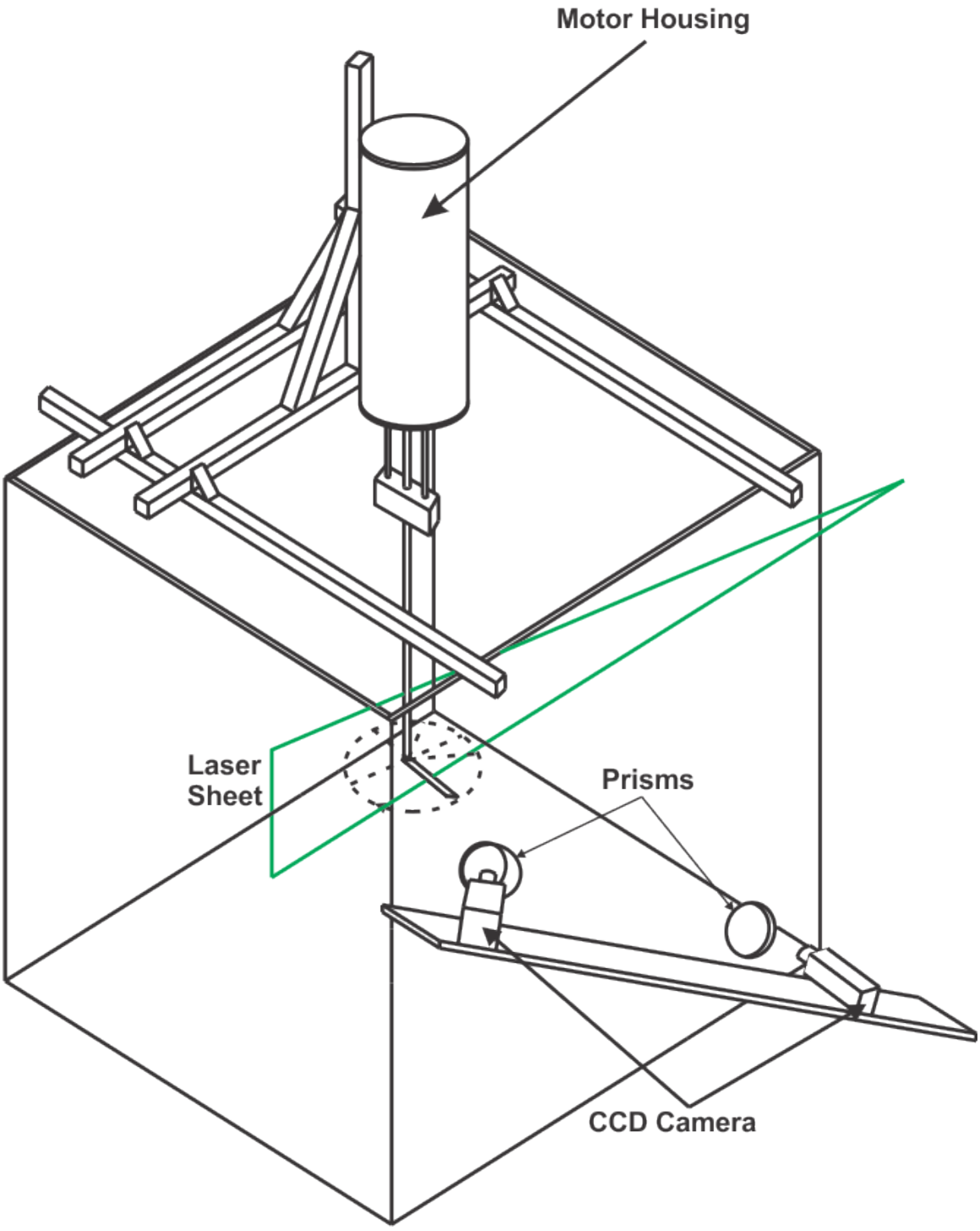


Figure 3.12: SPIV experimental setup used top calculate the vorticity transport discussed in detail in Section 4.5.

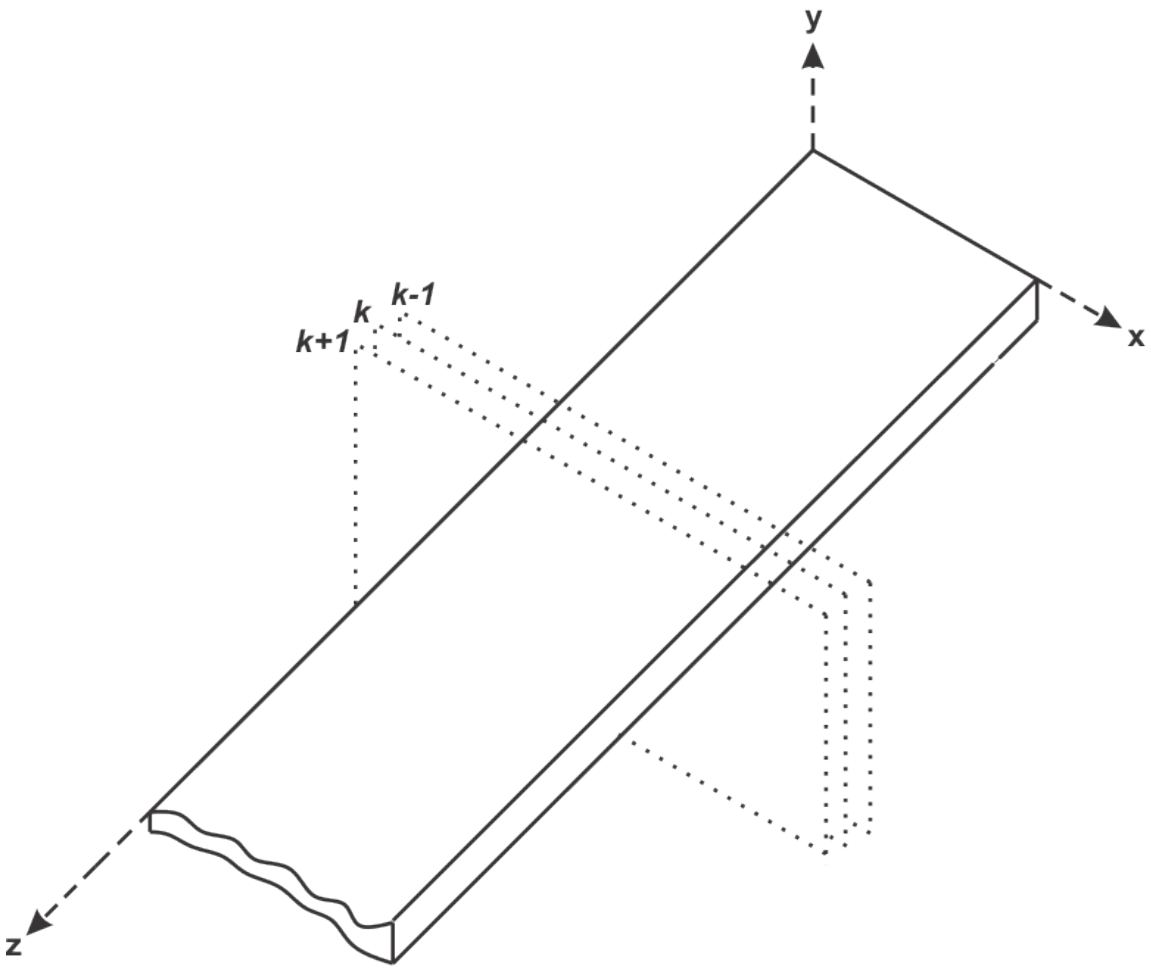


Figure 3.13: Zoomed in at a particular spanwise location to show the three chordwise laser planes needed to calculate derivatives in Equation 4.5.

# CHAPTER 4
# RESULTS AND DISCUSSION

The dynamics of the LEV development for various azimuthal positions, angles of attack, Reynolds numbers, spanwise locations, and aspect ratios are considered in this chapter. Circulation measurements are used to quantify variations in the parameters. In addition, a vorticity transport analysis was developed to investigate the dynamics of the LEV within a small control volume on the suction surface of the plate.

## 4.1 Temporal Evolution of LEV for Parameter Variations

### 4.1.1 Leading-Edge Features

A total of three trials were acquired for each configuration of azimuthal position, angle of attack, aspect ratio, Reynolds number, and spanwise location. Each one of these trials yielded an instantaneous velocity field from which the instantaneous vorticity field could be calculated. This is done discretely using Equation 3.2. Figures 4.1 - 4.23 show the effects of azimuthal position on the instantaneous, nondimensionalized vorticity fields ($\omega_z^* = (\omega_z c)/U_{tip}$) for constant angle of attack, aspect ratio, Reynolds number, and spanwise location. Figures 4.1 - 4.13 contain the data for the $\mathcal{AR}$= 4 plate at the 25% spanwise position, and Figures 4.14 - 4.23 show the data for the aspect ratio 2 plate at the 50% spanwise position.

In each of these images (Figures 4.1 - 4.36), the plate is moving from right to left. The image plane is defined by the vertically-oriented laser sheet, parallel

to the plate chord and entering the field of view on the right side. Once the laser plane impinges on the plate, a shadow is cast on the upstream (left) side of the plate. The bottom portion of the plate and the shadow created are masked out during the velocity field computations and are characterized in the images by a whited out region. Blue contours represent negative (clockwise) vorticity which constitute the LEV structure while red contours represent positive (counterclockwise) vorticity. A shear layer is seen separating from the leading-edge of the plate and rolling up into the LEV, essentially continuously feeding the LEV with negative vorticity. Beyond the LEV, on the downstream portion of the plate, there is an attached boundary layer (negative vorticity). The results indicate the presence of a single LEV along the chord of the plate, classifying our LEV dynamics into the "attached" LEV discussed in Section 2.2.1. An interesting characteristic in all of these images is the development of a region of counterclockwise vorticity which is generated on the surface of the plate from the interaction of the LEV with the plate.

In Figures 4.1 - 4.5, the LEV and positive vorticity are two distinct, coherent structures that are concentrated towards the leeward surface of the plate. Qualitatively, the overall structure of the LEV and positive vorticity do not appear to change for azimuthal positions between 90° and 270° suggesting the flow is quasi-steady. However, at $\psi = 320°$, the connection of the shear layer to the LEV is not as well defined in the other azimuthal positions, and the positive vorticity begins to lift off the surface of the plate. This observation could mean that the LEV's strength is relatively constant in the earlier stages of temporal development, but higher az-

imuthal positions might have unsteady effects such as the positive vorticity on the surface of the plate becoming on the same order of the LEV which may affect the LEV structure. Also, in Figures 4.1 - 4.5, the in-plane velocity components are shown by the vectors. All plots in Chapter 4 containing vectors show the in-plane velocity components in an inertial reference frame. The flow is seen wrapping around the leading-edge of the plate as it advances in the flow. As the flow moves in the downstream direction, it is driven downwards towards the surface of the plate. In the LEV region, there is an increase in the in-plane velocity components. At the downstream portion of the LEV, the in-plane velocity components are larger than the relative freestream velocity, and there is noticeable flow reversal on the downstream portion of the LEV near the surface of the plate. The magnitude of the flow reversal has a larger value than the magnitude of the in-plane velocity components seen in the shear layer. The high magnitude flow reversal is seen progressing towards the leading-edge of the plate beneath the LEV. In the region of positive vorticity, the magnitude of the flow reversal decreases and the direction of the velocity begins to reorient itself downwards, towards the surface of the plate.

Figure 4.6 shows the temporal results for the $\mathcal{R}$= 4 plate at the 25% spanwise location for $\alpha = 25°$ at a Re = 8,000. At $\psi = 90°$, the results are similar to the Re = 4,000 case as shown in Figure 4.1. In contrast with the $\psi = 90°$ case, the other azimuthal positions are qualitatively different than the Re = 4,000 case. One such difference is that the shear layer appears to be more rounded and is elevated higher from the surface of the plate. The increased elevation allows for a larger gap between

the LEV structure and the positive vorticity which is apparent in Figure 4.6b at an azimuthal position of $\psi = 180°$. Eventually at the subsequent azimuthal positions, the positive vorticity is more diffuse in the region below the shear layer and LEV, but its strength appears to be larger based on the contour levels. An important observation at $\psi = 180°$, 235°, 270°, and 320° is the positive vorticity becomes entrained into the LEV. This process is suspected to be driven by the LEV inducing a velocity in the direction of translation of the plate causing the positive vorticity to be swept upstream into the shear layer which feeds the LEV structure. Evidence of this hypothesis is perhaps most distinguishable at $\psi = 235°$ and 270° where the top portion of the counterclockwise vorticity is cut off by the shear layer and traces of positive vorticity can be seen transported downstream, eventually accumulating and amalgamating in the LEV.

The Re = 16,000 case for the $\mathcal{R}$= 4 plate at $\alpha = 25°$, presented in Figure 4.7, still shows the clockwise and counterclockwise vorticity as two organized structures at $\psi = 90°$. In this particular case, the negative vorticity appears to create an arch-like shape over the counterclockwise vorticity where in the previous cases, the LEV does not reattach to the plate, but is above the surface of the plate. At increasing azimuthal positions, the LEV becomes more disorganized and entrains of the positive vorticity into the LEV. Also, it is noticeable that the negative vorticity boundary layer on the downstream portion of the plate for $\psi = 235°$ is raised up off the surface of the plate. This is discussed in a more detail later on in Section 4.1.2 when examining the trailing-edge features, but is thought to be contributed to the flow wrapping around

the trailing-edge of the plate, violating the Kutta condition.

Figure 4.8 shows an angle of attack of 35° at a Re = 4,000 for the $\mathcal{R}$= 4 plate at the 25% spanwise position. Again, $\psi = 90°$ has an organized flow except the LEV appears to be larger in size compared to $\alpha = 25°$ in Figures 4.1 - 4.5, which is to be expected since the angle of attack has increased. The LEV and positive vorticity still remain mainly separated from one another except at $\psi = 235°$ where a small portion of the counterclockwise element gets entrained into the LEV. The shape of the LEV changes with azimuthal positions; in the earlier azimuthal positions ($\psi = 90°$, 180°, and 235°), the LEV is more elongated and tilted so the bottom of the LEV looks to be parallel with the chord line of the plate, but at later azimuthal positions ($\psi = 270°$ and 320°), the shear layer becomes thinner than in earlier positions which may allow the LEV to roll up more on itself creating the "rounder" LEVs shown in Figures 4.8d and 4.8e.

Similar observation for the $\psi = 90°$ position for the Re = 8,000 with the two separate structures is shown in Figure 4.9a. As with the $\alpha = 25°$ at Re = 8,000, the LEV becomes more disorganized at $\psi >180°$. There is some minor entrainment of the positive vorticity in the LEV at azimuthal positions 180° and 235° near the uppermost point of negative vorticity, but entrainment of the positive vorticity region is greatest at the two later azimuthal positions, $\psi = 270°$ and 320°.

The Re = 16,000 case has a similar trend to the Re = 8,000 case in Figure 4.9 except for $\psi = 90°$. Figure 4.10a shows that the entrainment of positive vorticity begins at earlier azimuthal positions for increasing Reynolds number. A possible ex-

planation for this phenomenon is the increased rotational speed results in a transition in the flow causing the flow to go from a laminar regime to a turbulent flow. The turbulent flow allows for the two vorticities to mix more efficiently in the LEV region.

The Re = 4,000 case for an angle of attack of 45° is conceptually similar to the other angles of attack at the same Reynolds number. However, for an $\alpha = 45°$ at $\psi = 180°$, the two structures do not remain separated, but instead, mix together with one another, clearly shown in Figure 4.11b. At $\psi = 90°$ and 180°, the shear layer is undoubtedly flatter and as the azimuthal position increases, the projection of the shear layer goes from being parallel to the x-axis to being oriented such that it is pointing to the upper right-hand corner of the image. The distinct location of the shear layer in $\psi = 180°$ could cause for more of the positive vorticity to be entrained into the LEV since it is closer to the induced velocity.

The trends for the Re = 8,000 and 16,000 for $\alpha = 45°$ appear to be similar to what has been discussed in the other cases. All cases exhibit positive vorticity being entrained into the LEV, and increasing azimuthal position causes the two structures to become more disorganized.

Generally, Figures 4.14 - 4.23 show similar trends for the $\mathcal{AR}$= 2 plate where the counterclockwise region becomes more entrained into the LEV with increasing azimuthal position. One important thing to note is the Re = 4,000 cases for the $\mathcal{AR}$= 2 plate do not show two explicit regions of vorticity for all azimuthal positions. Instead, Figures 4.14 - 4.18, 4.20, and 4.22 show that the earlier azimuthal positions are separated, but the later ones are not. Furthermore, since the Reynolds numbers

were matched based on their tip speeds, two different rotational speeds were used between the two aspect ratios to obtain matching Reynolds numbers. Therefore, for the $\mathcal{R}$= 2 plate at a Re = 4,000, the velocity of the plate at the imaging plane is the same as the $\mathcal{R}$= 4 plate at Re = 8,000.

In general, the aspect ratio 2 plate seems to entrain more of the positive vorticity within the LEV at earlier azimuthal positions ($\psi$ = 90° and 180°) where its aspect ratio 4 counterpart does not. It is not clear whether this characteristic is attributed to aspect ratio or relative spanwise location (b/s) since only one spanwise location on the aspect ratio 2 plate was investigated. However, two spanwise planes were acquired for the aspect ratio 4 plate, and the results for the temporal evolution for the 50% plane can be viewed in Figures 4.24-4.36.

Figures 4.24 - 4.28 show the $\mathcal{R}$= 4 plate at the 50% spanwise location at Re = 4,000 and $\alpha$ = 25° along with the in-plane velocity components. Now, the LEV consumes more than half of the chord line. Only at $\psi$ = 90° is the LEV seen to be a coherent region of negative vorticity, but as the azimuthal position increases, the integrity of the structure's shape breaks down. The rapid breakdown of the LEV could be attributed to the tip vortex inducing a tip-to-root flow which in turn decelerates the flow of the vortex core as described in delta wings vortex breakdowns[37, 57, 91, 110]. The shear layer is obviously larger at the 50% spanwise location which is to be expected since the velocity is higher at this radial position. The LEV looks like it possibly could be going through a shedding phase as described in Section 2.2.2 and shown in azimuthal positions 235° and 320° in Figures 4.26 and 4.28, respectively

where a small blob of negative vorticity looks to be separated from the main constituent.

As Reynolds number is increased, there is a significant drop in nondimensionalized, vorticity on the surface of the plate as shown in Figures 4.29 and 4.30. The nondimensionalized vorticity values were so low for a Re = 16,000 that the range of the contours needed to be changed in order to view the structures. This observation is likely contributed to enhanced mixing and annihilation of vorticity due to flow possibly transitioning from a laminar to turbulent at higher Reynolds numbers. Figure 4.29, which represents the 8,000 case for $\alpha = 25°$, shows that the flow appears to be stalled at majority of the azimuthal positions, but the 16,000 case in Figure 4.30 has the flow being attached in all azimuthal positions. This indicates that the integrity of the LEV structure with distance from the axis of rotation could be a function of Reynolds number, and the fact that the flow goes from attached to stalled and back to attached from Re = 4,000, 8,000, and 16,000, respectively, shows that there are different flow regimes for varying Reynolds number. To further validate these claims, more spanwise positions will need to be obtained to see the development of the LEV along the span of the plate.

Similar conclusions can be made for $\alpha = 35°$ and $45°$ at all Reynolds numbers. The LEV is larger than at the 25% spanwise location, and an attached LEV is seen over a larger portion of the chord line. There is a general trend where the earlier azimuthal positions have a LEV, but the later ones, indicate stall flow, where chaotic vorticity fields extend into the wake of the plate. It is noticeable that the dimen-

sionless vorticity values are lower at the 50% spanwise location suggesting that the strength of the LEV diminishes with distance from the rotational axis which is likely contributed to the tip vortex decelerating the LEV core causing bursting, or the tip vortex causing the vorticity to be turned into the streamwise direction. Qualitatively, the flow at the 50% spanwise location for the $AR = 4$ is highly complex making it difficult to say whether the flow is attached, shedding, or stalled. Figure 4.37 shows that for a single azimuthal position, there can be significant variation in the flow structure between the three trials. The fact that the flow patterns are inconsistent with azimuthal position; and in some cases, between trials; makes it difficult to quantify the strength of the LEV, and for this reason, the 50% spanwise location for the $AR = 4$ plate is not considered in calculating circulation.

### 4.1.2 Trailing-Edge Features

Some of the images, such as Figures 4.9, 4.11c, 4.11d, 4.12d, 4.12e, and 4.13e, show the development of a trailing-edge vortex (TEV). The presence of the TEV seems to have one of two effects on the vorticity field near the downstream portion of the plate. The first effect is the counterclockwise vorticity shed from TEV rolls up with the clockwise vorticity to form an amalgamated vortex as shown in Figure 4.12e. The other observation is the negative boundary layer vorticity on the downstream portion of the plate begins to separate from the surface of the plate and project into the wake as shown in Figure 4.11c. The fact that the TEV is not present at all azimuthal positions suggests it is an intermittent phenomenon.

## 4.2 Parameter Variations Comparisons

Figure 4.38 shows the development of the LEV structure and the region of positive vorticity generated on the surface of the plate with variation in Reynolds number and angle of attack for the aspect ratio 4 plate at $\psi = 90°$ at the 25% spanwise position. In Figure 4.38, the columns represent fixed angles of attack of 25°, 35°, and 45°, respectively with the rows corresponding to Reynolds numbers of 4,000, 8,000, and 16,000, respectively. At a constant Reynolds number, increasing angle of attack causes more of the surface vorticity to be entrained into the LEV which is shown best in the second row. For $\alpha = 25°$, increasing the Reynolds number from 4,000 to 8,000 does not appear to affect the shape of the LEV, but there are some minor changes when the Reynolds number is increased to 16,000. At Re = 16,000, the LEV is seen connecting to the plate just behind the downstream part of the region of positive vorticity. $\alpha = 35°$ has roughly the same shape between Re = 4,000 and 8,000 except at Re = 8,000 the shear layer is not as pronounce at the apex of the negative vorticity. Unlike the 25° angle of attack, the 35° angle of attack experiences a change in the shape of the LEV when the Reynolds number is increased to 16,000. The LEV contains portions of positive vorticity, but more importantly, the shape is more disorganized compared to the Re = 4,000 and 8,000 cases. Additionally, the LEV is not as elongated for a Reynolds number of 16,000. The LEV does not change much with Reynolds number for $\alpha = 45°$. Examining how angle of attack changes the shape of the LEV for a constant Reynolds number, it is clear that the shear layer begins to project up to the right more with increasing angle of attack. Furthermore,

the LEV goes from a more elongated shape at $\alpha = 25°$ and $35°$ to a rounder structure at $\alpha = 45°$. Overall the Reynolds number only appears to have minor effects on the structure of the LEV and entrainment of positive vorticity into the LEV.

Figure 4.39 shows the same data for the $\mathcal{AR}$= 2 plate at Re = 4,000 and 8,000 at the 50% spanwise position. The aspect ratio 2 plate's location of the LEV is seen touching back down to the plate at the back portion of the counterclockwise region where typical results for the $\mathcal{AR}$= 4 plate, the LEV is elevated from the surface of the plate. This reattachment of the LEV has been attributed to the tip vortex inducing a downwash flow[10] which is presumably stronger for $\mathcal{AR}$= 2 since the relative spanwise position is larger. Variations in Reynolds number are similar with the $\mathcal{AR}$= 4 plate, showing only minor changes in the shape of the LEV. Shape does not appear to be affected as intensely with increasing angle of attack, but it is obvious that the size of the LEV grows with increasing $\alpha$ for Re = 4,000. Lastly, the Re = 8,000 case shows that more of the positive vorticity is entrained into the LEV at higher angles of attack.

## 4.3 Circulation Measurements

For each combination of angle of attack, aspect ratio, azimuthal position, Reynolds number, and spanwise position, circulation measurements of the LEV structure were calculated (based on the spanwise component of vorticity) from the three instantaneous 2D PIV vorticity fields. For each vorticity field, the circulation was computed using Equation 4.1 and a user defined threshold was chosen such that the

circulation was insensitive to changes in the threshold.

$$\Gamma = \int \omega_z dA \approx \sum_N \omega_{z_{ij}} \Delta x \Delta y \tag{4.1}$$

The average of the three circulation measurements was used in the following discussion.

Figures 4.40 - 4.42 show the nondimensionalized circulation ($\Gamma^* = \Gamma/(cU_{tip})$) values of the LEV for $90° \leq \psi \leq 320°$ for Re = 4,000, 8,000, and 16,000, respectively. In general, there is a non-monotonic variation in $\Gamma^*$ with increasing azimuthal position in this range. For most cases (but not all), there is an apparent drop in circulation at an azimuthal position of approximately 230°. Beyond $\psi \approx 230°$, the circulation begins to rise again until the end of the azimuthal range investigated in this study. Measurements of the circulation of the positive vorticity were done in a similar manner, and the results showed that the counterclockwise region is approximately proportional to the LEV structure. For both aspect ratio plates, the nondimensionalized circulation of the LEV increases for increasing Reynolds number and angle of attack, independently. For each aspect ratio, Figures 4.43 and 4.44 show that the LEV's nondimensionalized circulation appears to be relatively insensitive to changes in Reynolds number.

Figures 4.40 and 4.41 depict for a given (dimensional) radial position, the smaller aspect ratio generated a higher nondimensionalized circulation measurement. However, this comparison looks at two different rotational speeds since the Reynolds numbers were based on the tip speed. If a local Reynolds number, $Re_{local}$, is defined

by Equation 4.2, the rotational speeds used in this study formulate values of 1,000, 2,000, and 4,000, respectively.

$$Re_{local} = \frac{cU_{local}}{\nu} \tag{4.2}$$

Using this new Reynolds number convention, the circulation can be nondimensionalized based on the local speed, $\Gamma^{**}$, as shown in Equation 4.3 and can be used to compare the results for both aspect ratios.

$$\Gamma^{**} = \frac{\Gamma}{cU_{local}} \tag{4.3}$$

Figures 4.45 and 4.46 show the results of the new nondimensionalization comparing the same angular velocity for both aspect ratios. The trend of the dominant aspect ratio has switched where the aspect ratio 2 plate generates a lower circulation value compared to the aspect ratio 4 plate. This result is likely contributed to the tip vortex bending $\omega_z$ vorticity into the streamwise direction essentially reducing $\Gamma^{**}$ which will be more severely affected for the smaller aspect ratio since the relative spanwise location is closer to the tip.

Thin airfoil theory predicts that the bound circulation on a translating flat plate in inviscid, potential flow will increase linearly with increasing angle of attack demonstrated in Equation 4.4[43].

$$\Gamma_{th} = \pi c U_{local} \sin\alpha \tag{4.4}$$

Table 4.1 shows the values obtained using Equation 4.4 and are graphed with

the mean experimental circulation values of the LEV ($\Gamma_{mean}$) in Figures 4.47 - 4.49. Additional plots are presented in Appendix A showing each azimuthal position for both aspect ratios in Figures A.1 - A.10. Figure 4.47 shows the $\mathcal{R}4$ plate's experimental circulation values for the LEV at $\psi = 90°$. This sample plot is a representation of the typical plots for the $\mathcal{R}4$ plate, showing the experimental data to appear linearly increasing over the range of angles of attack investigated. For this particular case, the experimental data is quite linear for the Re = 4,000 and 16,000 cases; however, there is some curvature to the Re = 8,000 case which more than likely would smooth out with more trials acquired. The linearity of the LEV circulation measurements is directly proportional to sin$\alpha$ and suggests that the data presented here is of good quality and reliability. Another important trait illustrated in Figure 4.47 is that the LEV circulation and theoretical bound circulation have different constant relationships with sin$\alpha$, meaning the differences between the two become increasingly bigger as the angle of attack increases for a fixed Reynolds number. However, the relative circulation ($\Gamma' = \Gamma_{mean}/\Gamma_{th}$) is nearly constant for varying angles of attack at a constant azimuthal position as shown in Tables 4.2 - 4.4. In most cases, with the changes in azimuthal position, the relative circulation gradually increases from $\psi = 90°$ to $\approx 180°$ then stays approximately constant, fluctuating around a steady-state value. The LEV circulation measurements for the $\mathcal{R}4$ plate are all well above the theoretical bound circulation which is in agreement with previous work discussed in Chapters 1 and 2 that the LEV is a main source of lift augmentation in rotating wings.

Although the $\mathcal{R}4$ plate's LEV circulation measurements were higher than

the theoretical bound circulation, that is not always the case for the $\mathcal{AR}$= 2 plate. Figure 4.48 shows an incident where the LEV circulation actually dropped below the bound circulation at $\psi = 180°$ and $\alpha = 35°$. This event could be explained by the range of circulation measurements over the three trials skewing $\Gamma_{mean}$. As shown in Figure 4.50, the variability in the circulation measurements where the upper error bar represents the highest circulation value in the three trials, and the bottom error bar represents the lowest circulation value. The origin of the error bars corresponds to the middle circulation value of the three trials.

Figure 4.49 represents a typical plot for a constant local Reynolds number for the $\mathcal{AR}$= 2 plate. Similar comments that were made concerning the $\mathcal{AR}$= 4 plate can be applied to the $\mathcal{AR}$= 2 plate. The experimental data is approximately linear showing that the LEV circulation is proportional to sin$\alpha$ except the slopes differ between the theoretical and experimental data for a given Reynolds number. The Re = 8,000 case at $\alpha = 25°$ is consistently close to the theoretical bound circulation values for all of the azimuthal positions.

The difference between the bound and LEV circulations for the $\mathcal{AR}$= 2 plate can be viewed in Tables 4.5 and 4.6. The trends are similar to the $\mathcal{AR}$= 4 tables, but comparatively, the $\mathcal{AR}$= 4 plate has a larger relative circulation value than the $\mathcal{AR}$= 2 plate. The larger aspect ratio plate experiences relative circulation values as much as 2.3 times greater than the theoretical bound circulation values while the $\mathcal{AR}$= 2 plate is unable to exceed 1.53 times the bound circulation value. This suggests the enhanced lift seen on rotating wings is mainly an inboard phenomenon as stated in

previous studies[98, 99].

### 4.4 Rossby Number Effects

As previously shown, an attached LEV was observed for both aspect ratio plates. It was hypothesized that one of the reasons for others to observe a shedding LEV was due to the configuration of their setup, in particular, the Rossby number (Ro = $R_{root}$/c; where $R_{root}$ is the radius from the axis of rotation to the start of the plate). In the previously discussed experiments, the Rossby number was 0.3125; a new study was conducted to determine if Rossby number affected the dynamics of the LEV by causing it to shed. Venkata and Jones (2012) had a Rossby number of 0.65 where they observed a shedding LEV on an $\mathcal{AR}$= 2 flat plate at angles of attack of 15° and 45° at the 50% spanwise location for a Re = 5,000. In that respect, a Rossby number of 0.8125 was chosen to evaluate the claim of Rossby number affecting the dynamics of the LEV.

Some preliminary tests were performed on both aspect ratio plates. Figure 4.51 shows the results for the $\mathcal{AR}$= 4 plate at a Re = 8,000 for an angle of attack of 35° for the range of azimuthal positions. It is apparent that even at a higher Ro, an attached LEV can still be observed. This suggests that something else may be controlling the dynamics of the LEV. One such mechanism could be the acceleration rate and distance before the plate reaches a constant angular velocity (Anya Jones, personal communication). However, this preliminary test reveals some interesting traits. Comparing to the Ro = 0.3125 case (Figure 4.6), the higher Rossby number

yielded a less coherent structure at all azimuthal positions. Furthermore, the size of LEV is larger for the Ro = 0.8125 case, which allowed it to entrain more of the positive vorticity inside the LEV. A nice future work comparison would be to do circulation measurements for this data at the 37.5% spanwise location for the Ro = 0.3125 case to show how the LEV's strength is affected by Rossby number.

Similar results were seen for the $\mathcal{R}$= 2 plate at the 50% spanwise location for a Ro = 0.8125.

## 4.5 Vorticity Transport Analysis

It was stated in Section 4.1 that there is an interaction between the counter-clockwise region of vorticity adjacent to the plate's surface and LEV structure, and it is hypothesized that this interaction could potentially cause significant annihilation of the LEV, which may help regulate the overall strength of the LEV and prevent it from detaching from the surface of the plate. To support this claim, SPIV was implemented as discussed in Section 3.2.4 to determine the contribution annihilation has of the governing physics of the problem.

The $\mathcal{R}$= 4 plate at a Reynolds number of 8,000 (based on tip speed) and an angle of attack of 35° for $\psi = 75°$, 90°, 120°, 180°, and 270° was the only configuration investigated. Nevertheless, a planar, chordwise control volume, shown in Figure 4.52, at the 25% spanwise location was used which examined the relevant sources and sinks of vorticity through the control volume. The conservation of vorticity through the control volume is expressed in Equation 4.5.

$$\frac{d\Gamma_z}{dt} = -\int_{A_z} U_z \frac{\partial \omega_z}{\partial z}\, dA_z + \int_{A_z} \left( \omega_y \frac{\partial U_z}{\partial y} + \omega_x \frac{\partial U_z}{\partial x} \right) dA_z + \int_{L_y} U_x \omega_z \, dL - Annihilation \quad (4.5)$$

This analysis only considers the transport of spanwise circulation, $\Gamma_z$, in particular, the circulation of the negative vorticity which was ensured by applying a vorticity threshold as discussed in Section 4.3. An average of five trials at each of the planes mentioned in Section 3.2.4 was used to evaluate the terms in Equation 4.5. The term on the left side represents the rate of change of circulation of the negative vorticity which is calculated by using a weighted central differencing scheme between three subsequent azimuthal positions and is shown discretely in Equation 4.6.

$$\frac{d\Gamma}{dt} = \frac{1}{2}\left( \frac{\Gamma_2 - \Gamma_1}{t_1} + \frac{\Gamma_1 - \Gamma_0}{t_2} \right) \quad (4.6)$$

A weighted central differencing scheme was needed since the spacing between azimuthal locations was not constant. In Equation 4.6, $\Gamma_0$, $\Gamma_1$, and $\Gamma_2$ are the "first", "second", and "third" azimuthal positions used to evaluate the vorticity transport analysis at a particular $\psi$ (e.g. to evaluate the term at $\psi = 90°$, values of $\Gamma$ at $\psi = 75°$, $90°$, and $120°$ were used). The $t_1$ term is the time it takes the blade to traverse from the "second" to the "third" position while $t_2$ is the time it takes the blade to rotate from the "first" to the "second" azimuthal position.

The first term on the right hand side is the rate of change of negative vorticity due to spanwise convection of a vorticity gradient. It is this term that others claim

to be the dominate term in transporting the flux of vorticity along the surface of the blade essentially regulating the strength of the LEV[30, 56, 57, 95]. The convection term was calculated discretely as shown in Equation 4.7.

$$\int_{A_z} U_z \frac{\partial \omega_z}{\partial z}\, dA_z = \sum U_z \frac{\partial \omega_z}{\partial z} X_g Y_g = \sum U_z \frac{\omega_{z_{k+1}} - \omega_{z_{k-1}}}{2Z_g} X_g Y_g \tag{4.7}$$

Where $U_z$, $\omega_{z_{k+1}}$, $\omega_{z_{k-1}}$, $Z_g$, $X_g$, and $Y_g$ is the spanwise velocity, spanwise vorticity at the *k+1 plane* (outboard most chordwise laser plane), spanwise vorticity at the *k-1 plane* (inboard most chordwise laser plane), spacing between chordwise laser planes, spacing between vectors generated in the PIV vector files in the streamwise direction, and spacing between vectors created in the PIV vector files in the vertical direction (y-direction), respectively. Recall, the *k-1*, *k*, and *k+1 planes* are shown in Figure 3.13.

The second term on the right side of Equation 4.5 accounts for tilting of streamwise and normal vorticity, $\omega_x$ and $\omega_y$, into the spanwise direction. This term is broken into two parts to calculate the contributions from the X- and Y-tilting; each one of these parts were calculated discretely shown in Equation 4.8 and 4.9, respectively.

$$\int_{A_z} \omega_x \frac{\partial U_z}{\partial x}\, dA_z = \sum \left( \frac{U_{z_{j+1}} - U_{z_{j-1}}}{2Y_g} - \frac{U_{y_{k+1}} - U_{z_{k-1}}}{2Z_g} \right) \left( \frac{U_{z_{i+1}} - U_{z_{i-1}}}{2X_g} \right) X_g Y_g \tag{4.8}$$

$$\int_{A_z} \omega_y \frac{\partial U_z}{\partial y}\, dA_z$$
$$= \sum \left( \frac{U_{x_{k+1}} - U_{x_{k-1}}}{2Z_g} - \frac{U_{z_{i+1}} - U_{z_{i-1}}}{2X_g} \right) \left( \frac{U_{z_{j+1}} - U_{z_{j-1}}}{2Y_g} \right) X_g Y_g \quad (4.9)$$

Where $i$ is a shift in the vector location in the x-direction while $j$ is a shift in the y-direction.

The third term evaluates the flux of spanwise vorticity into the control volume from the shear layer created at the leading-edge of the plate. Since the shear layer is unsteady, about 20 realizations were used to obtain a *representative* value for the third term. It was computed by averaging a series of vertical boundaries starting from the bottom point of boundary 1 in Figure 4.52 until slightly past the leading-edge to average out any non-uniformities created from instabilities associated with shear layers. The shear layer term can be represented discretely as demonstrated in Equation 4.10.

$$\int_{L_y} U_x \omega_z\, dL = \sum U_x \omega_z Y_g \quad (4.10)$$

Where $L_y$ is boundary 1 in Figure 4.52.

The sign convection of Equation 4.5 is such that a negative annihilation value refers to the destruction of negative vorticity in the control volume. Furthermore, it is assumed that there is no flux of vorticity through boundaries 2 and 3 shown in Figure 4.52. This was asserted by proper placement of the two boundaries so that the top boundary is above the LEV region, and since the LEV in this study is stationary,

the third boundary was applied far enough downstream to make sure there is no flux through boundary 3. Lastly, since typically counterclockwise vorticity is seen along the surface of the plate, it is assumed that the flux of vorticity across boundary 4 due to vorticity creation is negligible because only negative vorticity is accounted for. Additionally, the control volume was defined to be fixed to the plate such that the velocity at boundary 4 is zero. With the proper boundaries in place, it is assumed that whatever is not accounted for by these four terms is the contribution annihilation has on the LEV.

To calculate the in-plane vorticity components, $\omega_x$ and $\omega_y$, as well as the derivatives of velocities and spanwise vorticity, a second-order central difference scheme was implemented using the three laser planes, discussed in Section 3.2.4, each separated by 1 millimeter. Precision alignment pins on the mounting structure were used to accurately move the apparatus to ensure the correct shift with respect to the stationary camera and laser plane.

Figure 4.53 shows the values of each of the terms at the three azimuthal positions where the analysis was performed. The $\omega_x$ and $\omega_y$ tilting terms are the dominating terms in Equation 4.5, and they exhibit a highly symmetrical pattern suggesting that their net effect is mainly an exchange between in-plane vorticity with relatively small contribution to the spanwise component. This implies that the vorticity distribution inside the LEV is highly three-dimensional. The tilting terms appear to become relatively constant beyond $\psi = 120°$.

Figure 4.54 zooms in on the azimuthal axis of Figure 4.53 to closely exam-

ine the other terms in Equation 4.5. An unexpected result is the contribution the convection term has in the control volume. In the azimuthal positions below 120°, the annihilation term and convection term are in balance with one another. As the system approaches a steady-state at $\psi \approx 120°$, the convection and unsteady term vanish. This is in agreement with the 2D circulations measurements that were compared with the theoretical bound circulation (i.e. Table 4.3) since the $\Gamma'$ is relatively constant beyond $\psi = 180°$. This contradicts the spanwise flow arguments presented by Ellington's group and others claiming that spanwise flow keeps the LEV attached to the wing by transporting vorticity from the inboard locations outwards towards the tip[30, 67, 68, 69, 21, 22, 121]. Instead, the results presented here are similar to Birch and Dickinson [10] by showing that spanwise flow is not essential during steady-state. More importantly, after the initial transient (e.g. $\psi$ >120°), the shear layer and annihilation term are in balance with one another with minor variations being the differences between the $\omega_x$ and $\omega_y$ tilting terms. This strongly supports the claim that annihilation is an important factor in governing the strength of the LEV and thus ultimately keeping it attached to the LEV.

An error analysis was conducted on each of the terms and a detailed discussion is presented in Appendix B. The error analysis yielded uncertainties for the unsteady, convection, $\omega_x$ tilting, $\omega_y$ tilting, and shear layer terms of 15.2%, 2.6%, 4.7%, 4.7%, and 1.2%, respectively. The uncertainty for the annihilation term was determined by adding the uncertainties of the other terms in quadrature at each azimuthal position.

The three-dimensionality of the LEV region is supported by the spanwise

velocity measurements shown in Figures 4.55 - 4.59, which depicts how the spanwise velocity develops with time. There exists the development of two opposing pairs of spanwise velocities that appear inside the control volume where blue signifies a tip-to-root flow and red is a root-to-tip flow. The spanwise velocities for both flows grow in magnitude with increasing azimuthal angle. The appearance of two opposing spanwise velocities inside the LEV has been shown in the literature by Carr et al [17] using SPIV measurements done on similar aspect ratio plates. The magnitude of the spanwise velocities are not comparable with Carr et al [17] because their results show the earlier azimuthal positions (i.e. $\psi \leq 48°$), but their results do show an increase in the magnitudes as azimuthal position increases, which is consist with the current results.

To attempt to validate the spanwise velocities seen using SPIV, 2D PIV was used by creating a spanwise laser plane ($y$-$z$) 5 millimeters from the leading-edge to attempt to measure the spanwise velocity along the span of the plate. The averaged, nondimensionalized, spanwise velocity contours for the 2D experiments can be seen in Figure 4.60, and it is apparent that the spanwise flow at the inboard spanwise locations exceed the tip velocity. The magnitude of the spanwise flow measured using SPIV in the core of the root-to-tip flow was on average about $U_z^* = 0.5$ at $\psi = 180°$. The 2D data has approximately the same value, but it tends to be a little higher than the SPIV measurements. One possible explanation for this is the 2D data might need more trials to properly characterize the spanwise velocities because the three average trials produce jagged contours. The tip-to-root flow is not visible in the averaged

contours of the nondimensionalized spanwise velocity, but as shown in Figure 4.61, the instantaneous, nondimensionalized, spanwise velocity contours indicate a tip-to root velocity near the tip of the plate. Since the velocity of the tip-to-root flow is very small, those contours values were not shown in Figure 4.60.

Contour plots of the convection, X-tilting, and Y-tilting inside the control volume are shown in Figures 4.62 - 4.64. Figure 4.62 reveals that the main portion of the control volume where convection of $\Gamma_z$ due to a vorticity gradient occurs at the back, lower part of the LEV which coincides with the largest root-to-tip velocity gradients shown in Figures 4.55 - 4.59. On the other hand, Figures 4.63 and 4.64 show the regions where the dominant exchange of $\omega_x$ and $\omega_y$ occur, respectively. These results further confirm that the structure of the LEV is highly three-dimensional since the contours do not appear to show any dominate regions of tilting.

Table 4.1: Theoretical bound circulations in $mm^2/s$ computed according to Equation 4.4.

| | **Reynolds Number** | | |
|---|---|---|---|
| $\boldsymbol{\alpha}$ | **4,000** | **8,000** | **16,000** |
| **25**° | 1346 | 2691 | 5382 |
| **35**° | 1826 | 3652 | 7305 |
| **45**° | 2251 | 4503 | 9005 |

Table 4.2: Relative circulation ($\Gamma'$) values for the $\mathcal{AR}$= 4 plate at a $Re_{local}$ = 4,000 for the azimuthal range examined.

| | $\alpha$ | | |
|---|---|---|---|
| $\psi$ | **25°** | **35°** | **45°** |
| **90°** | 1.40 | 1.51 | 1.62 |
| **180°** | 1.57 | 1.76 | 2.23 |
| **235°** | 1.78 | 1.92 | 1.99 |
| **270°** | 1.83 | 1.82 | 2.06 |
| **320°** | 1.93 | 1.91 | 2.02 |

Table 4.3: Relative circulation ($\Gamma'$) values for the $\mathcal{AR}$= 4 plate at a $Re_{local}$ = 8,000 for the azimuthal range examined.

| | $\boldsymbol{\alpha}$ | | |
|---|---|---|---|
| $\boldsymbol{\psi}$ | **25°** | **35°** | **45°** |
| **90°** | 1.50 | 1.77 | 1.77 |
| **180°** | 1.90 | 1.99 | 2.07 |
| **235°** | 1.93 | 2.05 | 2.15 |
| **270°** | 1.91 | 2.04 | 2.09 |
| **320°** | 2.10 | 2.35 | 2.07 |

Table 4.4: Relative circulation ($\Gamma'$) values for the $\mathcal{AR}$= 4 plate at a $Re_{local}$ = 16,000 for the azimuthal range examined.

| | $\boldsymbol{\alpha}$ | | |
|---|---|---|---|
| $\boldsymbol{\psi}$ | **25°** | **35°** | **45°** |
| **90°** | 1.62 | 1.67 | 1.79 |
| **180°** | 1.91 | 1.85 | 2.08 |
| **235°** | 1.99 | 2.07 | 2.00 |
| **270°** | 2.17 | 2.17 | 2.13 |
| **320°** | 2.28 | 2.01 | 2.11 |

Table 4.5: Relative circulation ($\Gamma'$) values for the $\mathcal{AR}$= 2 plate at a $Re_{local}$ = 8,000 for the azimuthal range examined.

| | $\alpha$ | | |
|---|---|---|---|
| $\psi$ | **25°** | **35°** | **45°** |
| **90°** | 0.91 | 1.14 | 1.25 |
| **180°** | 1.02 | 1.28 | 1.46 |
| **235°** | 1.14 | 1.38 | 1.53 |
| **270°** | 1.15 | 1.35 | 1.50 |
| **320°** | 1.19 | 1.37 | 1.42 |

Table 4.6: Relative circulation ($\Gamma'$) values for the $\mathcal{AR}$= 2 plate at a $Re_{local}$ = 16,000 for the azimuthal range examined.

| | $\boldsymbol{\alpha}$ | | |
|---|---|---|---|
| $\boldsymbol{\psi}$ | **25°** | **35°** | **45°** |
| **90°** | 1.15 | 1.10 | 1.14 |
| **180°** | 1.13 | 0.97 | 1.45 |
| **235°** | 1.31 | 1.24 | 1.50 |
| **270°** | 1.28 | 1.50 | 1.49 |
| **320°** | 1.31 | 1.44 | 1.38 |

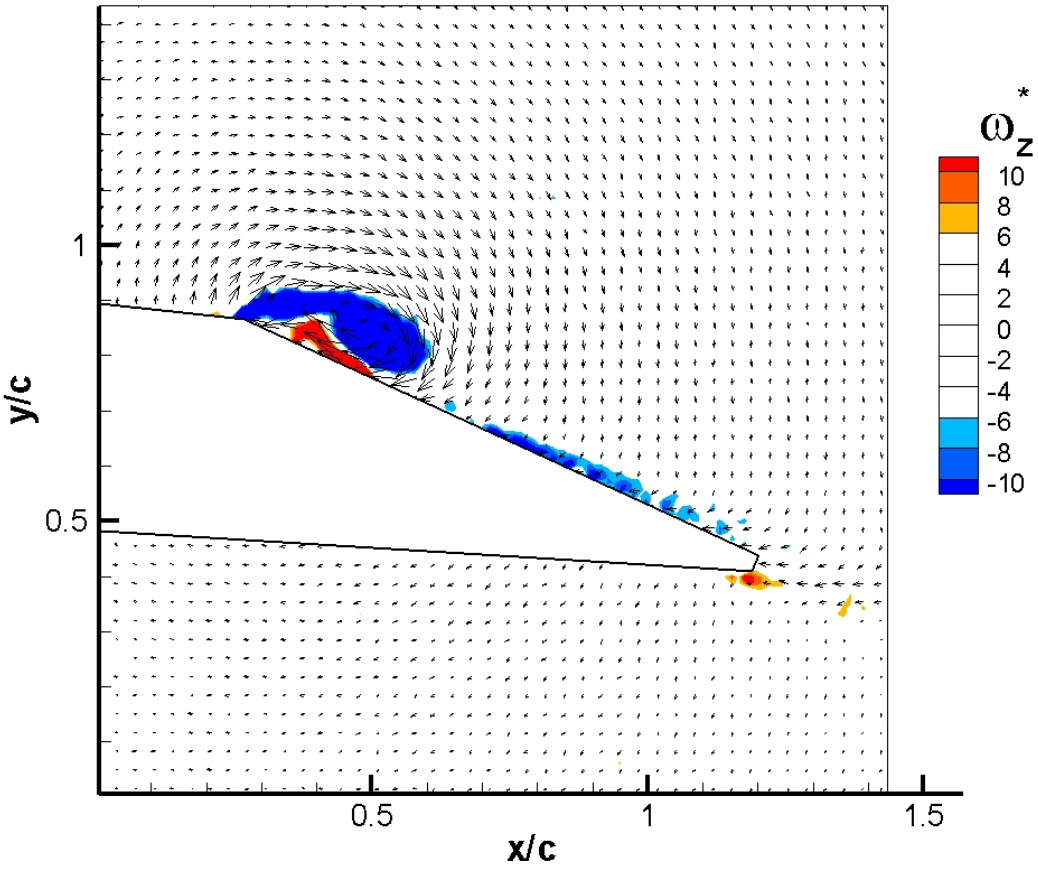


Figure 4.1: Nondimensionalized, instantaneous vorticity field at $\psi = 90°$ for the 25% spanwise location on the $\mathcal{A}R4$ plate at an $\alpha = 25°$ and Reynolds number of 4,000. In-plane velocity components are shown by the vectors.

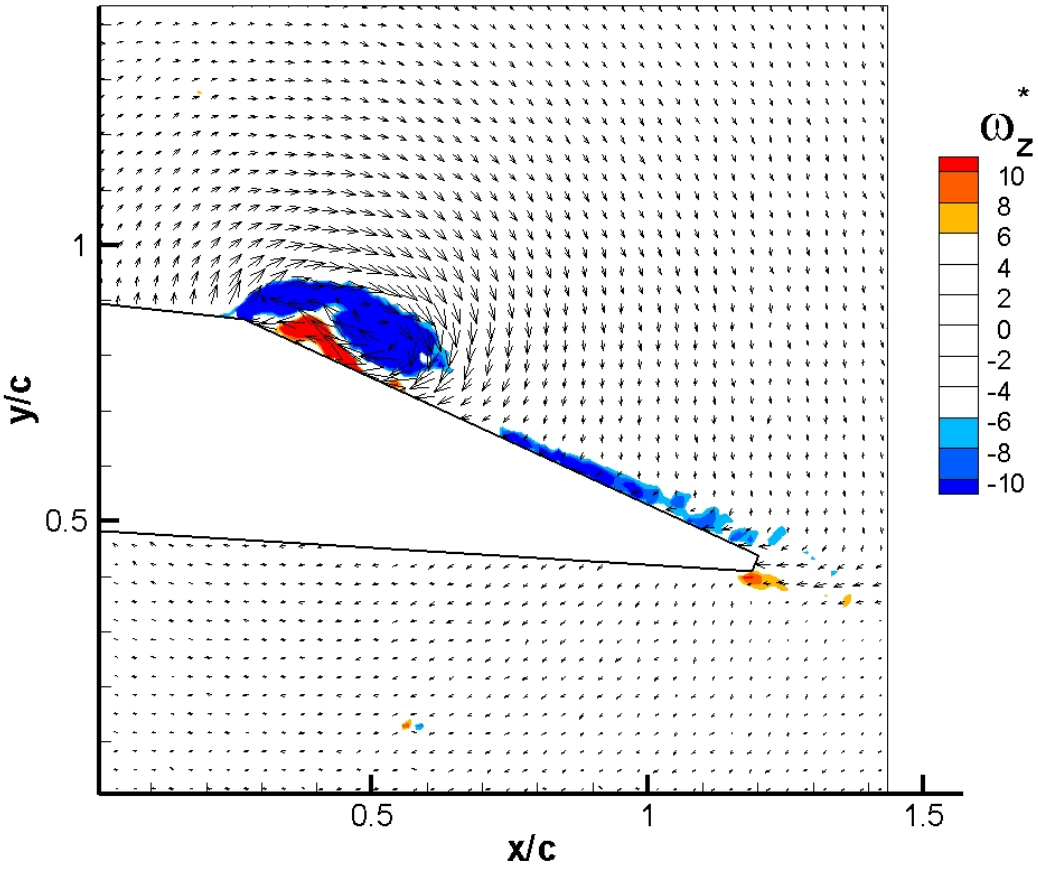


Figure 4.2: Nondimensionalized, instantaneous vorticity field at $\psi = 180°$ for the 25% spanwise location on the $\mathcal{A}R4$ plate at an $\alpha = 25°$ and Reynolds number of 4,000. In-plane velocity components are shown by the vectors.

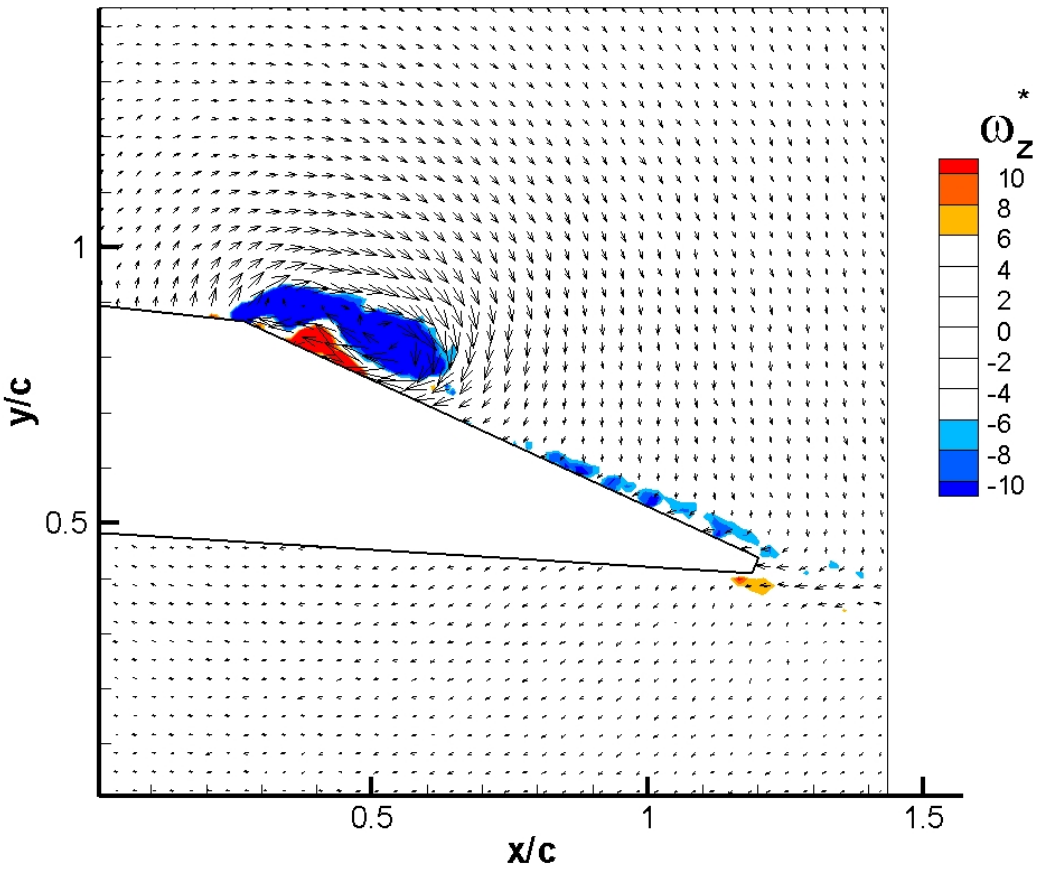


Figure 4.3: Nondimensionalized, instantaneous vorticity field at $\psi = 235°$ for the 25% spanwise location on the $\mathcal{A}R4$ plate at an $\alpha = 25°$ and Reynolds number of 4,000. In-plane velocity components are shown by the vectors.

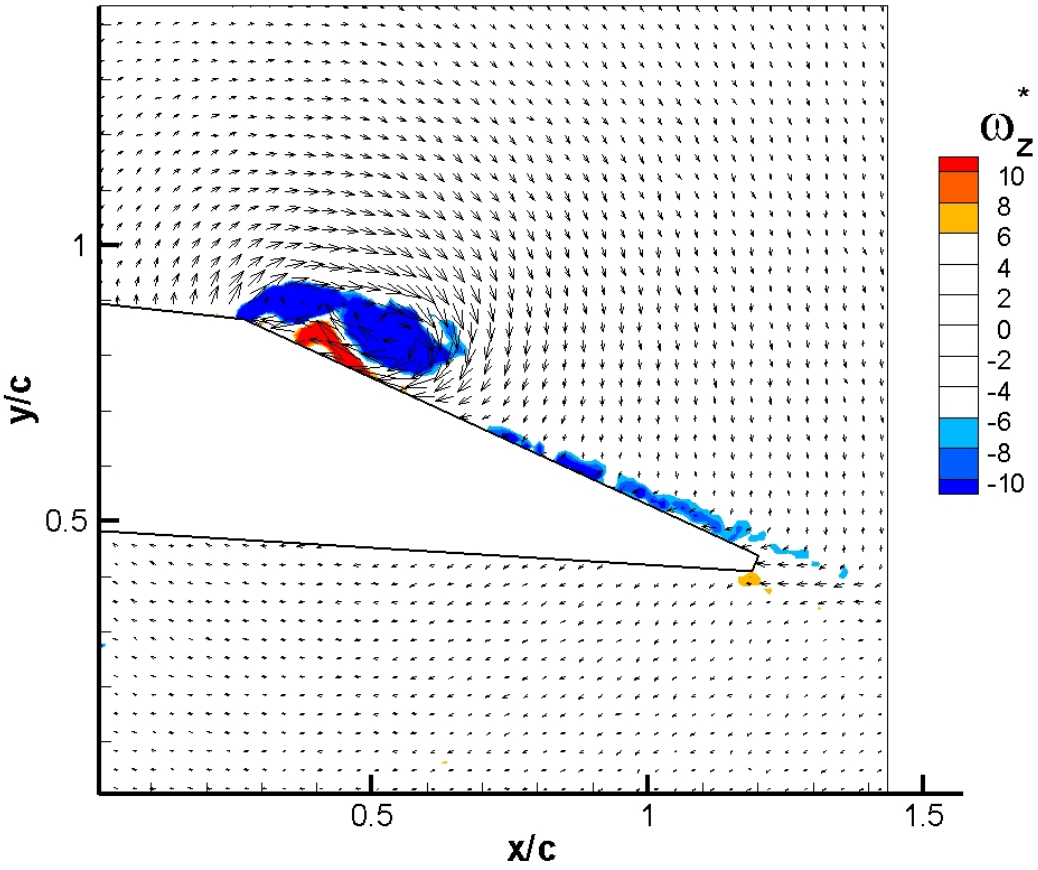


Figure 4.4: Nondimensionalized, instantaneous vorticity field at $\psi = 270°$ for the 25% spanwise location on the $\mathcal{A}R4$ plate at an $\alpha = 25°$ and Reynolds number of 4,000. In-plane velocity components are shown by the vectors.

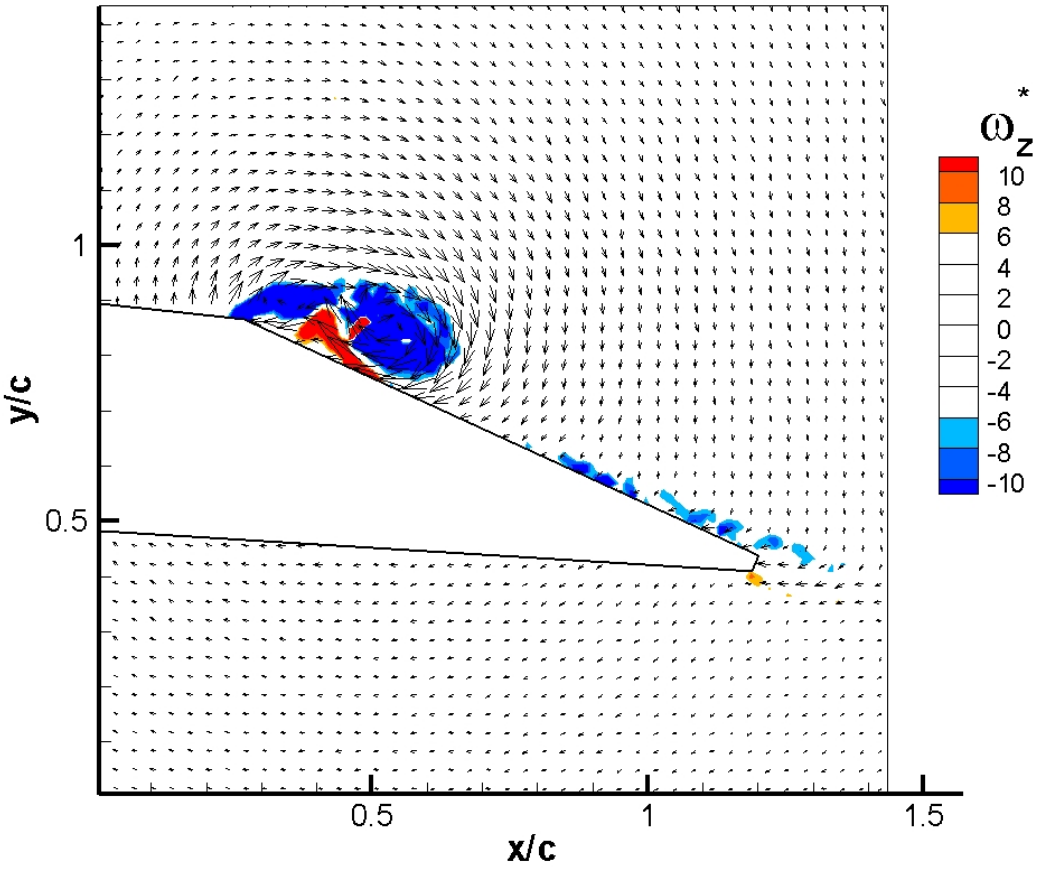


Figure 4.5: Nondimensionalized, instantaneous vorticity field at $\psi = 320°$ for the 25% spanwise location on the $\mathcal{A}R4$ plate at an $\alpha = 25°$ and Reynolds number of 4,000. In-plane velocity components are shown by the vectors.

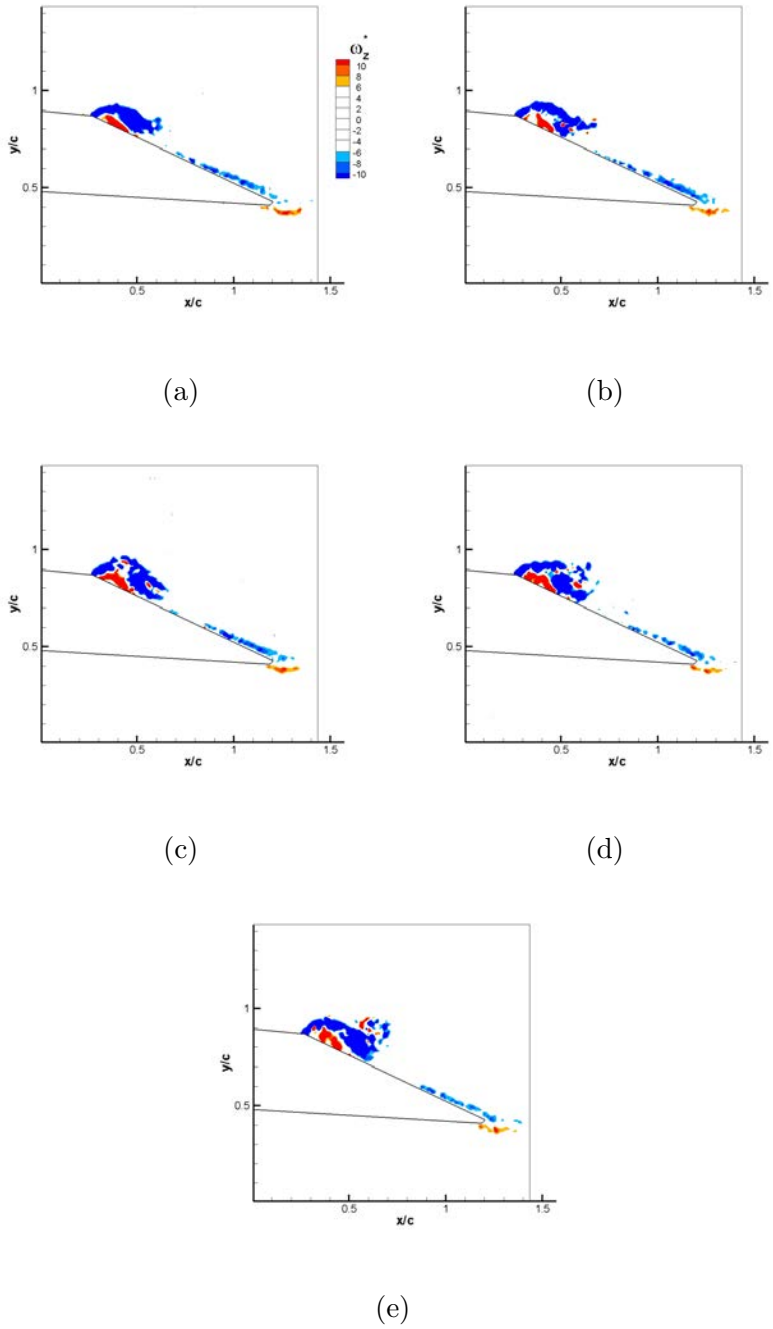


Figure 4.6: Temporal evolution of the nondimensionalized, instantaneous vorticity fields at the 25% spanwise location for the $\mathcal{R}4$ plate at an $\alpha = 25°$ and Reynolds number of 8,000. a.) $\psi = 90°$ b.) $\psi = 180°$ c.) $\psi = 235°$ d.) $\psi = 270°$, and e.) $\psi = 320°$.

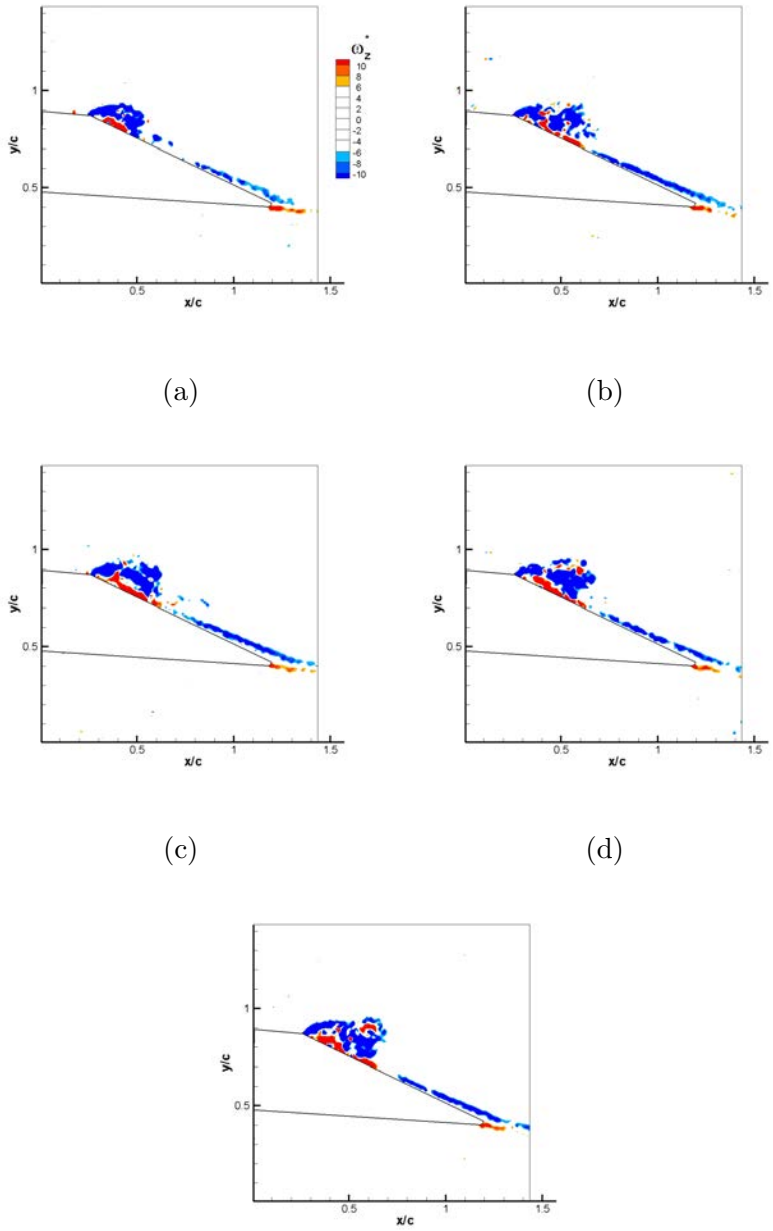


Figure 4.7: Temporal evolution of the nondimensionalized, instantaneous vorticity fields at the 25% spanwise location for the $\mathcal{R}4$ plate at an $\alpha = 25°$ and Reynolds number of 16,000. a.) $\psi = 90°$ b.) $\psi = 180°$ c.) $\psi = 235°$ d.) $\psi = 270°$, and e.) $\psi = 320°$.

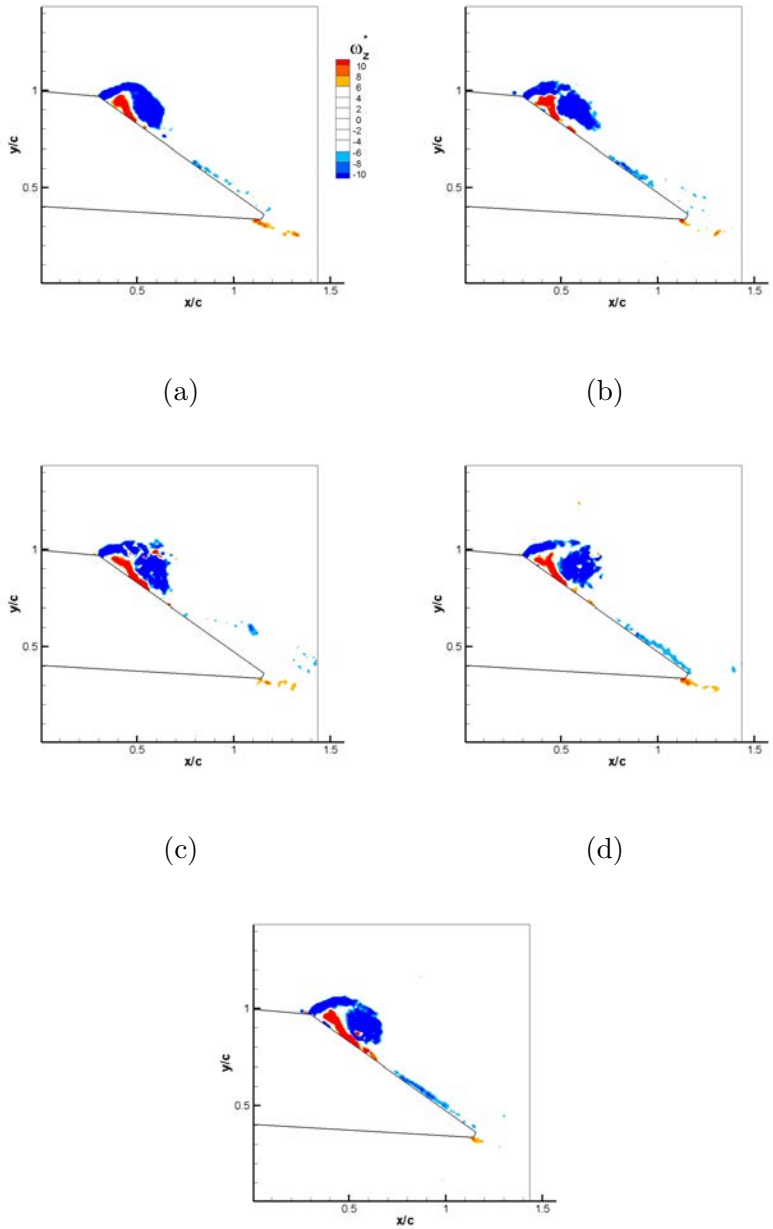


Figure 4.8: Temporal evolution of the nondimensionalized, instantaneous vorticity fields at the 25% spanwise location for the $\mathcal{A}R4$ plate at an $\alpha = 35°$ and Reynolds number of 4,000. a.) $\psi = 90°$ b.) $\psi = 180°$ c.) $\psi = 235°$ d.) $\psi = 270°$, and e.) $\psi = 320°$.

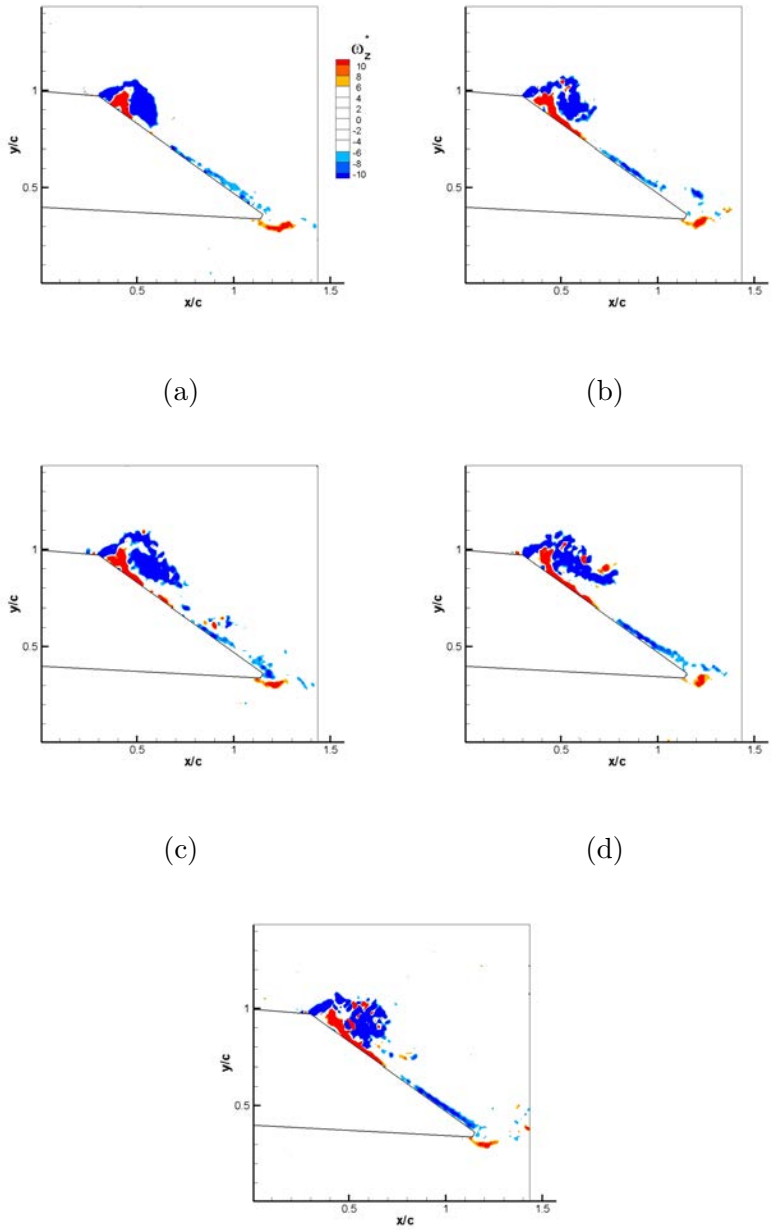


Figure 4.9: Temporal evolution of the nondimensionalized, instantaneous vorticity fields at the 25% spanwise location for the $\mathcal{A}R4$ plate at an $\alpha = 35°$ and Reynolds number of 8,000. a.) $\psi = 90°$ b.) $\psi = 180°$ c.) $\psi = 235°$ d.) $\psi = 270°$, and e.) $\psi = 320°$.

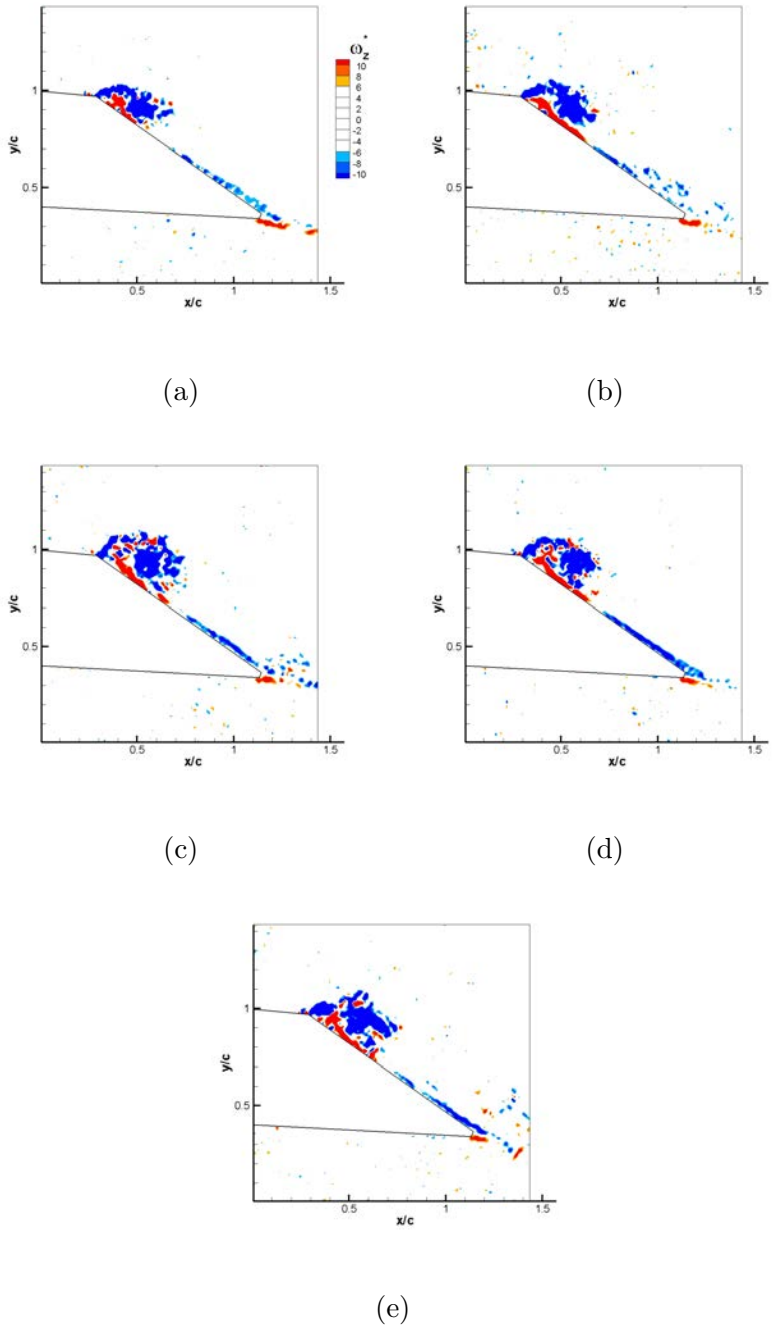


Figure 4.10: Temporal evolution of the nondimensionalized, instantaneous vorticity fields at the 25% spanwise location for the $\mathcal{A}R4$ plate at an $\alpha = 35°$ and Reynolds number of 16,000. a.) $\psi = 90°$ b.) $\psi = 180°$ c.) $\psi = 235°$ d.) $\psi = 270°$, and e.) $\psi = 320°$.

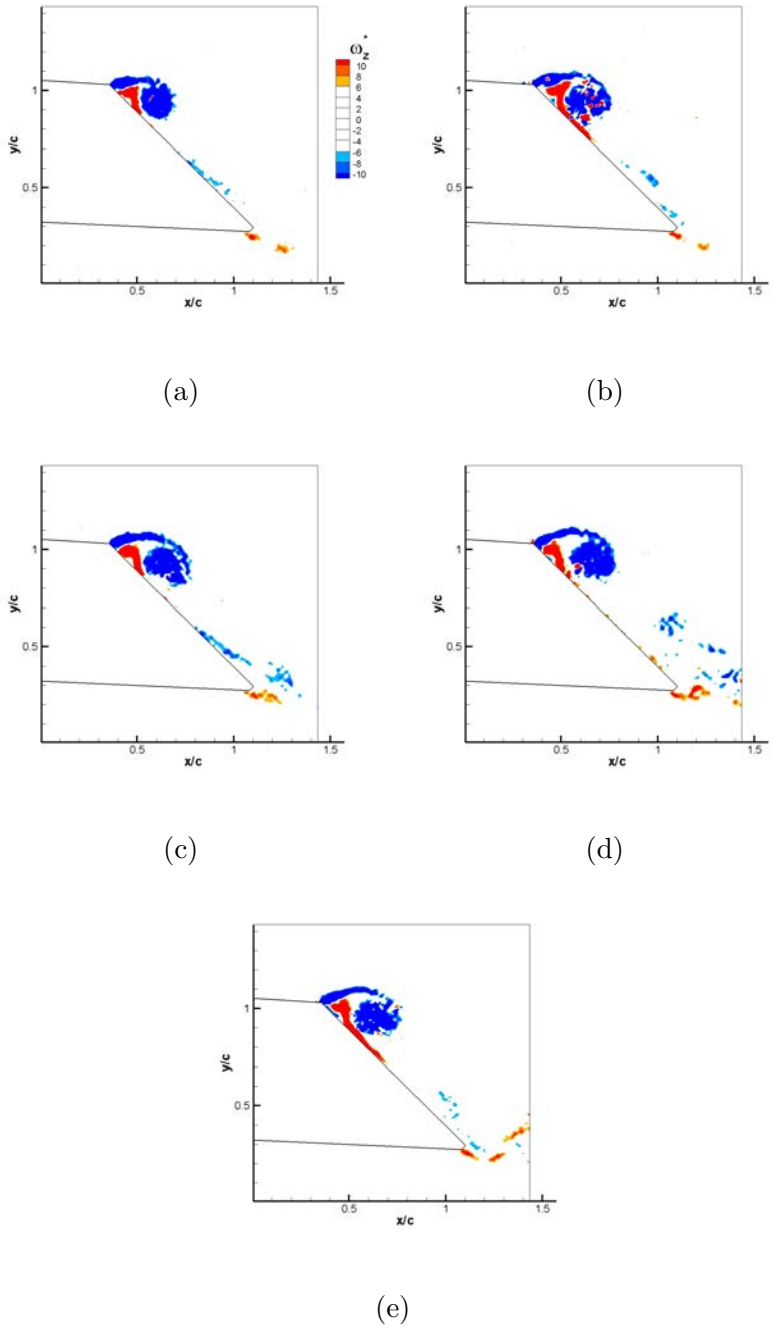


Figure 4.11: Temporal evolution of the nondimensionalized, instantaneous vorticity fields at the 25% spanwise location for the $\mathcal{A}R4$ plate at an $\alpha = 45°$ and Reynolds number of 4,000. a.) $\psi = 90°$ b.) $\psi = 180°$ c.) $\psi = 235°$ d.) $\psi = 270°$, and e.) $\psi = 320°$.

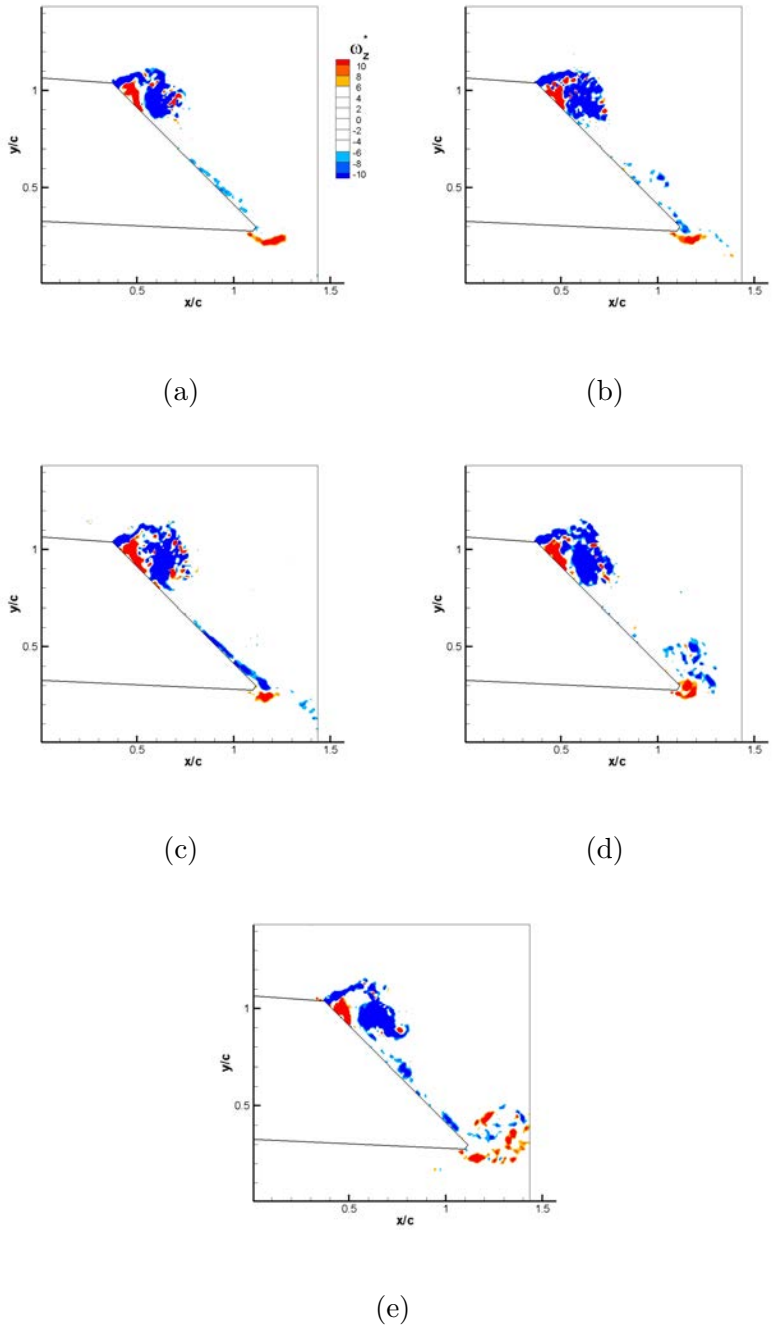


Figure 4.12: Temporal evolution of the nondimensionalized, instantaneous vorticity fields at the 25% spanwise location for the $\mathcal{A}R4$ plate at an $\alpha = 45°$ and Reynolds number of 8,000. a.) $\psi = 90°$ b.) $\psi = 180°$ c.) $\psi = 235°$ d.) $\psi = 270°$, and e.) $\psi = 320°$.

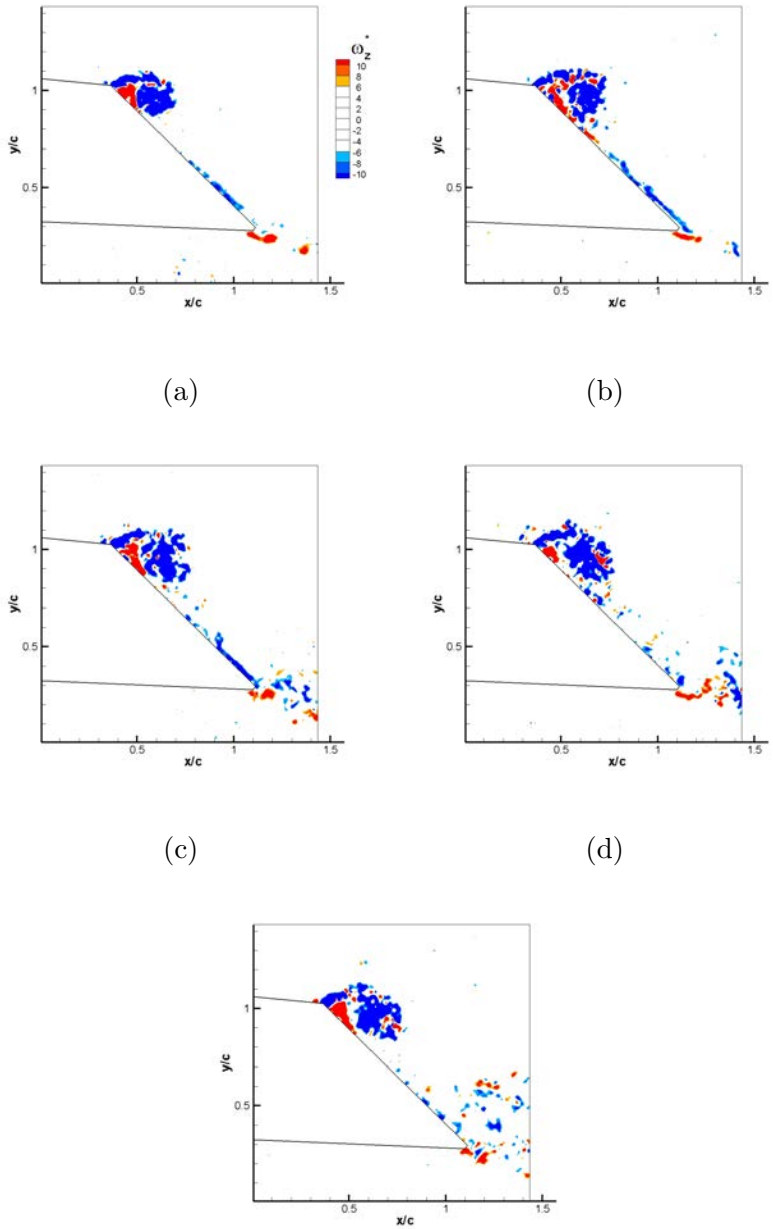


Figure 4.13: Temporal evolution of the nondimensionalized, instantaneous vorticity fields at the 25% spanwise location for the $\mathcal{A}R4$ plate at an $\alpha = 45°$ and Reynolds number of 16,000. a.) $\psi = 90°$ b.) $\psi = 180°$ c.) $\psi = 235°$ d.) $\psi = 270°$, and e.) $\psi = 320°$.

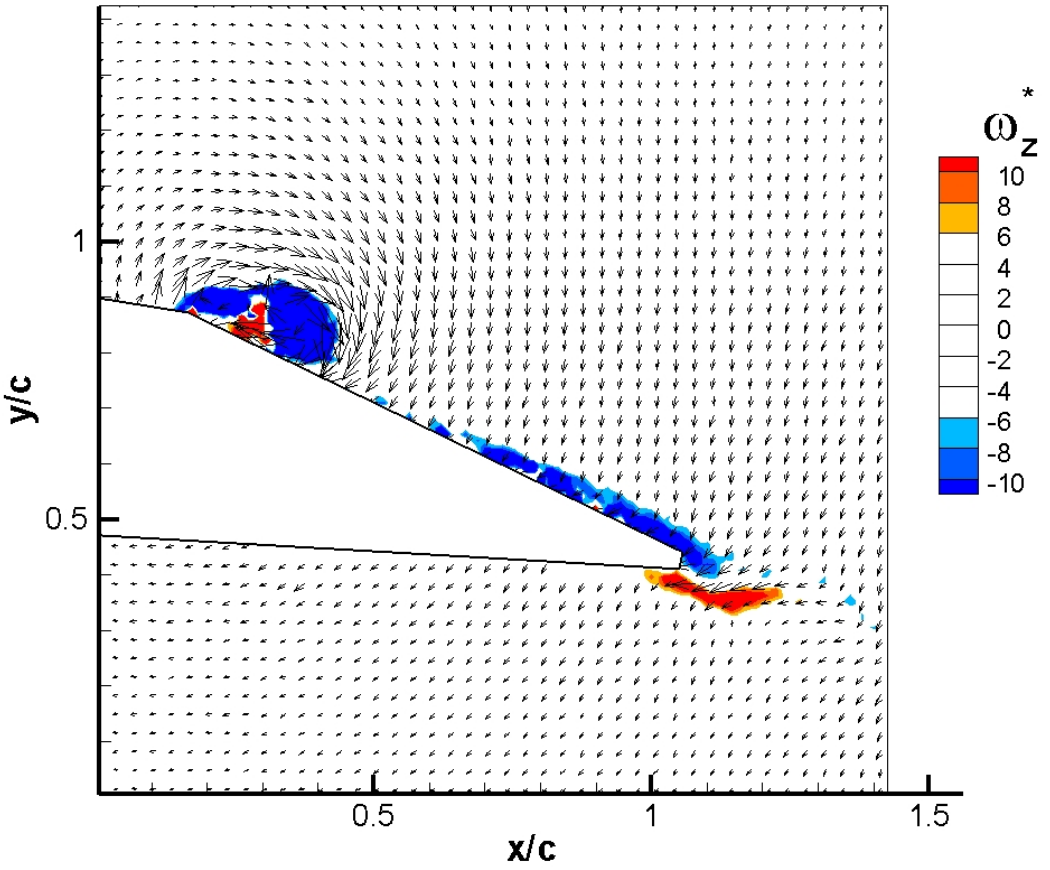


Figure 4.14: Nondimensionalized, instantaneous vorticity field at $\psi = 90°$ for the 50% spanwise location on the $\mathcal{A}R2$ plate at an $\alpha = 25°$ and Reynolds number of 4,000. In-plane velocity components are shown by the vectors.

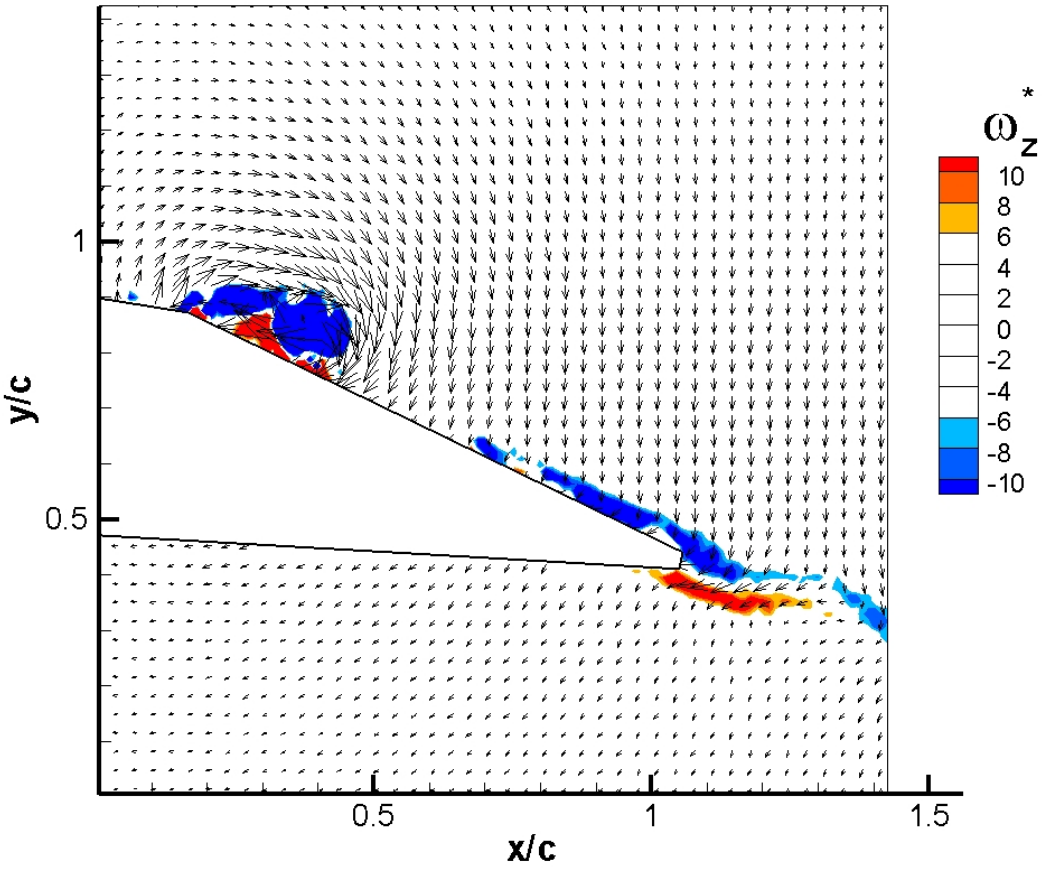


Figure 4.15: Nondimensionalized, instantaneous vorticity field at $\psi = 180°$ for the 50% spanwise location on the $\mathcal{A}R2$ plate at an $\alpha = 25°$ and Reynolds number of 4,000. In-plane velocity components are shown by the vectors.

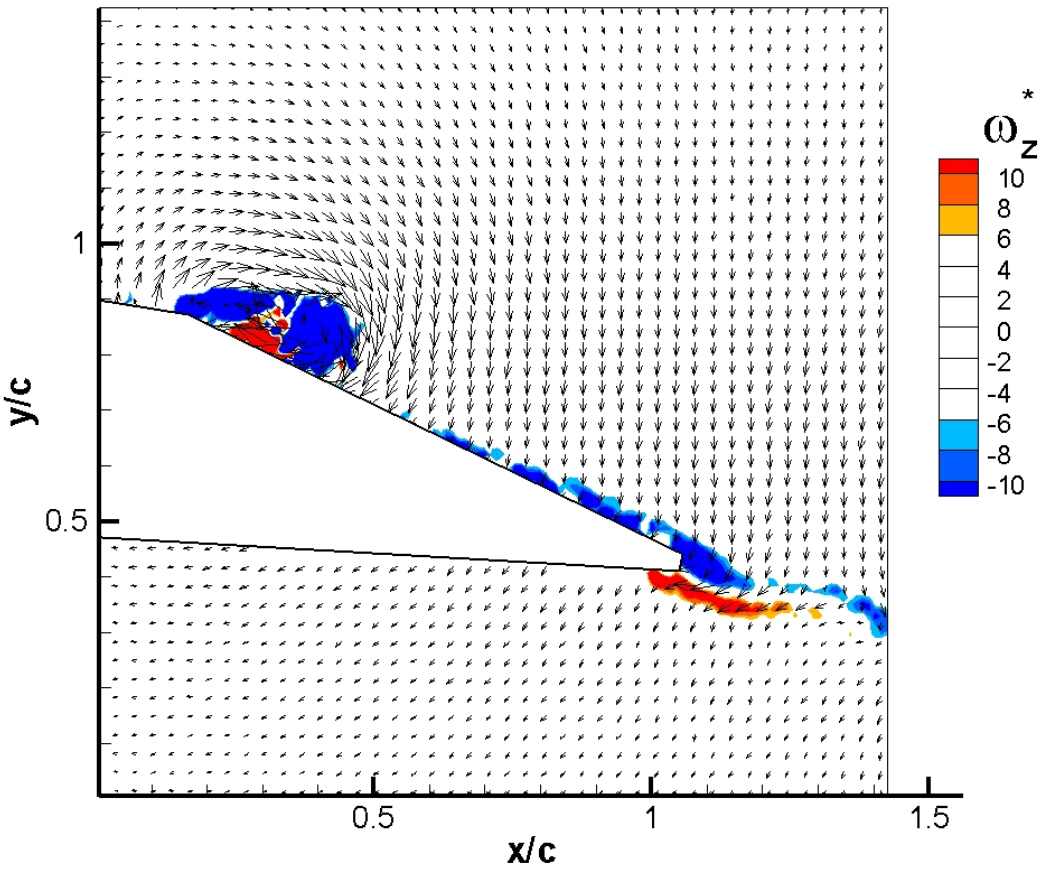


Figure 4.16: Nondimensionalized, instantaneous vorticity field at $\psi = 235°$ for the 50% spanwise location on the $\mathcal{A}R2$ plate at an $\alpha = 25°$ and Reynolds number of 4,000. In-plane velocity components are shown by the vectors.

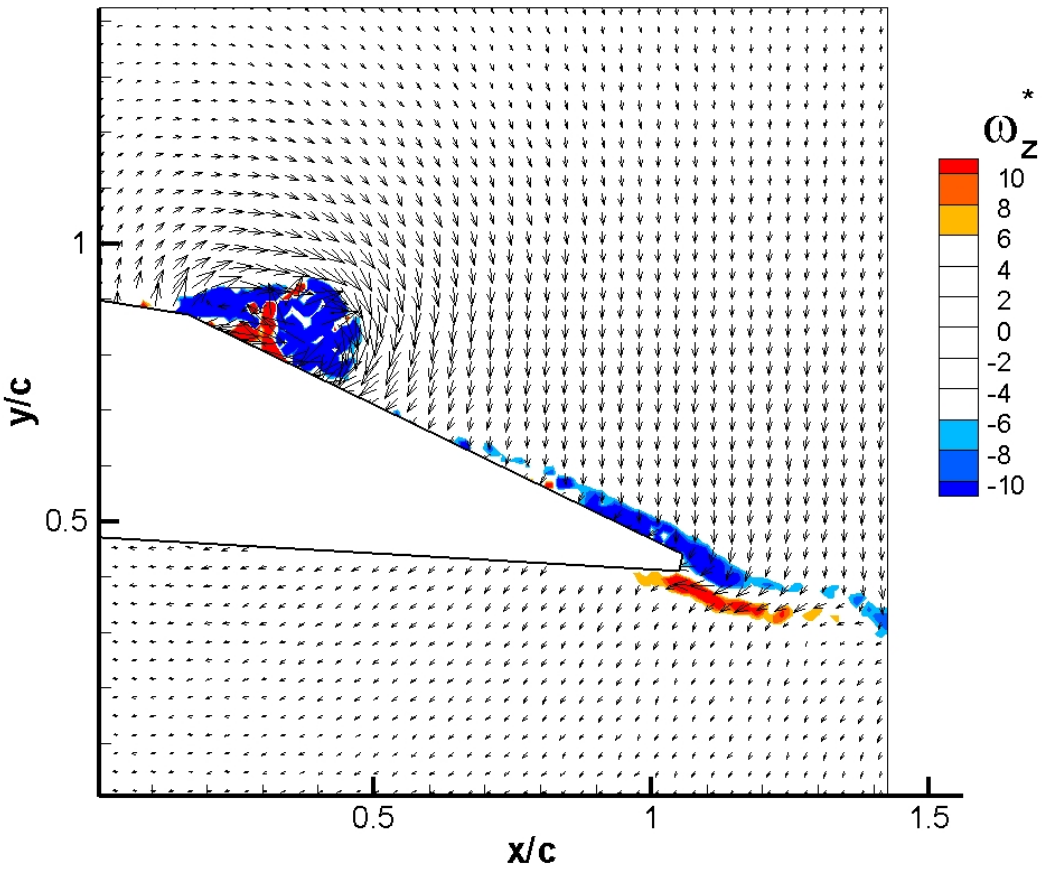


Figure 4.17: Nondimensionalized, instantaneous vorticity field at $\psi = 270°$ for the 50% spanwise location on the $\mathcal{A}R2$ plate at an $\alpha = 25°$ and Reynolds number of 4,000. In-plane velocity components are shown by the vectors.

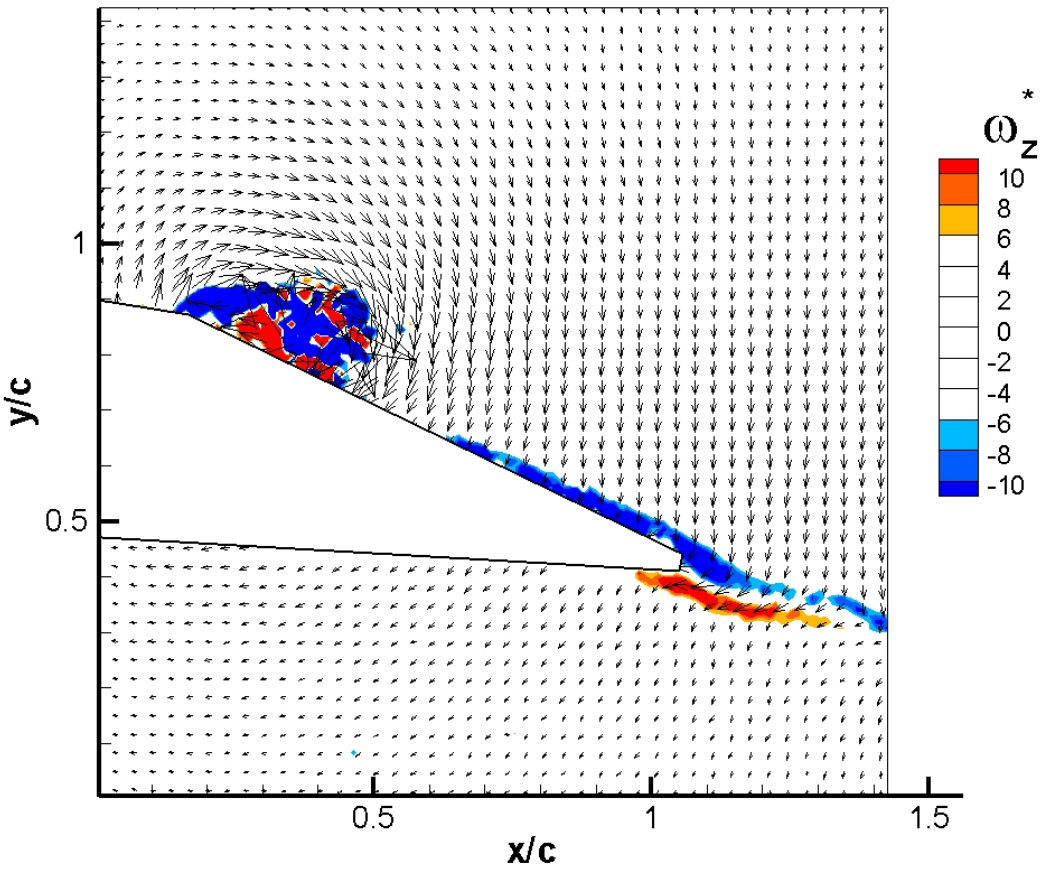


Figure 4.18: Nondimensionalized, instantaneous vorticity field at $\psi = 320°$ for the 50% spanwise location on the $\mathcal{A}R2$ plate at an $\alpha = 25°$ and Reynolds number of 4,000. In-plane velocity components are shown by the vectors.

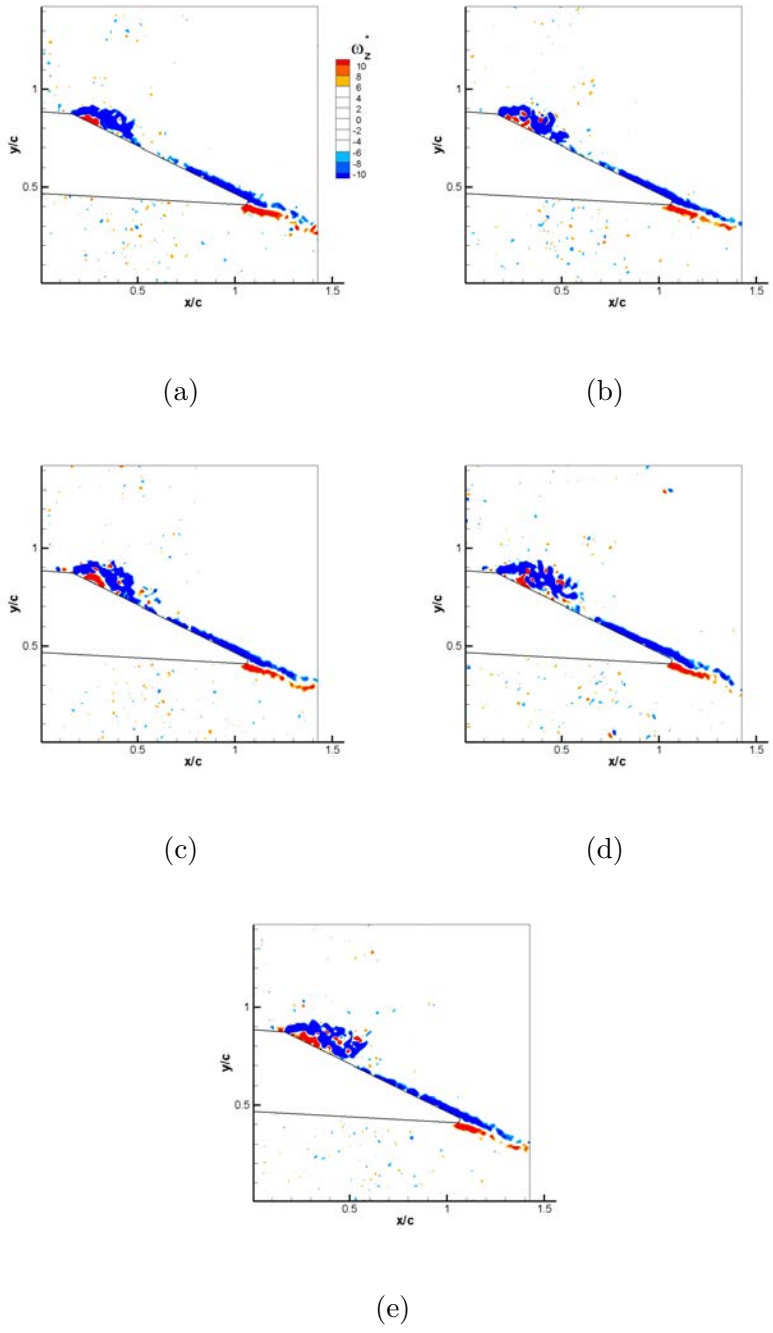


Figure 4.19: Temporal evolution of the nondimensionalized, instantaneous vorticity fields at the 50% spanwise location for the $\mathcal{R}2$ plate at an $\alpha = 25°$ and Reynolds number of 8,000. a.) $\psi = 90°$ b.) $\psi = 180°$ c.) $\psi = 235°$ d.) $\psi = 270°$, and e.) $\psi = 320°$.

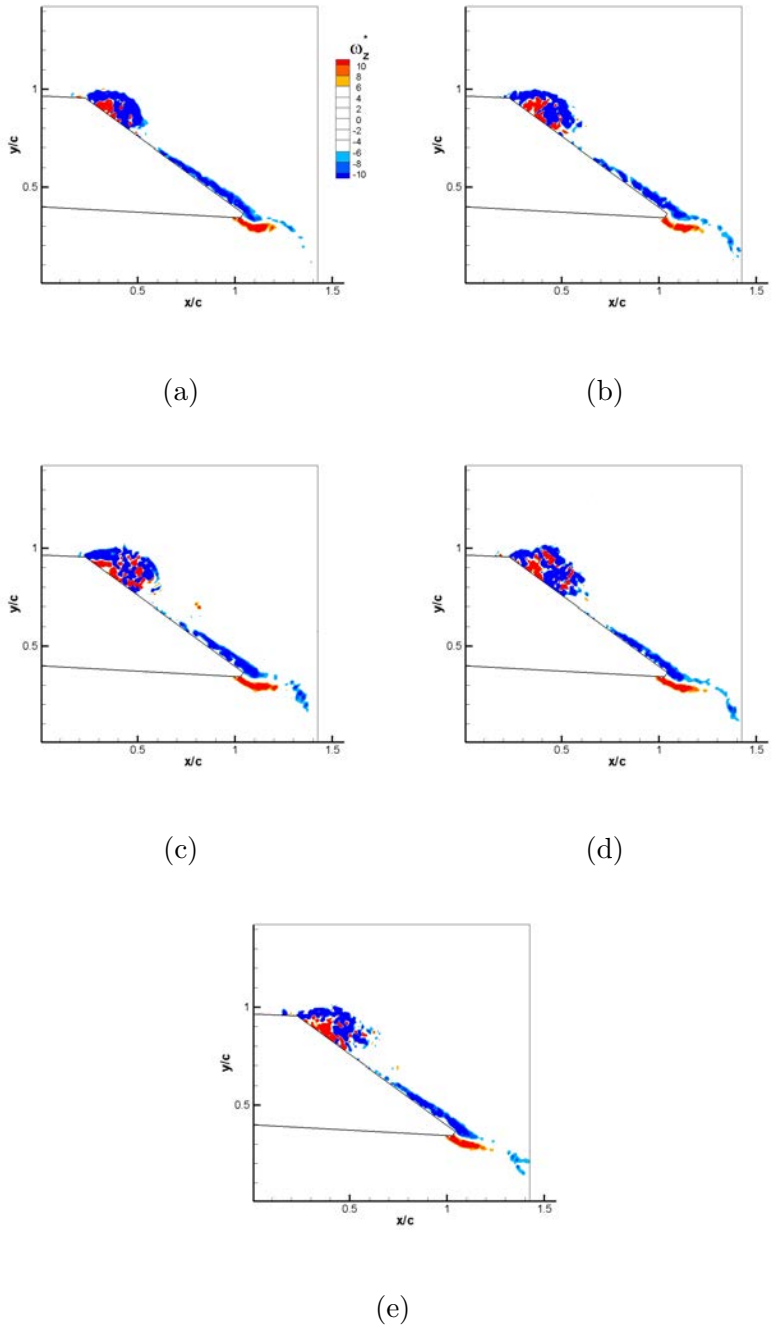


Figure 4.20: Temporal evolution of the nondimensionalized, instantaneous vorticity fields at the 50% spanwise location for the $\mathcal{R}2$ plate at an $\alpha = 35°$ and Reynolds number of 4,000. a.) $\psi = 90°$ b.) $\psi = 180°$ c.) $\psi = 235°$ d.) $\psi = 270°$, and e.) $\psi = 320°$.

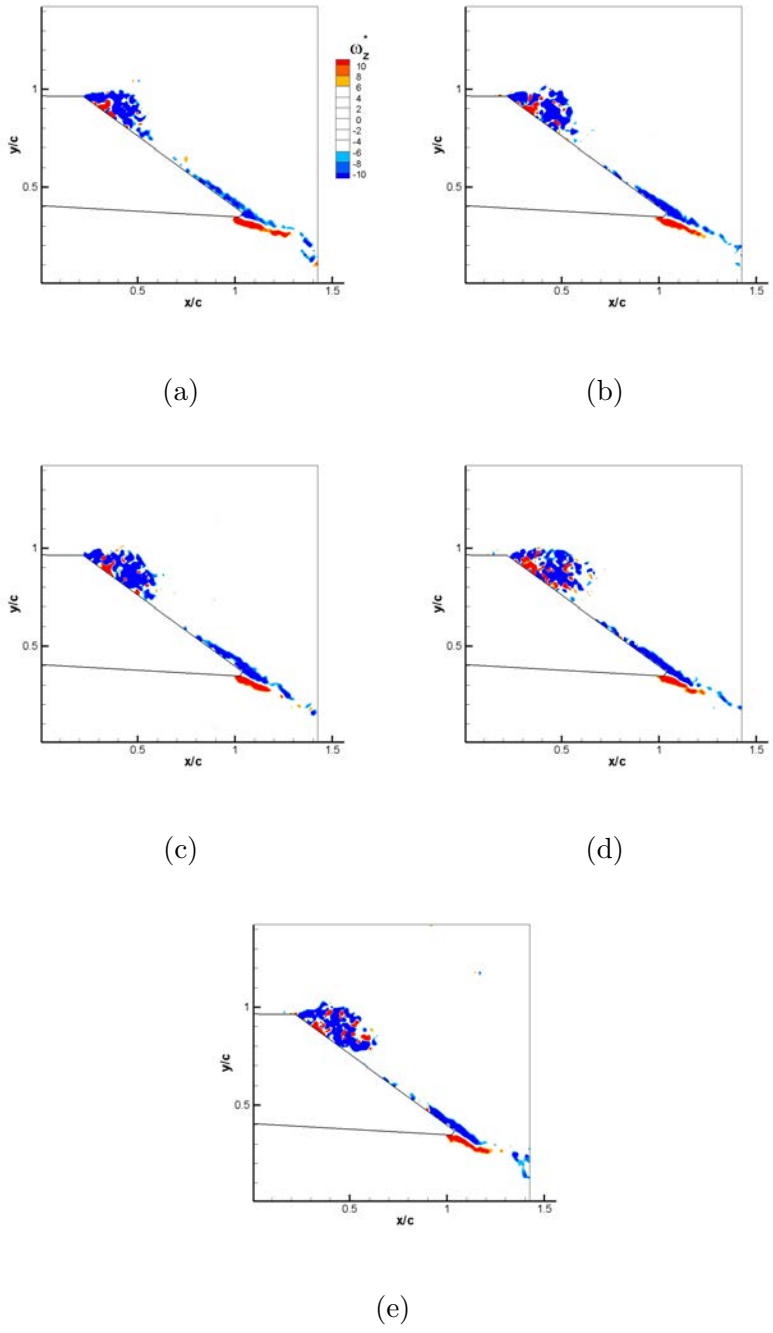


Figure 4.21: Temporal evolution of the nondimensionalized, instantaneous vorticity fields at the 50% spanwise location for the $\mathcal{R}2$ plate at an $\alpha = 35°$ and Reynolds number of 8,000. a.) $\psi = 90°$ b.) $\psi = 180°$ c.) $\psi = 235°$ d.) $\psi = 270°$, and e.) $\psi = 320°$.

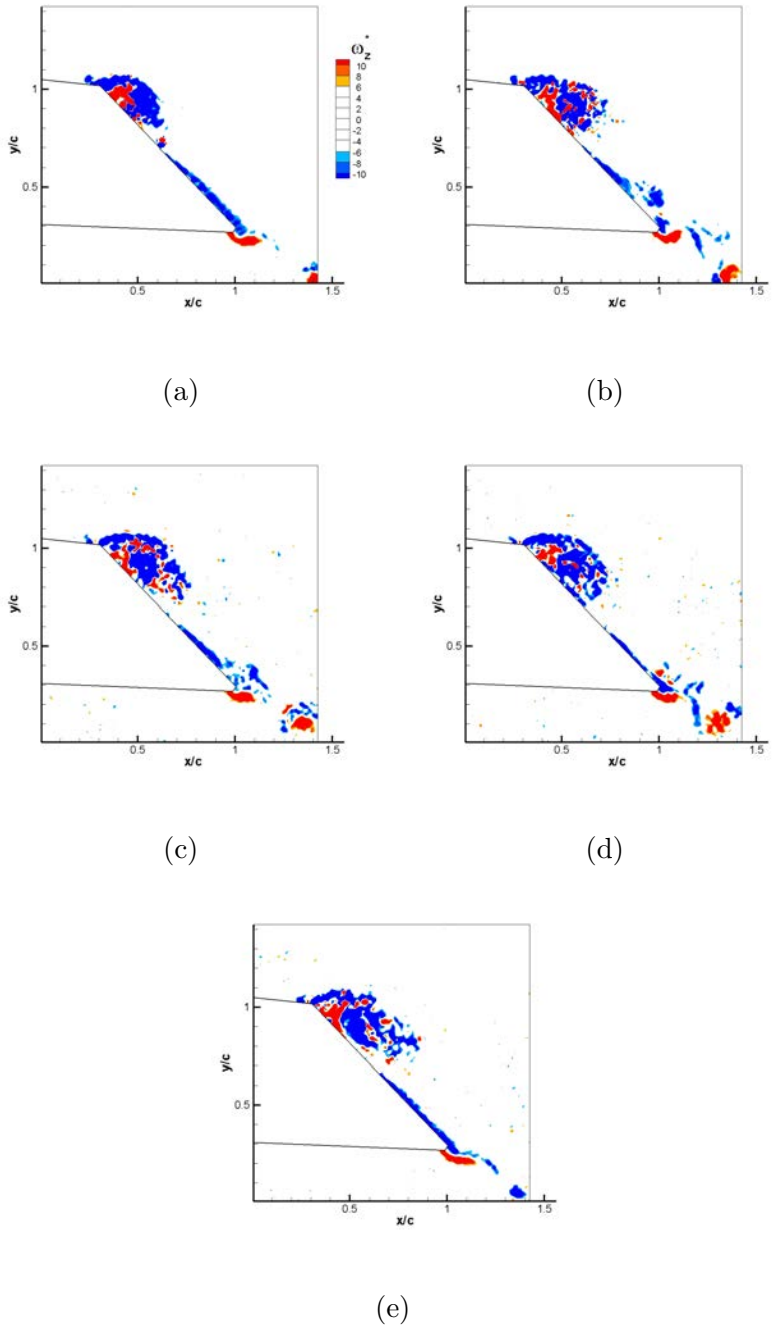


Figure 4.22: Temporal evolution of the nondimensionalized, instantaneous vorticity fields at the 50% spanwise location for the $\mathcal{R}2$ plate at an $\alpha = 45°$ and Reynolds number of 4,000. a.) $\psi = 90°$ b.) $\psi = 180°$ c.) $\psi = 235°$ d.) $\psi = 270°$, and e.) $\psi = 320°$.

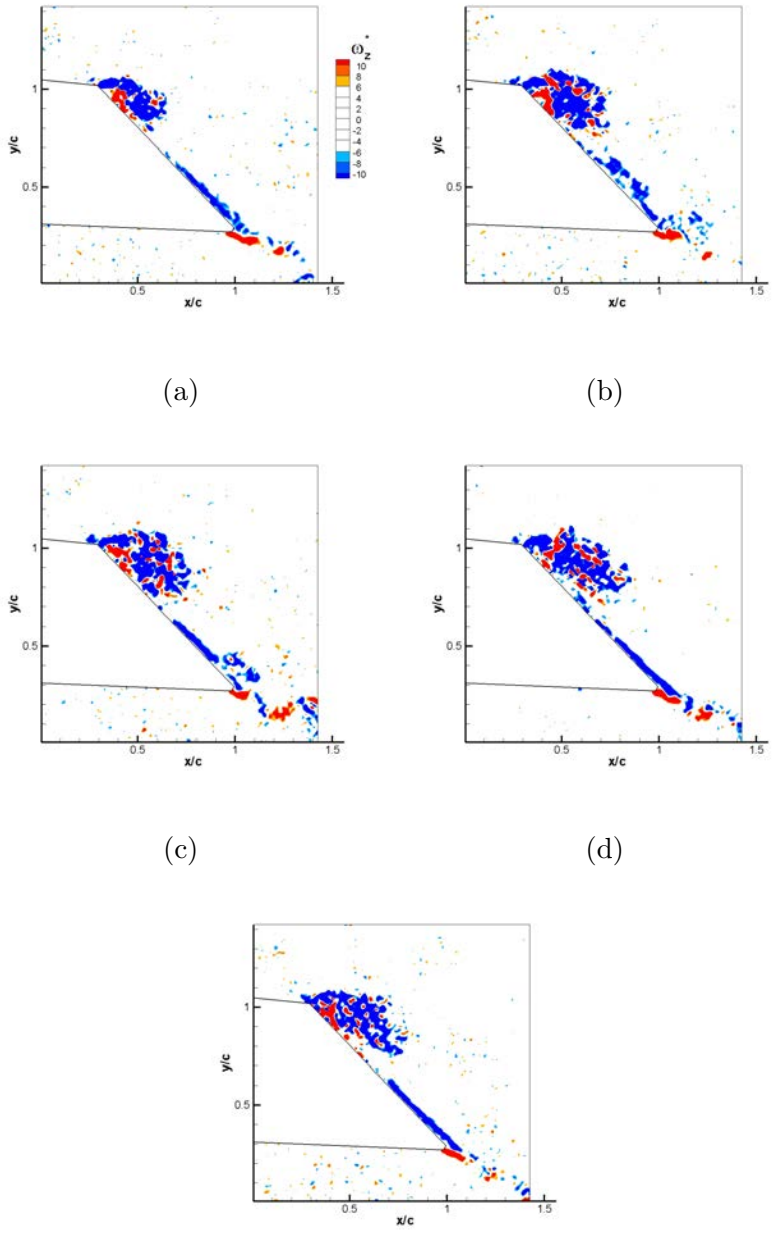


Figure 4.23: Temporal evolution of the nondimensionalized, instantaneous vorticity fields at the 50% spanwise location for the $\mathcal{A}R2$ plate at an $\alpha = 45°$ and Reynolds number of 8,000. a.) $\psi = 90°$ b.) $\psi = 180°$ c.) $\psi = 235°$ d.) $\psi = 270°$, and e.) $\psi = 320°$.

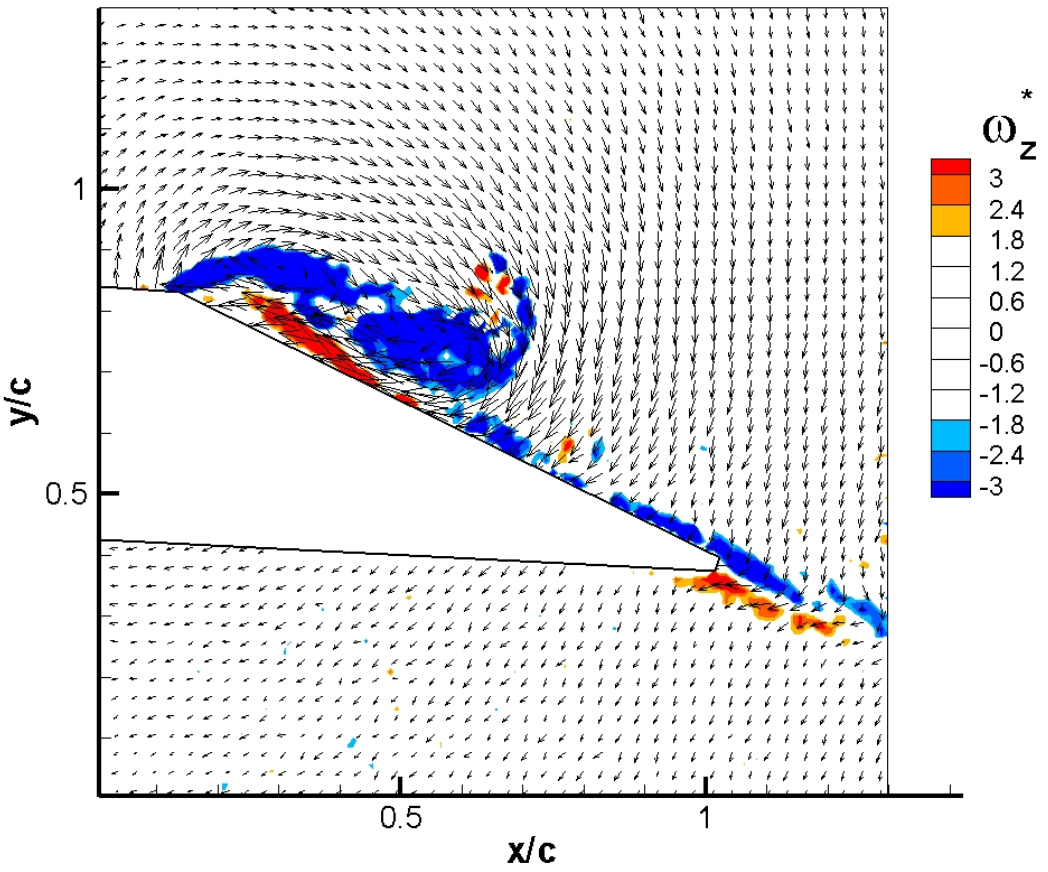


Figure 4.24: Nondimensionalized, instantaneous vorticity field at $\psi = 90°$ for the 50% spanwise location on the $\mathcal{A}R4$ plate at an $\alpha = 25°$ and Reynolds number of 4,000. In-plane velocity components are shown by the vectors.

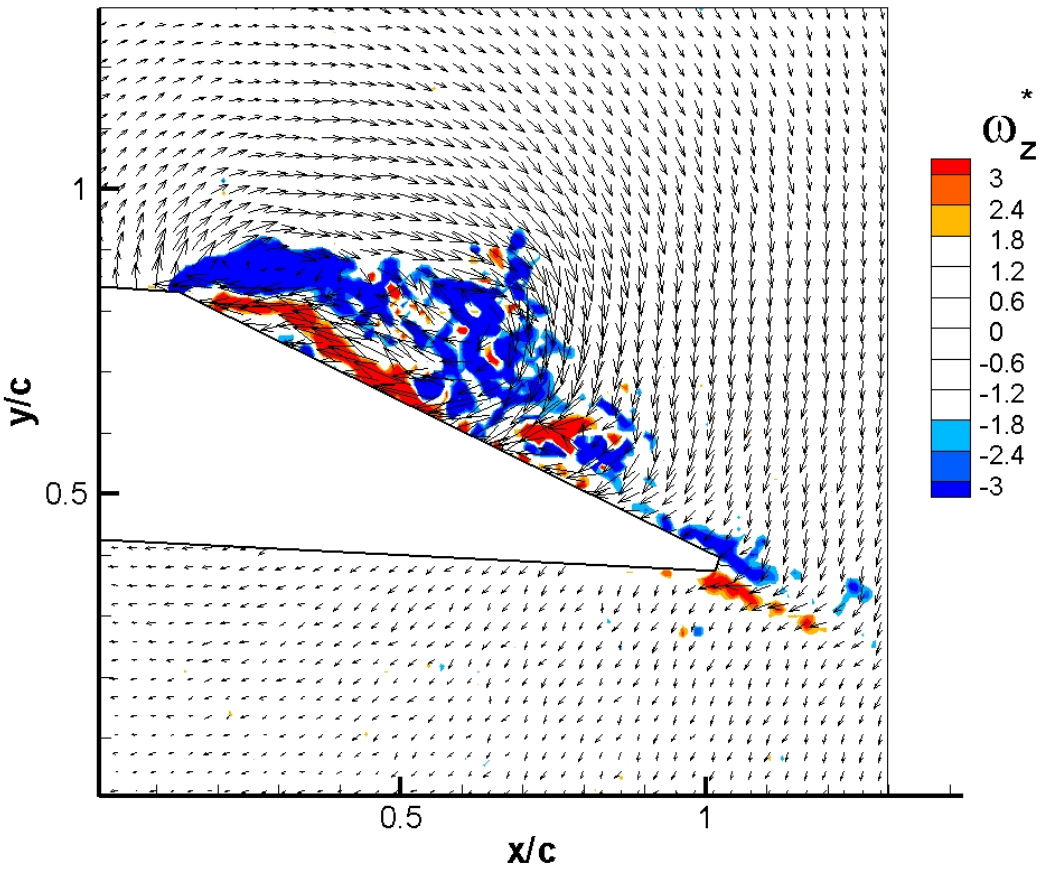


Figure 4.25: Nondimensionalized, instantaneous vorticity field at $\psi = 180°$ for the 50% spanwise location on the $\mathcal{A}R4$ plate at an $\alpha = 25°$ and Reynolds number of 4,000. In-plane velocity components are shown by the vectors.

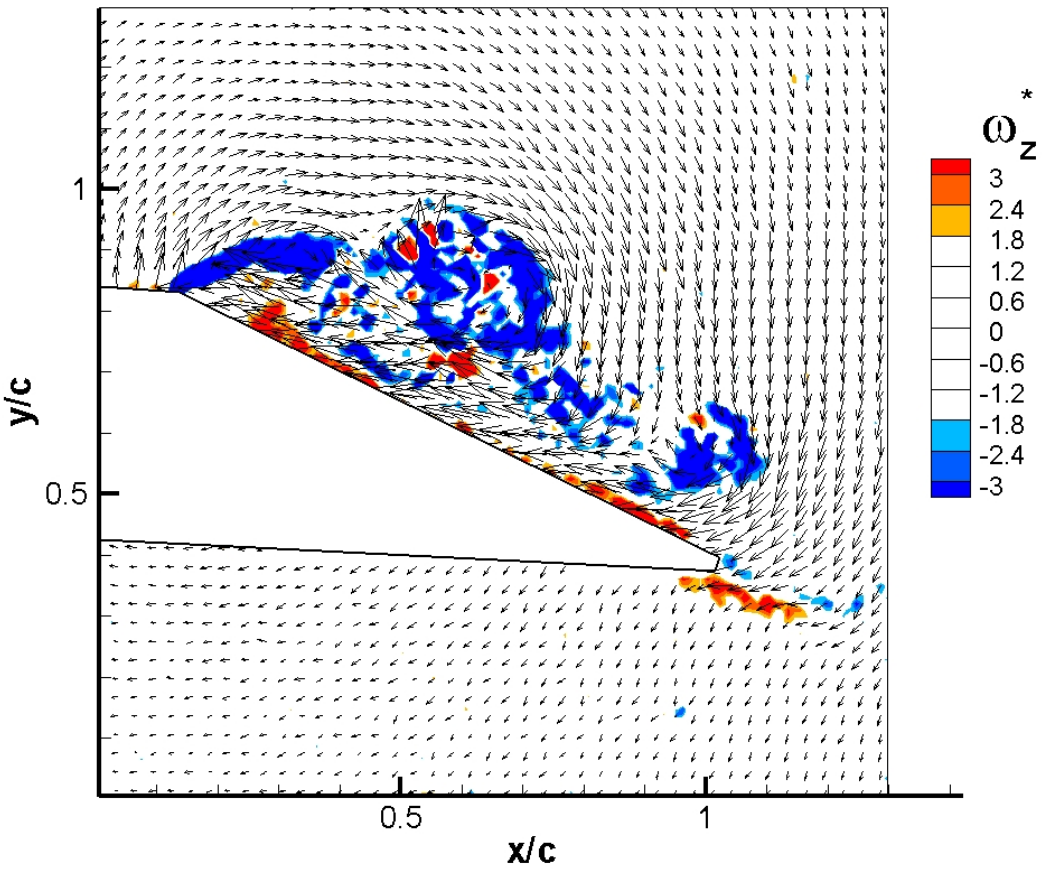


Figure 4.26: Nondimensionalized, instantaneous vorticity field at $\psi = 235°$ for the 50% spanwise location on the $\mathcal{A}R4$ plate at an $\alpha = 25°$ and Reynolds number of 4,000. In-plane velocity components are shown by the vectors.

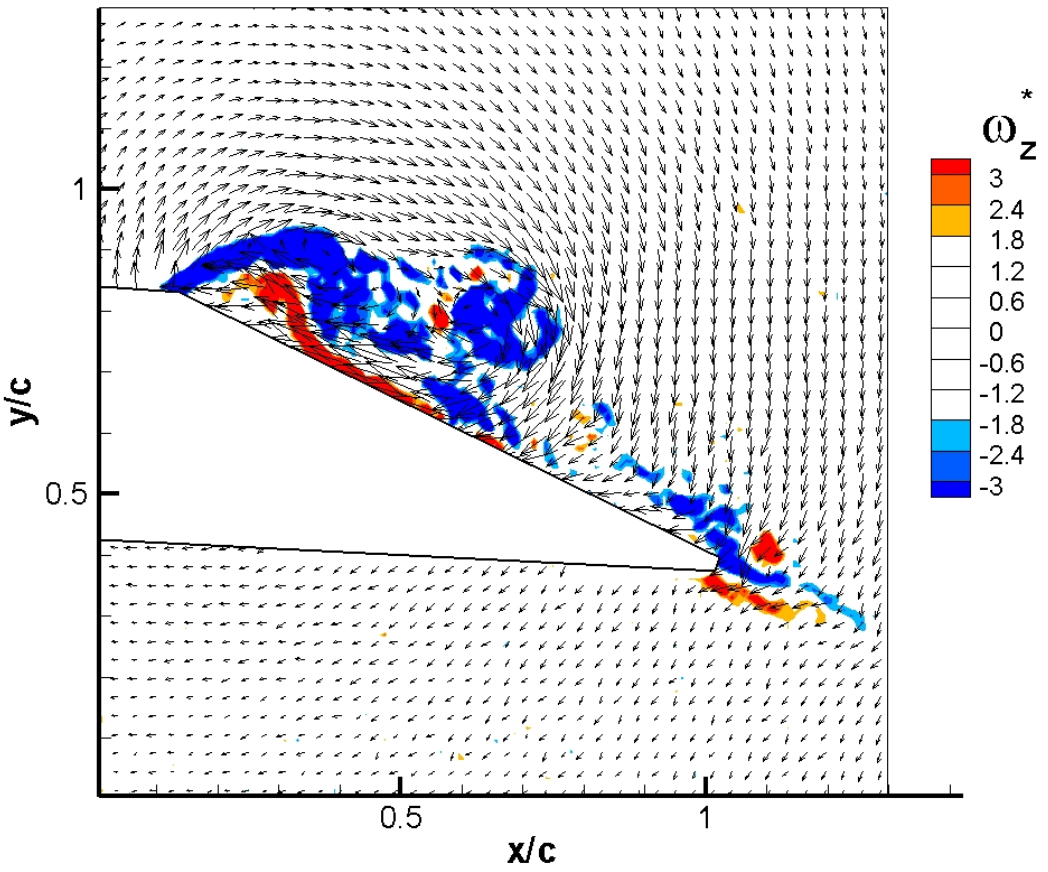


Figure 4.27: Nondimensionalized, instantaneous vorticity field at $\psi = 270°$ for the 50% spanwise location on the $\mathcal{A}R4$ plate at an $\alpha = 25°$ and Reynolds number of 4,000. In-plane velocity components are shown by the vectors.

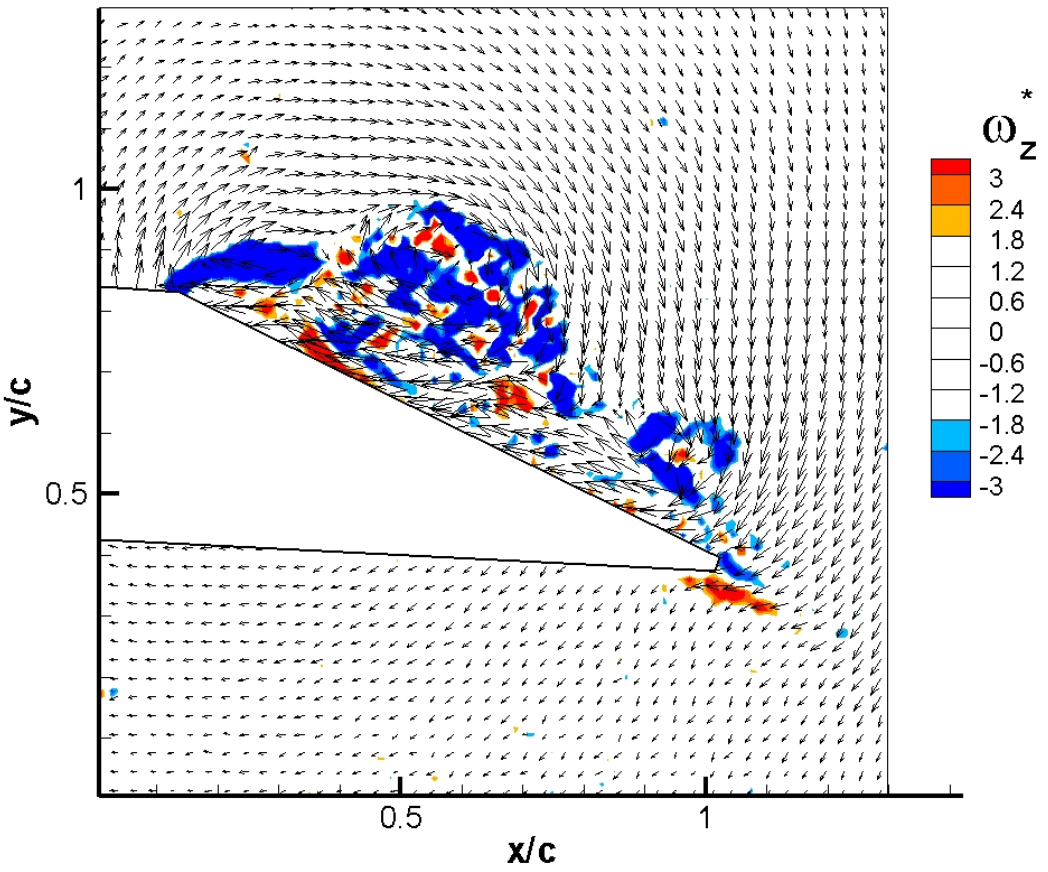


Figure 4.28: Nondimensionalized, instantaneous vorticity field at $\psi = 320°$ for the 50% spanwise location on the $\mathcal{A}R4$ plate at an $\alpha = 25°$ and Reynolds number of 4,000. In-plane velocity components are shown by the vectors.

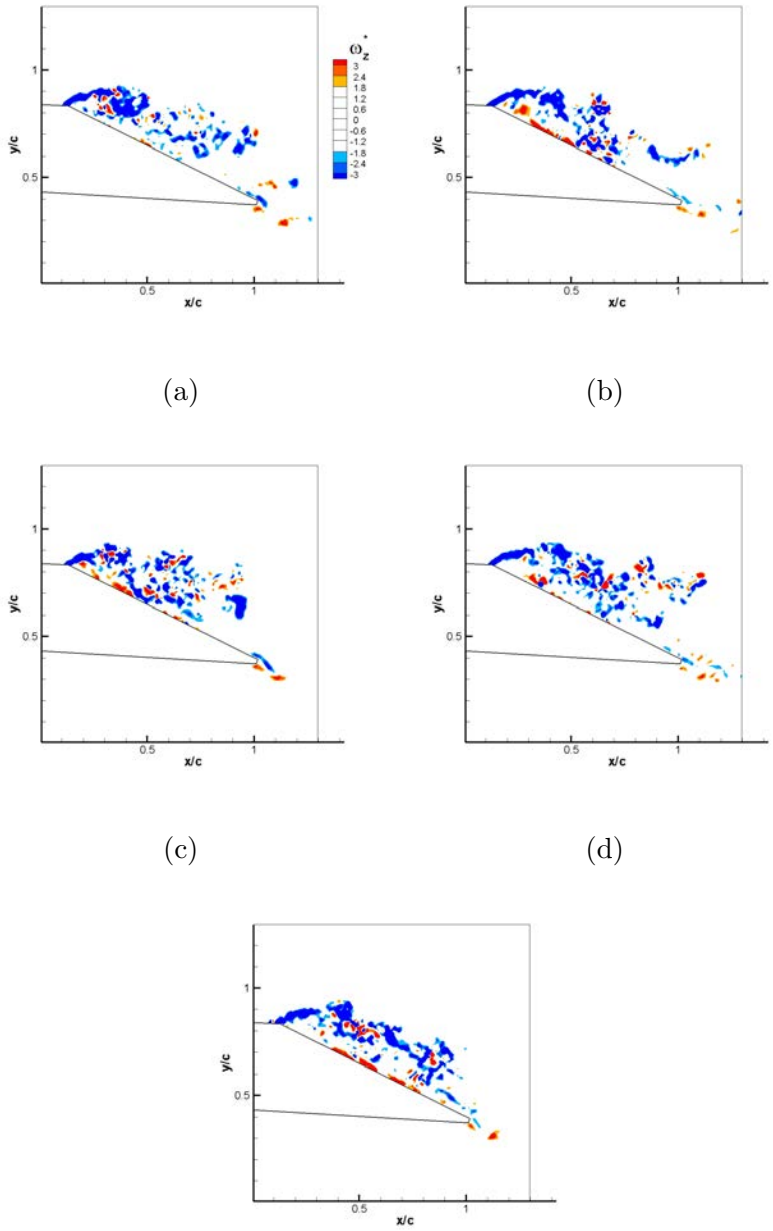


Figure 4.29: Temporal evolution of the nondimensionalized, instantaneous vorticity fields at the 50% spanwise location for the $\mathcal{A}R4$ plate at an $\alpha = 25°$ and Reynolds number of 8,000. a.) $\psi = 90°$ b.) $\psi = 180°$ c.) $\psi = 235°$ d.) $\psi = 270°$, and e.) $\psi = 320°$.

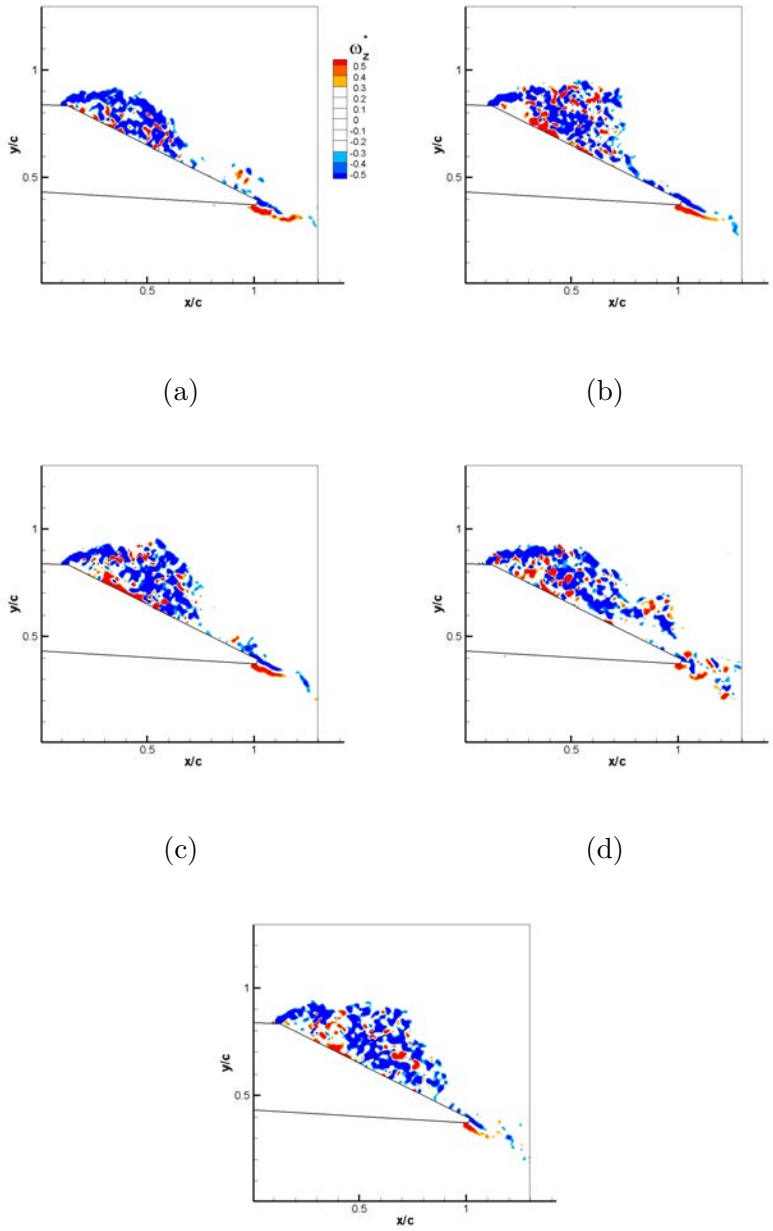


Figure 4.30: Temporal evolution of the nondimensionalized, instantaneous vorticity fields at the 50% spanwise location for the $\mathcal{A}R4$ plate at an $\alpha = 25°$ and Reynolds number of 16,000. a.) $\psi = 90°$ b.) $\psi = 180°$ c.) $\psi = 235°$ d.) $\psi = 270°$, and e.) $\psi = 320°$.

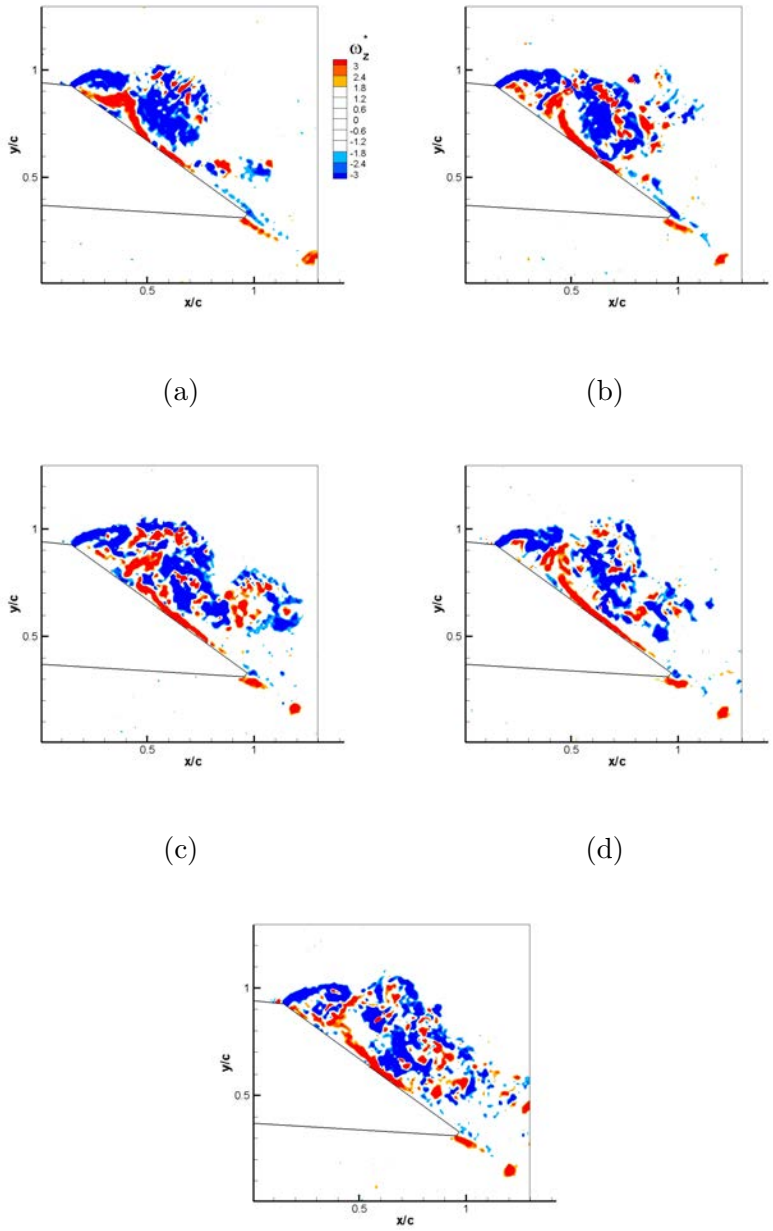


Figure 4.31: Temporal evolution of the nondimensionalized, instantaneous vorticity fields at the 50% spanwise location for the $\mathcal{A}R4$ plate at an $\alpha = 35°$ and Reynolds number of 4,000. a.) $\psi = 90°$ b.) $\psi = 180°$ c.) $\psi = 235°$ d.) $\psi = 270°$, and e.) $\psi = 320°$.

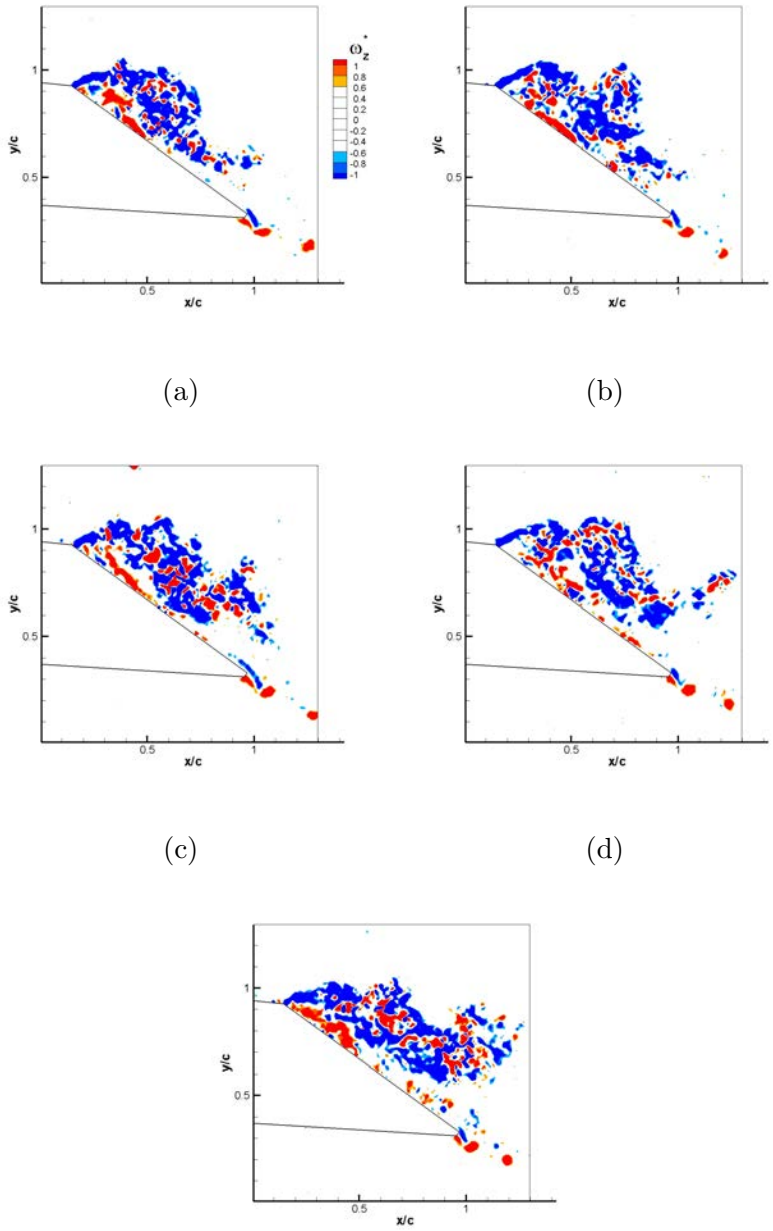


Figure 4.32: Temporal evolution of the nondimensionalized, instantaneous vorticity fields at the 50% spanwise location for the $\mathcal{A}R4$ plate at an $\alpha = 35°$ and Reynolds number of 8,000. a.) $\psi = 90°$ b.) $\psi = 180°$ c.) $\psi = 235°$ d.) $\psi = 270°$, and e.) $\psi = 320°$.

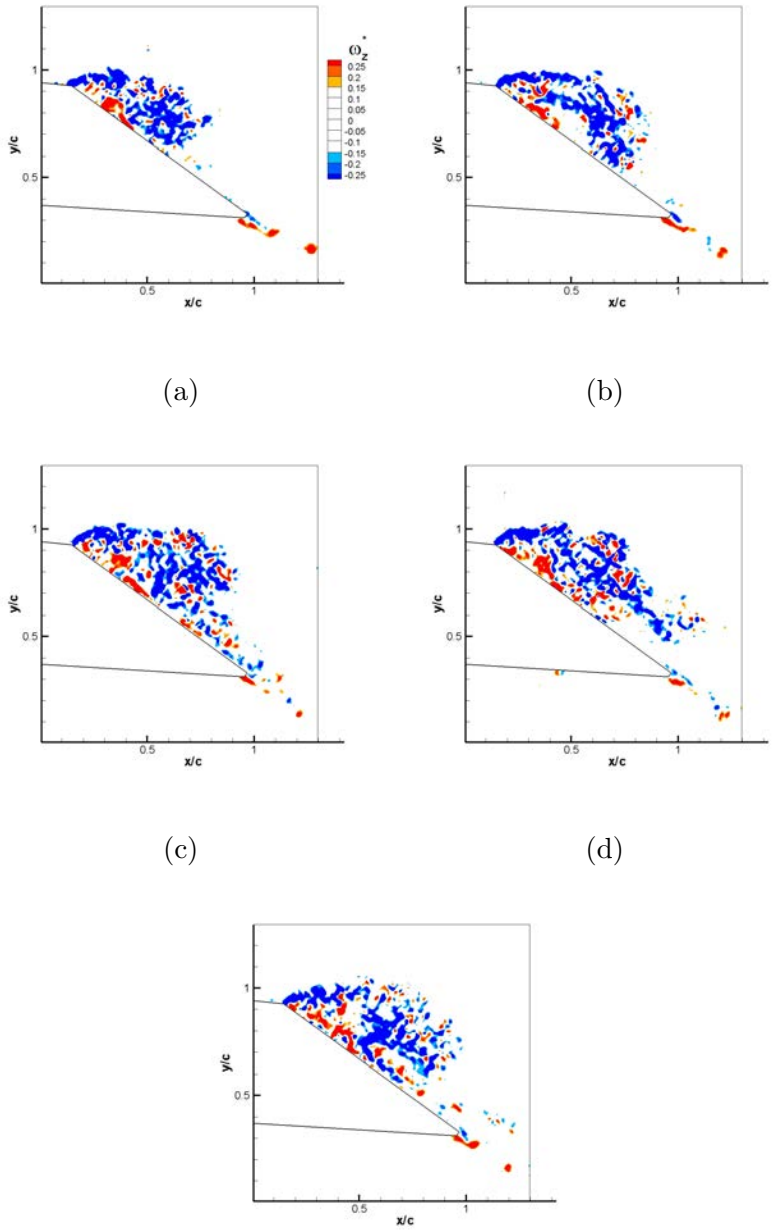


Figure 4.33: Temporal evolution of the nondimensionalized, instantaneous vorticity fields at the 50% spanwise location for the $\mathcal{A}R4$ plate at an $\alpha = 35°$ and Reynolds number of 16,000. a.) $\psi = 90°$ b.) $\psi = 180°$ c.) $\psi = 235°$ d.) $\psi = 270°$, and e.) $\psi = 320°$.

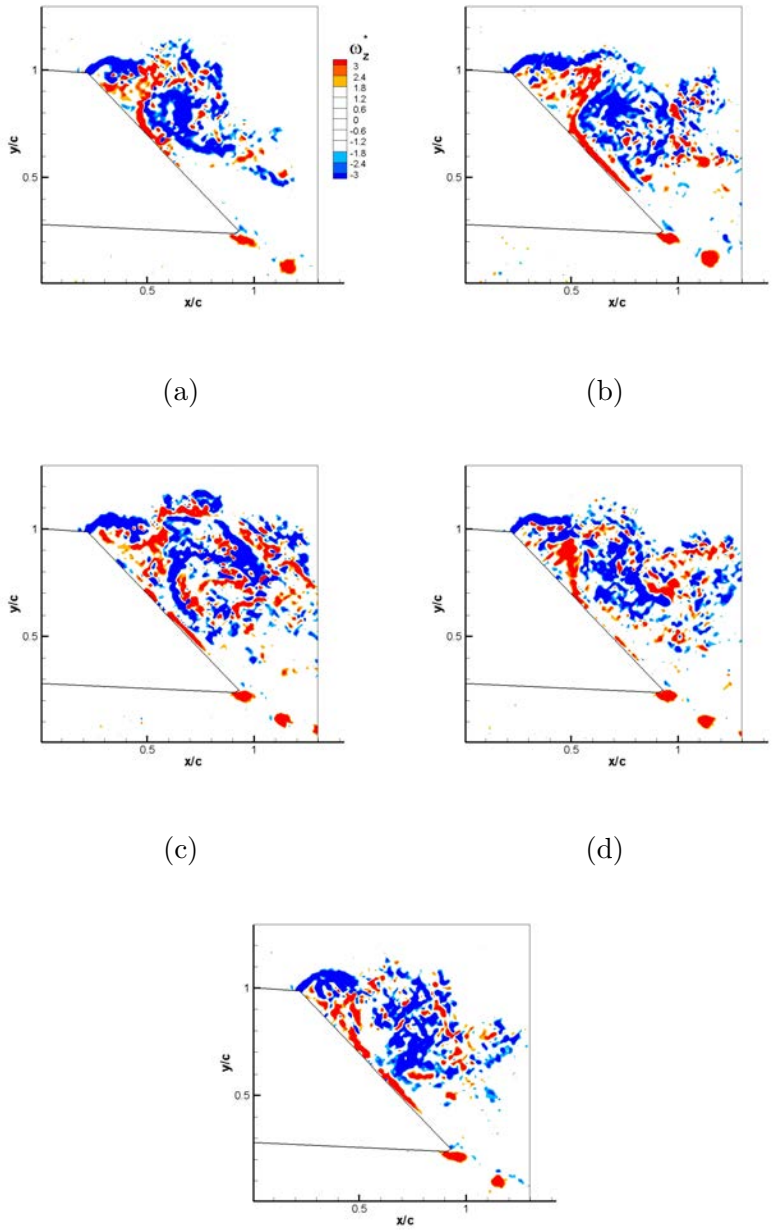


Figure 4.34: Temporal evolution of the nondimensionalized, instantaneous vorticity fields at the 50% spanwise location for the $\mathcal{A}R4$ plate at an $\alpha = 45°$ and Reynolds number of 4,000. a.) $\psi = 90°$ b.) $\psi = 180°$ c.) $\psi = 235°$ d.) $\psi = 270°$, and e.) $\psi = 320°$.

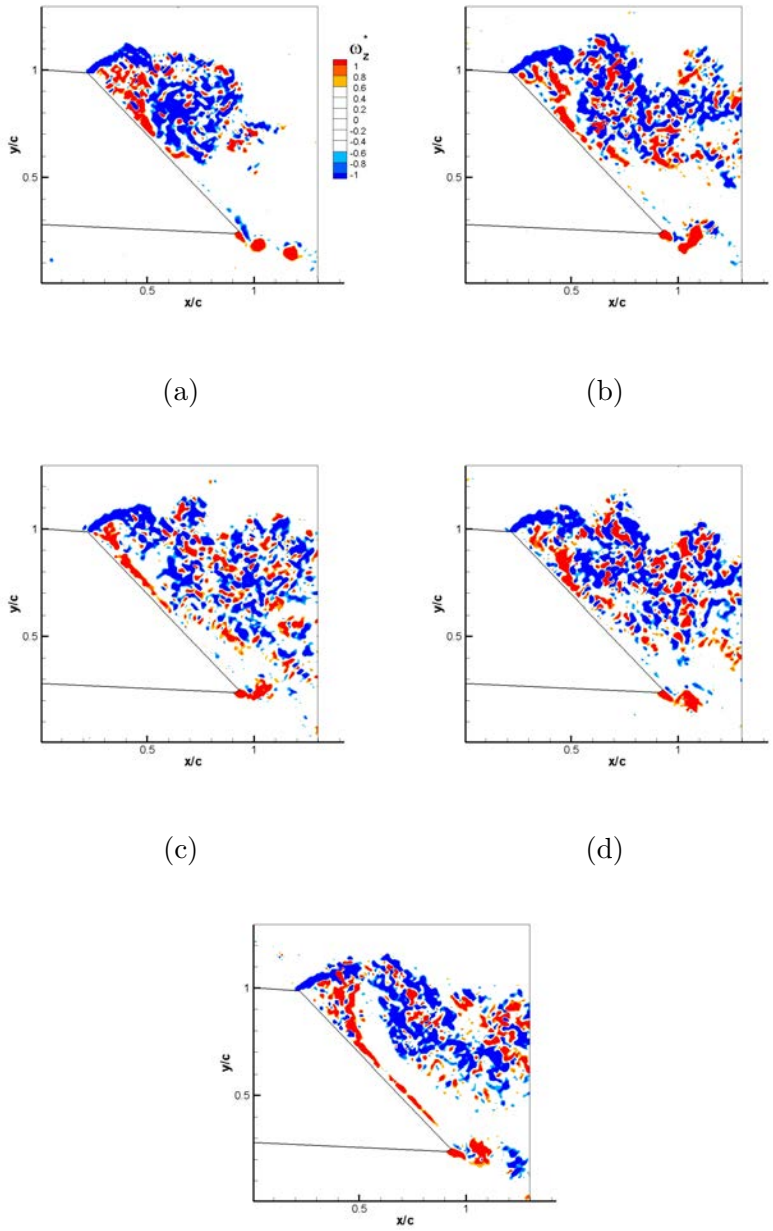


Figure 4.35: Temporal evolution of the nondimensionalized, instantaneous vorticity fields at the 50% spanwise location for the $\mathcal{A}R4$ plate at an $\alpha = 45°$ and Reynolds number of 8,000. a.) $\psi = 90°$ b.) $\psi = 180°$ c.) $\psi = 235°$ d.) $\psi = 270°$, and e.) $\psi = 320°$.

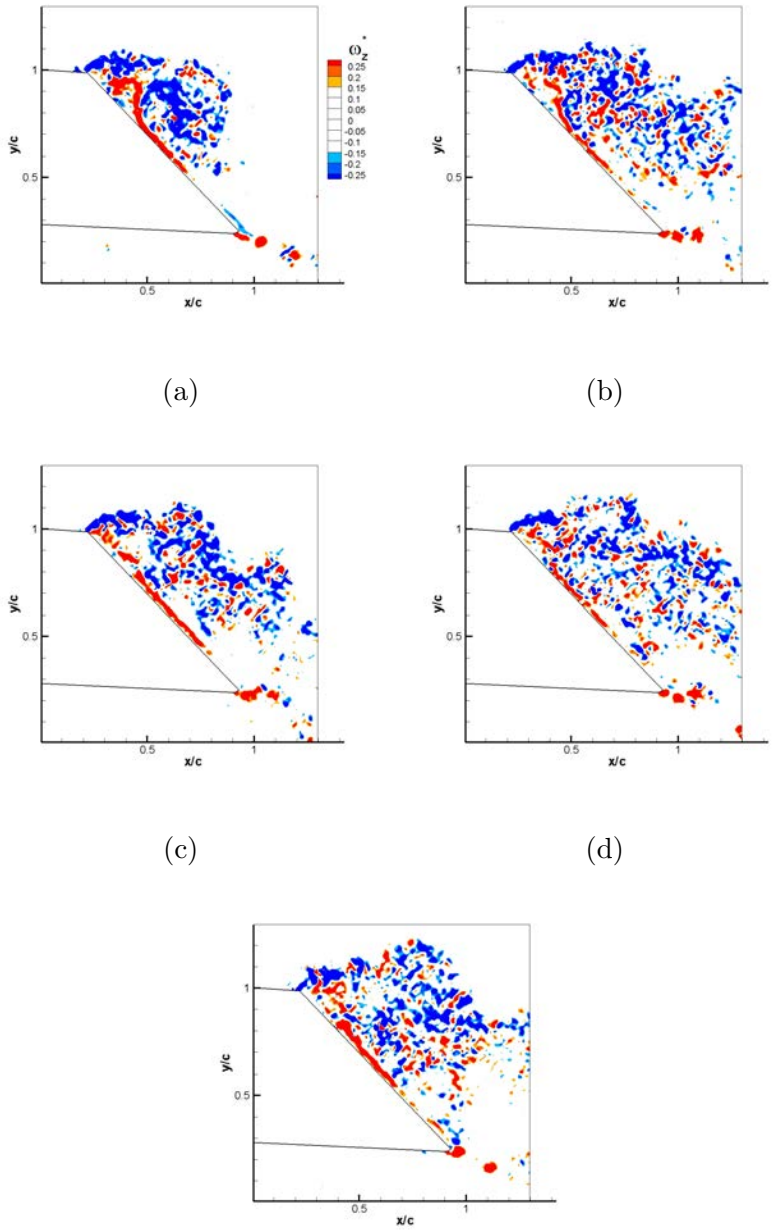


Figure 4.36: Temporal evolution of the nondimensionalized, instantaneous vorticity fields at the 50% spanwise location for the $\mathcal{R}4$ plate at an $\alpha = 45°$ and Reynolds number of 16,000. a.) $\psi = 90°$ b.) $\psi = 180°$ c.) $\psi = 235°$ d.) $\psi = 270°$, and e.) $\psi = 320°$.

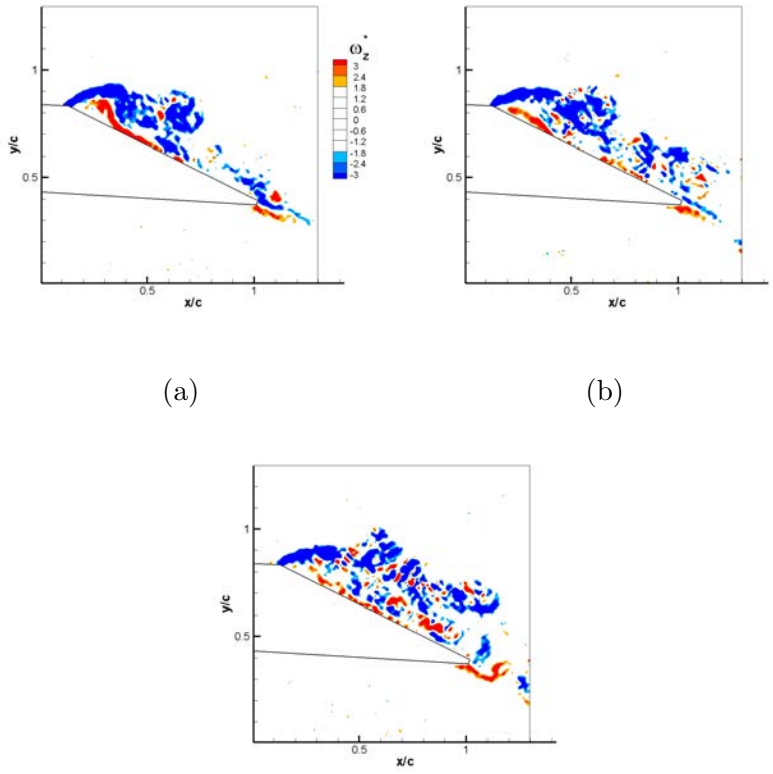


Figure 4.37: Three trials of nondimensionalized, vorticity fields obtained for $\psi = 270°$ at a Re = 4,000 and $\alpha = 25°$ for the $\mathcal{R}4$ plate.

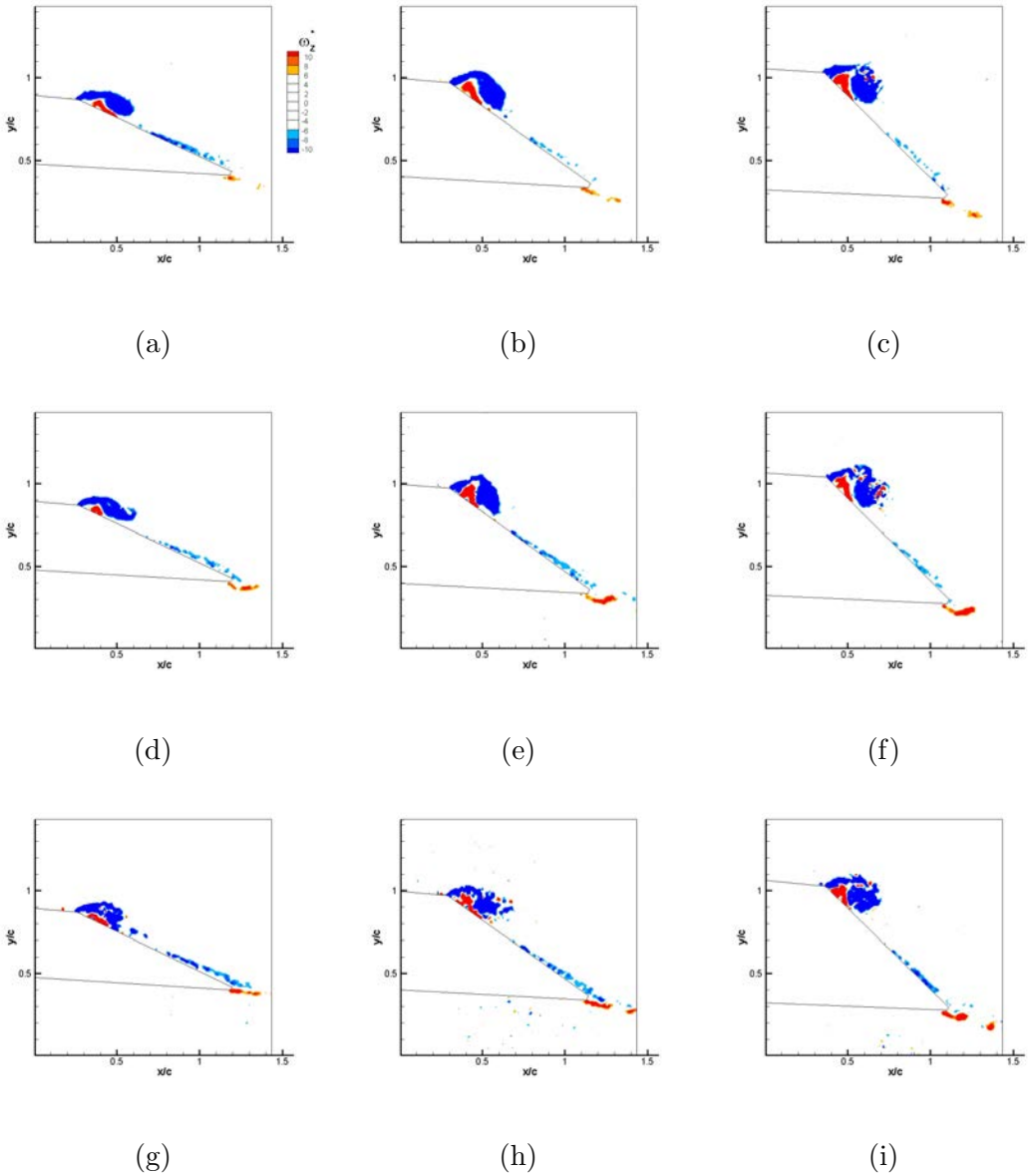


Figure 4.38: Instantaneous nondimensionalized vorticity of the LEV structure for the aspect ratio 4 plate at $\psi = 90°$ with variations in Reynolds number and angle of attack. The top row shows how the structure varies with angle of attack for a Reynolds number of 4,000. The middle and bottom row hold the Reynolds number constant at 8,000 and 16,000 respectively. Each column, the angle of attack is remained constant where the first, second, and third column have angles of attack of 25°, 35°, and 45°, respectively.

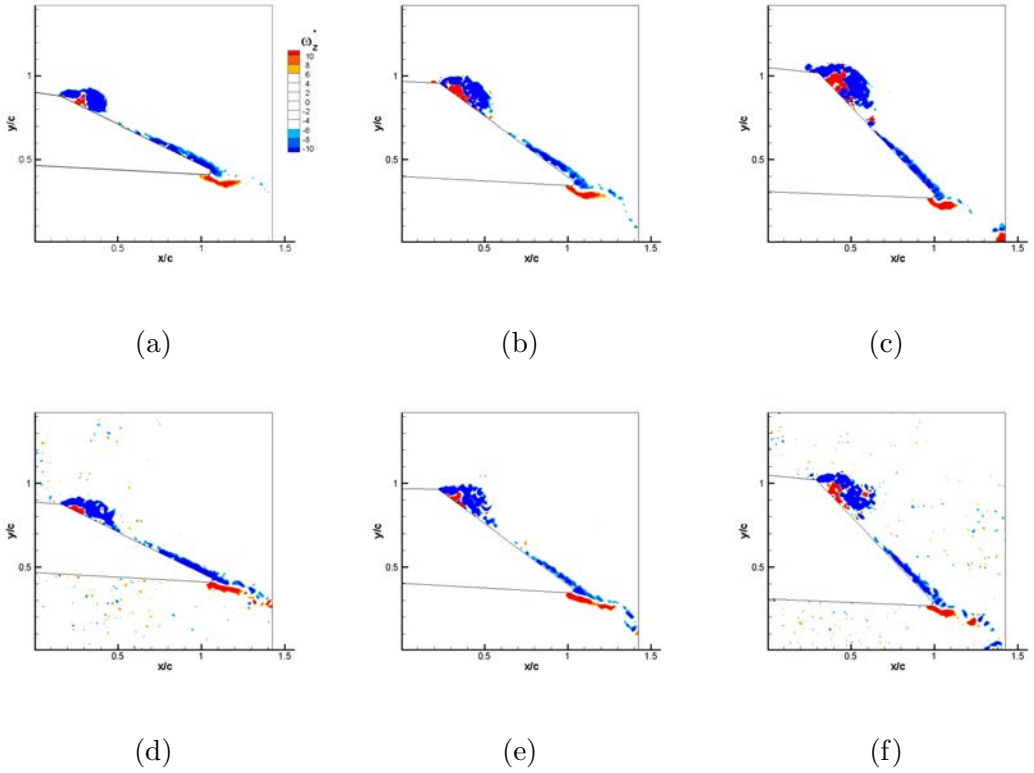


Figure 4.39: Instantaneous nondimensionalized vorticity of the LEV structure for the aspect ratio 2 plate at $\psi = 90°$ with variations in Reynolds number and angle of attack. The top row shows how the structure varies with angle of attack for a Reynolds number of 4,000. The bottom row holds the Reynolds number constant at 8,000. Each column, the angle of attack is remained constant where the first, second, and third column have angles of attack of 25°, 35°, and 45°, respectively.

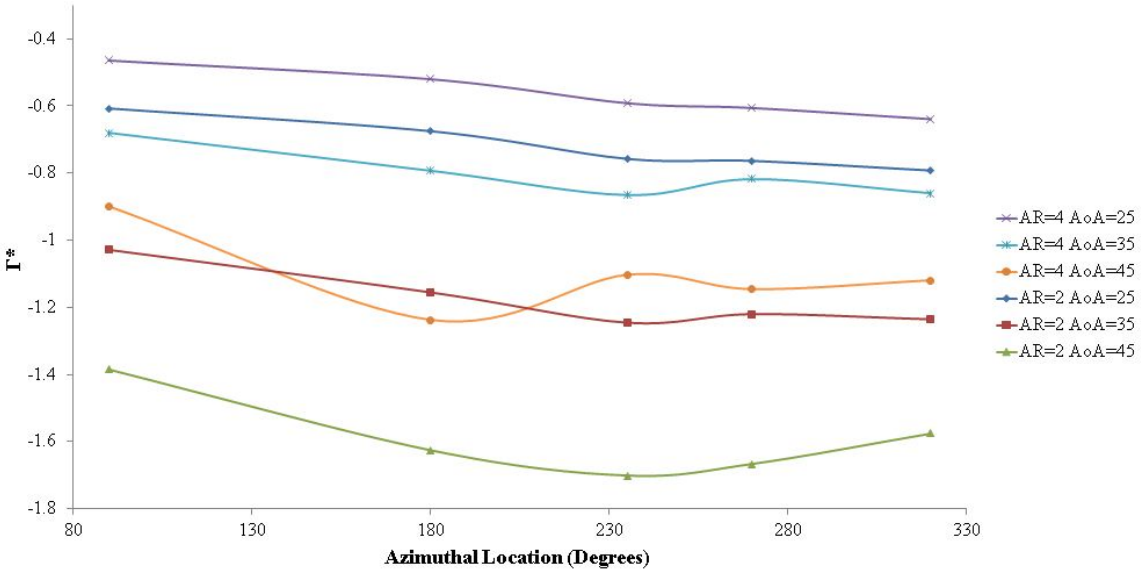


Figure 4.40: Nondimensionalized circulation measurements of the LEV for both plates at Re = 4,000 (based on the tip velocity) for azimuthal locations between 90° and 320°.

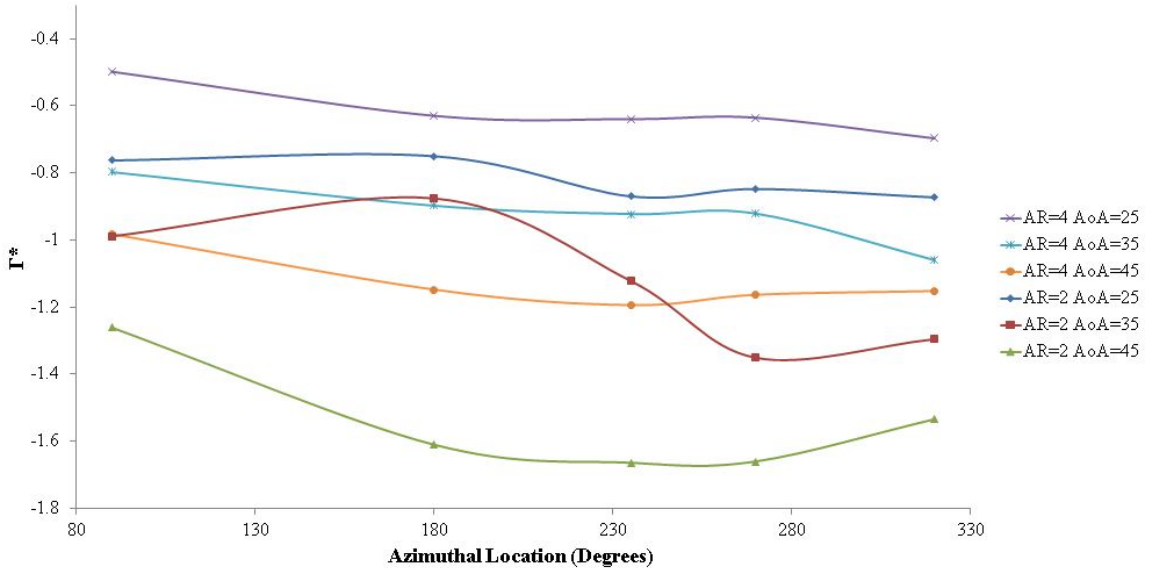


Figure 4.41: Nondimensionalized circulation measurements of the LEV for both plates at Re = 8,000 (based on the tip velocity) for azimuthal locations between 90° and 320°.

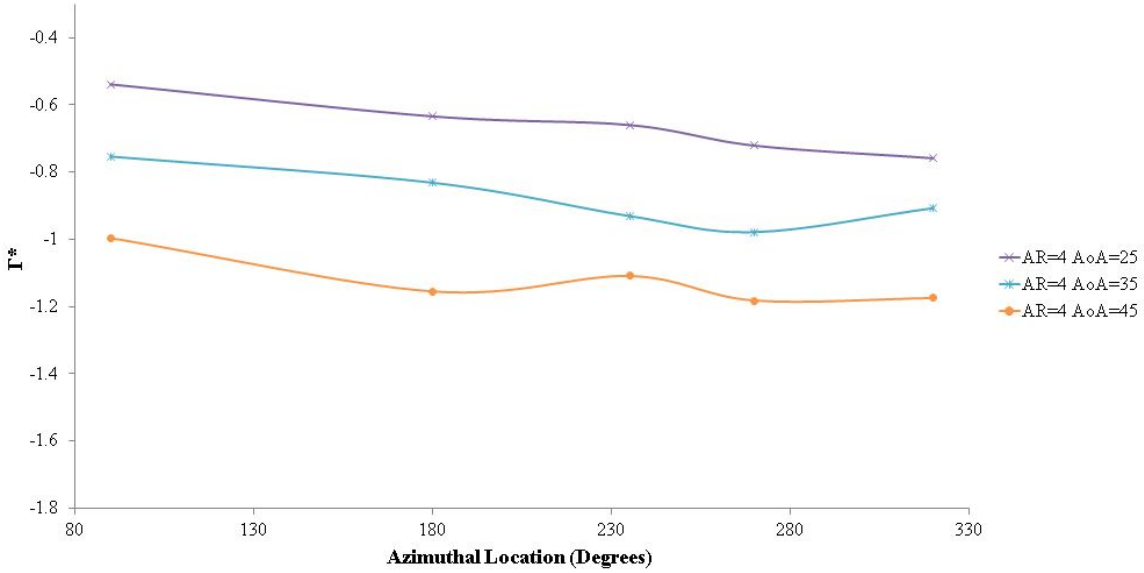


Figure 4.42: Nondimensionalized circulation measurements of the LEV for the $\mathcal{R}$= 4 plate at Re = 16,000 (based on the tip velocity) for azimuthal locations between 90° and 320°.

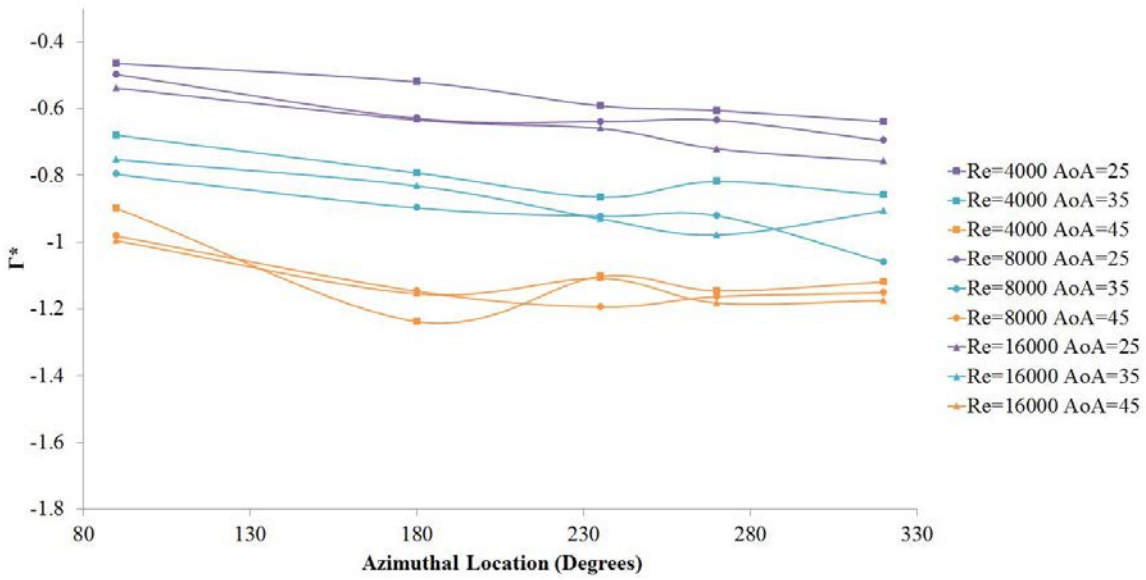


Figure 4.43: The $\mathcal{R}$= 4 plate's nondimensionalized circulation values for all conditions investigated.

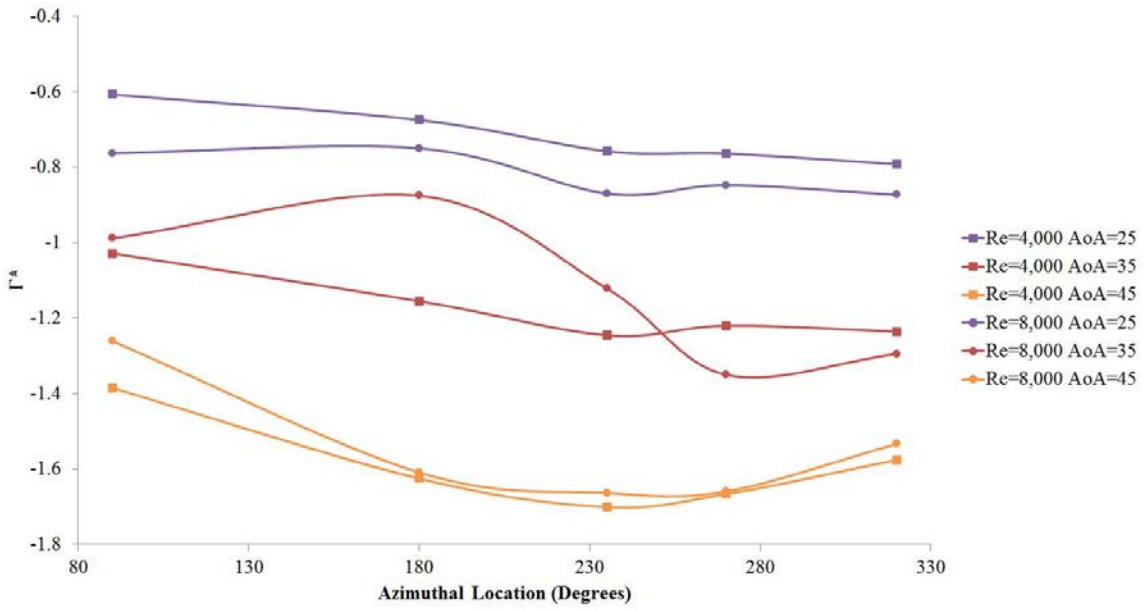


Figure 4.44: The $\mathcal{R}= 2$ plate's nondimensionalized circulation values for all conditions investigated.

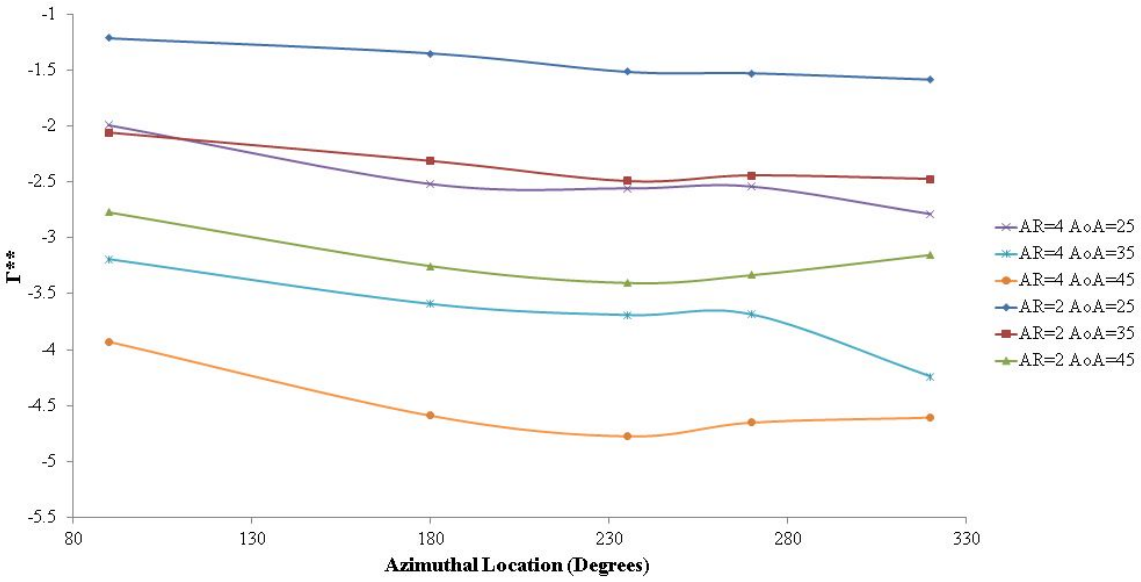


Figure 4.45: Nondimensionalized circulation measurements of the LEV for both plates at Re = 2,000 (based on the local velocity at the b = 25.4 mm spanwise location) for varying azimuthal locations between 90° and 320°.

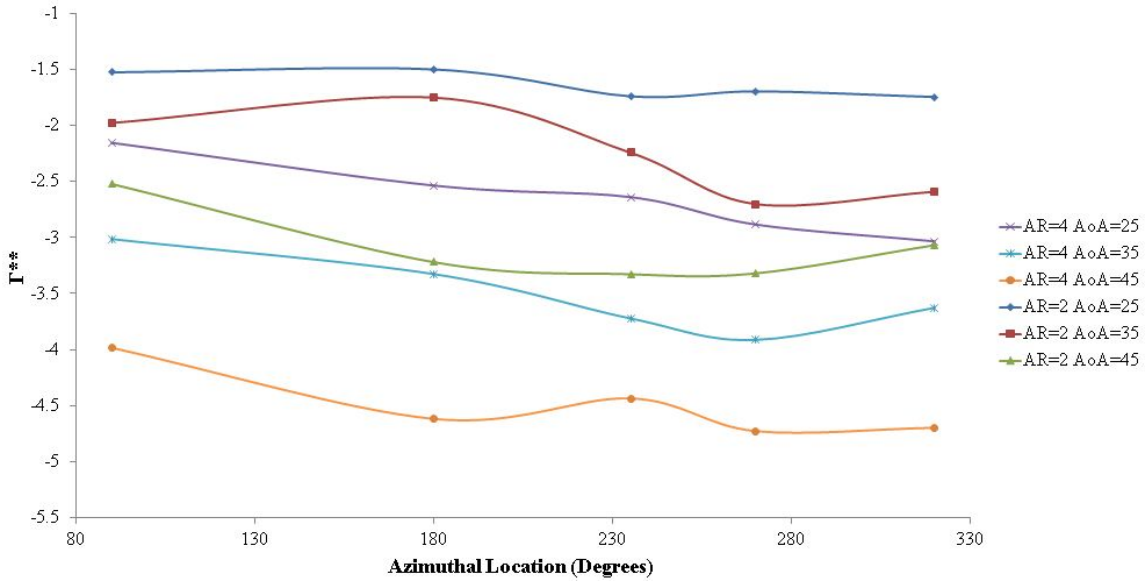


Figure 4.46: Nondimensionalized circulation measurements of the LEV for both plates at Re = 4,000 (based on the local velocity at the b = 25.4 mm spanwise location) for varying azimuthal locations between 90° and 320°.

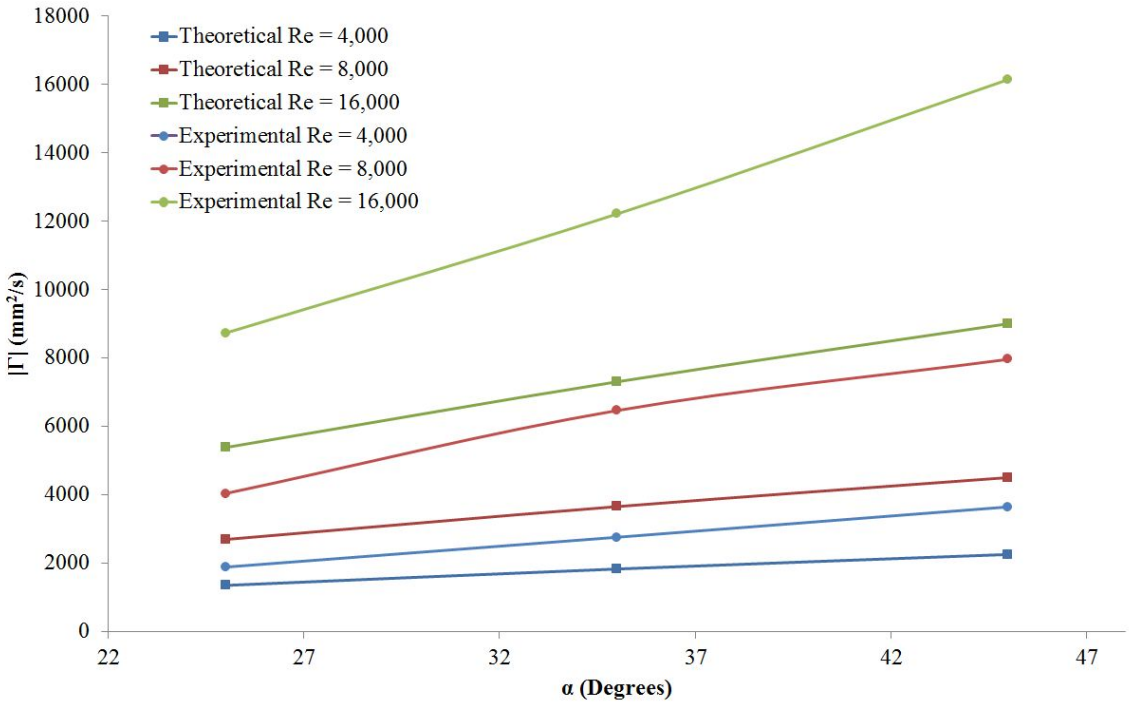


Figure 4.47: $\psi = 90°$ dimensional theoretical bound circulation and experimental circulation values of the LEV for the $\mathcal{R}$= 4 plate.

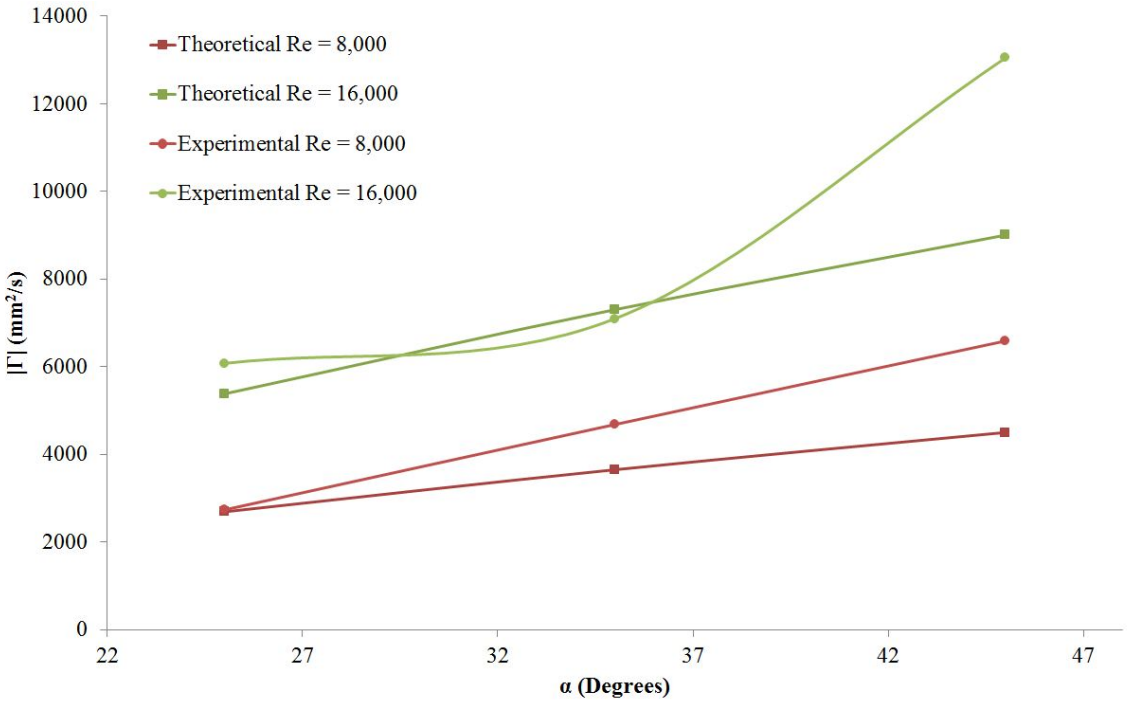


Figure 4.48: $\psi = 180°$ dimensional theoretical bound circulation and experimental circulation values of the LEV for the $\mathcal{R}= 2$ plate.

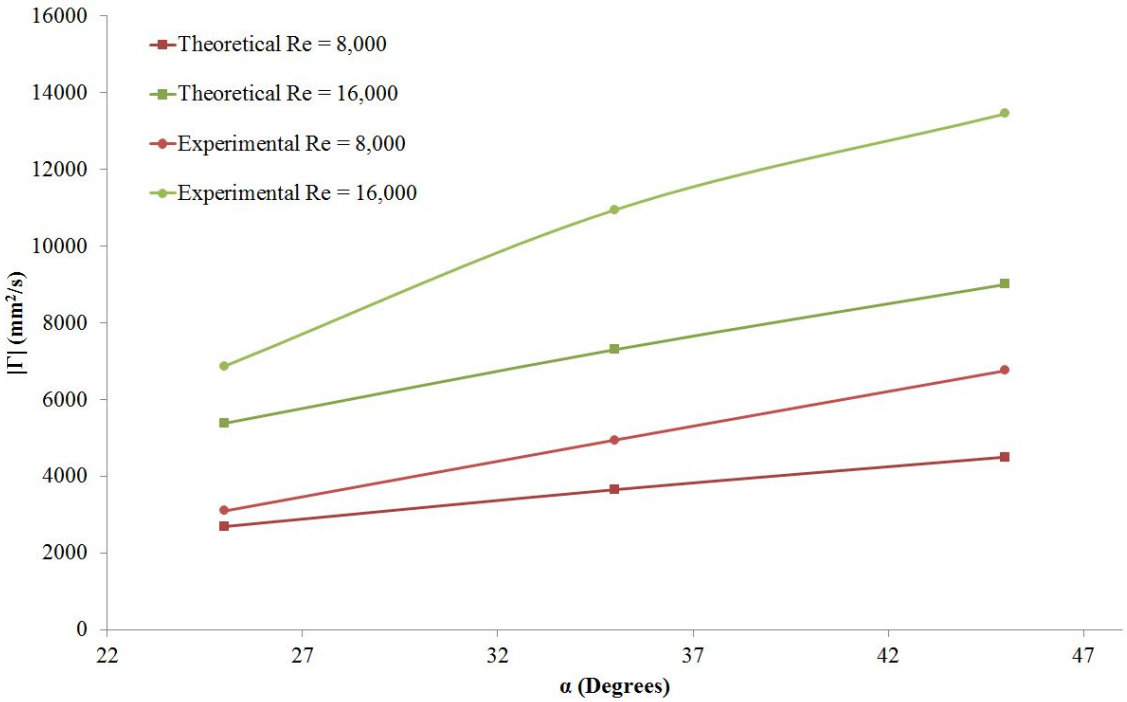


Figure 4.49: $\psi = 270°$ dimensional theoretical bound circulation and experimental circulation values of the LEV for the $\mathcal{R}$= 2 plate.

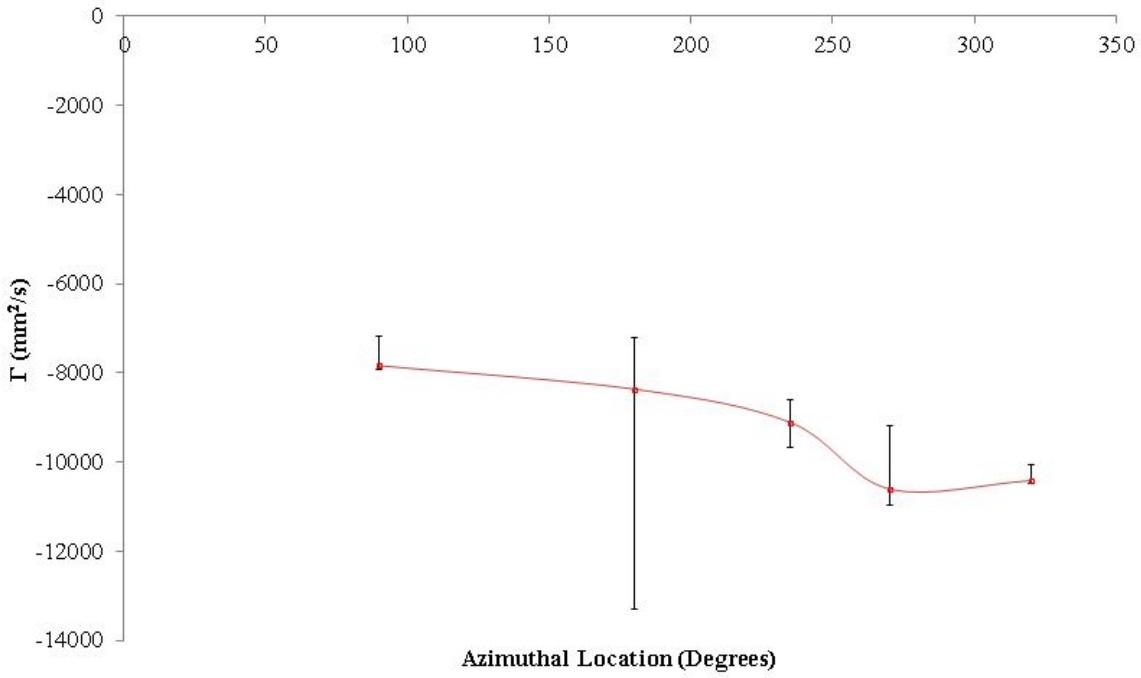


Figure 4.50: The range of LEV circulation values for the $AR$= 2 plate for $Re_{local}$ = 16,000 over the azimuthal range at $\alpha = 35°$.

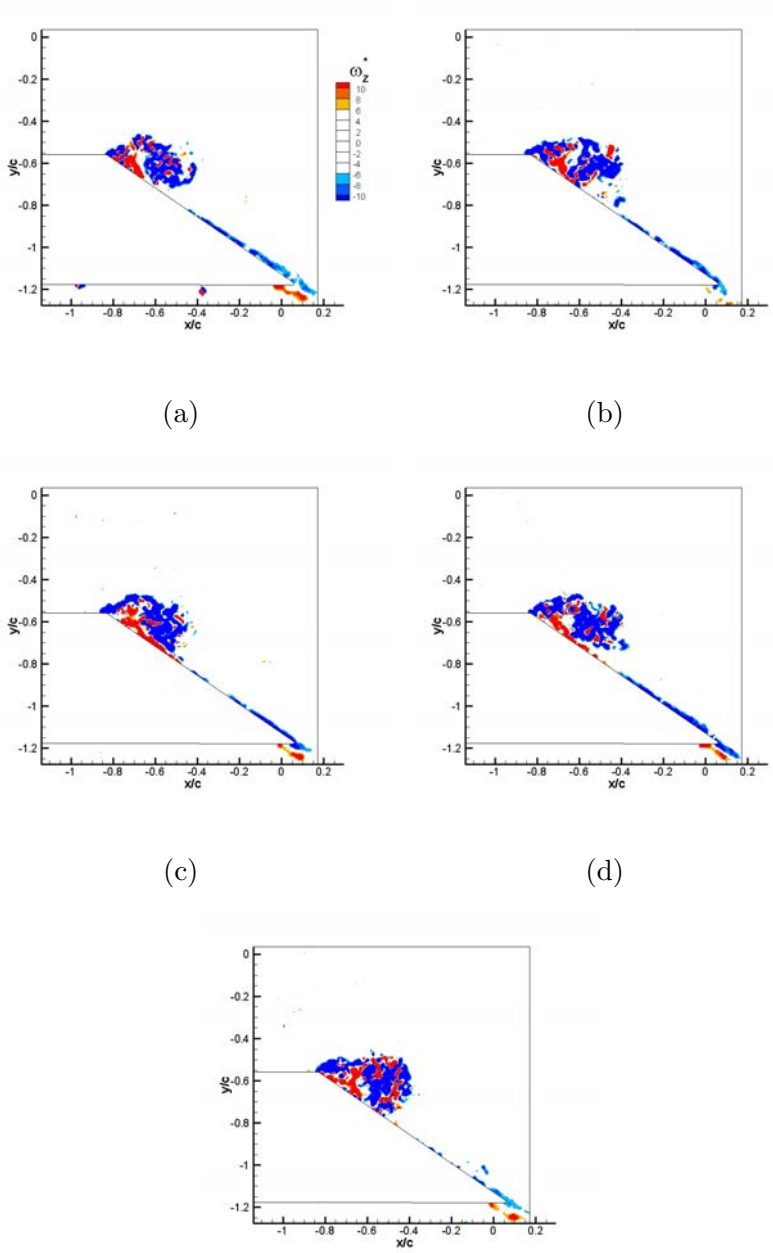


Figure 4.51: Temporal evolution of the nondimensionalized, instantaneous, vorticity fields at the 25% spanwise location for the $\mathcal{A}4$ plate for a Ro = 0.8125 at an $\alpha = 35°$ and Reynolds number of 8,000. a.) $\psi = 90°$ b.) $\psi = 180°$ c.) $\psi = 235°$ d.) $\psi = 270°$, and e.) $\psi = 320°$.

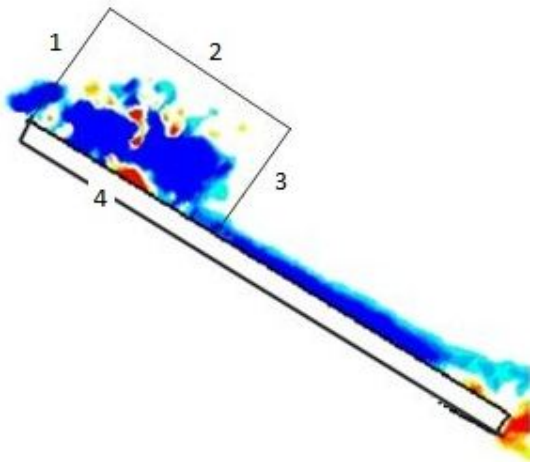


Figure 4.52: A depiction of the control volume used in Equation 4.5.

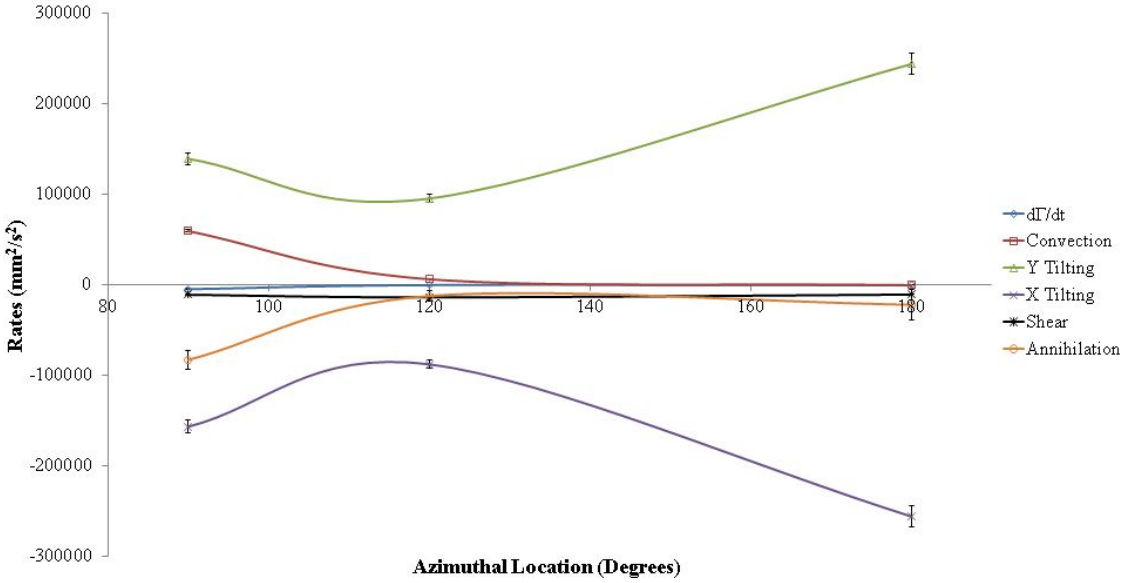


Figure 4.53: The rate of change of spanwise clockwise circulation for each of the terms in Equation 4.5.

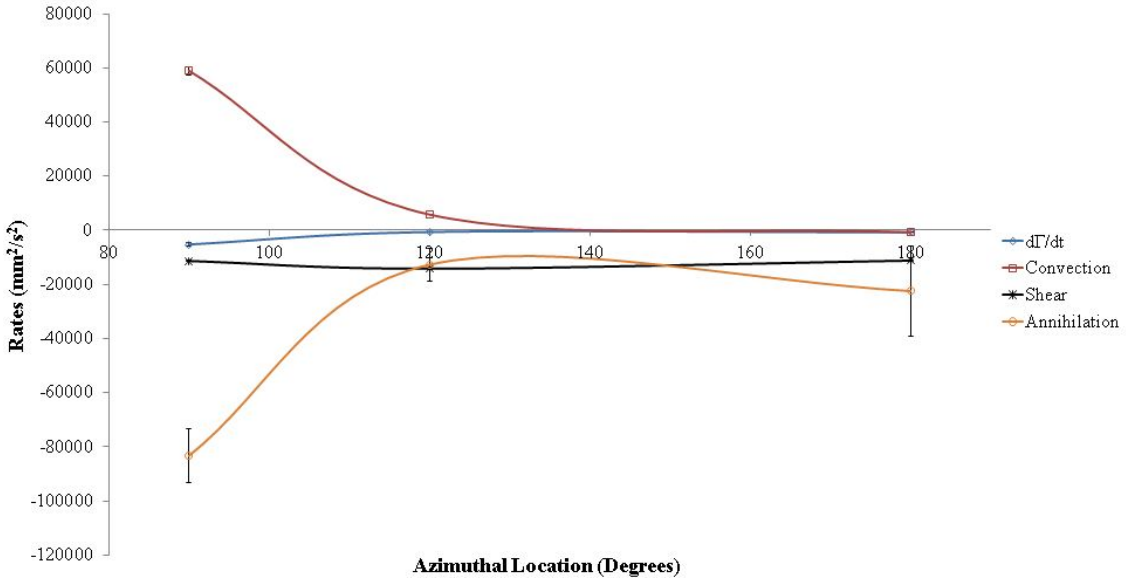


Figure 4.54: Zoomed in results of Figure 4.53 to show a more detailed view on the azimuthal location axis.

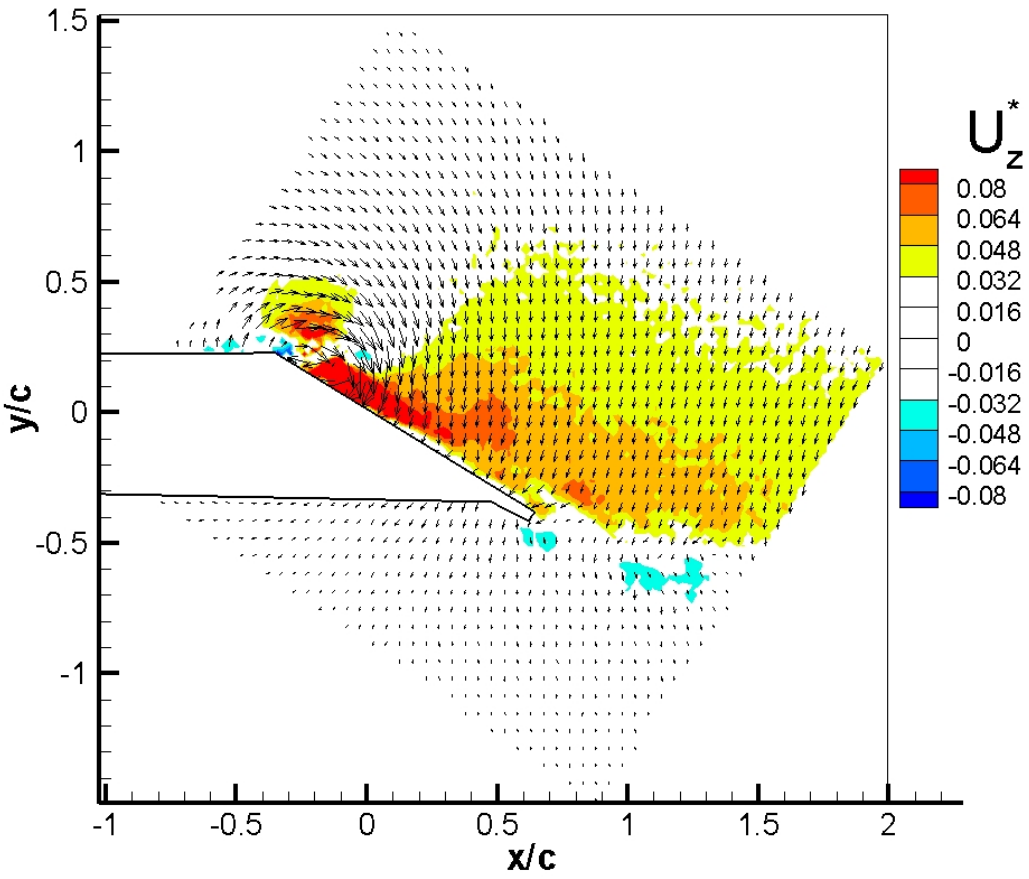


Figure 4.55: Nondimensionalized spanwise velocity ($U_z^* = U_z/U_{tip}$) at the *k plane* for $\psi = 75°$ averaged over 5 trials. In-plane velocity components are shown by the vectors.

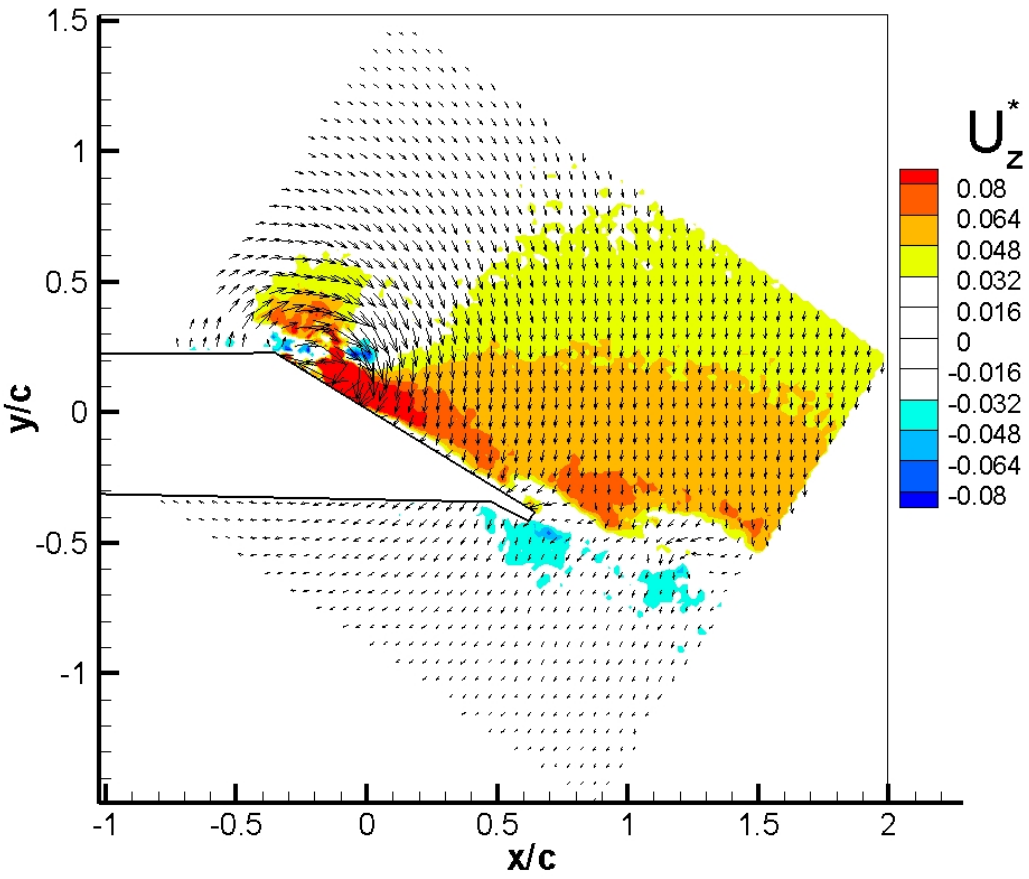


Figure 4.56: Nondimensionalized spanwise velocity ($U_z^* = U_z/U_{tip}$) at the *k plane* for $\psi = 90°$ averaged over 5 trials. In-plane velocity components are shown by the vectors.

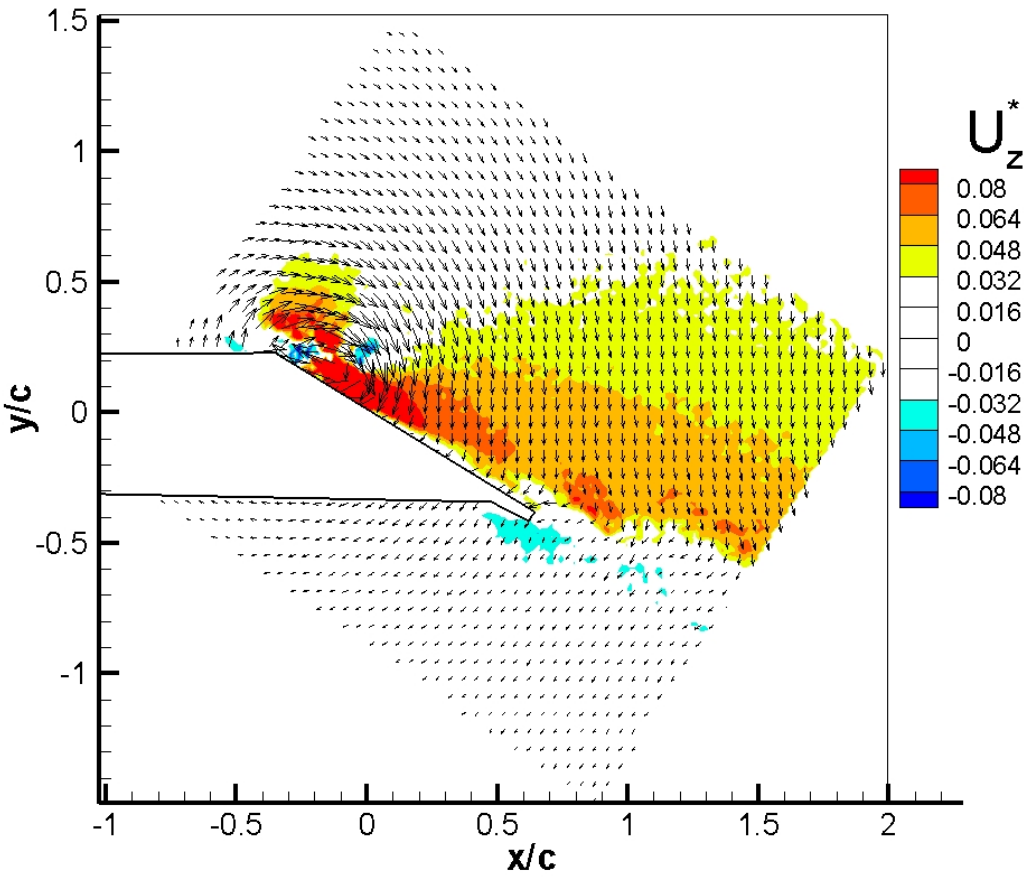


Figure 4.57: Nondimensionalized spanwise velocity ($U_z^* = U_z/U_{tip}$) at the *k plane* for $\psi = 120°$ averaged over 5 trials. In-plane velocity components are shown by the vectors.

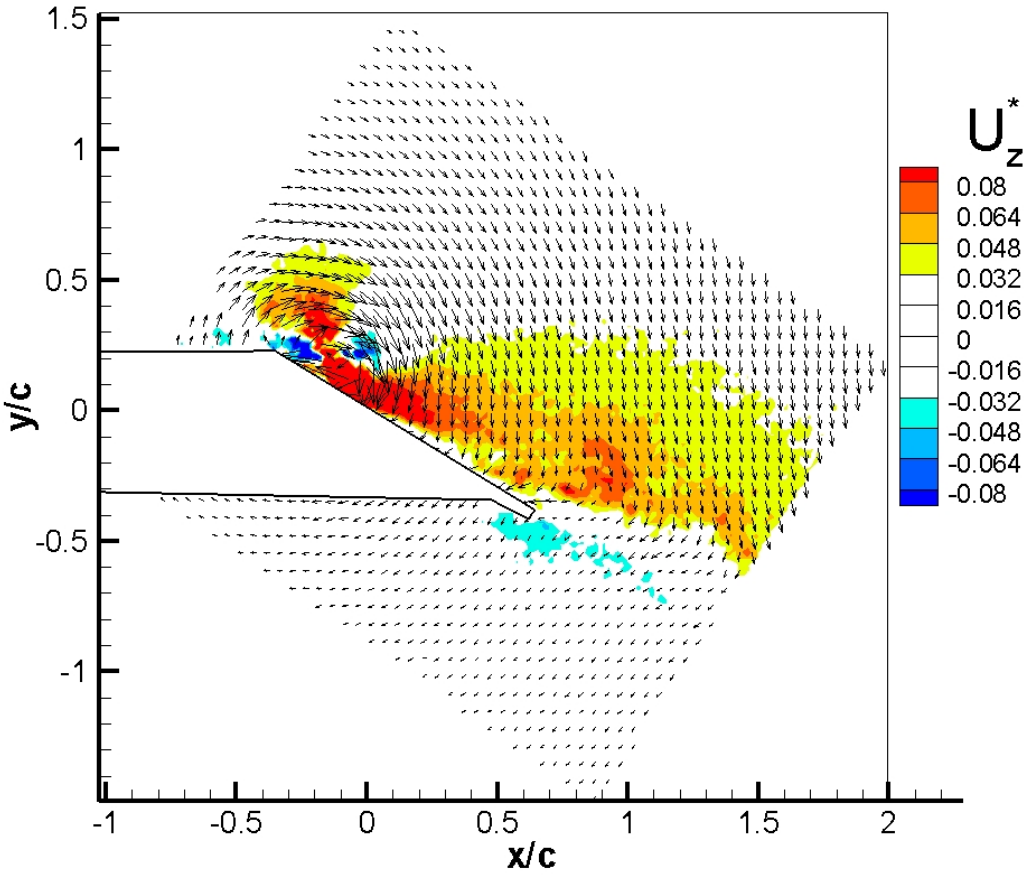


Figure 4.58: Nondimensionalized spanwise velocity ($U_z^* = U_z/U_{tip}$) at the *k plane* for $\psi = 180°$ averaged over 5 trials. In-plane velocity components are shown by the vectors.

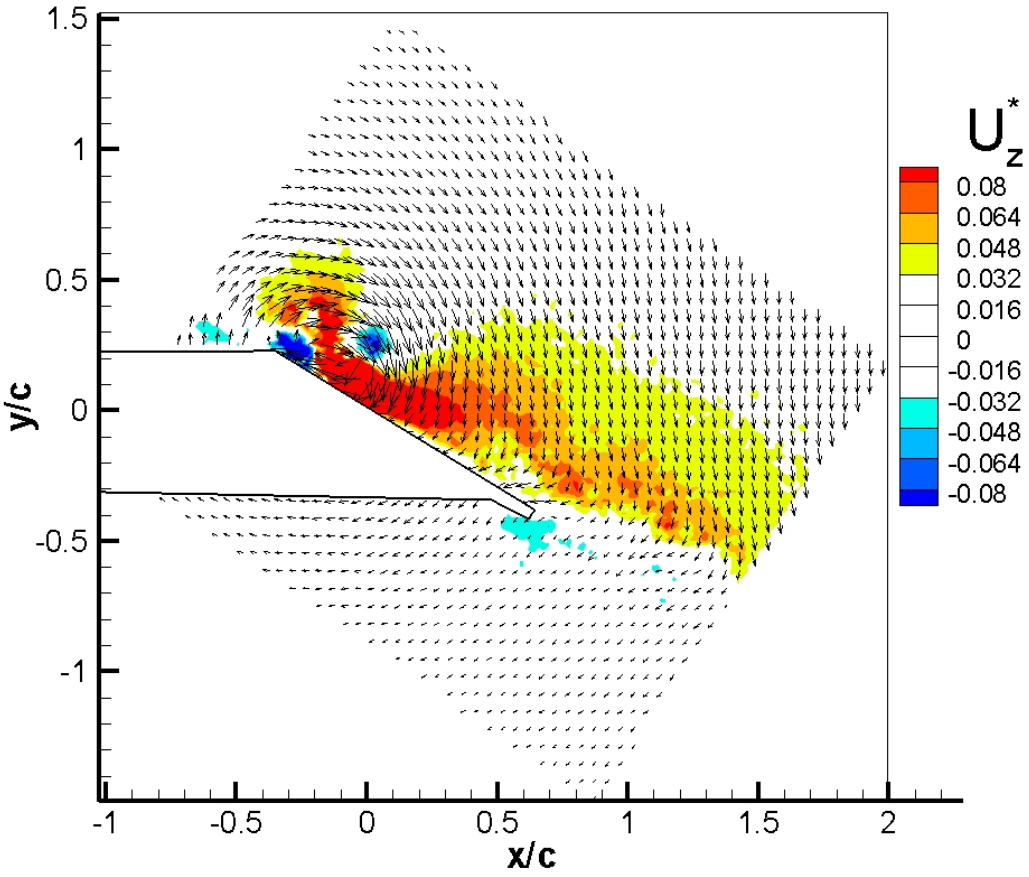


Figure 4.59: Nondimensionalized spanwise velocity ($U_z^* = U_z/U_{tip}$) at the *k plane* for $\psi = 270°$ averaged over 5 trials. In-plane velocity components are shown by the vectors.

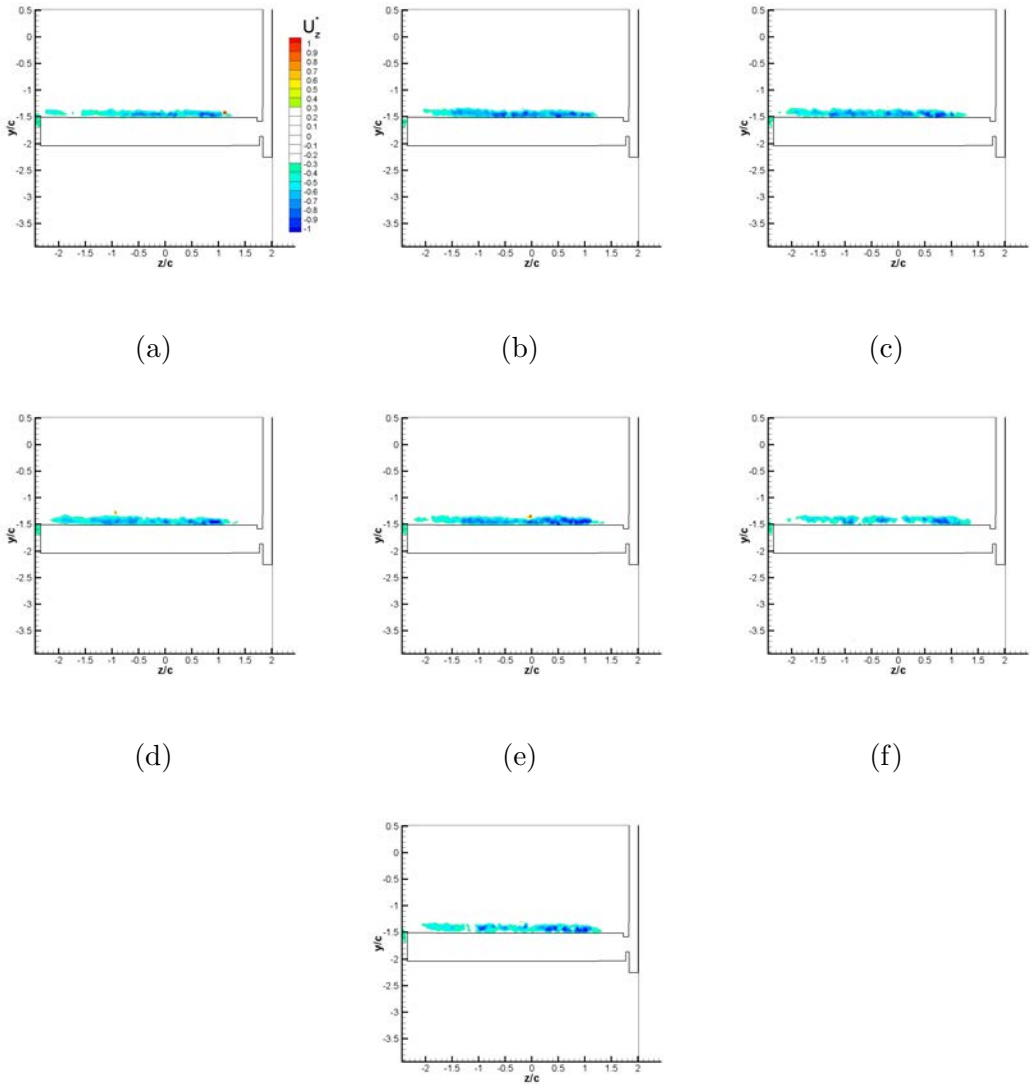


Figure 4.60: Averaged, nondimensionalized, spanwise velocity ($U_z^* = U_z/U_{tip}$) for: a.) $\psi = 75°$ b.) $\psi = 90°$ c.) $\psi = 120°$ d.) $\psi = 180°$ e.) $\psi = 235°$ f.) $\psi = 270°$ g.) $\psi = 320°$.

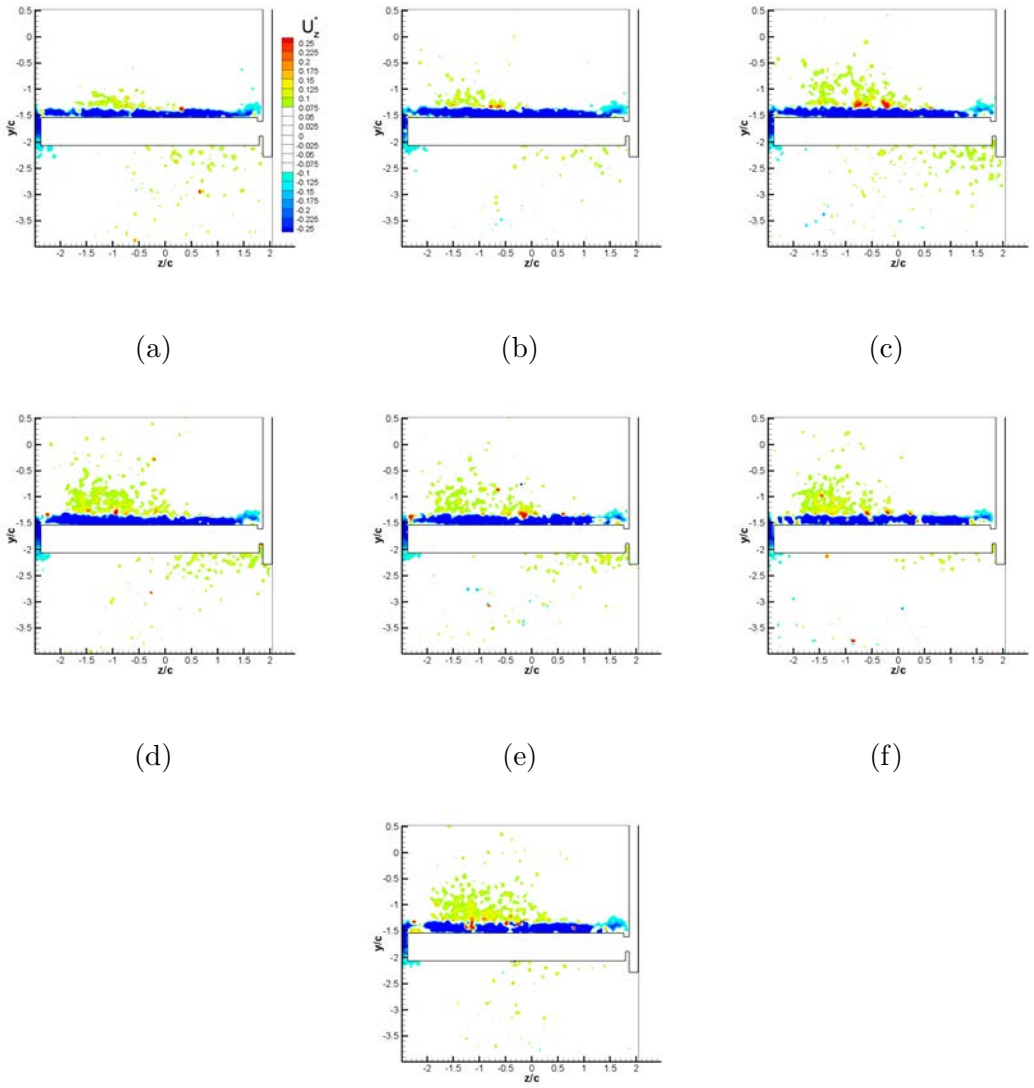

Figure 4.61: Instantaneous, nondimensionalized, spanwise velocity ($U_z^* = U_z/U_{tip}$) for: a.) $\psi = 75°$ b.) $\psi = 90°$ c.) $\psi = 120°$ d.) $\psi = 180°$ e.) $\psi = 235°$ f.) $\psi = 270°$ g.) $\psi = 320°$.

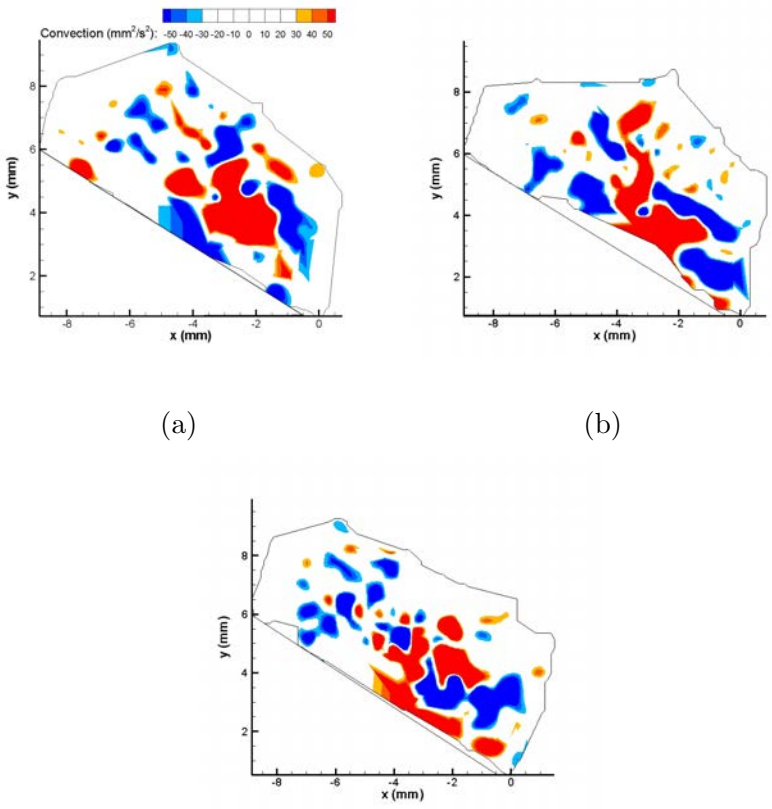


Figure 4.62: Contours of vorticity transport inside the control volume due to the convection term in Equation 4.5. a.) $\psi = 90°$ b.) $\psi = 120°$ and c.) $\psi = 180°$.

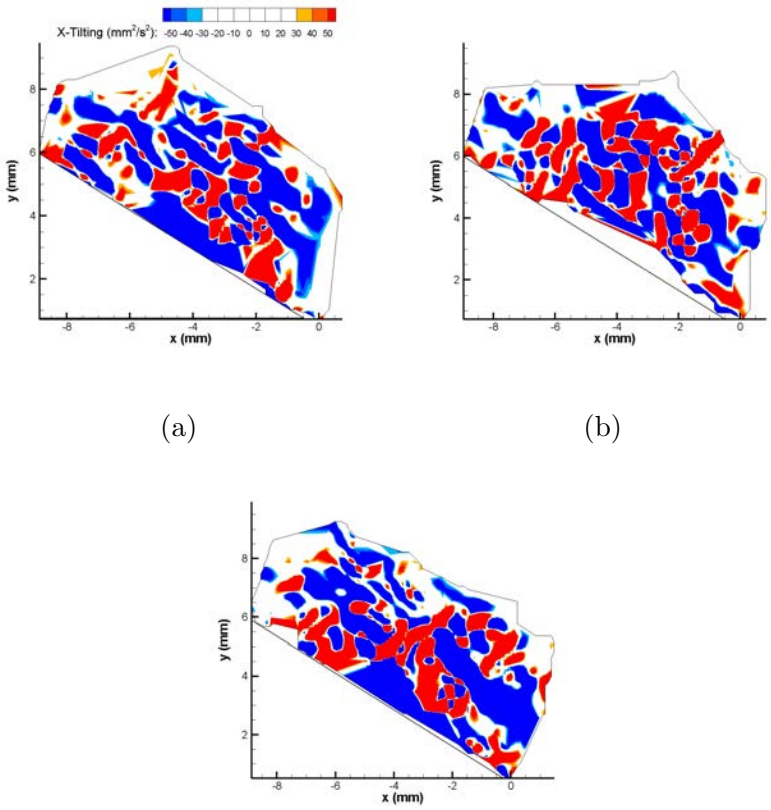


Figure 4.63: Contours of vorticity transport inside the control volume due to the X-tilting term in Equation 4.5. a.) $\psi = 90°$ b.) $\psi = 120°$ and c.) $\psi = 180°$.

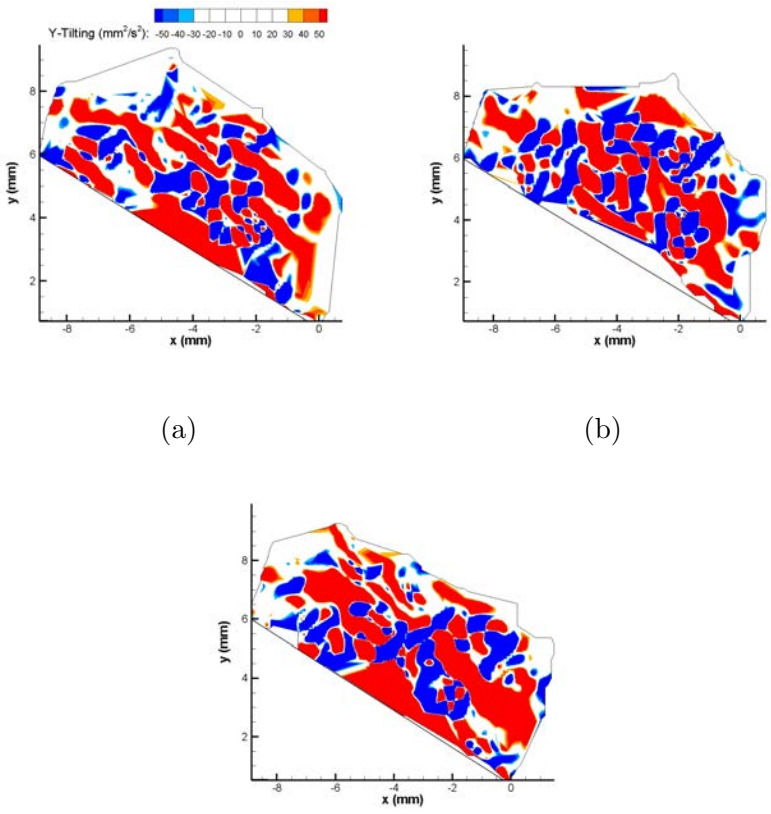


Figure 4.64: Contours of vorticity transport inside the control volume due to the Y-tilting term in Equation 4.5. a.) $\psi = 90°$ b.) $\psi = 120°$ and c.) $\psi = 180°$.

# CHAPTER 5
# CONCLUSIONS AND FUTURE WORK

Chapters 1 and 2 introduced the motivation behind studying purely rotating blades and their applications in realistic applications such as flapping flight, helicopters, and wind turbine aerodynamics. Previous studies indicated the presence of a LEV which accounted for high lift coefficients and allowed for the plate to maintain attached flow at higher angles of attack where translational cases, synonymous to fixed wing aircraft, would be in a stall regime. Ellington et al [30] claimed in his study that the spanwise flow inside the core of the LEV stabilized the LEV and limited its strength from becoming too large. However, Birch and Dickinson [10] showed that hindering the spanwise flow on the surface of the blade did not cause the LEV to become unstable. Also, some groups such as Jones and Babinsky [45], Jones et al [47], Grandlund et al [36], and Venkata and Jones [107] have observed the LEV undergoing a shedding while Devoria et al [23], Carr et al [17], Lentink and Dickinsion [56, 57], Ansari et al [4], and Ozen and Rockwell [75] have seen a single LEV that remains concentrated towards the leading-edge of the plate. An experimental investigation of a flat plate of various aspect ratios was conducted, examining variations in angle of attack, azimuthal position, Reynolds number, and spanwise position in a quiescent flow with the plate moving in a starting motion. The results indicated that, at least for the present case, annihilation of negative vorticity inside the LEV is primarily responsible for regulating the strength of the LEV and prevents it from becoming too large which would cause the LEV to detach. Furthermore, spanwise flow was shown

not to be important when the plate reached a steady-state at $\psi \gtrapprox 120°$.

## 5.1 Conclusions

The nondimensional circulation of the LEV, $\Gamma^*$, increases with increasing angle of attack, but it is relatively insensitive to Reynolds number variations. Additionally, the 2D PIV experiments showed that with increasing azimuthal position, the LEV begins to entrain more of positive vorticity on the suction surface of the plate. The LEV begins to entrain more of the counterclockwise region by means of inducing a velocity in the direction of the leading-edge such that the positive vorticity is captured by the shear layer and redistributed into the LEV. This observation inspired the development of a vorticity transport analysis, discussed in Chapter 4, in which the time rate of change of the LEV circulation, convection, tilting of negative vorticity, and shear layer contributions in a control volume were estimated, and the remainder in the balance was associated with the annihilation between the positive vorticity and the LEV. Inside the LEV, the transport of vorticity is dominated by the tilting of $\omega_x$ and $\omega_y$ vorticity into and out of the spanwise direction which implies a highly, three-dimensional distribution of vorticity in the LEV. SPIV measurements of the spanwise velocity further validate this claim by showing four separate peaks in spanwise velocity magnitude where two of them show a strong root-to-tip flow while the other two are tip-to-root flows. 2D PIV measurements of the spanwise velocity 5 millimeters from the leading-edge exhibit a dominant root-to-tip flow, but there is noticeable tip-to-root velocity gradient created above the plate towards the tip of the plate.

During the developmental stages of the LEV, the annihilation term seems to be in balance with the convection term, but with increasing azimuthal position the convection term becomes less important. Beyond $\psi = 120°$ the plate approaches a steady state, and it is observed that the unsteady and convection terms go to zero. The key aspect to this analysis is the shear layer and annihilation terms are in balance with one another with the small variations being associated with differences in the X- and Y-tilting terms, which suggests that annihilation is the dominant factor in regulating the strength of the LEV for $\psi \gtrapprox 120°$ . It is therefore proposed that the annihilation between the positive vorticity and LEV is a new and important mechanism to be considered in rotating wings.

## 5.2 Future Work

The present study only investigated a few spanwise positions along the plates. Therefore, it would be beneficial to examine more chordwise planes to see how the LEV develops and to examine the effects spanwise position on the circulation of the LEV. Multiple spanwise locations will provide insight into the effects of the tip vortex which, as mentioned in Chapter 2, was postulated by Shy et al [88] and Birch and Dickinson [10, 88] to promote LEV attachment to some extent.

Furthermore, higher angles of attack should be looked at to determine when the plate will eventually become stalled. This leads to several questions such as "do larger or smaller aspect ratios experience stall sooner?" Pressure tap measurements along the span would provide insight to the torsional stresses experience along the

plate that may be detrimental to the plate especially at higher angles of attack when the inboard spanwise locations tend to maintain flow attachment while outboard locations are typically stalled.

The study presented here only examines one configuration when performing the vorticity transport analysis. More cases need to be investigated to further support the validity of the claim that annihilation is an important factor in governing the strength of the LEV for the general rotating wing or blade. Also, additional spanwise planes need to be obtained to confirm the spanwise velocities seen using chordwise SPIV measurements. This will require further conditioning of the plate's surface (such as with fluorescent paint) to reduce reflections and thus obtain more detail in these experiments.

Also, a method needs to be developed to objectively define whether the LEV is attached or shedding throughout the span of the plate, or is some other paradigm needed.

The next step in this research is to fully submerge the mechanism inside a water channel which will create opportunities to look at the effects a free-stream velocity might have on the flow. In conjunction with a free-stream velocity, the mechanism may be yawed with respect to the free-stream and experiments may be performed to see the effects of dynamic stall.

# APPENDIX A
# PLOTS OF THEORETICAL BOUND CIRCULATION AND EXPERIMENTAL MEASUREMENTS OF LEV CIRCULATION

This chapter contains the plots for both aspect ratio plates comparing the experimentally measured LEV strengths with the bound circulation computed theoretically using thin airfoil theory using Equation 4.4. Figures A.1 - A.5 show the $\mathcal{R}$= 4 plate's LEV circulation compared to the bound circulation over the range of azimuthal positions investigated. As discussed in Section 4.3, the LEV strength increases approximately linearly at all azimuthal positions. Small curvatures in the LEV strength, such as the Re = 8,000 in Figure A.1, Re = 4,000 & 16,000 in Figure A.2, Re = 16,000 in Figure A.3, and Re = 8,000 & 16,000 in Figure A.5, are likely explained by the small number of trials acquired (3) which variations in the LEV strength could slightly skew the mean. With more trials acquired for each case, the LEV strength will likely become more linear. In all cases, the LEV circulation is seen to be larger than its theoretical bound circulation suggesting that the LEV is a significant source of lift augmentation. From $180° \leq \psi \leq 270°$ the circulation of the LEV at a Re = 8,000 follows the theoretical bound circulation for Re = 16,000 over the range of angles of attack; however, the LEV's strength surpasses the theoretical value at $\psi = 320°$. The same can be said for the LEV's circulation at Re = 4,000 and the bound circulation at Re = 8,000 from $180° \leq \psi \leq 320°$. From these results, the claim can be made that the LEV is unsteady during the initial transients (i.e. $\psi$ <180°), but then approaches a steady-state beyond $\psi = 180°$.

Figures A.6 - A.10 show the same comparison of LEV strength and theoretical bound circulation values for a fixed azimuthal position except now the LEV strength is for the $\mathcal{R}= 2$ plate. Generally, the same arguments that were said about the $\mathcal{R}4$ plate can be said for the $\mathcal{R}2$ plate with the LEV circulation being characterized as linear over the angles of attack investigated except having different constants proportional to $\sin\alpha$ between the theoretical and experimental results for a given Reynolds number. There is a specific occasion where the LEV actually dips below the bound circulation value in Figure A.7 for Re = 16,000. As discussed in Section 4.3 and shown in Figure 4.50, the dip in the LEV's strength is likely contributed to an outlier measurement of the circulation skewing the mean LEV measurement ($\Gamma_{mean}$).

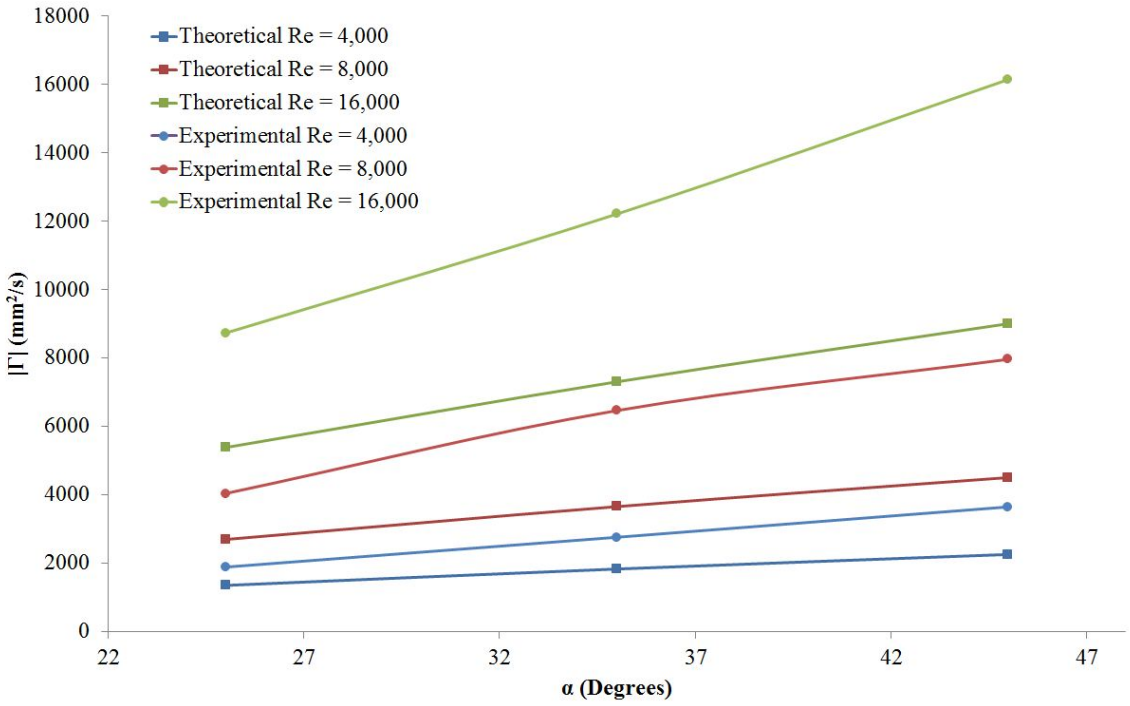


Figure A.1: $\psi = 90°$ dimensional theoretical bound circulation and experimental circulation values of the LEV for the $\mathcal{R}$= 4 plate.

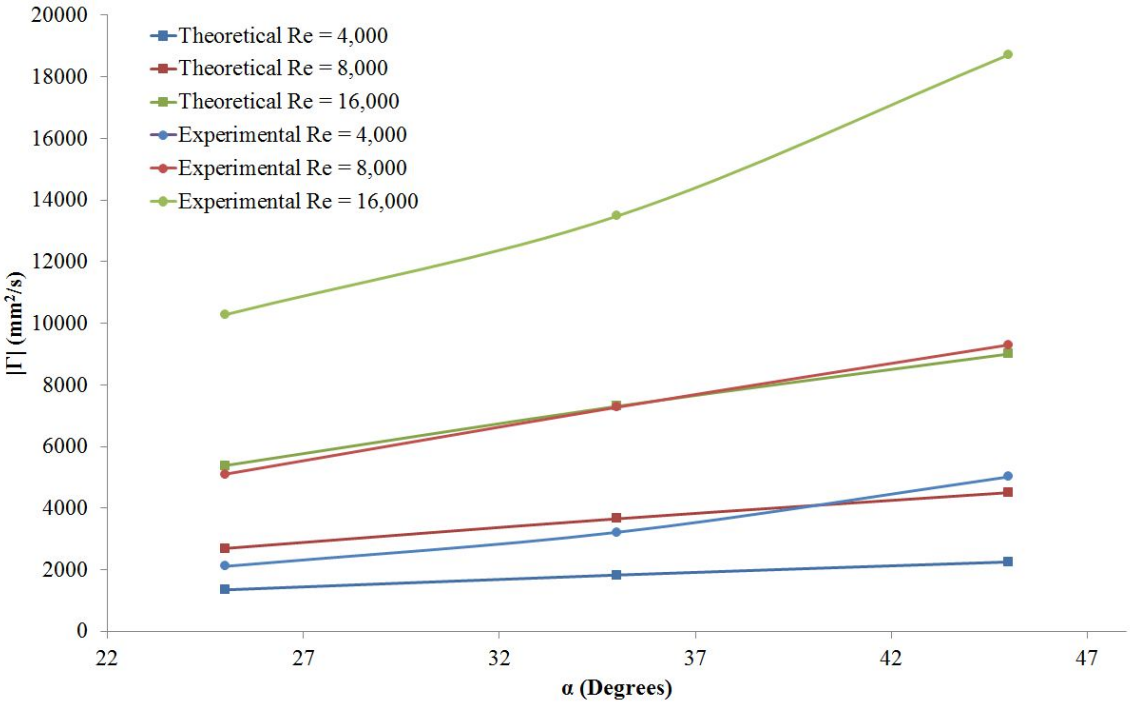


Figure A.2: $\psi = 180°$ dimensional theoretical bound circulation and experimental circulation values of the LEV for the $\mathcal{R}$= 4 plate.

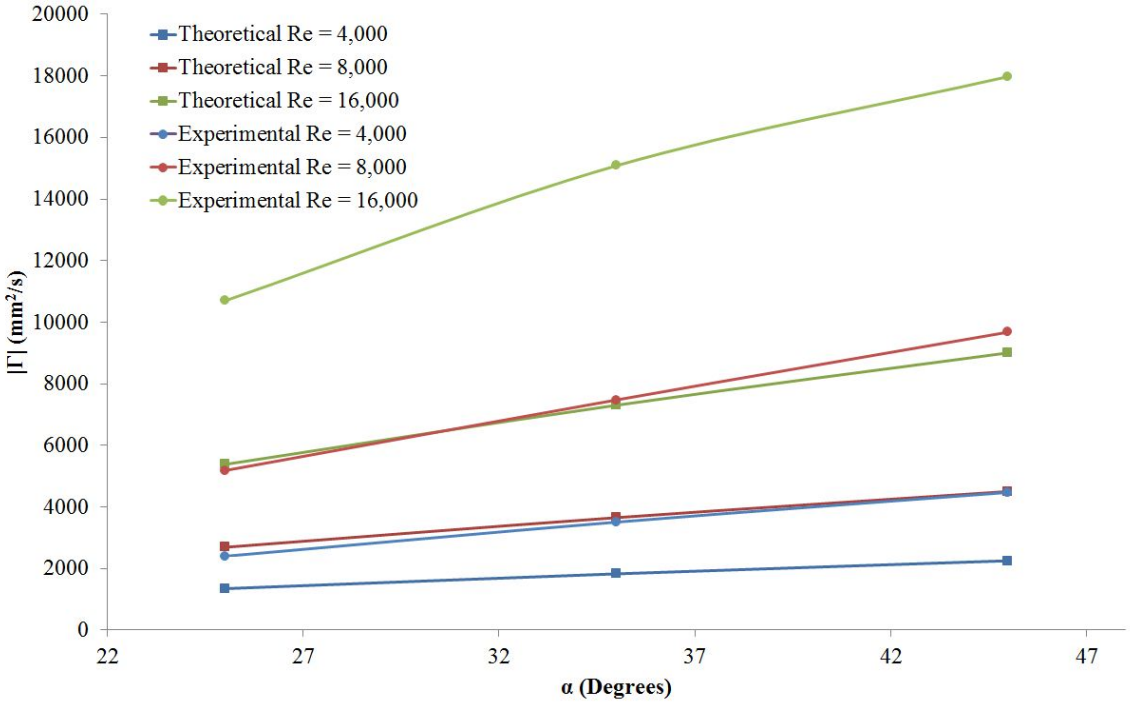


Figure A.3: $\psi = 235°$ dimensional theoretical bound circulation and experimental circulation values of the LEV for the $\mathcal{R}$= 4 plate.

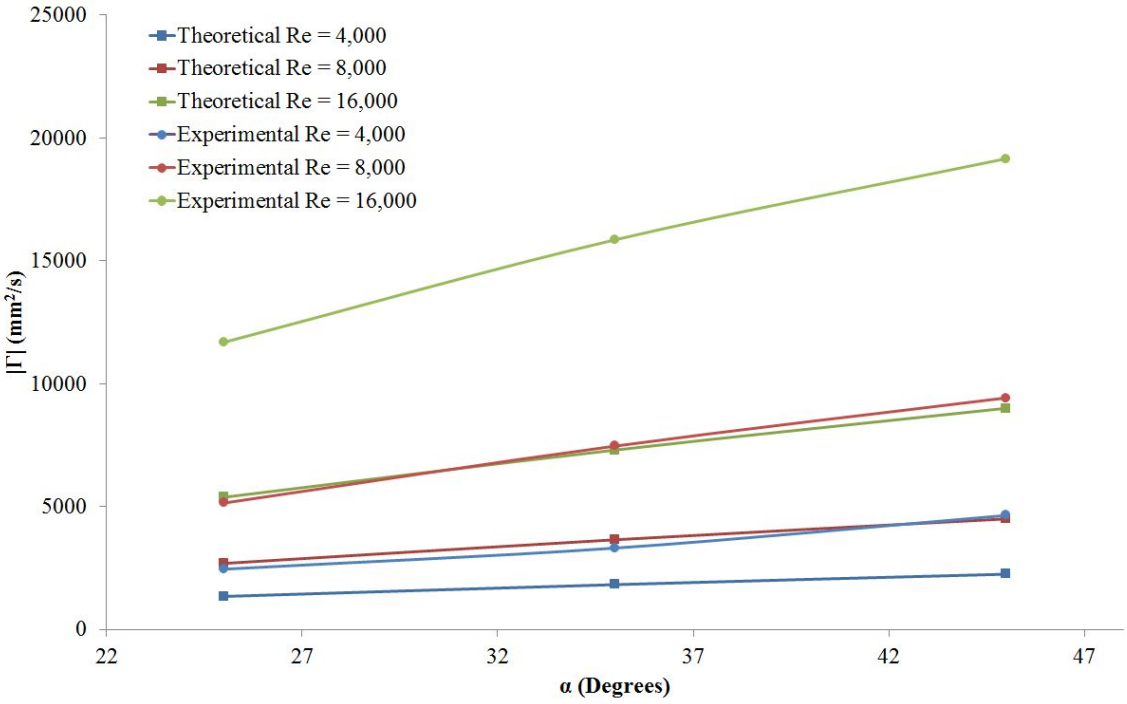


Figure A.4: $\psi = 270°$ dimensional theoretical bound circulation and experimental circulation values of the LEV for the $\mathcal{R}$= 4 plate.

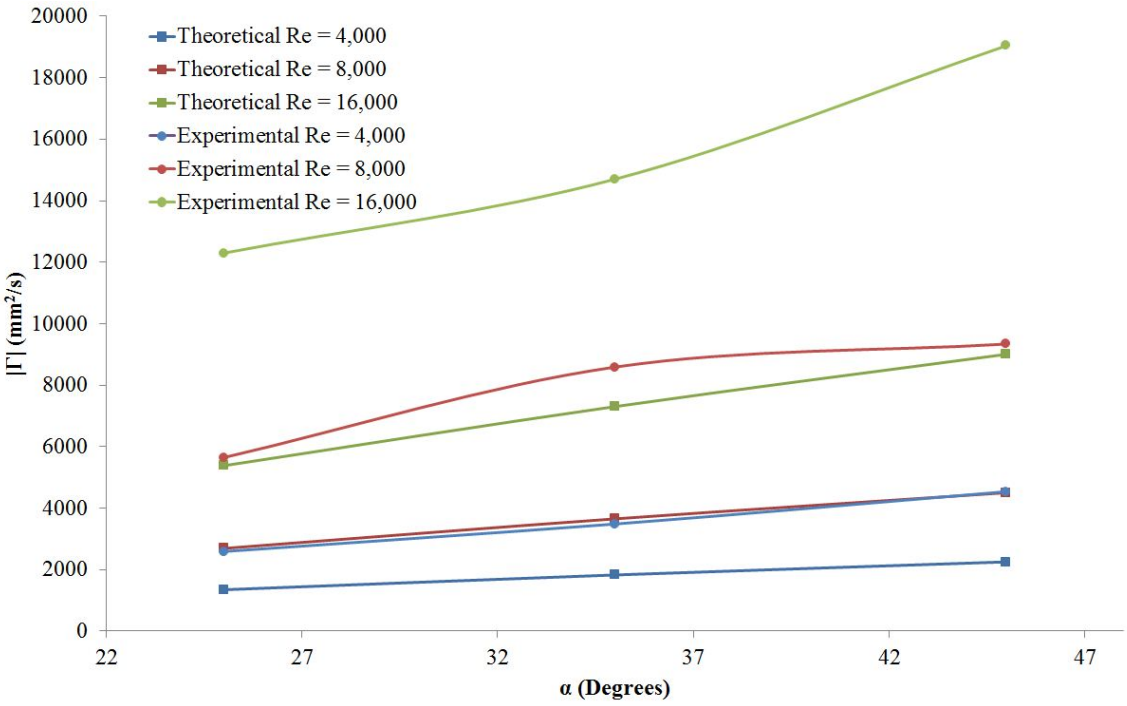


Figure A.5: $\psi = 320°$ dimensional theoretical bound circulation and experimental circulation values of the LEV for the $\mathcal{R}$= 4 plate.

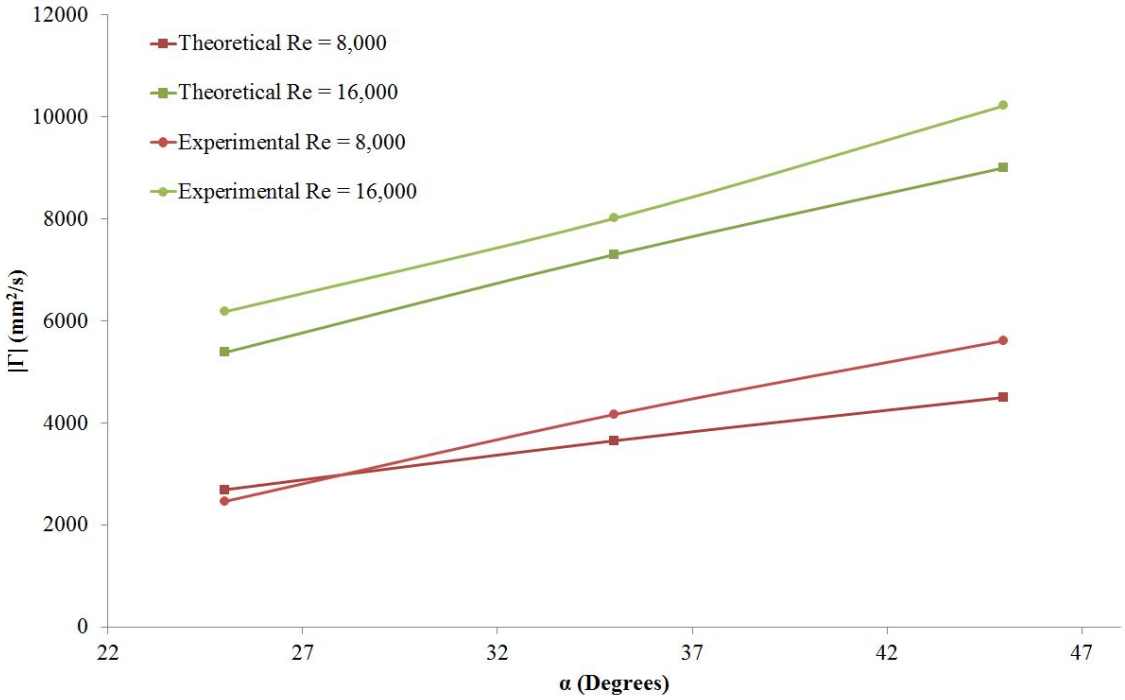


Figure A.6: $\psi = 90°$ dimensional theoretical bound circulation and experimental circulation values of the LEV for the $\mathcal{R}= 2$ plate.

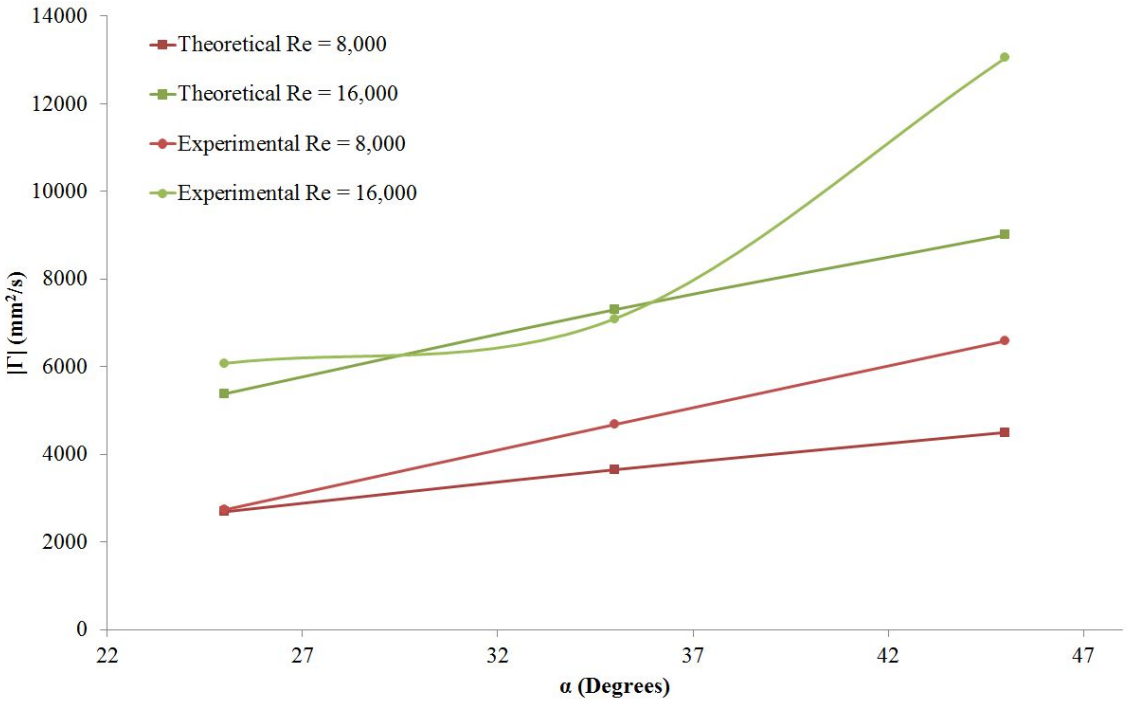


Figure A.7: $\psi = 180°$ dimensional theoretical bound circulation and experimental circulation values of the LEV for the $\mathcal{R}= 2$ plate.

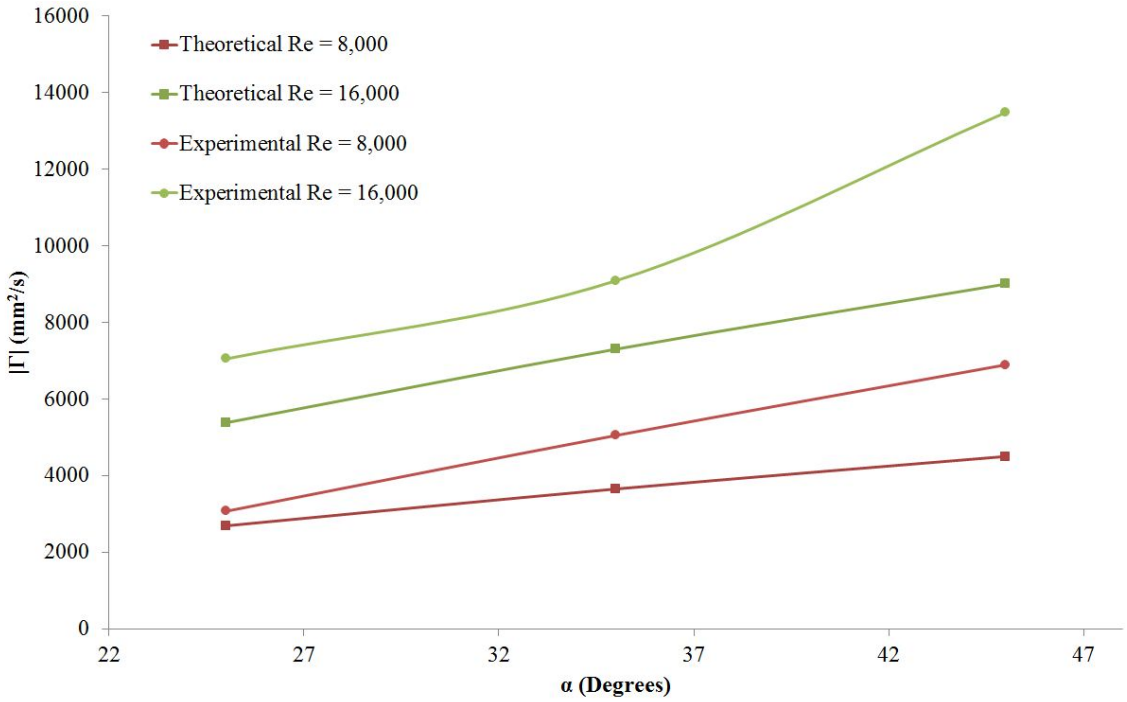


Figure A.8: $\psi = 235°$ dimensional theoretical bound circulation and experimental circulation values of the LEV for the $\mathcal{R}= 2$ plate.

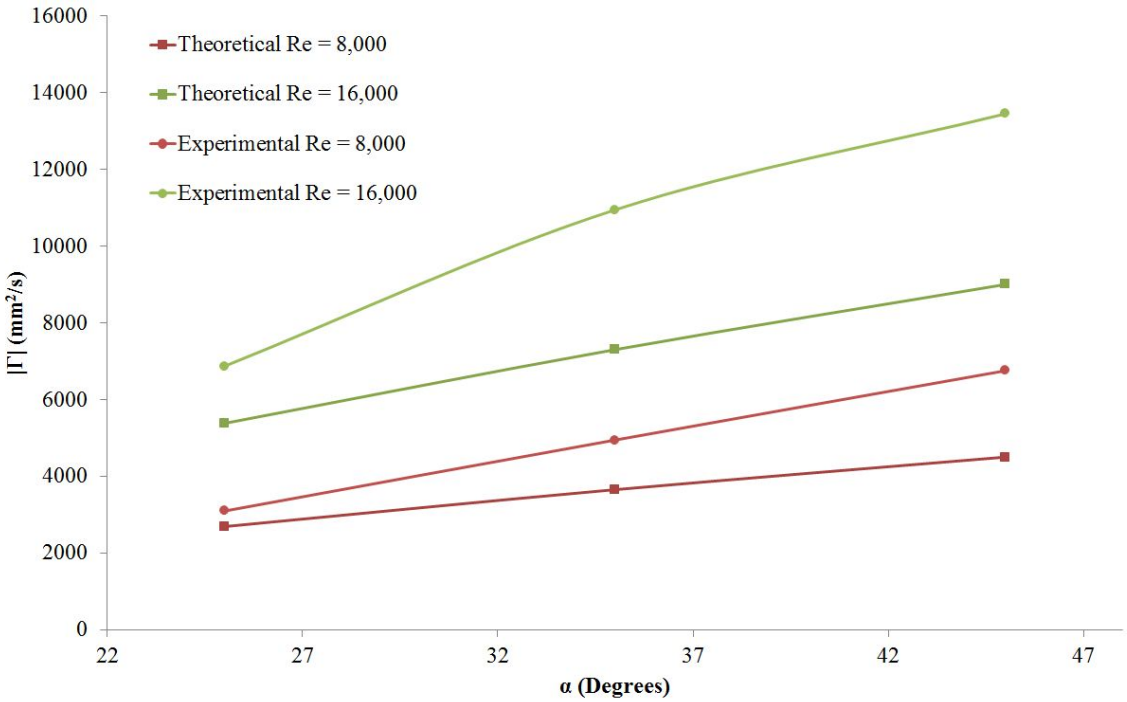


Figure A.9: $\psi = 270°$ dimensional theoretical bound circulation and experimental circulation values of the LEV for the $\mathcal{R}= 2$ plate.

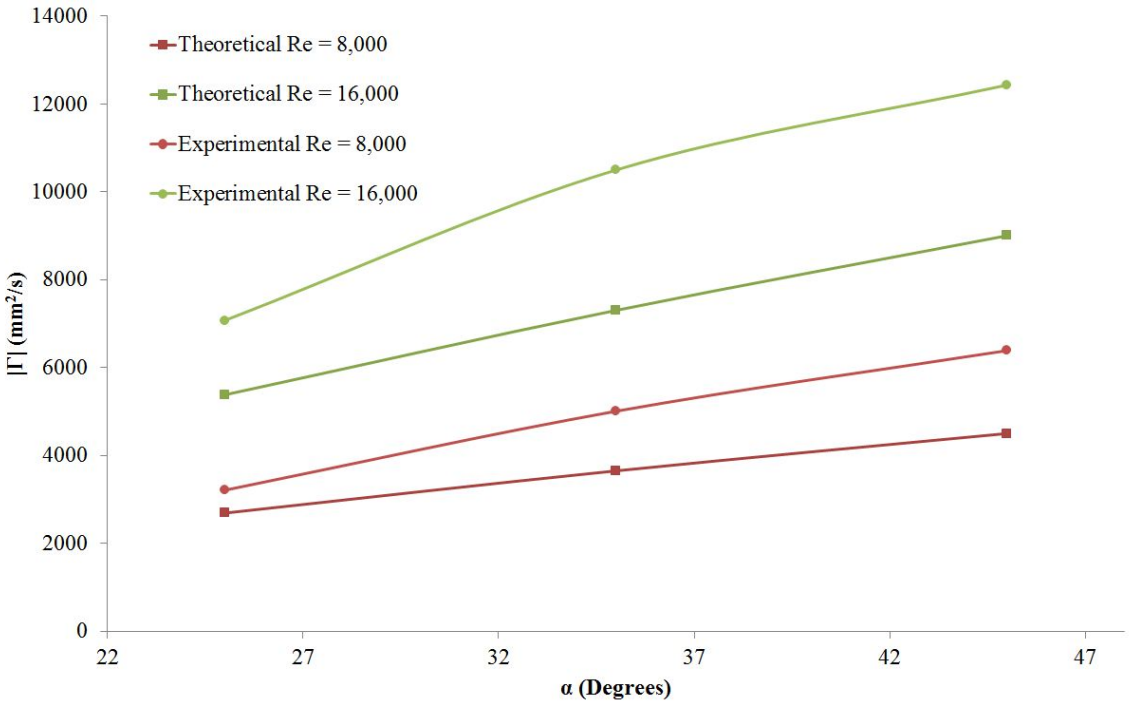


Figure A.10: $\psi = 320°$ dimensional theoretical bound circulation and experimental circulation values of the LEV for the $\mathcal{R}= 2$ plate.

# APPENDIX B
# VORTICITY TRANSPORT ERROR PROPAGATION

This chapter aims at providing a detailed account on the analysis of the uncertainties of the terms in Equation 4.5. This chapter tries to give a conservative estimate of the errors, but it is not a rigorous analysis. Simplifications and generalizations were made to facilitate the quantifications of each uncertainty of the terms. An uncertainty in the PIV data was assumed based on the literature and quality of the data, and from the assumed values, a general uncertainty, designated by $\sigma$, for each of the terms can be calculated at an individual point. In the following sections, mention of the *k-1*, *k*, and *k+1 planes* are in reference to the three chordwise laser planes shown in Figure 3.13 created to obtain the SPIV measurements.

## B.1 Convection Term

From Equation 4.5, the convection term is calculated discretely as described in Equation 4.7. Using the generalization presented in Equation 4.7, a relative error for a single point in the analysis may be calculated and is shown by Equation B.1.

$$conv = U_z \frac{\omega_{z_{k+1}} - \omega_{z_{k-1}}}{2Z_g} X_g Y_g \tag{B.1}$$

Where $U_z$, $\omega_{z_{k+1}}$, $\omega_{z_{k-1}}$, $Z_g$, $X_g$, and $Y_g$ is the spanwise velocity, spanwise vorticity at the *k+1 plane* (outboard most chordwise laser plane), spanwise vorticity at the *k-1 plane* (inboard most chordwise laser plane), spacing between chordwise laser planes, spacing between vectors generated in the PIV vector files in the streamwise

direction, and spacing between vectors created in the PIV vector files in the vertical direction (y-direction), respectively.

Now, in order to successfully propagate the error from the DPIV measurements, partial derivatives of the convection term need to be taken with respect to each of the possible sources of error. The partial derivatives for each component are shown in Equations B.2 - B.7.

$$\frac{\partial conv}{\partial U_z} = \frac{\omega_{z_{k+1}} - \omega_{z_{k-1}}}{2Z_g} X_g Y_g \tag{B.2}$$

$$\frac{\partial conv}{\partial \omega_{z_{k+1}}} = \frac{U_z X_g Y_g}{2Z_g} \tag{B.3}$$

$$\frac{\partial conv}{\partial \omega_{z_{k-1}}} = \frac{-U_z X_g Y_g}{2Z_g} \tag{B.4}$$

$$\frac{\partial conv}{\partial X_g} = U_z Y_g \frac{\omega_{z_{k+1}} - \omega_{z_{k-1}}}{2Z_g} \tag{B.5}$$

$$\frac{\partial conv}{\partial Y_g} = U_z X_g \frac{\omega_{z_{k+1}} - \omega_{z_{k-1}}}{2Z_g} \tag{B.6}$$

$$\frac{\partial conv}{\partial Z_g} = \frac{-U_z X_g Y_g \left(\omega_{z_{k+1}} - \omega_{z_{k-1}}\right)}{2Z_g^2} \tag{B.7}$$

Adding the errors in quadrature, the general overall uncertainty for the convection term is expressed in Equation B.8.

$$\sigma_{conv} = \left[ \left( \frac{\partial conv}{\partial U_z} \sigma_{U_z} \right)^2 + \left( \frac{\partial conv}{\partial \omega_{z_{k+1}}} \sigma_{\omega_{z_{k+1}}} \right)^2 + \left( \frac{\partial conv}{\partial \omega_{z_{k-1}}} \sigma_{\omega_{z_{k-1}}} \right)^2 + \left( \frac{\partial conv}{\partial X_g} \sigma_{X_g} \right)^2 + \left( \frac{\partial conv}{\partial Y_g} \sigma_{Y_g} \right)^2 + \left( \frac{\partial conv}{\partial Z_g} \sigma_{Z_g} \right)^2 \right]^{\frac{1}{2}} \quad \text{(B.8)}$$

To evaluate the convection term's uncertainty, the uncertainties presented on the right hand side of Equation B.8 need to be calculated. In this analysis, the uncertainties in the vector spacing ($\sigma_{X_g}$, $\sigma_{Y_g}$, and $\sigma_{Z_g}$) are assumed to be negligible. A conservative estimate for the uncertainties in the spanwise velocity and spanwise vorticities were calculated and are demonstrated in the subsequent equations.

The velocity vectors are calculated using PIV by first using a cross-correlation analysis to determine a mean particle displacement within a sub-window of the domain between the two images and dividing by the time interval separating the image pair[79]. The spanwise velocity, $U_z$, can be defined in this manner and is shown in Equation B.9.

$$U_z = \frac{\Delta z}{M \Delta t} \quad \text{(B.9)}$$

Where $M$ is the magnification ratio. The total uncertainty in the spanwise velocity can be obtained by once again taking partial derivatives of $U_z$ with respect to the terms that will contribute error. The cameras were calibrated with the laser plane using a LaVision # 20 calibration plate in which the camera was focused directly on the plate's dots allowing the DaVis 8.0 software to fit a third-order polynomial to the view, essentially dewarping the image. From the fit, the correlation was considered to

be of "excellent" quality with root-mean-square (RMS) of the fit to be less than 0.3 pixels. Since the calibration was of high quality, the uncertainty in the magnification ratio is assumed to not be a major component of uncertainty in the spanwise velocity. The resulting uncertainty for the spanwise velocity is given in Equation B.10.

$$\sigma_{U_Z} = \left[ \left( \frac{\partial U_z}{\partial \Delta z} \sigma_{\Delta z} \right)^2 + \left( \frac{\partial U_z}{\partial \Delta t} \sigma_{\Delta t} \right)^2 \right]^{\frac{1}{2}} \tag{B.10}$$

The uncertainty in $\Delta t$ is determined by the laser timing and can be as high as 10 to 100 nanoseconds which is subject to the electrical supply conditions and optical settings (Dr. Steve Anderson, LaVision Inc., personal communication), but since $\Delta t$ times were on the order of hundreds (some cases thousands) of microseconds, the uncertainty associated with $\Delta t$ is assumed to be negligible. The resulting uncertainty used in the analysis for the spanwise velocity is:

$$\sigma_{U_z} = \frac{\sigma_{\Delta z}}{M \Delta t} \tag{B.11}$$

Factors that influence PIV errors are large particle sizes, improper seeding of particles, particle displacement, and out-of-plane motion[1, 41, 79]. Huang et al. [41] proposed a representative uncertainty in the displacement determined by DPIV analysis to be approximately 0.1 pixels. Prasad and Adrian [77] stated that the uncertainty in the out-of-plane motion in SPIV could be 4 times as large as the in-plane components. Obtaining accurate estimates of PIV uncertainty in situ is not possible due to the widely-varying sources of error from vector to vector. With the influence of these publications, advancements in technology, and the quality of the

data obtained, the assumed uncertainties for the change in pixel position for $\sigma_{\Delta x}$, $\sigma_{\Delta y}$, $\sigma_{\Delta z}$ were 0.1, 0.1, and 0.3 pixels, respectively.

Out-of-plane vorticity components were calculated using the central difference scheme presented in Equation 3.2. To determine the uncertainty in the vorticity values, the potential sources of errors were added in quadrature as demonstrated in Equation B.12.

$$\sigma_{\omega_z} = \left[ \left( \frac{1}{2X_g} \sigma_{U_{y_{i+1}}} \right)^2 + \left( \frac{-1}{2X_g} \sigma_{U_{y_{i-1}}} \right)^2 + \left( \frac{-1}{2Y_g} \sigma_{U_{x_{j+1}}} \right)^2 + \left( \frac{1}{2Y_g} \sigma_{U_{x_{j-1}}} \right)^2 \right]^{\frac{1}{2}} \tag{B.12}$$

Where

$$\sigma_{U_{x_{j+1}}} = \sigma_{U_{x_{j-1}}} = \sigma_{U_x} \tag{B.13}$$

$$\sigma_{U_{y_{i+1}}} = \sigma_{U_{y_{i-1}}} = \sigma_{U_y} \tag{B.14}$$

$$\sigma_{\omega_{z_{k+1}}} = \sigma_{\omega_{z_{k-1}}} = \sigma_{\omega_z} \tag{B.15}$$

From the previous explanation, the uncertainties for $\sigma_{U_x}$ and $\sigma_{U_y}$ are described by Equations B.16 and B.17, respectively.

$$\sigma_{U_x} = \frac{\sigma_{\Delta x}}{M \Delta t} \tag{B.16}$$

$$\sigma_{U_y} = \frac{\sigma_{\Delta y}}{M\Delta t} \tag{B.17}$$

The simplifications yield:

$$\sigma_{\omega_z} = \left( \frac{\sigma_{U_y}^2}{2X_g^2} + \frac{\sigma_{U_x}^2}{2Y_g^2} \right)^{\frac{1}{2}} \tag{B.18}$$

Plugging the assumptions and simplifications into Equation B.8, the modified uncertainty in the convection term is displayed in Equation B.19.

$$\sigma_{conv} = \left[ \left( \frac{\omega_{z_{k+1}} - \omega_{z_{k-1}}}{2Z_g} X_g Y_g \sigma_{U_z} \right)^2 + 2 \left( \frac{U_z X_g Y_g}{2Z_g} \sigma_{\omega_z} \right)^2 \right]^{\frac{1}{2}} \tag{B.19}$$

The values of the vector spacing is known. $Z_g$ is 1 millimeter which is determined from the spacing between the pin holes drilled by a Haas CNC machine. $X_g$ and $Y_g$ were evaluated using a data file exported from LaVision and then having a Matlab program determining the spacing between vector points. $X_g$ and $Y_g$ were both determined to be 0.4240 millimeters.

Figure B.1 shows contours of the spanwise velocity at the 90° azimuthal position. From the figure, the "dark red" contour was used as a representative value for the spanwise velocity which corresponded to a value of 80 mm/s.

For $\omega_{z_{k+1}}$, the 270° azimuthal position was used to determine a representative value for the uncertainty analysis. In Matlab, an average of spanwise vorticity less than -50 $s^{-1}$ (the threshold used to calculate the circulation values) was computed for the entire image to obtain -104 $s^{-1}$. A similar method was used for $\omega_{z_{k-1}}$ to get a representative value of -116 $s^{-1}$ except the 90° azimuthal position was used in order

to have a more drastic difference resulting in a more conservative estimate of the total uncertainty.

The last thing needed prior to calculating the actual value for the uncertainty of the convection term is the approximate number of vectors in a control volume. A rectangular cross-section was used as the control volume, and from the dimension of the vector spacing, it was determined to have approximately $N = 810$ vectors in a section of the control volume.

During the processing of the SPIV images, a window size of 32 $\times$ 32 was used. This implied the magnification ratio was 0.0133 mm/pixel. Lastly, the $\Delta t$ used between laser pulses for the data acquired was 500 microseconds. Using these values, the uncertainties can be obtained as seen below:

$$\sigma_{U_z} = 7.98\frac{mm}{s} \tag{B.20}$$

$$\sigma_{U_x} = \sigma_{U_y} = 2.66\frac{mm}{s} \tag{B.21}$$

$$\sigma_{\omega_z} = 6.273\frac{1}{s} \tag{B.22}$$

$$\sigma_{conv} = 64.372\frac{mm^2}{s^2} \tag{B.23}$$

From Equation B.1, a representative convection value is evaluated to be 86.29 $mm^2/s^2$. An approximation of the relative error in the entire convection term may

be calculated using these values. First, the convection term, expressed in Equation 4.7, can be calculated as the sum of each of the convection values at individual points (Equation B.1) inside the control volume which is shown mathematically in Equation B.24.

$$CONV = \sum_{i=1}^{N} conv_i \tag{B.24}$$

Where $CONV$ is the entire contribution convection has inside the LEV. From here, the total uncertainty in $CONV$ ($\delta_{CONV}$) is shown in Equation B.25.

$$\delta_{CONV} = \left[ \sum_{i=1}^{N} \left( \frac{\partial CONV}{\partial conv_i} \right)^2 \sigma_{conv_i}^2 \right]^{\frac{1}{2}} \tag{B.25}$$

The quantity, $\partial CONV / \partial conv_i$, is equal to 1 which simplifies Equation B.25 to:

$$\delta_{CONV} = \left[ N \sigma_{conv_i}^2 \right]^{\frac{1}{2}} \tag{B.26}$$

Equation B.26 allows for $\delta_{CONV}$ to be represented by the following expression.

$$\delta_{CONV} = \sqrt{N} \sigma_{conv_i} \tag{B.27}$$

Finally, using Equations B.24 and B.27, a ratio of the total uncertainty of the convection term and the overall convection value can be calculated using a singular point as a representative value. This idea is shown in Equation B.28.

$$\frac{\delta_{CONV}}{CONV} = \frac{\sqrt{N}\sigma_{conv_i}}{Nconv_i} \tag{B.28}$$

Then, using Equation B.28, the relative error for the convection term was calculated using Equation B.29.

$$Rel_{error_{conv}} = \left| \frac{\sigma_{conv}}{conv\sqrt{N}} \right| \times 100\% \tag{B.29}$$

The relative error in the convection term was $\pm$ 2.62%. This process of defining the relative error is applied to the other terms in Sections B.2 - B.5, but is not shown for the sake of repetition.

## B.2 Unsteady Term

The unsteady contribution to the vorticity transport analysis was calculated by using the circulation at three consecutive azimuthal positions measured at the $k$ *plane*. The entire flux analysis was performed at the "second" azimuthal position of the three measurements. The unsteady term was calculated using a weighted central difference scheme generalized in Equation B.30.

$$unsteady = \frac{1}{2}\left(\frac{\Gamma_2 - \Gamma_1}{t_1} + \frac{\Gamma_1 - \Gamma_0}{t_2}\right) \tag{B.30}$$

Where $\Gamma_0$, $\Gamma_1$, and $\Gamma_2$ are the "first", "second", and "third" azimuthal positions used in the analysis. The $t_1$ term is the time it takes the blade to traverse from the "second" to the "third" position while $t_2$ is the time it takes the blade to rotate from the "first" to the "second" azimuthal position.

As with the convection term, partial derivatives were calculated to determine the potential sources of error. Equations B.31 - B.35 show the partial derivatives.

$$\frac{\partial unsteady}{\partial \Gamma_2} = \frac{1}{2t_1} \tag{B.31}$$

$$\frac{\partial unsteady}{\partial \Gamma_1} = \frac{-1}{2t_1} + \frac{1}{2t_2} \tag{B.32}$$

$$\frac{\partial unsteady}{\partial \Gamma_0} = \frac{-1}{2t_2} \tag{B.33}$$

$$\frac{\partial unsteady}{\partial t_1} = \frac{-\left(\Gamma_2 - \Gamma_1\right)}{2t_1^2} \tag{B.34}$$

$$\frac{\partial unsteady}{\partial t_2} = \frac{-\left(\Gamma_1 - \Gamma_0\right)}{2t_2^2} \tag{B.35}$$

Adding the errors in quadrature, the general uncertainty for the unsteady term is expressed by Equation B.36.

$$\sigma_{unsteady} = \left\{ \left[\frac{1}{2t_1}\sigma_{\Gamma_2}\right]^2 + \left[\left(\frac{-1}{2t_1} + \frac{1}{2t_2}\right)\sigma_{\Gamma_1}\right]^2 + \left[\frac{-1}{2t_2}\sigma_{\Gamma_0}\right]^2 + \left[\frac{-\left(\Gamma_2 - \Gamma_1\right)}{2t_1^2}\sigma_{t_1}\right]^2 + \left[\frac{-\left(\Gamma_1 - \Gamma_0\right)}{2t_2^2}\sigma_{t_2}\right]^2 \right\}^{\frac{1}{2}} \tag{B.36}$$

To determine the circulation of a vortex, a Matlab code was implemented using a vorticity threshold for a specified area. This method is described discretely in Equation 4.1. Where the uncertainty in $\Gamma$ is:

$$\sigma_\Gamma = \sigma_{\omega_{z_{ij}}} \Delta x \Delta y \sqrt{N} \tag{B.37}$$

Using Equations 4.1 and B.37, relative uncertainty in the circulation is proportional to the relative uncertainty of the vorticity.

$$\frac{\sigma_\Gamma}{\Gamma} = \frac{\sigma_{\omega_{z_{ij}}} \Delta x \Delta y \sqrt{N}}{N \omega_{z_{ij}} \Delta x \Delta y} = \frac{\sigma_{\omega_{z_{ij}}}}{\omega_{z_{ij}} \sqrt{N}} \tag{B.38}$$

The time it takes to move between azimuthal positions is given by Equations B.39 and B.40.

$$t_1 = \frac{1}{\Omega} (\psi_2 - \psi_1) \tag{B.39}$$

$$t_2 = \frac{1}{\Omega} (\psi_1 - \psi_0) \tag{B.40}$$

Where $\Omega$ is the angular velocity, and the general uncertainties in these times are given by Equations B.41 and B.42, respectively.

$$\sigma_{t_1} = \left[ \left( \frac{\partial t_1}{\partial \psi_2} \sigma_{\psi_2} \right)^2 + \left( \frac{\partial t_1}{\partial \psi_1} \sigma_{\psi_1} \right)^2 + \left( \frac{\partial t_1}{\partial \Omega} \sigma_\Omega \right)^2 \right]^{\frac{1}{2}} \tag{B.41}$$

$$\sigma_{t_2} = \left[ \left( \frac{\partial t_2}{\partial \psi_1} \sigma_{\psi_1} \right)^2 + \left( \frac{\partial t_2}{\partial \psi_0} \sigma_{\psi_0} \right)^2 + \left( \frac{\partial t_2}{\partial \Omega} \sigma_\Omega \right)^2 \right]^{\frac{1}{2}} \tag{B.42}$$

To perform the error analysis, the azimuthal positions of 75°, 90°, and 120° were used since this was the earliest azimuthal position investigated where it was hypothesized that the LEV was still in development. This would allow for a more

conservative estimate of the errors. The circulation measurements of the LEV at the *k plane* for each of the three azimuthal positions were -2702.3, -3487.9, and -3651.0 $mm^2/s$, respectively. The angular velocity was $180°/s$ which yielded $t_1 = 0.1667$ and $t_2 = 0.0833$ seconds. With the assumptions the uncertainty associated with the angular velocity, $\sigma_\Omega$, was assumed to be negligible, and the maximum error in positioning the azimuthal location was 2°, the uncertainty in $t_1$ and $t_2$ were both 0.016 seconds.

A similar method used in calculating a representative vorticity value for the convection term was used in the unsteady analysis as well for each of the azimuthal positions at the *k plane*. This resulted in $\omega_{z_{75°}}$, $\omega_{z_{90°}}$, and $\omega_{z_{120°}}$ equaling -125, -116, and -112 $s^{-1}$, respectively.

Applying the above assumptions and values into Equation B.30 and B.36, results in 793.8 and -5202 $mm^2/s^2$, respectively. Using Equation B.43, the relative error in the unsteady term is ± 15.2%.

$$Rel_{error_{unsteady}} = \left| \frac{\sigma_{unsteady}}{unsteady} \right| \times 100\% \tag{B.43}$$

## B.3 Y-Tilting Term

The discrete representation for the Y-tilting term is shown in Equation 4.9. For a single vector location, the Y-tilting term can be expressed by Equation B.44.

$$Y_{Tilting} = \left( \frac{U_{x_{k+1}} - U_{x_{k-1}}}{2Z_g} - \frac{U_{z_{i+1}} - U_{z_{i-1}}}{2X_g} \right) \left( \frac{U_{z_{j+1}} - U_{z_{j-1}}}{2Y_g} \right) X_g Y_g \tag{B.44}$$

The partial derivatives of the Y-tilting term with respect to the potential sources of errors are given in Equations B.45 - B.53.

$$\frac{\partial Y_{Tilting}}{\partial U_{x_{k+1}}} = \frac{X_g \left(U_{z_{j+1}} - U_{z_{j-1}}\right)}{4Z_g} \tag{B.45}$$

$$\frac{\partial Y_{Tilting}}{\partial U_{x_{k-1}}} = \frac{-X_g \left(U_{z_{j+1}} - U_{z_{j-1}}\right)}{4Z_g} \tag{B.46}$$

$$\frac{\partial Y_{Tilting}}{\partial U_{z_{i+1}}} = \frac{-\left(U_{z_{j+1}} - U_{z_{j-1}}\right)}{4} \tag{B.47}$$

$$\frac{\partial Y_{Tilting}}{\partial U_{z_{i-1}}} = \frac{\left(U_{z_{j+1}} - U_{z_{j-1}}\right)}{4} \tag{B.48}$$

$$\frac{\partial Y_{Tilting}}{\partial U_{z_{j+1}}} = \frac{X_g}{2}\left(\frac{U_{x_{k+1}} - U_{x_{k-1}}}{2Z_g} - \frac{U_{z_{i+1}} - U_{z_{i-1}}}{2X_g}\right) \tag{B.49}$$

$$\frac{\partial Y_{Tilting}}{\partial U_{z_{j-1}}} = \frac{-X_g}{2}\left(\frac{U_{x_{k+1}} - U_{x_{k-1}}}{2Z_g} - \frac{U_{z_{i+1}} - U_{z_{i-1}}}{2X_g}\right) \tag{B.50}$$

$$\frac{\partial Y_{Tilting}}{\partial Z_g} = \frac{-X_g \left(U_{x_{k+1}} - U_{x_{k-1}}\right)\left(U_{z_{j+1}} - U_{z_{j-1}}\right)}{4Z_g^2} \tag{B.51}$$

$$\frac{\partial Y_{Tilting}}{\partial X_g} = \frac{\left(U_{x_{k+1}} - U_{x_{k-1}}\right)\left(U_{z_{j+1}} - U_{z_{j-1}}\right)}{4Z_g} \tag{B.52}$$

$$\frac{\partial Y_{Tilting}}{\partial Y_g} = 0 \tag{B.53}$$

Adding the sources of error in quadrature, the general uncertainty in the Y-tilting term is shown in Equation B.54.

$$\sigma_{Y_{Tilting}} = \left[ \left( \frac{\partial Y_{Tilting}}{\partial U_{x_{k+1}}} \sigma_{U_{x_{k+1}}} \right)^2 + \left( \frac{\partial Y_{Tilting}}{\partial U_{x_{k-1}}} \sigma_{U_{x_{k-1}}} \right)^2 + \left( \frac{\partial Y_{Tilting}}{\partial U_{z_{i+1}}} \sigma_{U_{z_{i+1}}} \right)^2 + \left( \frac{\partial Y_{Tilting}}{\partial U_{z_{i-1}}} \sigma_{U_{z_{i-1}}} \right)^2 + \left( \frac{\partial Y_{Tilting}}{\partial U_{z_{j+1}}} \sigma_{U_{z_{j+1}}} \right)^2 + \left( \frac{\partial Y_{Tilting}}{\partial U_{z_{j-1}}} \sigma_{U_{z_{j-1}}} \right)^2 + \left( \frac{\partial Y_{Tilting}}{\partial X_g} \sigma_{X_g} \right)^2 + \left( \frac{\partial Y_{Tilting}}{\partial Y_g} \sigma_{Y_g} \right)^2 + \left( \frac{\partial Y_{Tilting}}{\partial Z_g} \sigma_{z_g} \right)^2 \right]^{\frac{1}{2}} \quad \text{(B.54)}$$

Again, the following assumptions were made:

$$\sigma_{X_g} \approx \sigma_{Y_g} \approx \sigma_{Z_g} \approx 0 \quad \text{(B.55)}$$

$$\sigma_{U_{x_{k+1}}} = \sigma_{U_{x_{k-1}}} = \sigma_{U_x} \quad \text{(B.56)}$$

$$\sigma_{U_{z_{i+1}}} = \sigma_{U_{z_{i-1}}} = \sigma_{U_{z_{j+1}}} = \sigma_{U_{z_{j-1}}} = \sigma_{U_z} \quad \text{(B.57)}$$

The $U_x$ velocity contours for the 90° azimuthal position at the *k-1* and *k+1 planes* are presented in Figure B.2. The top portion of the figure shows the *k-1 plane* while the bottom is the *k+1 plane*. The red contours symbolize velocities moving from left to right while the blue contours show velocities moving from right to left. Comparing the *k-1* and *k+1 planes* in the region where the $U_x$ velocity contours switch from red to blue, there is as much as a 0.1 m/s difference in this region. However, it was estimated for the control volume used in the vorticity transport analysis that

a 0.5 m/s difference between the *k-1* and *k+1 planes* would result in a conservative estimate of the error.

Similarly, Figure B.3 shows the $U_z$ contours for the 270° azimuthal position at the *k plane*. This azimuthal position was chosen because it had the most dramatic changes in velocity gradient from red to blue. In the transition from red to blue contours, the change in the spanwise velocity, $U_z$, from one vector to another can be as high as 0.8 m/s, but 0.3 m/s was selected as a representative value for the entire control volume.

Using these values, results in an uncertainty for the Y-tilting term, $\sigma_{Y_{Tilting}}$, to be 89.01 $mm^2/s^2$, and a representative Y-tilting term equal to -66 $mm^2/s^2$. Equation B.58 is used to determine the relative error for the Y-tilting term, and after plugging in the values, the relative error is ± 4.73%.

$$Rel_{error_{Y_{Tilting}}} = \left| \frac{\sigma_{Y_{Tilting}}}{Y_{Tilting}\sqrt{N}} \right| \times 100\% \tag{B.58}$$

## B.4 X-Tilting Term

The discrete representation of the X-tilting term is given in Equation 4.8. A single vector location can be expressed by Equation B.59.

$$X_{Tilting} = \left( \frac{U_{z_{j+1}} - U_{z_{j-1}}}{2Y_g} - \frac{U_{y_{k+1}} - U_{z_{k-1}}}{2Z_g} \right) \left( \frac{U_{z_{i+1}} - U_{z_{i-1}}}{2X_g} \right) X_g Y_g \tag{B.59}$$

The partial derivatives of the X-tilting term with respect to the potential sources of error are:

$$\frac{\partial X_{Tilting}}{\partial U_{z_{j+1}}} = \frac{U_{z_{i+1}} - U_{z_{i-1}}}{4} \tag{B.60}$$

$$\frac{\partial X_{Tilting}}{\partial U_{z_{j-1}}} = \frac{U_{z_{i-1}} - U_{z_{i+1}}}{4} \tag{B.61}$$

$$\frac{\partial X_{Tilting}}{\partial U_{y_{k+1}}} = \frac{-Y_g \left(U_{z_{i+1}} - U_{z_{i-1}}\right)}{4Z_g} \tag{B.62}$$

$$\frac{\partial X_{Tilting}}{\partial U_{y_{k-1}}} = \frac{Y_g \left(U_{z_{i+1}} - U_{z_{i-1}}\right)}{4Z_g} \tag{B.63}$$

$$\frac{\partial X_{Tilting}}{\partial U_{z_{i+1}}} = \frac{Y_g}{2}\left(\frac{U_{z_{j+1}} - U_{z_{j-1}}}{2Y_g} - \frac{U_{y_{k+1}} - U_{y_{k-1}}}{2Z_g}\right) \tag{B.64}$$

$$\frac{\partial X_{Tilting}}{\partial U_{z_{i-1}}} = \frac{-Y_g}{2}\left(\frac{U_{z_{j+1}} - U_{z_{j-1}}}{2Y_g} - \frac{U_{y_{k+1}} - U_{y_{k-1}}}{2Z_g}\right) \tag{B.65}$$

$$\frac{\partial X_{Tilting}}{\partial X_g} = 0 \tag{B.66}$$

$$\frac{\partial X_{Tilting}}{\partial Y_g} = \frac{-\left(U_{y_{k+1}} - U_{y_{k-1}}\right)\left(U_{z_{i+1}} - U_{z_{i-1}}\right)}{4Z_g} \tag{B.67}$$

$$\frac{\partial X_{Tilting}}{\partial Y_g} = \frac{-Y_g \left(U_{y_{k+1}} - U_{y_{k-1}}\right)\left(U_{z_{i+1}} - U_{z_{i-1}}\right)}{4Z_g^2} \tag{B.68}$$

The general uncertainty in the X-tilting is expressed in Equation B.69 assuming the contributions of the errors can be added in quadrature.

$$\sigma_{X_{Tilting}} = \left[ \left( \frac{\partial X_{Tilting}}{\partial U_{z_{j+1}}} \sigma_{U_{z_{j+1}}} \right)^2 + \left( \frac{\partial X_{Tilting}}{\partial U_{z_{j-1}}} \sigma_{U_{z_{j-1}}} \right)^2 + \left( \frac{\partial X_{Tilting}}{\partial U_{y_{k+1}}} \sigma_{U_{y_{k+1}}} \right)^2 + \left( \frac{\partial X_{Tilting}}{\partial U_{y_{k-1}}} \sigma_{U_{y_{k-1}}} \right)^2 + \left( \frac{\partial X_{Tilting}}{\partial U_{z_{i+1}}} \sigma_{U_{z_{i+1}}} \right)^2 + \left( \frac{\partial X_{Tilting}}{\partial U_{z_{i-1}}} \sigma_{U_{z_{i-1}}} \right)^2 + \left( \frac{\partial X_{Tilting}}{\partial X_g} \sigma_{X_g} \right)^2 + \left( \frac{\partial X_{Tilting}}{\partial Y_g} \sigma_{Y_g} \right)^2 + \left( \frac{\partial X_{Tilting}}{\partial Z_g} \sigma_{Z_g} \right)^2 \right]^{\frac{1}{2}} \quad \text{(B.69)}$$

The same assumptions in Equations B.55 and B.57 were applied here along with Equation B.70.

$$\sigma_{U_{y_{k+1}}} = \sigma_{U_{y_{k-1}}} = \sigma_{U_y} \quad \text{(B.70)}$$

It is known from the Y-tilting term analysis that $\sigma_{U_z}$ is approximately 30 m/s. Using Figure B.4, there is an estimated average difference between the *k-1* and *k+1 planes* of 50 mm/s in the control volume of the analysis. Applying the values, the uncertainty in the X-tilting term was calculated to be 89.01 $mm^2/s^2$ while the X-tilting term was 66 $mm^2/s^2$. Then, Equation B.71 was used to determine the relative error for the X-tilting term which was ± 4.73%.

$$Rel_{error_{X_{Tilting}}} = \left| \frac{\sigma_{X_{Tilting}}}{X_{Tilting}\sqrt{N}} \right| \times 100\% \quad \text{(B.71)}$$

## B.5 Shear Layer Term

The shear layer term was evaluated discretely as described in Equation 4.10. The calculation of a single vector for the shear layer term is shown in Equation B.72.

$$shear = U_x \omega_z Y_g \tag{B.72}$$

Again, taking partial derivatives:

$$\frac{\partial shear}{\partial U_x} = \omega_z Y_g \tag{B.73}$$

$$\frac{\partial shear}{\partial \omega_z} = U_x Y_g \tag{B.74}$$

$$\frac{\partial shear}{\partial Y_g} = U_x \omega_z \tag{B.75}$$

The general uncertainty of the shear layer term is expressed in Equation B.76.

$$\sigma_{shear} = \left[ \left( \frac{\partial shear}{\partial U_x} \sigma_{U_x} \right)^2 + \left( \frac{\partial shear}{\partial \omega_z} \sigma_{\omega_z} \right)^2 + \left( \frac{\partial shear}{\partial Y_g} \sigma_{Y_g} \right)^2 \right]^{\frac{1}{2}} \tag{B.76}$$

Figures B.5 and B.6 show that a representative $U_x$ velocity and $\omega_z$ vorticity value over the left boundary is 100 mm/s and -100 $s^{-1}$, respectively. Those values yield an uncertainty in the shear layer term of 289.9 $mm^2/s^2$ and a value of -4240 $mm^2/s^2$ for Equation 4.10.

Finally, the relative error in the shear layer was calculated to be ± 1.24% using Equation B.77. $N_y$ is the number of vectors along the left boundary which was estimated to be 30 vectors.

$$Rel_{error_{shear}} = \left| \frac{\sigma_{shear}}{shear \sqrt{N_y}} \right| \times 100\% \tag{B.77}$$

## B.6 Annihilation Term

The annihilation term was solved using Equation 4.5. The uncertainty in the annihilation term at a particular azimuthal position was determined by adding in quadrature the uncertainties of the convection, unsteady, Y-tilting, X-tilting, and shear layer terms:

$$\sigma_{annihilation} = \sqrt{\sigma_{conv}^2 + \sigma_{unsteady}^2 + \sigma_{Y_{Tilting}}^2 + \sigma_{X_{Tilting}}^2 + \sigma_{shear}^2} \tag{B.78}$$

From there, the relative error in the annihilation term at a given azimuthal position is calculated using Equation B.79.

$$Rel_{error_{annihilation}} = \left| \frac{\sigma_{annihilation}}{annihilation} \right| \times 100\% \tag{B.79}$$

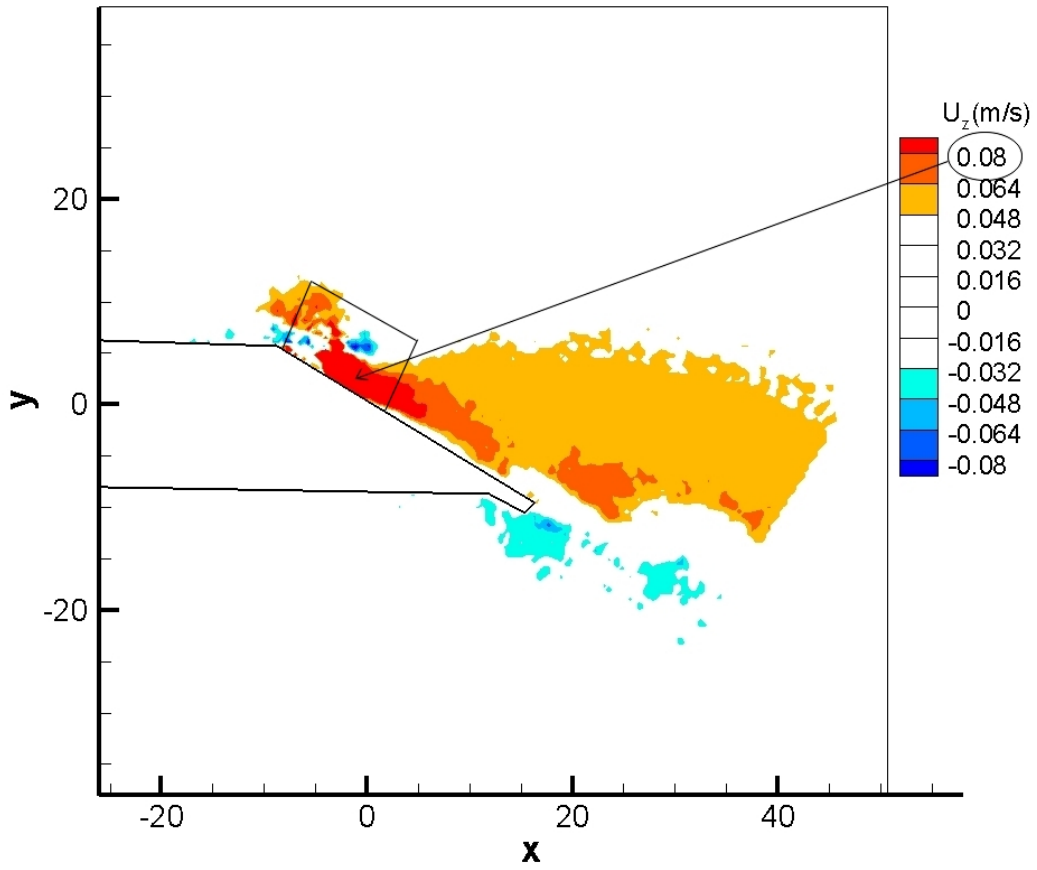


Figure B.1: Spanwise velocity for the 90° azimuthal position at the *k plane*.

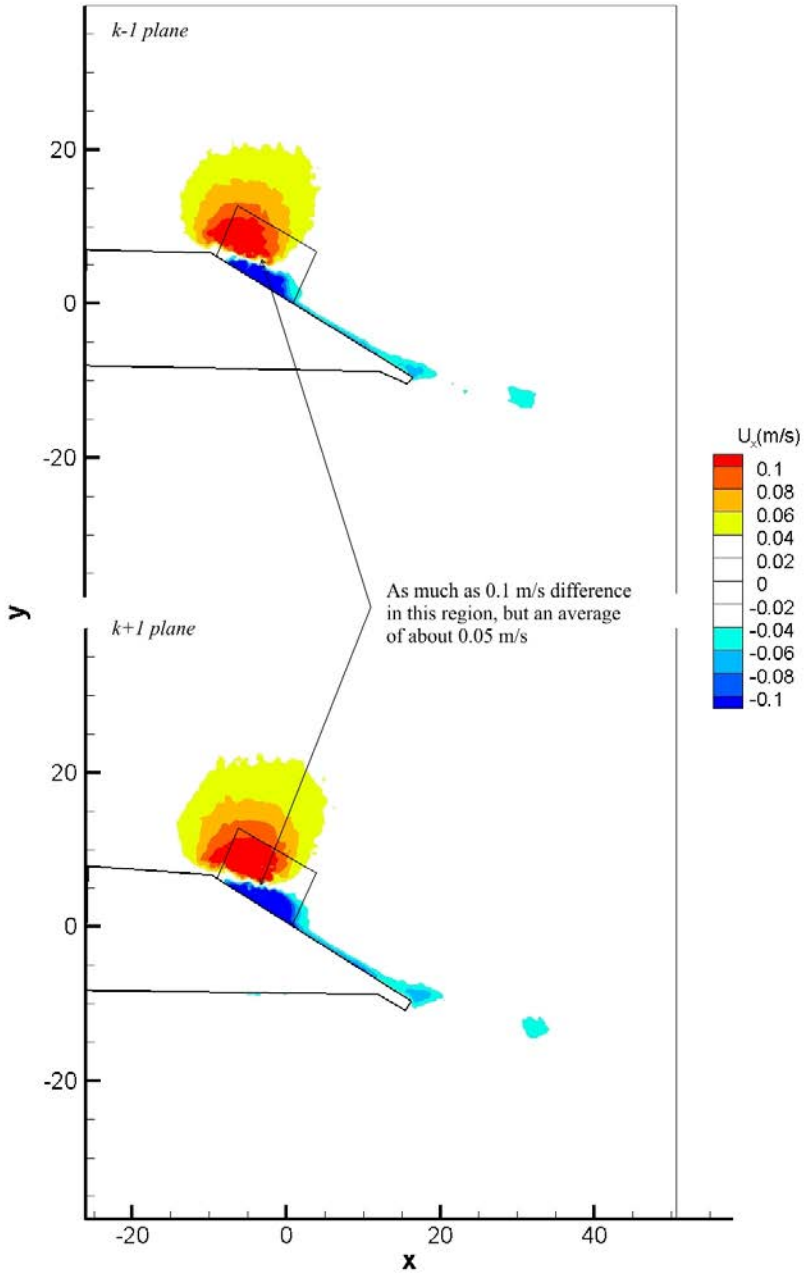


Figure B.2: $U_x$ contours of the *k-1* and *k+1 planes* for the 90° azimuthal position which were used to determine a representative difference of $U_x$ in the control volume of the vorticity transport analysis.

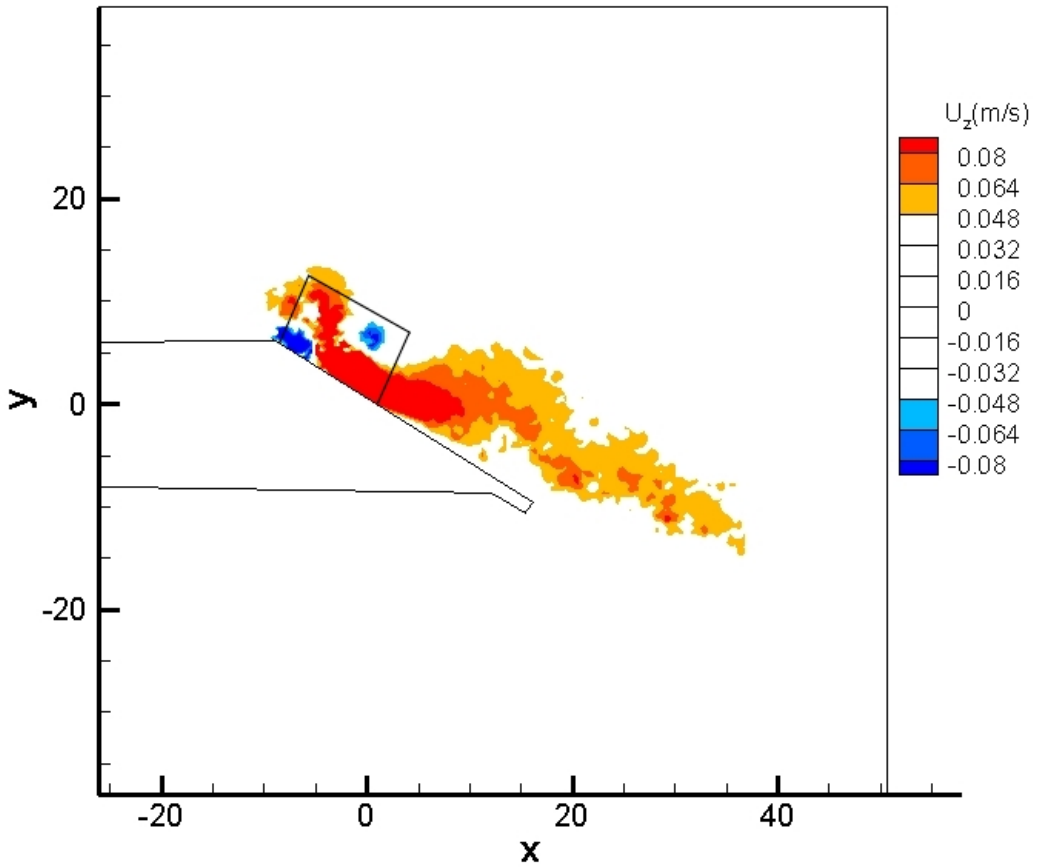


Figure B.3: Spanwise velocity, $U_z$, contours at the *k plane* for the 270° azimuthal position.

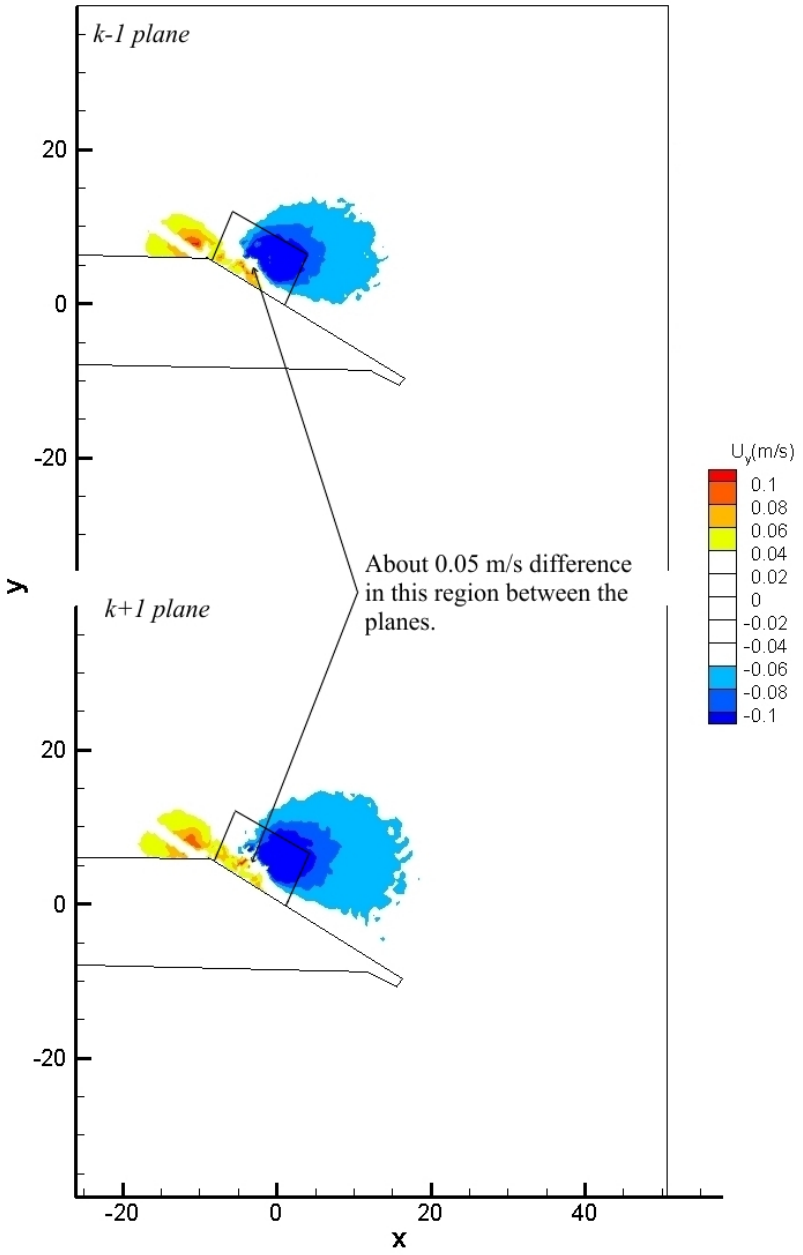


Figure B.4: The $U_y$ component of the velocity at the 90° azimuthal position for the *k-1* and *k+1 planes*. The top portion of the image shows the *k-1 plane* while the bottom is the *k+1 plane*.

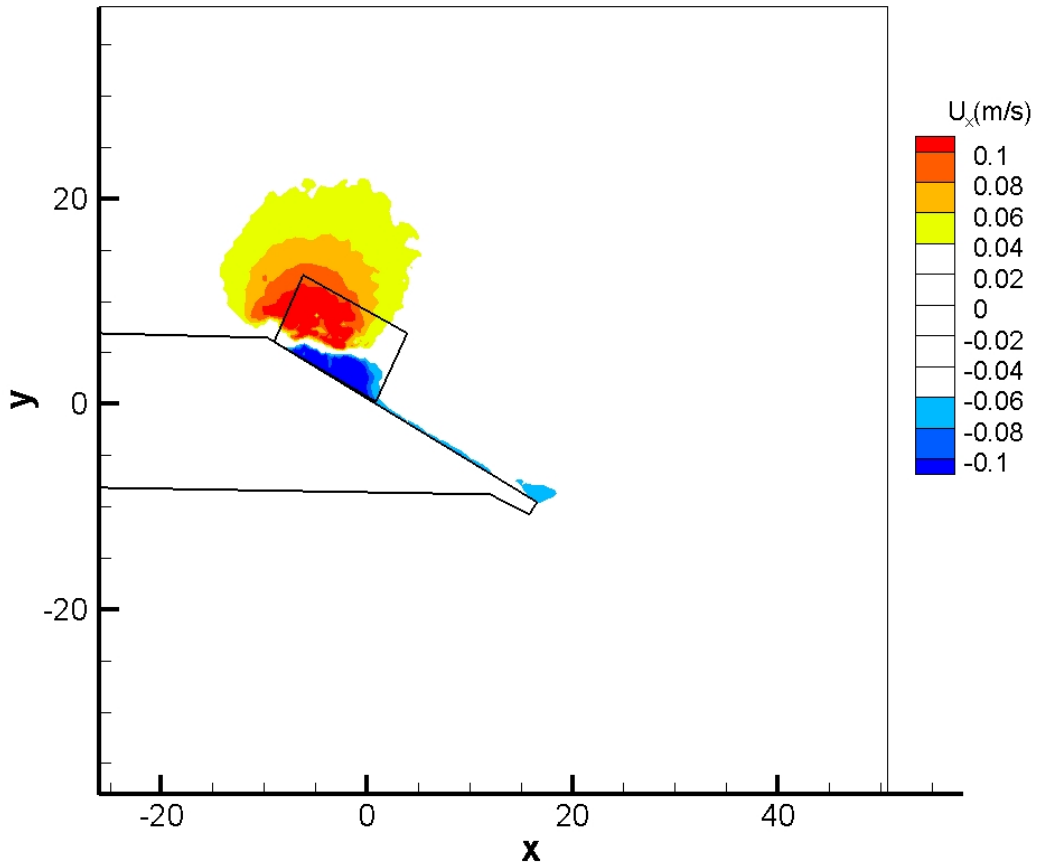


Figure B.5: $U_x$ component of the velocity at the 90° azimuthal position for the $k$ *plane.*

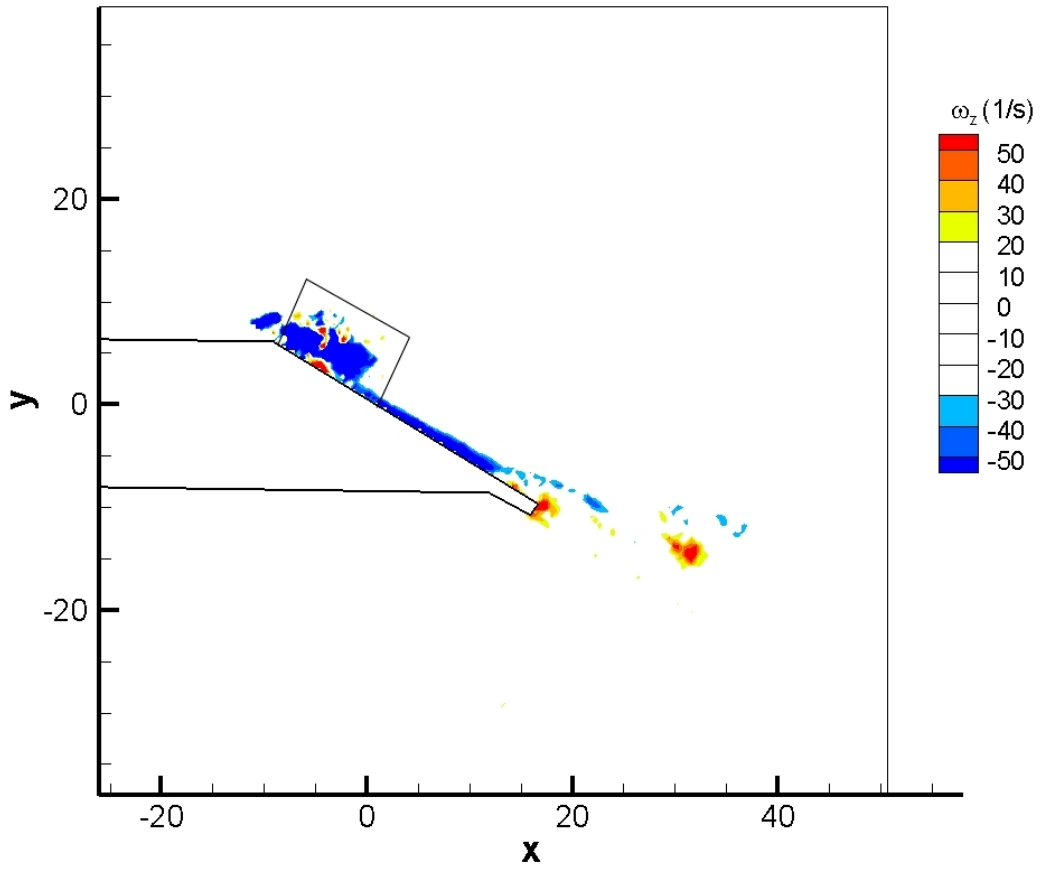


Figure B.6: Vorticity contours at the *k plane* for the 90° azimuthal position.

# REFERENCES


[1] R. J. Adrian. Twenty years of particle image velocimetry. *Exp. Fluids*, 39:159–169, 2005.

[2] R. McN. Alexander. *Advances in Comparative and Environmental Physiology*. Springer-Verlag, 1992.

[3] D. L. Altshuler, R. Dudley, and C. P. Ellington. Aerodynamic forces of revolving hummingbird wings and wing models. *J. Zoology.*, 264:327–332, 2004.

[4] S. A. Ansari, K. Knowles, and R. Żbikowski. Insectlike flapping wings in the hover part 1: Effect of wing kinematics. 45(6):1945–1954, 2008.

[5] S. A. Ansari, N. Phillips, G. Stabler, P. C. Wilkins, R. Żbikowski, and K. Knowles. Experimental investigation of some aspects of insect-like flapping flight aerodynamics for application to micro air vehicles. *Exp. Fluids*, 46:777–798, 2009.

[6] H. Aono, F. Liang, and H. Liu. Near- and far-field aerodynamics in insect hovering flight: An integrated computational study. *J. Exp. Biol.*, 211:239–257, 2007.

[7] R. Bainbridge. The speed of swimming of fish as related to size and to the frequency and amplitude of the tailbeat. *J. Exp. Biol.*, 35:109–133, 1958.

[8] R. Bainbridge. Caudal fin and body movement in the propulsion of some fish. *J. Exp. Biol.*, 40:23–56, 1963.

[9] T. S. Beddoes. A synthesis of unsteady aerodynamic effects including stall hysteresis. *Vertica*, 1:113–123, 1976.

[10] J. M. Birch and M. H. Dickinson. Spanwise flow and the attachment of the leading-edge vortex on insect wings. 412:729–733, 2001.

[11] F. Bohorquez, P. Samuel, J. Sirohi, D. Pines, L. Rudd, and R. Perel. Design analysis and hover performance of a rotating wing micro air vehicle. *J. Amer. Helicopter Soc.*, 48(2):80–90, 2003.

[12] R. J. Bomphrey, N. J. Lawson, N. J. Harding, G. K. Taylor, and A. L. R. Thomas. The aerodynamics of textitManduca sexta: Digital particle image velocimetry analysis of the leading edge vortex. *J. Exp. Biol.*, 208:1079–1094, 2005.

[13] S.-P. Breton, F. N. Coton, and G. Moe. A study on rotational effects and different stall delay models using a prescribed wake vortex scheme and nrel phase vi experiment data. *WIND ENERGY*, 11:459–482, 2008.

[14] M. D. Brodetsky, E. Krause, S. B. Nikiforov, A. A. Pavlov, A. M. Kharitonov, and A. M. Shevchenko. Evolution of vortex structures on the leeward side of a delta wing. *J. Appl. Mech. Tech. Phys.*, 42(2):243–254, 2001.

[15] T. Burton, D. Sharpe, N. Jenkins, and E. Bossanyi. *Wind Energy Handbook*. John Wiley & Sons, LTD, 2009.

[16] L. W. Carr. Progress in analysis and prediction of dynamic stall. *J. Aircraft*, 25:6–17, 1988.

[17] Z. Carr, C. Chen, and M. J. Ringuette. The effect of aspect ratio on the three-dimensional vortex formation of rotating flat-plate wings. In *50th AIAA Aerospace Sciences Meeting including the New Horizons Forum and Aerospace Exposition*, Nashville, Tennessee, 9–12 January 2012.

[18] F. O. Carta. An analysis of the stall flutter instability of helicopter rotor blades. *J. Amer. Helicopter Soc.*, 12:1–18, 1967.

[19] L. Chen and J. J. Wang. Numerical simulations of leading-edge vortex core axial velocity for flow over delta wings. *Sci. China Ser. E*, 52(7):2029–2036, 2009.

[20] J. M. Délery. Robert legendre and henri werlé: Toward the elucidation of three-dimensional separation. *Annu. Rev. Fluid Mech.*, 33:129–154, 2001.

[21] C. Van den Berg and C. P. Ellington. The three-dimensional leading-edge vortex of a 'hovering' model hawkmoth. *Phil. Trans. R. Soc. Lond. B*, 352:329–340, 1997a.

[22] C. Van den Berg and C. P. Ellington. The vortex wake of a 'hovering' model hawkmoth. *Phil. Trans. R. Soc. Lond. B*, 352:317–328, 1997a.

[23] A. DeVoria, P. Mahajan, and M. J. Ringuette. Vortex formation and saturation for low-aspect-ratio rotating flat plates at low reynolds number. In *49th AIAA Aerospace Sciences Meeting including the New Horizons Forum and Aerospace Exposition*, Orlando, Florida, 4–7 January 2011.

[24] A. C. DeVoria and M. J. Ringuette. Vortex formation and saturation for low-aspect-ratio rotating flat-plate fins. *Expts. Fluids*, 52(2):441–462, 2012.

[25] K. P. Dial. An inside look at how birds fly: Experimental studies of the internal and external processes controlling flight. In *38th Report the Aerospace Profession Symposium Proceedings*, Beverly Hills, California, 1994.

[26] M. H. Dickinson and K. G. Götz. Unsteady aerodynamic performance of model wings at low reynolds numbers. *J. Exp. Biol.*, 174:45–64, 1993.

[27] M. H. Dickinson, F. Lehmann, and S. P. Sane. Wing rotation and the aerodynamic basis of insect flight. 284(5422):1954–60, 1999.

[28] A. B. Dubois and C. S. Ogilvy. Forces on the tail surface pf swimming fish: Thrust, drag and acceleration in bluefish (*Pomatomus saltatrix*). *J. Exp. Biol.*, 77:225–241, 1978.

[29] J. Ekaterinaris, A. Cricelli, and M. Platzer. A zonal method for unsteady viscous compressible airfoil flows. *J. Fluids Struct.*, 8:107–123, 1994.

[30] C. P. Ellington, C. van den Berg, A. P. Willmott, and A. L. R. Thomas. Leading-edge vortices in insect flight. *Nature*, 384:626–630, 1996.

[31] R. Ennos. Unconventional aerodynamics. *Nature*, 344:491–491, 1990.

[32] S. T. Gangwani. Synthesized airfoil data method for prediction of dynamic stall and unsteady airloads. *Vertica*, 8(2):93–118, 1984.

[33] B. S. Gerber, J. L. Tangler, E. P. N. Duque, and J. D. Kocurek. Peak and post-peak power aerodynamics from phase vi nasa ames wind turbine data. *Transactions of the ASME*, 127:192–199, 2005.

[34] P. Gopalakrishnan and D. K. Tafti. Effect of rotation kinematics and angle of attack on flapping flight. *AIAA J.*, 47(11):2505–2519, 2009.

[35] P. Gopalakrishnan and D. K. Tafti. Effect of wing flexibility on lift and thrust production in flapping flight. *AIAA J.*, 48(5):865–877, 2009.

[36] K. Granlund, M. Ol, L. Bernal, and S. Kast. Experiments on free-to-pivot hover motions of flat plates. In *40th Fluid Dynamics Conference and Exhibit*, Chicago, Illinois, 28 June–1 July 2010.

[37] D. I. Greenwell. Simple engineering model for delta-wing vortex breakdown. *J. Aircraft*, 40:402–405, 2002.

[38] M. M. Hands, D. A. Simms, L. J. Fingersh, D. W. Jager, J. R. Cotrell, S. Schreck, and S. M. Larwood. Unsteady aerodynamics experiment phase vi: Wind tunnel test configurations and available data campaigns. Technical Report NREL/TP-500-29955, National Renewable Energy Laboratory, Golden, Colorado, December 2001.

[39] F. D. Harris. Preliminary study of radial flow effects on rotor blades. *J. Amer. Helicopter Soc.*, 11(3):1–21, 1966.

[40] H. Hu, A. Gopa Kumar, G. Abate, and R. Albertani. An experimental study of flexible membrane wings in flapping flight. In *47th AIAA Aerospace Sciences Meeting including the New Horizons Forum and Aerospace Exposition*, Orlando, Florida, 5–8 January 2009.

[41] H. Huang, D. Dabiri, and M. Gharib. On errors of digital particle image velocimetry. *Meas. Sci. Tech.*, 8:1427–1440, 1997.

[42] J. R. Hunter and J. R. Zweifel. Swimming speed, tail beat frequency, tail beat amplitude, and size in jack mackerel *Trachurus symmetricus*, and other fishes. *Fishery Bulletin*, 69:253–266, 1971.

[43] Jr. J. D. Anderson. *Fundamentals of Aerodynamics*. McGraw-Hill, 2001.

[44] W. Johnson. *Helicopter Theory*. Dover Publications, 1994.

[45] A. R. Jones and H. Babinsky. Unsteady lift generation on rotating wings at low reynolds numbers. *J. Aircraft*, 47(3):1013–1021, 2010.

[46] A. R. Jones and H. Babinsky. Leading edge vortex development on a waving wing at reynolds numbers between 10,000 and 60,000. AIAA Paper 2011-393, 2011.

[47] A. R. Jones, C. W. Pitt Ford, and H. Babinsky. Three-dimensional effects on sliding and waving wings. *J. Aircraft*, 48(2):633–644, 2011.

[48] K. D. Jones, C. M. Dohring, and M. E. Platzer. Time-domain analysis of low-speed airfoil flutter. *AIAA J.*, 34:1027–1033, 1996.

[49] M. Keennon, K. Klingebiel, H. Won, and A. Andriukov. Development of the nano hummingbird: A tailless flapping wing micro air vehicle. In *50th AIAA Aerospace Sciences Meeting including the New Horizons Forum and Aerospace Exposition*, Nashville, Tennessee, 9–12 January 2012.

[50] M. Kliss, C. Somps, and M. W. Luttges. Stable vortex structures: A flat plate model of dragonfly hovering. *J. Theor. Biol.*, 136:209–228, 1989.

[51] T. G. Lang and D. A. Daybell. Porpoise performance tests in sea-water tank. Technical Report NAVWEPS Report 8060, NOTS TP 3063, U.S. Naval Ordnance Test Station, China Lake, California, 1963.

[52] J. G. Leishman. Challenges in modelling the unsteady aerodynamics of wind turbines. *WIND ENERGY*, 5:85–132, 2002.

[53] J. G. Leishman. *Principles of Helicopter Aerodynamics*. Cambridge University Press, 2 edition, 2006.

[54] J. G. Leishman and T. S. Beddoes. A generalised model for airfoil unsteady aerodynamics behaviour and dynamic stall using indicial method. In *42nd Annual Forum of the American Helicopter Society*, Washington D.C., June 1986.

[55] J. G. Leishman and T. S. Beddoes. A semi-empirical model for dynamic stall. *J. Amer. Helicopter Soc.*, 34:3–17, 1989.

[56] D. Lentink and M. H. Dickinson. Biofluiddynamic scaling of flapping, spinning and translating fins and wings. *J. Exp. Biol.*, 212:2691–2704, 2009a.

[57] D. Lentink and M. H. Dickinson. Rotational accelerations stabilize leading edge vortices on revolving fly wings. *J. Exp. Biol.*, 212:2705–2719, 2009b.

[58] G. C. Lewin and H. Haj-Hariri. Modelling thrust generation of a two-dimensional heaving airfoil in a viscous flow. *J. Fluid Mech.*, 492:339–362, 2003.

[59] M. J. Lighthill. On the weis-fogh mechanism of lift generation. *J. Fluid Mech.*, 60:1–17, 1973.

[60] T. T. Lim, C. J. Teo, K. B. Lua, and K. S. Yeo. On the prolong attachment of leading edge vortex on a flapping wing. *Mod. Phys. Lett. B*, 23(3):357–360, 2009.

[61] H. Liu. Computational biological fluid dynamics: Digitizing and visualizing animal swimming and flying. *Integr. Comp. Biol.*, 42:1050–1059, 2002.

[62] H. Liu and K. Kawachi. A numerical study of insect flight. *Journal of Computational Physics*, 146:124–156, 1998.

[63] M. Luttges. Accomplished insect fliers. In *Frontiers in Experimental Fluid Mechanics*, pages 429–456. Berlin: Springer, 1989.

[64] K. W. Mangler and J. H. B. Smith. A theory of the flow past a slender delta wing with leading edge separation. *P. Roy. Soc. Lond. A Mat.*, 251(1265):200–217, 1959.

[65] S. Mao and H. Hamdani. A study on the mechanism of high-lift generation by an airfoil in unsteady motion at low reynolds number. *ACTA MECHANICA SINICA*, 17(2):97–114, 2001.

[66] S. Mao and W. Jianghao. Large aerodynamic forces on a sweeping wing at low reynolds number. *ACTA MECHANICA SINICA*, 20(1):24–31, 2004.

[67] T. Maxworthy. Experiments on the Weis-Fogh mechanism of lift generation by insects in hovering flight. Part 1. Dynamics of the 'fling'. *J. Fluid Mech.*, 93(1):47–63, 1979.

[68] T. Maxworthy. The fluid dynamics of insect flight. *Annu. Rev. Fluid Mech.*, 13:329–350, 1981.

[69] T. Maxworthy. The formation and maintenance of a leading-edge vortex during the forward motion of an animal wing. *J. Fluid Mech.*, 587:471–475, 2007.

[70] L. A. Miller and C. S. Peskin. When vortices stick: An aerodynamic transition in tiny insect flight. *J. Exp. Biol.*, 207:3073–3088, 2004.

[71] A. Mitchell, S. Morton, and J. Forsythe. Analysis of delta wing vortical substructures using detached-eddy simulation. *AIAA-2002-2968*, 2002.

[72] W. Nachtigall. Rasche richtungsänderungen und torsionen schwingender fliegenflügel und hypothesen über zugeordnete instationäre strömungseffekte. *J. Comp. Physiol.*, 133:351–355, 1979.

[73] A. J. Niven and R. A. McD. Galbraith. Modelling dynamic stall vortex inception at low mach numbers. *Aeronautical Journal*, 101:67–76, 1997.

[74] M. F. M. Osborne. Aerodynamics of flapping flight with application to insects. *J. Exp. Biol.*, 28:221–245, 1951.

[75] C. A. Ozen and D. Rockwell. Flow structure on a rotating plate. *Expts. Fluids*, (52):207–223, 2012.

[76] E. Polhamus. Application of the leading-edge-suction analogy of vortex lift to the drag due to lift of sharp-edge delta wings. Technical Report NASA TN D-4739, Langley Research Center, Hampton, VA, August 1968.

[77] A. K. Prasad and R. J. Adrian. Stereoscopic particle image velocimetry applied to liquid flows. *Expts. Fluids*, 15:49–60, 1993.

[78] V. Y. Pyatetsky. Kinematic characteristics of some fast marine fishes. *Bionika*, 4:11–20, 1970.

[79] M. Raffel, C. Willert, S. T. Wereley, and J. Kompenhans. *Particle Image Velocimetry: A Practical Guide*. Springer, Berlin, 2 edition, 2007.

[80] R. Ramamurti and W. Sandberg. A three-dimensional computational study of the aerodynamic mechanisms of insect flight. *J. Exp. Biol.*, 205:1507–1518, 2002.

[81] M. Ramasamy and J. G. Leishman. Phase-locked particle image velocimetry measurements of a flapping wing. *J. Aircraft*, 43(6):1867–1875, 2006.

[82] M. Ramasamy, J. G. Leishman, and T. E. Lee. Flow field of a rotating wing mav. *J. Aircraft*, 44(4):1236–1244, 2007.

[83] M. A. Reavis and M. W. Luttges. Aerodynamic forces produced by a dragonfly. *AIAA Paper 88-0330*, 1988.

[84] T. S. R. Reddy and K. R. V. Kaza. Analysis of an unswept propfan blade with a semiempirical dynamic stall model. Technical Report NASA Technical Memorandum 4083, The University of Toledo and National Aeronautics and Space Administration, Toledo, Ohio and Cleveland, 1989.

[85] P. G. Saffman and J. S. Sheffield. Flow over a wing with an attached free vortex. *Studies in Applied Mathematics*, 57:107–117, 1977.

[86] S. P. Sane and M. H. Dickinson. The aerodynamic effects of wing rotation and a revised quasi-steady model of flapping flight. *J. Exp. Biol.*, 205:1087–1096, 2002.

[87] T. Sarpkaya. A critical review of the intrinsic nature of vortex induced vibrations. Technical report, Naval Postgraduate School, 2003.

[88] W. Shyy, P. Trizilla, C. k. Kang, and H. Aono. Can tip vortices enhance lift of a flapping wing. *AIAA J.*, 47(2):289–293, 2009.

[89] D. Simms, S. Schreck, M. Hand, and L. J. Fingersh. Nrel unsteady aerodynamics experiment in the nasa-ames wind tunnel: A comparison of predictions to measurements. Technical Report NREL/TP-500-29494, National Renewable Energy Laboratory, Golden, Colorado, June 2001.

[90] C. Somps and M. Luttges. Dragonfly flight: Novel uses of unsteady separated flows. *Science*, 228(4705):1326–1329, 1985.

[91] R. E. Spall, T. B. Gatski, and C. E. Grosch. A criterion for vortex breakdown. *Phys. Fluids*, 30:3434–3440, 1987.

[92] G. R. Spedding and T. Maxworthy. The generation of circulation and lift in a rigid two-dimensional fling. *J. Fluid Mech.*, 165:247–272, 1986.

[93] R. B. Srygley and A. L. R. Thomas. Unconventional lift-generating mechanisms in free-flying butterflies. *Nature*, 420:660–664, 2002.

[94] M. Sun and J. Tang. Unsteady aerodynamic force generation by a model fruit fly wing in flapping motion. *J. Exp. Biol.*, 205:55–70, 2002.

[95] M. Sun and J. Wu. Large aerodynamic forces on a sweeping wing at low reynolds number. *ACTA MECHANICA SINICA*, 20(1):24–30, 2004.

[96] S. Sunada, K. Kawachi, I. Watanabe, and A. Azuma. Fundamental analysis of three-dimensional 'near fling'. *J. Exp. Biol.*, 183:217–248, 1993.

[97] C. Tang and M. Hafez. Finite element/finite volume simulations of viscous flows based on a zonal navier-stokes formulation: Part ii. 17:225–242, 2003.

[98] J. L. Tangler. The nebulous art of using wind tunnel aerofoil data for predicting rotor performance. *WIND ENERGY*, 5:245–257, 2002.

[99] J. L. Tangler. Insight into wind turbine stall and post-stall aerodynamics. *WIND ENERGY*, 7:247–260, 2004.

[100] G. K. Taylor, R. L. Nudds, and A. L. R. Thomas. Flying and swimming animals cruis at a strouhal number tuned for high power efficiency. *Nature*, 425:707–711, 2003.

[101] G. S. Triantafyllou, M. S. Triantafyllou, and M. A. Grosenbaugh. Optimal thrust development in oscillating foils with application to fish propulsion. *J. Fluid Struct.*, 7:205–224, 1993.

[102] C. Tropea, A. L. Yarin, and J. F. Foss. *Springer Handbook of Experimental Fluid Mechanics*. Springer-Verlag Berlin Heidelberg, 2007.

[103] I. H. Tuncer and M. F. Platzer. Thrust generation due to airfoil flapping. *AIAA J.*, 34:324–331, 1996.

[104] J. R. Usherwood. The aerodynamic forces and pressure distribution of a revolving pigeon wing. *Expts. Fluids*, 46:991–1003, 2009.

[105] J. R. Usherwood and C. P. Ellington. The aerodynamics of revolving wings i. model hawkmoth wings. *J. Exp. Biol.*, 205:1547–1564, 2002a.

[106] J. R. Usherwood and C. P. Ellington. The aerodynamics of revolving wings ii. propeller force coefficients from mayfly to quail. *J. Exp. Biol.*, 205:1565–1576, 2002b.

[107] S. K. Venkata and A. R. Jones. Effects of acceleration and pitch variations on a rotating wing. In *50th AIAA Aerospace Sciences Meeting including the New Horizons Forum and Aerospace Exposition*, Nashville, Tennessee, 09–12 January 2012.

[108] J. J. Videler. Swimming movements, body structure and propulsion in cod *Gadus morhua*. In *Vertebrate Locomotion*, pages 1–27, 1981.

[109] J. J. Videler and F. Hess. Fast continuous swimming of two pelagic predators, saithe (*Pollachius virens*) and mackerel (*Scomber scombrus*): A kinematic analysis. *J. Exp. Biol.*, 109:209–228, 1984.

[110] M. R. Visbal. Computed unsteady structure of spiral vortex breakdown on delta wings. *AIAA Paper 96-2074*, 1996.

[111] O. De Vries. On the theory of the horizontal-axis wind turbine. *Annu. Rev. Fluid Mech.*, 15:77–96, 1983.

[112] H. Wagner. Über die enstehung des dynamischen auftriebes von tragflügeln. *Zeitschrift für Angewandte Mathematik und Mechanik*, 5:17–35, 1925.

[113] P. W. Webb. The swimming energetics of trout: I. thrust and power output at cruising speeds. *J. Exp. Biol.*, 55:489–520, 1971.

[114] P. W. Webb. Effects of partial caudal-fin amputation on the kinematics and metabolic rate of underyearling sockeye salmon (*Oncorhynchus nerka*) at steady swimming speeds. *J. Exp. Biol.*, 59:565–581, 1973.

[115] P. W. Webb and R. S. Keyes. Swimming kinematics of sharks. *Fishery Bulletin*, 80:803–812, 1982.

[116] P. W. Webb and P. T. Kostecki. The effect of size and swimming speed on locomotor kinematics of rainbow trout. *J. Exp. Biol.*, 109:77–95, 1984.

[117] T. Weis-Fogh. Quick estimates of flight fitness in hovering animals including novel mechanisms for lift production. *J. Exp. Biol.*, 59:169–230, 1973.

[118] H. Werlé. Méthodes de visualisation des Écoulements hydrauligues. *Houille Blanche*, pages 587–595, 1963.

[119] P. Wilkins and K. Knowles. Investigation of aerodynamics relevant to flapping-wing micro air vehicles. In *18th AIAA Computational Fluid Dynamics Conference*, Miami, FL, 2007.

[120] P. Wilkins and K. Knowles. The leading-edge vortex and aerodynamics of insect-based flapping-wing micro air vehicles. *Aeronaut J.*, 113:253–262, 2009.

[121] A. P. Willmott, C. P. Ellington, and A. L. R. Thomas. Flow visualization and unsteady aerodynamics in the flight of the hawkmoth, *Manduca sexta*. *Phil. Trans. R. Soc. Lond. B*, 352:303–316, 1997.

[122] L. z. Yang and Z. h. Gao. Computation of field structure and aerodynamic characteristics of delta wings at high angles of attack. *Appl. Math. Mech.*, 26(6):797–806, 2005.

[123] J. M. Zanker. The wing beat of *Drosophila melanogaster*. i. kinematics. *Phil. Trans. R. Soc. B*, 327(1238):1–18, 1990.

[124] J. M. Zanker. The wing beat of *Drosophila melanogaster*. ii. dynamics. *Phil. Trans. R. Soc. B*, 327(1238):19–44, 1990.

[125] J. M. Zanker. The wing beat of *Drosophila melanogaster*. iii. control. *Phil. Trans. R. Soc. B*, 327(1238):45–64, 1990.

[126] R. Żbikowski. On aerodynamic modelling of an insect-like flapping wing in hover for micro air vehicles. *Phil. Trans. R. Soc. A*, 360:273–290, 2002.